DEPARTMENT OF COMMERCE · UNITED STATES ·
75
Stimulating America's Progress
1913-1988

NBS TECHNICAL NOTE 1319

U.S. DEPARTMENT OF COMMERCE/National Bureau of Standards

Generation of Standard Electromagnetic Fields in a TEM Cell

Motohisa Kanda
R. David Orr

*T*he National Bureau of Standards[1] was established by an act of Congress on March 3, 1901. The Bureau's overall goal is to strengthen and advance the nation's science and technology and facilitate their effective application for public benefit. To this end, the Bureau conducts research to assure international competitiveness and leadership of U.S. industry, science and technology. NBS work involves development and transfer of measurements, standards and related science and technology, in support of continually improving U.S. productivity, product quality and reliability, innovation and underlying science and engineering. The Bureau's technical work is performed by the National Measurement Laboratory, the National Engineering Laboratory, the Institute for Computer Sciences and Technology, and the Institute for Materials Science and Engineering.

The National Measurement Laboratory

Provides the national system of physical and chemical measurement; coordinates the system with measurement systems of other nations and furnishes essential services leading to accurate and uniform physical and chemical measurement throughout the Nation's scientific community, industry, and commerce; provides advisory and research services to other Government agencies; conducts physical and chemical research; develops, produces, and distributes Standard Reference Materials; provides calibration services; and manages the National Standard Reference Data System. The Laboratory consists of the following centers:

- Basic Standards[2]
- Radiation Research
- Chemical Physics
- Analytical Chemistry

The National Engineering Laboratory

Provides technology and technical services to the public and private sectors to address national needs and to solve national problems; conducts research in engineering and applied science in support of these efforts; builds and maintains competence in the necessary disciplines required to carry out this research and technical service; develops engineering data and measurement capabilities; provides engineering measurement traceability services; develops test methods and proposes engineering standards and code changes; develops and proposes new engineering practices; and develops and improves mechanisms to transfer results of its research to the ultimate user. The Laboratory consists of the following centers:

- Applied Mathematics
- Electronics and Electrical Engineering[2]
- Manufacturing Engineering
- Building Technology
- Fire Research
- Chemical Engineering[3]

The Institute for Computer Sciences and Technology

Conducts research and provides scientific and technical services to aid Federal agencies in the selection, acquisition, application, and use of computer technology to improve effectiveness and economy in Government operations in accordance with Public Law 89-306 (40 U.S.C. 759), relevant Executive Orders, and other directives; carries out this mission by managing the Federal Information Processing Standards Program, developing Federal ADP standards guidelines, and managing Federal participation in ADP voluntary standardization activities; provides scientific and technological advisory services and assistance to Federal agencies; and provides the technical foundation for computer-related policies of the Federal Government. The Institute consists of the following divisions:

- Information Systems Engineering
- Systems and Software Technology
- Computer Security
- Systems and Network Architecture
- Advanced Computer Systems

The Institute for Materials Science and Engineering

Conducts research and provides measurements, data, standards, reference materials, quantitative understanding and other technical information fundamental to the processing, structure, properties and performance of materials; addresses the scientific basis for new advanced materials technologies; plans research around cross-cutting scientific themes such as nondestructive evaluation and phase diagram development; oversees Bureau-wide technical programs in nuclear reactor radiation research and nondestructive evaluation; and broadly disseminates generic technical information resulting from its programs. The Institute consists of the following Divisions:

- Ceramics
- Fracture and Deformation[3]
- Polymers
- Metallurgy
- Reactor Radiation

Generation of
Standard Electromagnetic Fields
in a TEM Cell

Motohisa Kanda
R. David Orr

Electromagnetic Fields Division
Center for Electronics and Electrical Engineering
National Engineering Laboratory
National Bureau of Standards
Boulder, Colorado 80303-3328

CONTENTS

Generation of Standard Electromagnetic Fields
in a TEM Cell

Motohisa Kanda
R. David Orr

This paper documents the facilities and procedures used by the National Bureau of Standards to calibrate radio frequency electric field probes using a transverse electromagnetic (TEM) cell. The advantages, limitations, and physical characteristics of TEM cells are presented. Impedance, field uniformity, and mode structure, critical aspects of a cell as a standard field enclosure, are discussed. The paper concludes with sections on setup and measurement procedures for users, uncertainty in the standard field, and statistical control of the calibration system. Copies of key references are included to provide ready access to the details of topics summarized in the text.

Key words: antenna; antenna calibration; calibration; electromagnetic field; radio frequency; standard field; TEM cell; transverse electromagnetic cell.

1. Introduction

The National Bureau of Standards (NBS) uses three different methods for generating radio frequency (rf) electromagnetic (EM) fields of known frequency, field strength, and polarization [1]. The facilities and their approximate frequency ranges are (1) transverse electromagnetic (TEM) cells (10 kHz-150 MHz); (2) a 30 m x 60 m open-site ground screen (25 MHz-1000 MHz, and (3) a 5 m x 6.7 m x 8.5 m anechoic chamber (500 MHz-40 GHz). This report summarizes the physical and electrical properties of TEM cells and the NBS measurement methods for exploiting their well characterized EM field.

The error budget is presented to quantify just how well the field is characterized, and references include the details of each topic or procedure summarized. This report, therefore, serves to document the procedures and equipment used by NBS to generate and evaluate standard EM fields within TEM cells. Donaldson et al. [2] discuss TEM cells and other enclosures used for generating known radio frequency fields. Their paper provides a useful background for the present report. Except for reference [3], which contains TEM cell construction details and engineering drawings, copies of all cited references are provided with this report.

2. Advantages and Limitations

Two of the three facilities mentioned in the previous section are containers (the TEM cell and anechoic chamber), and the third (the open site) is a half space. Each is an environment into which a signal source projects an EM field. For the open site and anechoic chamber, the source is an antenna, and thus the performance of these two facilities as environments for known EM fields is subject to the limitations of the antennas themselves. Because antennas are bandwidth limited, field measurements over a given frequency range may require more than one antenna. The finite extent of an open site or anechoic chamber may force the measurement point into the near field of the antenna where the radiated field is not planar and where, therefore, the uncertainty in computed field values is greater.

In open site and anechoic chamber measurements, an antenna is the transducer between EM waves on a transmission line and the radiated EM field. However, the TEM cell (fig. 1) is just an enlarged portion of a transmission line and thus eliminates the need for a transducer. As an rf field enclosure, the cell is operated from dc to the frequency at which higher order modes of propagation appear. Over this frequency range the cell supports only TEM plane waves. Thus, in eliminating the source antenna, the TEM cell avoids near-field problems and has only an upper frequency limit. The exterior of the cell is a grounded metal enclosure which shields the internal plane wave field from the external electromagnetic environment and, conversely, contains that field which otherwise would radiate into the surroundings and perhaps interfere with associated equipment. The primary shortcomings of the TEM cell are the upper frequency limit and the restricted working space within the cell compared with an open site or anechoic chamber. The latter is particularly severe in the smaller, higher frequency cells.

In sum, the TEM cell is a shielded enclosure for rf plane wave fields. It is of simple construction and, in its smaller versions, is portable. The field is well characterized and is sufficiently uniform to be useful in the calibration of EM field probes and in susceptibility measurements. Higher frequency operation is attained with a smaller cell but at the expense of working volume within the cell.

3. Physical Characteristics

Details for the construction of a TEM cell are given in [3] and the configuration of a typical cell is shown in figure 1.

The test portion of the cell (enclosing the uniform, well characterized plane wave field) is the center section which is an expanded rectangular "coaxial" transmission line (RCTL) in which the center conductor (the septum) is a thin sheet of metal supported parallel to two opposite walls of the cell. (Some authors refer to the TEM cell as a rectangular-strip transmission line and use the term "rectangular coaxial transmission line" for a line with a thicker center conductor. We use the latter notation to be consistent with the references summarized in this paper). The shell of the cell can be square or rectangular in cross section with the septum either midway between opposite walls (a symmetric cell) or offset from the center plane of the cell (an asymmetric cell) [4]. The trade-off between test volume and field uniformity determines which cell configuration is best for a given application.

The NBS cell that is the subject of this report is used for creating a known EM field in which radio-frequency field probes are calibrated for use as transfer standards, hazard level probes, or general purpose field probes. Because such probes are usually small and their calibration requires a very well defined plane wave field, NBS uses a cell that is rectangular and symmetric with a 2:1 cross section aspect ratio (a/b in fig. 1) at the test volume. The septum is parallel to the large walls of the cell and is supported by dielectric rods. The cell is constructed of 3.2 mm aluminum sheet which is sufficiently rigid to give the cell dimensional stability. The central region of the cell (the "box" between the two tapered sections) is 1.2 m x 0.6 m in cross section and 1.2 m in length. The tapers at each end of the cell electrically match the central region to a 50 Ω input transmission line and a 50 Ω termination at the output end of the cell. Each tapered section is terminated with a coaxial connector whose center conductor is attached to the septum. Access to the test volume is through either of two doors, one in each of two adjoining walls at the test volume.

3

4. Electrical Characteristics

As a device whose purpose is to provide NBS-traceable calibrations of EM field probes, the TEM cell discussed in this report should have (1) minimum impedance mismatch with its input transmission line and the load terminating its output; (2) a known uniform field throughout the test volume (the region in which the device to be calibrated is placed), and (3) a known upper frequency limit.

4.1 Impedance

The characteristic impedance of an RCTL can be expressed in terms of C_o, the capacitance per unit length of transmission line [5] as

$$Z_o = \frac{1}{vC_o} = \frac{1}{\frac{1}{\sqrt{\mu_o \epsilon_o}} C_o} = \frac{\eta_o \epsilon_o}{C_o} \tag{1}$$

where $\eta_o \simeq 120\pi$ Ω is the intrinsic impedance of free space, $\epsilon_o \simeq 10^{-9}/36\pi$ F/m is the free space permittivity, $\mu_o = 4\pi \times 10^{-7}$ H/m is the free space permeability, and $v = (\mu_o \epsilon_o)^{-1/2} \simeq 3 \times 10^8$ m/s. C_o is given in terms of the cell geometry by the approximate expression

$$\frac{C_o}{\epsilon_o} \simeq 4 \ [\frac{a}{b} - \frac{2}{\pi} \ln (\sin \frac{\pi g}{2b})] - \frac{\Delta C}{\epsilon_o} \tag{2}$$

where the dimensions a, b, and g are shown in figure 1. ΔC accounts for the interaction of the edges of the septum with one another. Equation (2) is applicable and ΔC is negligible when

$$\frac{a}{b} \geq 1, \text{ and } \frac{w}{b} \geq 1/2. \tag{3}$$

These conditions are satisfied by the NBS TEM calibration cell. For several values of a/w (cell width with respect to septum width), the dependence of cell capacitance per unit length on a/b is shown in figure 2. Subject to the conditions in eq (3), eqs (1) and (2) can thus be used to determine the septum width necessary to give a 50 Ω characteristic impedance to a cell of known relative dimension, a/b. By means of laboratory models and a time

domain reflectometer, the septum width can be adjusted to minimize reflections along the RCTL and determine the optimum septum shape required to produce the desired cell characteristic impedance.

4.2 Field Uniformity

The unperturbed electric field within the central portion of the cell, as shown in figure 3, has been well characterized by measurements of electric field vs. position in the cell [4] and by theoretical expressions for the cell electric field vs. position [5]. These data are relative values giving the field variation with respect to the field at the center point of the cell between the septum and side wall. When P watts is transmitted through the cell, the absolute electric field in volts per meter at the center of the cell test volume is computed from the expression

$$E = \frac{\sqrt{PR}}{d} \qquad (4)$$

where R is the real part of the cell characteristic impedance in ohms and d is the distance in meters between the septum and side wall that bound the test volume (in figure 1, d=b). This absolute electric field point serves to "calibrate" the relative field data from which the absolute electric field can then be obtained at any point within the test volume.

The theoretical expression for field distribution was derived for an empty cell. The measured field distribution was obtained with a calibrated dipole probe small enough to cause negligible distortion of the field within the cell. However, if a probe to be calibrated occupies one-fifth to one-third of the septum-to-wall distance, there would be some field distortion (in the form of field enhancement) due to the probe shorting out part of the field between septum and wall. In other words, because of the presence of the probe the physical configuration of the cell would differ significantly from the configuration on which the standard field determination was based. Therefore, the EM field within the cell would deviate from the theoretically and experimentally determined distribution and would not have the value at the center point given by eq. (4). To preserve the integrity of the environment giving rise to the standard field, the probe to be calibrated should occupy less than one-third of the septum-to-wall distance.

Theoretical and experimental analyses [4, 6] have been done on field distortion due to a rectangular metal object in a TEM cell. Spiegel et al. [7] have used a quasi-static approximation and numerical integration to derive expressions for the electric field in a TEM cell. Their results are in close agreement with [5]. They have also obtained analytical expressions for the x and y components of the cell magnetic field.

4.3 Higher Order Modes

A very useful feature of the TEM cell as a source of plane wave rf fields is its ability to support fields down to zero frequency. As the name of the cell suggests, these fields are in the TEM mode. The maximum frequency at which the cell provides such a well characterized electro-magnetic environment is determined by the low-frequency cutoff of the first higher order mode. This frequency can be interpreted equivalently as the lowest frequency at which the first higher order mode can exist in a given cell, or as the highest frequency at which the TEM mode exists alone. The cutoff frequencies of the higher order modes depend purely on the cell geometry and have been determined theoretically and experimentally by a number of observers [8, 9, 10]. Figure 4 shows this dependence on geometry for several TEM cell modes whose cutoff wavelengths are computed from Gruner's analysis [8]. Weil and Gruner [11] give an alternative presentation of the first eleven higher order mode cutoff frequencies by plotting them as a function of cell aspect ratio (a/b) for several values of cell characteristic impedance.

As the frequency is increased and some of the power entering the cell couples into higher order modes, those modes are superimposed upon and thus degrade the field configuration of the pure TEM mode. When a higher order mode first appears, it behaves as a traveling wave that reflects back and forth within the cell and which, if not replenished by incoming power, would vanish due to wall losses. Reflection occurs within the cell tapers where the cross section of each taper has narrowed to that of a waveguide whose cutoff frequency is lower than the field frequency within the cell. This traveling wave condition is the first type of perturbation inflicted on the TEM mode by a newly appearing higher order mode.

6

As the frequency is further increased, the guide wavelength λ_g of the field in the cell decreases until it is twice the distance between the two reflection planes (one in each taper). That is, the effective length of the cell is then $\lambda_g/2$ and a cavity resonance that enhances the fields of the higher order mode is established. Thus, these modes perturb the TEM mode through their presence either as traveling waves or standing waves. Theoretical and experimental analyses of mode cutoff and resonance frequencies are given in [12, 13].

In his measurements of the E fields of higher order modes, Hill [12] observed that a given mode may not be detectable between its cutoff frequency and its first resonance frequency. (He speculates that within this frequency range the guide wavelength may be too long with respect to the cell length for the wave to develop.) For this reason, the frequency response of a cell contains windows within which the cell field is primarily the TEM mode even though the field frequency is above cutoff for some higher order modes. These windows in the cell's mode structure vs. frequency may be usable for purposes such as investigating the electromagnetic susceptibility of or emissions from an electronic component. In general, however, the field configuration within the cell after the onset of higher order modes is sufficiently complex and uncertain that NBS uses the calibration cell only in the pure TEM mode region below the cutoff frequency of the first higher order mode. When a cell is used as a standard field source, the analyses of higher order modes are useful only for predicting the lowest cutoff frequency; that is, the highest frequency at which the cell field is reliably pure TEM. For the present cell this limit is approximately 150 MHz. Table 1 gives the dimensions and TE_{10} cutoff frequencies for several NBS TEM cells.

Table 1. Dimensions and TE_{10} cutoff frequencies (f_c) for some NBS TEM cells. When used for calibrating electric field probes, the cell must be operated at less than f_c.

Cell Dimensions			Cell Form Factor	TE_{10} Cutoff Frequency
2a	2b	2w	a/b	(MHz)
	(cm)			
300	300	249	1.0	29
120	120	100	1.0	72
100	60	72	1.67	128
120	60	82.8	2.0	125
50	30	36	1.67	256
30	20	22.8	1.5	408
12	12	10	1.0	718

5. Field Measurement Procedures

The creation of a known rf field within a TEM cell is accomplished by applying a voltage, V, between two parallel plates (septum and cell wall) a distance, d, apart. The electric field at the center of the region between the plates is then E = V/d volts per meter. The geometry and construction of the cell are basic (fig. 1). As a consequence of this conceptual and practical simplicity, the procedure for establishing and computing a standard rf field is also straightforward.

As rf power flows through the cell, the field within the cell can be determined by either of two measurement methods. In figure 5a the output of a signal generator is amplified, cleansed by a low pass filter, passed through the cell, and almost completely absorbed by the 50 Ω termination on the output port of the cell. An rf voltmeter reads the septum-to-wall voltage by means of the voltmeter tee connector at the cell input port.

In figure 5b, the voltmeter and tee are replaced by a dual directional coupler whose side arms are terminated by power meters that read the incident and reflected power at the cell input port. From the net power, P watts, entering the cell and the real part, R ohms, of the cell complex impedance, eq (4) gives the rf electric field, E volts per meter, at the

8

center point of the test volume between septum and wall,

$$E = \frac{\sqrt{PR}}{d} \tag{4}$$

At lower frequencies where the length of the propagating wave is several times the cell length, the methods are equivalent. Regardless of the voltage standing wave ratio (VSWR), the voltage measured at the input port will not differ significantly from the value at the cell center. However, at higher frequencies the voltage standing wave could be short enough to cause noticeable voltage variation between the cell center and either end. For example, suppose a measurement of incident and reflected power at the cell input indicates a VSWR of 1.2:1. This means that, due to a standing voltage wave on the transmission line (including the cell), the maximum line voltage is 20% greater than the minimum line voltage. The distance between the maximum and minimum voltage points is one quarter of the line wavelength λ. Therefore, if the distance from the cell input to the cell center is much less than $\lambda/4$ (that is, the cell is electrically small), a voltage measurement at the cell input will be a good approximation to the voltage at the cell center. If the cell is electrically large, the input line voltage could be 20% greater than the line voltage at the cell center. Thus, the operator must consider the VSWR on the line and the electrical length of the cell in deciding if a voltage measurement at the cell input gives a sufficiently accurate value of the TEM electric field at the cell center. If not, a better value for this field can be obtained by using a time domain reflectometer to measure the line impedance at the cell center. The electric field is then computed from eq (4). In another procedure, a vector voltmeter is used to measure the incident and reflected complex voltages at the cell input. The field at the cell center is obtained by using transmission line equations (or the Smith chart) to translate the line voltage (or line impedance) to the cell center. The frequency and power limitations of the system components such as directional coupler, voltmeter, and power sensors may also determine which measurement method to use. The power handling capacity of the present components sets an upper limit of about 200 V/m to the cell field.

6. Setup and Measurement Procedure

6.1 Setup

1. Check the interior of the cell to be sure that it is clean, that nothing was left in it from a previous measurement, and that the septum's supports and electrical connections are sound.

2. If the absence of a dedicated calibration setup requires gathering and interconnecting components, examine all connectors for obvious defects such as bent center pins, broken or bent spring-loaded receptacles, and dirty or worn mating surfaces. A dimensional mismatch between connectors should be corrected because it may result in either poor electrical contact or the need for extreme closing force which may damage the connectors.

3. Use only the highest quality terminations (that is, lowest VSWR) when outfitting a TEM cell as a calibration facility, and do not exceed their quoted frequency and power specifications.

In Section 4.3 we discussed how higher order modes deteriorate the TEM field configuration within the cell. Further distortion is caused by waves reflected back into the cell from a poorly matched termination on the cell output port. While higher order modes are so intractable that they limit the frequency range over which the cell serves as a standard field enclosure, reflections from the output port can be greatly reduced by employing high quality terminations. The endpoints of the cell are 50 Ω type N connectors and therefore the output termination must be as close as possible to 50 Ω. For example, 150 W terminations are commercially available with a maximum VSWR of 1.1 (reflection coefficient magnitude = $|\Gamma| \simeq 0.05$) from dc to 1.5 GHz; 5 W and 10 W terminations can be obtained with a maximum VSWR of 1.03 ($|\Gamma| \simeq 0.01$).

4. Regularly recalibrate voltmeters and power meters required for the calibration. This will verify the measurement uncertainty which is assigned to them in deriving the net uncertainty quoted for the calibration service. These well characterized meters should be dedicated to the measurement setup and thus made part of the documentation history

of the calibration.

5. Calibrate directional couplers and attenuators over the frequency range of the TEM cell. This provides a more accurate value of coupling factors and attenuation at each measurement frequency than the nominal values furnished by the manufacturer.

6. Interconnect the system components as shown in figure 5a or 5b. If power rather than voltage is being measured, use eq (4) to compute the net power needed to give the maximum electric field required for the calibration. From this value and the forward coupling factor of the directional coupler, compute the power that will be incident on the forward power sensor. Be sure that the sensor is rated to handle this power; if necessary, insert an attenuator between the sensor and coupler sidearm. (The cell characteristic impedance is near enough to 50 Ω that, for the present purpose, the computed net power to the cell may be used to approximate the incident power at the coupler).

In general, be aware of power, voltage, and frequency ratings of all components in the setup. Exceeding these ratings may damage some components or cause them to function outside their optimum operating range.

If the amplifier is driven near its rated output or if its performance deteriorates, a low pass filter at its output will attenuate signal frequency harmonics that may be introduced during amplification. As the frequency is varied, other filters may have to be used in order that the filter cutoff frequency is always less than the second harmonic

of the signal frequency.

7. Orient the probe in the cell according to the type of measurement specified by the customer. The probe handle, fixed or mounted in a rotator, enters the cell through small doors in the cell walls. The

field sensor is positioned at the length and width center of the septum and midway between the septum and wall. Battery-powered probes have a switch to check the battery condition. This should be done before and after each calibration.

8. Prepare a well organized data sheet. It should contain not only columns for all parameters to be varied and measured (and perhaps quantities to be computed), but also spaces for the date, time of day, names of the observers, description of the measurement, and identification of all the equipment used (for example, serial numbers as well as model number so that specific individual components are identified). Such information is essential if the measurement has to be repeated or the data and setup referred to at a later date when the observer's detailed recollections have faded.

6.2 Measurement

1. Turn on all instruments and allow them time to stabilize.

2. a. Calibrate the power sensors against the power meters' internal reference sources.
b. If a voltmeter is being used to set the field within the cell, calibrate the voltmeter at each frequency and voltage at which a measurement is to be made.

3. Set the signal generator to the first measurement frequency and adjust the signal level until the rf voltmeter (or power meters) corresponds to the desired electric field in the cell.

4. Record frequency, rf voltage on (or power through) the cell, and the probe response as displayed by the probe metering circuit.

5. Because setup impedances and the signal generator output vary with frequency, decrease the signal level before changing to the next measurement frequency. This reduces the risk of exceeding the power rating of some components at the new frequency.

6. Perform the measurements at the remaining frequencies and record all data.

7. Repeat the measurement at the first frequency and compare the two probe readings at this frequency to verify the stability of system parameters during the calibration. In the course of the calibration (or previous calibrations) the observers will have acquired a sense of system repeatability. If the original and comparison probe readings differ by more than this expected repeatability, the system should be checked to find the cause of the discrepancy and then the calibration repeated.

7. Standard Field Uncertainty

Following the analysis in [4], the expression for the percent uncertainty in the standard field is obtained from eq (4) and has the form

$$\Delta E(\%) \simeq \left| \ 1/2 \ (\frac{\Delta P}{P} + \frac{\Delta R}{R}) + \frac{\Delta d}{d} + \epsilon_E \right| \ \times \ 100 \tag{5}$$

where ΔP, ΔR and Δd are absolute uncertainties in the net cell power, P, the real part of the cell complex impedance, R, and the septum-to-wall distance, d. In deriving eq (5) higher order error terms were neglected. The quantity ϵ_E is the fractional field nonuniformity due to a test object that occupies no more than approximately one-fifth of the septum to wall distance; ϵ_E was evaluated through field mapping with a small probe. The fractional uncertainties in eq (5) are:

• net power to cell: ±0.03 (power at coupler side arms: ±0.01; coupling factors: ±0.02),

• real part of cell impedance: ±0.03,

• septum-to-wall distance: ±0.01; and

• field nonuniformity: ±0.06.

The total percent uncertainty in the computed standard electric field is then

$$\Delta E(\%) \simeq \left| 1/2 \ (0.03 + 0.03) + 0.01 + 0.06 \right| \ \times \ 100 = 10\%, \text{ or } \simeq 0.8 \text{ dB}.$$

8. Statistical Control

Before a measurement is begun, the operator must verify that the TEM cell system is operating properly. We must therefore define what we mean by "proper operation" and specify which cell parameter (and its value or range of values) will be used to indicate that condition.

13

Because of the mechanical and electrical simplicity of the system, the reflection coefficient of the cell (as a measure of cell impedance) characterizes the operating condition of the cell. The impedance of the cell is affected by deteriorated or broken electrical contacts, a change in septum orientation within the cell (due to loose or broken dielectric supports), objects in the cell, and the impedance of the nominally 50 Ω termination on the output port of the cell (see item 3 in Section 6.1). The influences of these factors on the cell impedance can be detected by measuring the power or voltage reflection coefficient at the input to the cell. In this role as a revealer of things amiss, the reflection coefficient (through its dependence on the cell impedance) not only monitors the condition of the system but also gauges the quality of the system's performance. This function is often assigned to any suitable device (called a check standard) whose response to the system in which it is placed indicates the operating condition of that system. In the present case, a check standard might be a small antenna located within the cell to act as an indicator of the cell electric field. Then, if the antenna did not give the expected response to a reference level of rf power entering the cell, this discrepancy would alert the user to a possible fault in the cell system. However, any check standard will introduce some perturbation into the system it is monitoring. This concern does not arise here because impedance, while providing the same surveillance as a check standard, is an intrinsic property of the cell.

A record of the cell's performance history will be maintained in the form of a statistical data base from which control charts for the reflection coefficient will be developed and used. The data for these charts are obtained by measuring the cell's reflection coefficient each time the cell is used. When adequate data have been obtained on the system, the proper control chart methodology will be determined. Typical control charts monitor not only the mean value of a measurement process but also the spread, or dispersion, in that process. The control limits for each chart are determined from the statistical properties of the underlying measurement data. The magnitude of the cell voltage reflection coefficient approaches zero as the cell impedance is matched more closely to the transmission line and to the cell termination. Therefore, the control chart for the mean

14

voltage reflection coefficient magnitude will not have a lower control limit.

The cell reflection coefficient was measured at 100 MHz for each of three commercially available terminations on the cell output port. The magnitude of the voltage reflection coefficient for the empty cell ranged from 0.027 to 0.029. This very low value indicated an excellent impedance match at the cell input and output ports and that the cell itself was operating properly. Therefore, the cell operating point on the voltage reflection coefficient control chart will be approximately 0.028.

The cell operating condition may also be monitored by an electric field probe as a check standard to sense the cell field as the indicator quantity. In principle this is a workable method and has the advantage of monitoring the cell field directly. The probe would be positioned in the cell at a predetermined point and orientation, and the rf power into the cell set to some reference level. The probe response would then be the parameter used for statistical control. A deficiency in this scheme is that it depends on the repeatibility of power settings and the operator's ability to reproduce the position and orientation of the probe in the cell. The uncertainty in these experimental factors (power settings and probe positioning) will introduce additional components of error into the data used for the control charts. Thus the effectiveness of this method for evaluating the operating condition of the cell may be reduced. Monitoring the cell performance by reflection coefficient measurements does not require critically positioning a detector in the cell or setting an absolute power level; only power ratios are used. For any such control scheme, the statistical properties of experimental data on the TEM cell must be determined before the proper control chart methodology can be developed. Here we are suggesting an approach that is reasonable from both a statistical and an engineering perspective.

9. Summary

A TEM cell is employed for creating standard electromagnetic fields. The most important electrical properties of the cell in establishing a known electromagnetic field are the cell characteristic impedance, the highest frequency at which the cell can operate in the TEM mode, and the field uniformity between septum and side wall. All three properties have been

documented by theoretical analyses supported by measurements. Field nonuniformity introduced by the presence of a test object in the cell has been evaluated by field mapping in the vicinity of the object. Electromagnetic fields up to about 150 MHz and 200 V/m can be produced with an uncertainty of ±0.8 dB.

10. Acknowledgements

The authors thank Dennis L. Friday for his review of and contributions to Section 8 of this paper and M. L. Crawford for providing original figure artwork.

11. References

[1]   Larsen, E. B. Techniques for producing standard EM fields from 10 kHz to 10 GHz for evaluating radiation monitors. Proc. Symp. on Electromag. Fields in Biolog. Systems; 1978 June; Ottawa, Canada. 96-112.

[2]   Donaldson, E. E.; Free, W. R.; Robertson, D. W.; Woody, J. A. Field measurements made in an enclosure. Proc. IEEE 66(4): 464-472; 1978 April.

[3]   Decker, W. F.; Wilson, W.A.; Crawford, M. L. Construction of a large transverse electromagnetic cell. Nat. Bur. Stand. (U.S.) Tech. Note 1011; 1979 February.

[4]   Crawford, M. L. Generation of standard EM fields using TEM transmission cells. IEEE Trans. Electromagn. Compat. EMC-16(4): 189-195; 1974 November.

[5]   Tippet, J. C.; Chang, D. C. Radiation characteristics of dipole sources located inside a rectangular, coaxial transmission line. Nat. Bur. Stand. (U.S.) NBSIR 75-829; 1976 January.

[6]   Kanda, M. Electromagnetic field distortion due to a conducting rectangular cylinder in a transverse electromagnetic cell. IEEE Trans. Electromagn. Compat. EMC-24(3): 294-301; 1982 August.

[7]   Spiegel, R. J.; Joines, W. T.; Blackman, C. F.; Wood, A. W. A method for calculating electric and magnetic fields in TEM cells at ELF. IEEE Trans. Electromagn. Compat. EMC-29(4):265-272; 1987 November.

[8]   Gruner, L. Higher order modes in rectangular coaxial waveguides. IEEE Trans. Microwave Theory Tech. MTT-15(8): 483-485; 1967 August.

[9]   Tippet, J. C.; Chang, D.C.; Crawford, M. L. An analytical and experimental determination of the cutoff frequencies of higher order TE modes in a TEM cell. Nat. Bur. Stand. (U.S.) NBSIR 76-841; 1976 June.

[10]   Tippet, J. C.; Chang, D. C. Higher order modes in rectangular coaxial line with infinitely thin conductor. Nat. Bur. Stand. (U.S.) NBSIR 78-873; 1978 March.

[11]   Weil, C.; Gruner, L. High-order mode cutoff in rectangular striplines. IEEE Trans. Microwave Theory Tech. MTT-32(6):638-641; 1984 June.

[12]   Hill, D. A. Bandwidth limitations of TEM cells due to resonances. J. Microwave Power. 18(2): 181-195; 1983.

[13]   Wilson, P. F.; Ma, M. T. Simple approximate expressions for higher order mode cutoff and resonant frequencies in TEM cells IEEE Trans. Electromagn. Compat. EMC-28(3): 125-130; 1986 August.
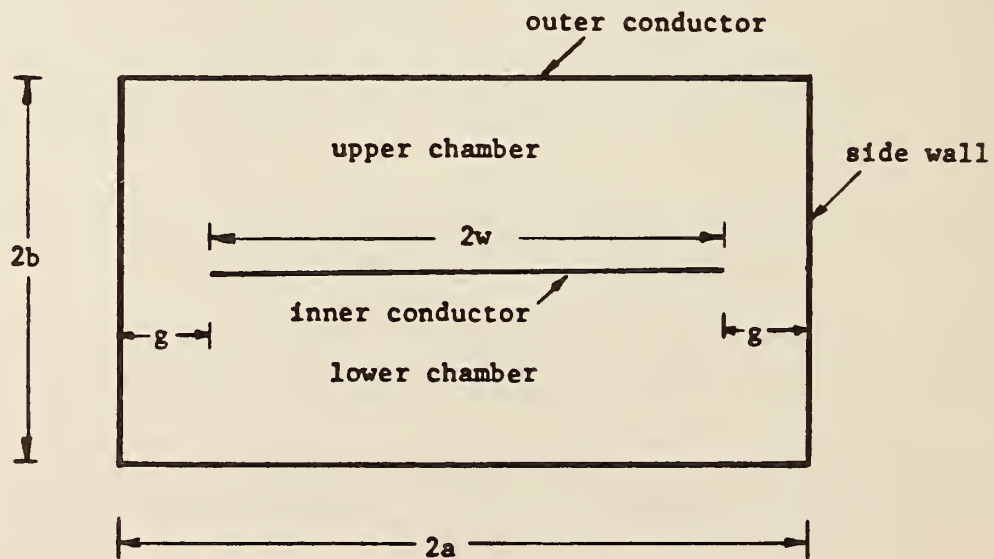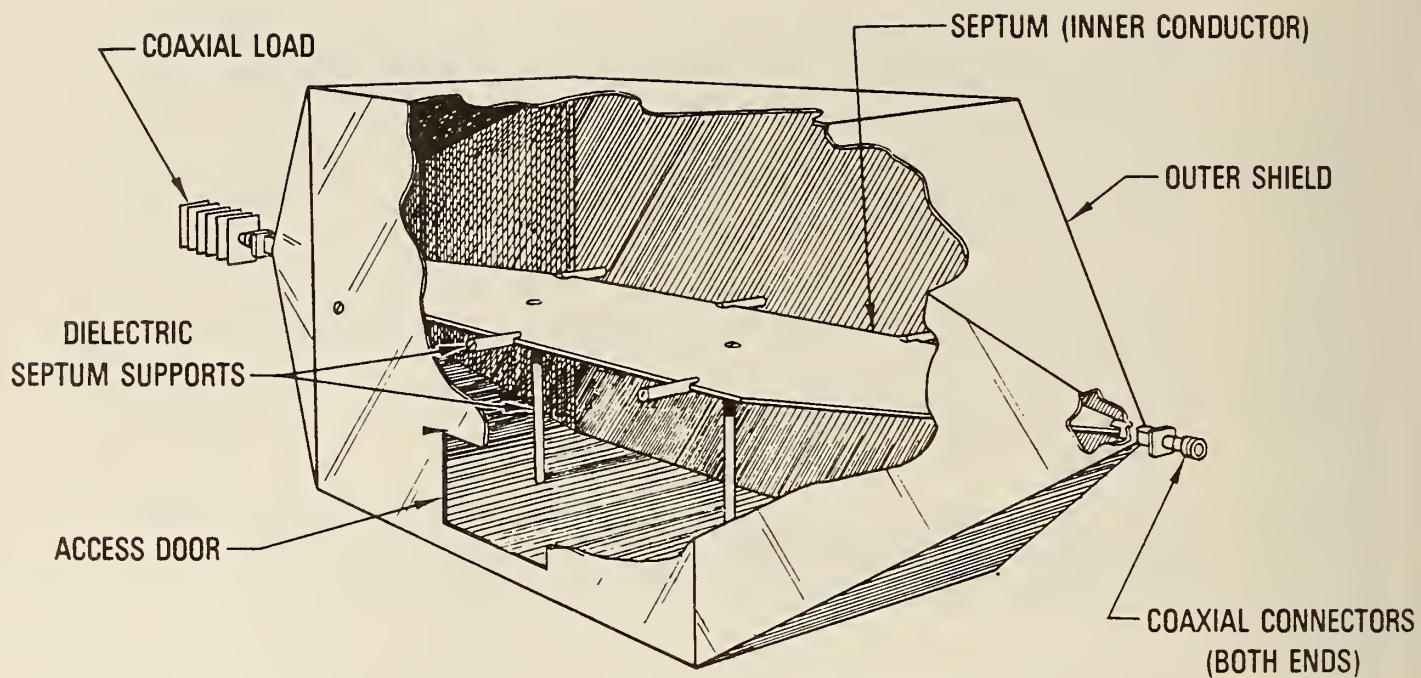
Figure 1. A typical NBS TEM Cell.
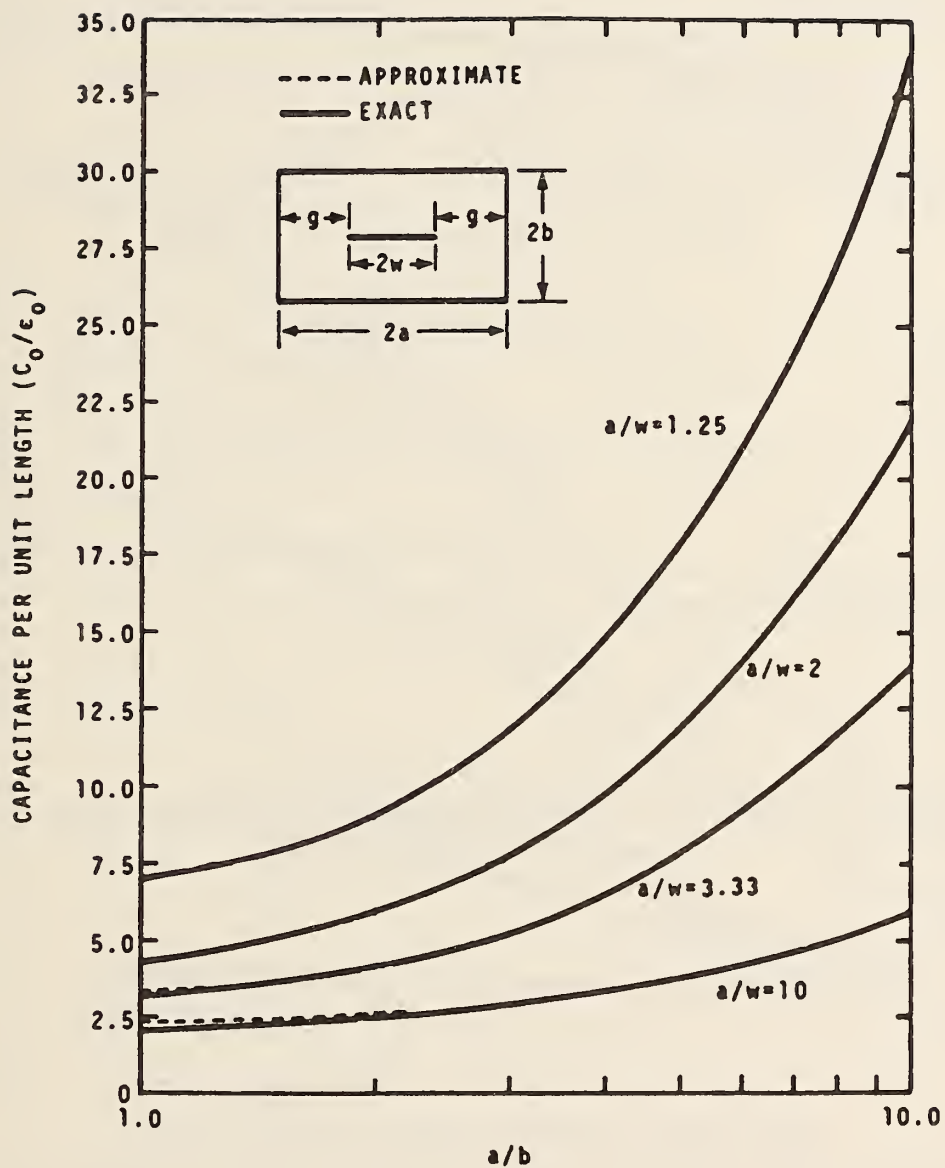
Figure 2. Capacitance per unit length of a TEM cell as a function of cell geometry [5].
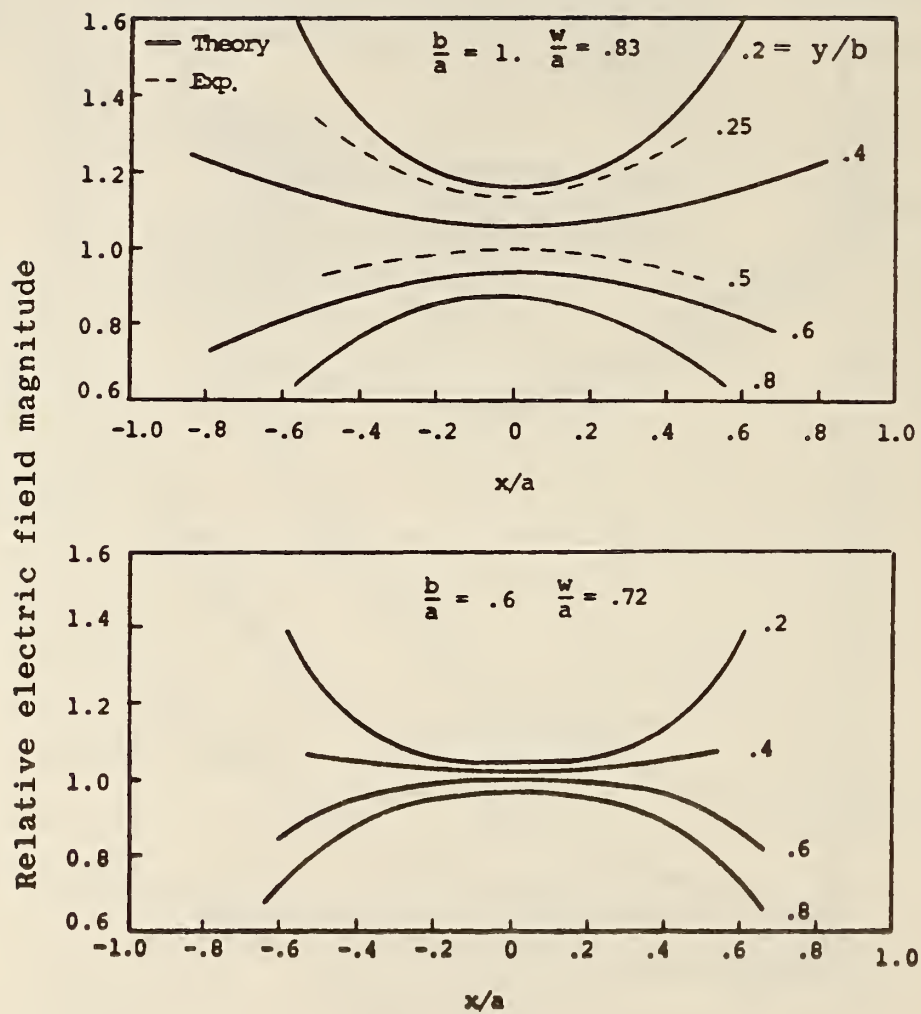
Figure 3. Computed and measured values of the total electric field magnitude, normalized to the TEM cell central electric field V/d volts per meter [4, 5].
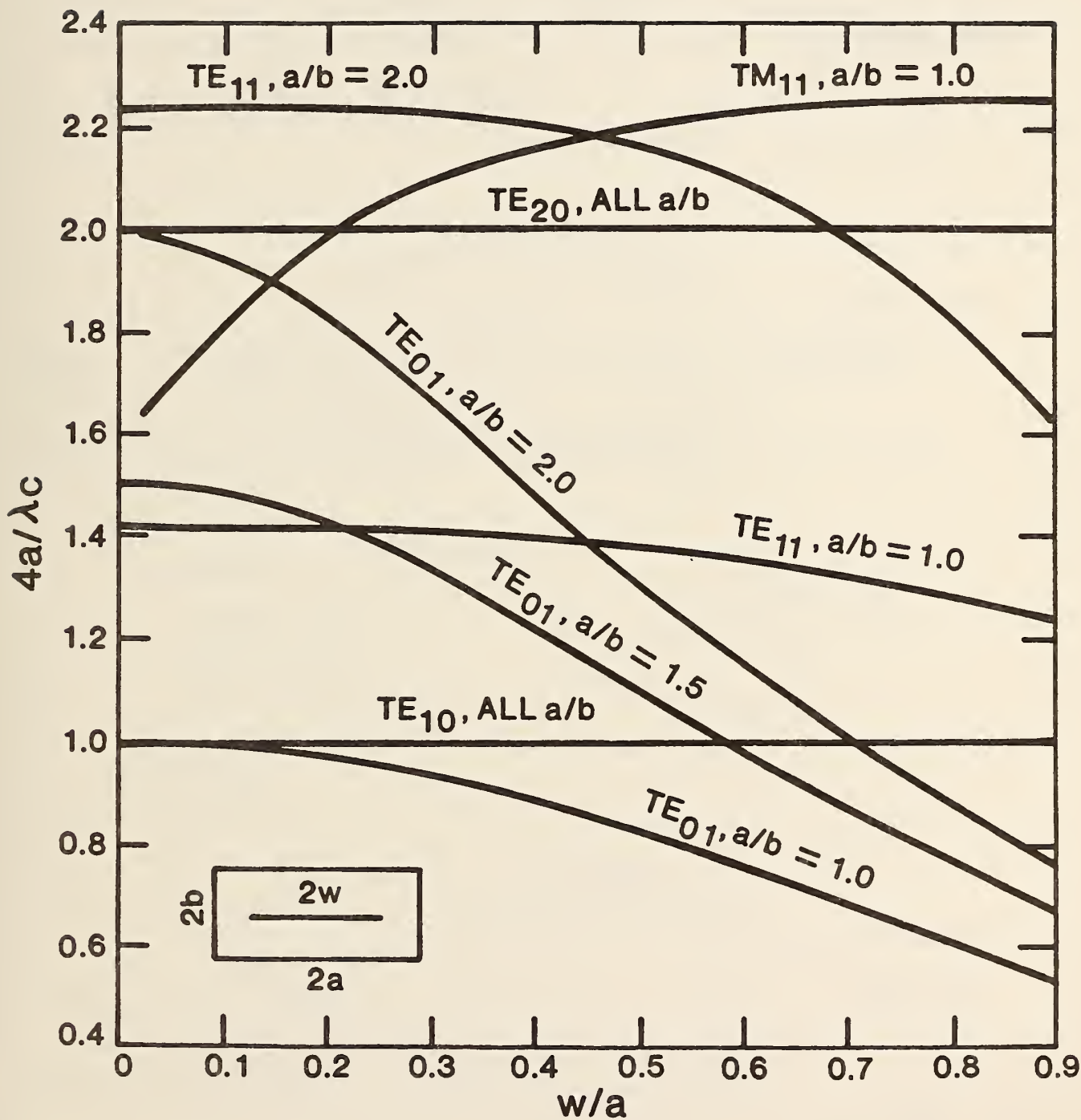
Figure 4. Cutoff wavelengths of some higher order modes as a
function of TEM cell geometry [8].
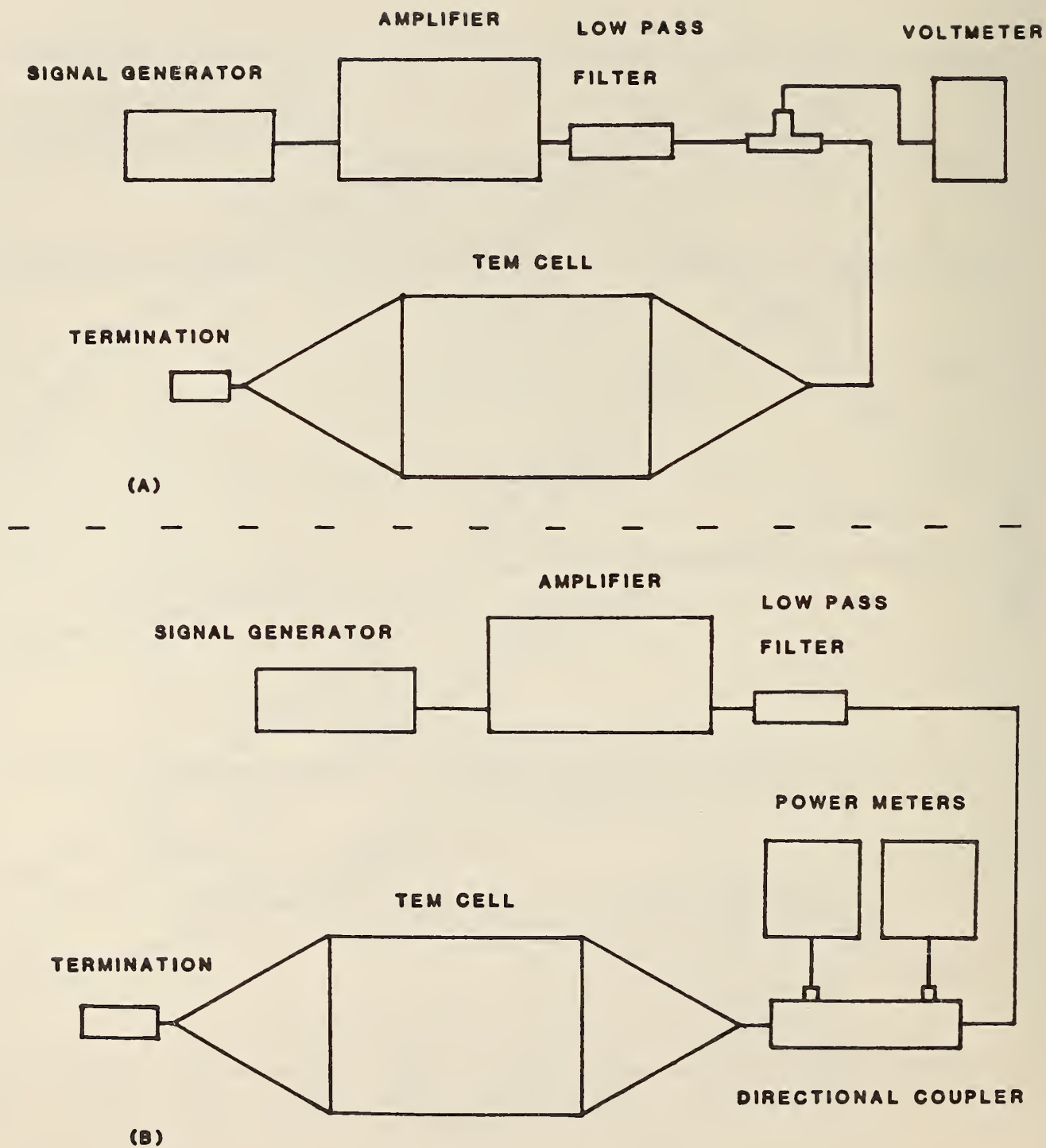
Figure 5. Setup for determining the TEM cell standard field from a measurement of: a) septum-to-wall voltage; b) net power into the cell.

Appendix A

Larsen, E. B. "Techniques for producing standard EM fields from 10 kHz to 10 GHz for evaluating radiation monitors."

Reprinted from the Proceedings of the 1978 Symposium on Electromagnetic Fields in Biological Systems, 1978 June; Ottawa, Canada.

TECHNIQUES FOR PRODUCING STANDARD EM FIELDS
FROM 10 kHz to 10 GHz FOR EVALUATING RADIATION MONITORS

E.   B. Larsen
Electromagnetic Fields Division
National Bureau of Standards
Boulder, Colorado 80303

1.   Introduction

The approach used at the National Bureau of Standards (NBS) for evaluating
and calibrating rf radiation monitors is to generate a calculable or "standard"
field and then immerse the probe of the monitor being tested in this known
field. The optimum type of field-generating instrumentation depends on the
frequency band and desired accuracy. A convenient device at frequencies up to
300 MHz is a rectangular "coaxial" transmission line known as a transverse elec-
tromagnetic mode (TEM) cell. In the frequency range of 300 to 1000 MHz, a series
of rectangular waveguide transmission lines can be used to generate a field with
approximately known intensity. Also, in the frequency range of 100 to 500 MHz,
high-level fields extending over a larger volume can be produced at an outdoor
field site in the near zone of open-end waveguide radiators. Calibrating fields
above 500 MHz are produced in an anechoic chamber by a series of standard-gain
pyramidal horns. In all cases it is possible to calculate the electric and
magnetic field strengths (and equivalent free-space power density) in terms of
the measured power flow through the cell or waveguide, or the power delivered to
the open-end waveguide or horn antenna. Standard fields can be established over
the entire frequency range up to 10 GHz with an uncertainty less than ± 0.5 dB.
The purpose of this paper is to describe the above techniques, suggesting a pre-
ferred approach for each frequency band in the total 10-kHz to 10-GHz range.

2.   Description of techniques for generating known field intensities
      for calibrating radiation hazard monitors

2.1 TEM cells, 10 kHz to 300 MHz

A TEM cell consists of a large 50-ohm transmission line in which the
center conductor is a flat metal strip and the outer (grounded) conductor has
a rectangular cross section. Two TEM cells are used at NBS to cover the lower
frequency bands. The larger one has a 0.6 m x 1 m cross section and a length

of 2 meters. It is accurate for frequencies up to about 150 MHz, but above this frequency higher-order waveguide modes may cause errors. A smaller cell, with a smaller calibrating volume, is used to cover the 150- to 300-MHz frequency band.

At frequencies sufficiently low so that only the principal wave (TEM mode) propagates through the cell, a uniform and calculable electromagnetic field is established [1,2, and 3]. The electric field at these frequencies, midway between the center conductor and the bottom of the cell, is given by the equation:

$$E = \frac{V}{D} = \frac{\sqrt{50\ P}}{D} \tag{1}$$

where:

E = Electric field strength, volts/meter,

V = Voltage between the center conductor and the outer cell wall, volts,

D = Distance from the center conductor to the bottom of the cell, meters,

P = Power transmitted through the cell, watts,

50 = Characteristic impedance of the transmission cell,

= Resistance of the terminating load, ohms.

A block diagram of the instrumentation used to produce a standard field by means of a TEM cell is given in figure 1. The field intensity, as calculated from equation (1), can then be used to calibrate a radiation hazard meter or a small transfer probe with an uncertainty of ± 0.5 dB [3 and 4]. An electrically short dipole 5 cm long is used at NBS as a transfer probe since its response is essentially flat vs. signal frequency [3, 5, and 6].

2.2 Waveguide chambers, 300 to 1000 MHz

For the frequency range of 300 to 1000 MHz, NBS makes use of a set of three waveguide sections, each having a rectangular cross section with width-to-height (aspect) ratio of two to one. A block diagram of the instrumentation is given in figure 2. The length of each guide "cell" exceeds two wavelengths over the specified frequency band, in order to create a fairly uniform field within the guide. Electromagnetic power is transmitted through the guide to a matched resistive load, and the upper frequency in each guide is limited to that in which operation is in the dominant TE_{10} mode. In this well-known case, the direction of the electric field vector is across the narrow face of the guide, as shown in the following sketch.
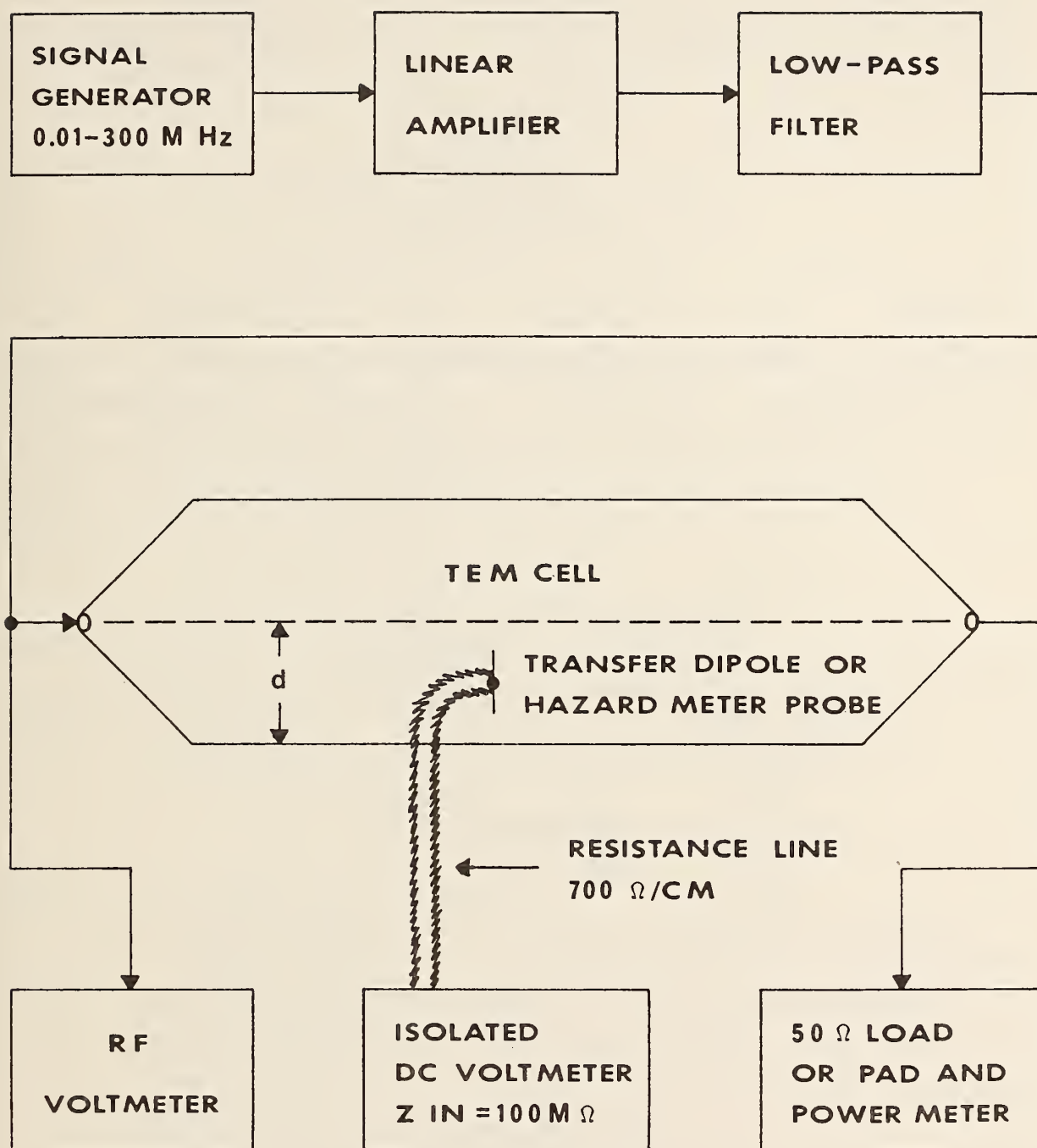
Figure 1. Instrumentation for generating a known electromagnetic field in a TEM cell to calibrate a dipole transfer probe or an rf radiation monitor.
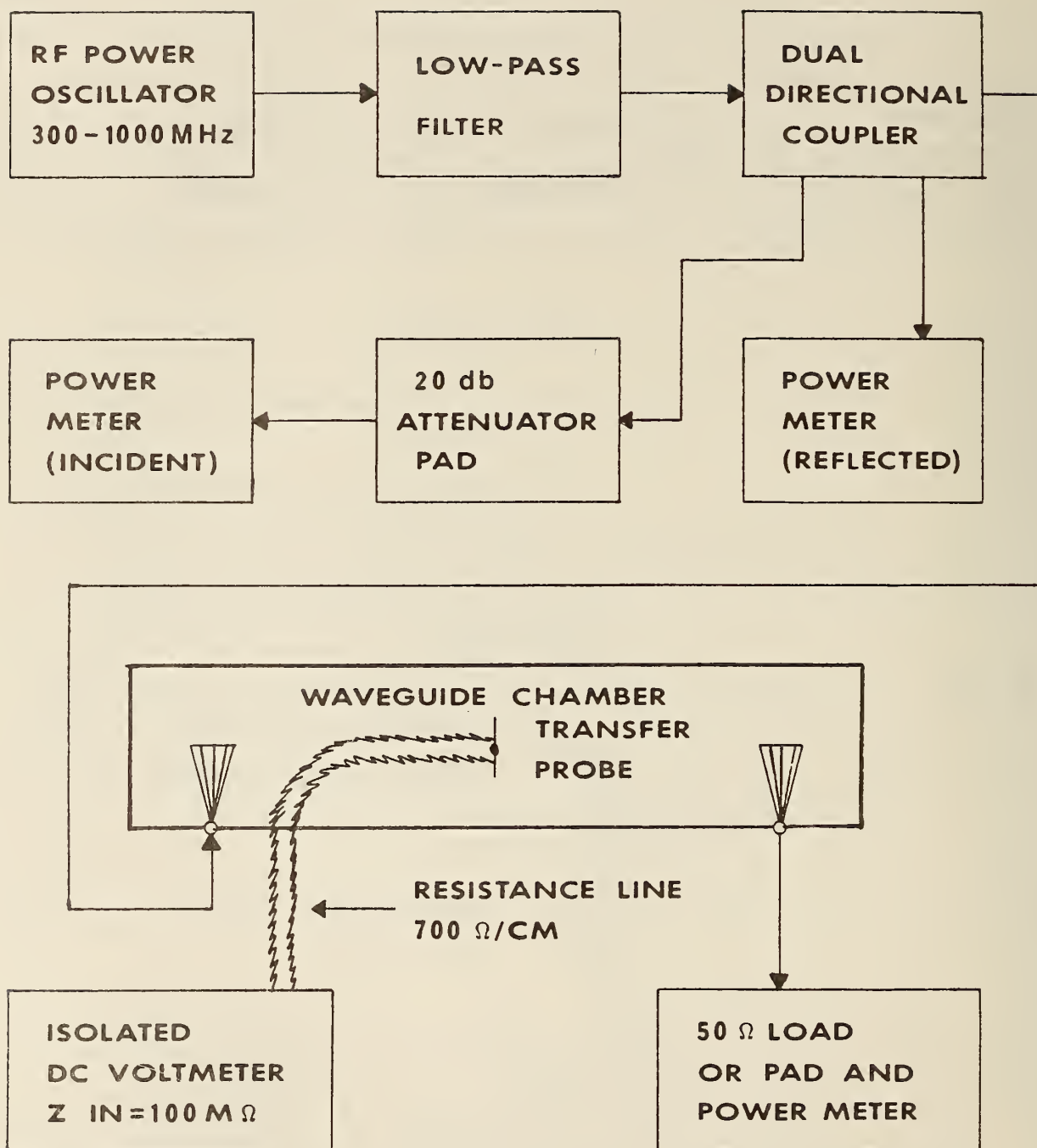
Figure 2. Instrumentation for generating an electromagnetic field in a waveguide chamber.
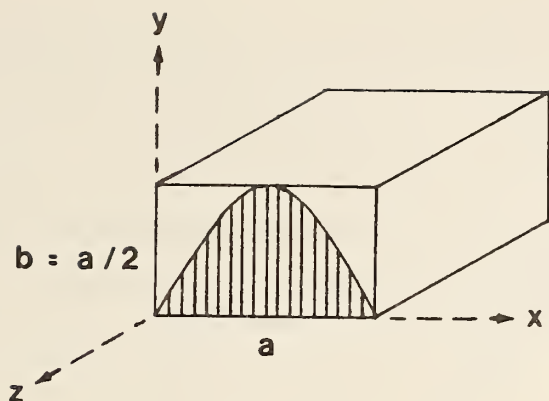
The E-field amplitude (E_y) is constant in the y direction and varies sinusoidally in the x direction. Propagation is in the z direction. Assuming good conductivity of the waveguide walls, air dielectric, and sinusoidal excitation, the lowest "cutoff" frequency which will propagate in the guide (f_{co}) is given by:

$$f_{co} = \frac{1.5 \times 10^8}{a}$$

where f_{co} is in Hertz and a is the guide width in meters.

The largest or "cutoff" wavelength is given by $\lambda_{co} = 2a$. The wavelength inside the guide (λ_{wg}) for these operating conditions is given by:

$$\frac{1}{\lambda_{wg}} = \sqrt{\left(\frac{1}{\lambda_o}\right)^2 - \left(\frac{1}{\lambda_{co}}\right)^2} \tag{2}$$

where λ_o is the free-space wavelength.

The transverse impedance (Z_w) of the wave traveling in the guide is:

$$Z_w = \frac{-E_y}{H_x} = Z_o\left(\frac{\lambda_{wg}}{\lambda_o}\right) = \frac{Z_o}{\sqrt{1 - (\lambda_o/2a)^2}} \tag{3}$$

where:

   Z_w = Wave impedance in the guide, ohms, and

   Z_o = Intrinsic impedance of free space $\simeq$ 377 ohms.

The E and H fields at the center of a rectangular waveguide can be obtained from the equations:

$$E_y = \sqrt{\frac{2\, Z_w\, P_z}{ab}} \qquad \text{and} \qquad H_x = \sqrt{\frac{2\, P_z}{Z_w\, ab}} \tag{4}$$

29

where:

E_y = RMS magnitude of the E field in the center of the waveguide, V/m

H_x = RMS magnitude of the H field in the guide center, A/m

P_z = Total power flow in the guide, watts, and

ab = Cross section area of the waveguide in square meters = $0.5 \, a^2$.

The above equations can also be used to calculate the power required to produce a desired E or H field in the center of the guide. The value of an "equivalent" free-space power density at the center of the guide, in W/m^2, is given by:

$$S_o \equiv \frac{E^2}{Z_o} = \left[\frac{2P}{ab}\right] \left(\frac{Z_w}{Z_o}\right) \quad . \tag{5}$$

However, the uncertainty of the calculated field in a waveguide is quite large (2 dB or more) due to standing waves which may occur in the guide at certain frequencies. It is thus necessary to check the field uniformity in a waveguide calibration chamber by measuring the field strength with a short dipole probe which has been checked and is known to be essentially flat over the frequency range in question [3]. A typical calibration curve for an electrically short dipole is shown in figure 3. The amplitude range covered is 1 to 1000 V/m which corresponds to a free-space power density range of about 0.25 $\mu W/cm^2$ to 250 mW/cm^2. By this procedure the uncertainty of the calibrating field within a waveguide cell can be established with an uncertainty of $\pm$ 0.5 dB [7 and 8].

2.3 Open-end waveguide radiators, outdoor field site, 100 to 500 MHz

Another approach now being evaluated to cover the 100 to 500 MHz frequency range involves the use of large waveguide launchers [1 and 3]. This technique is especially useful for occasional calibrations of larger antennas and probes which would cause perturbation of the field inside a TEM cell or waveguide chamber. The open-end guide (OEG) is placed at ground level at an outdoor field site, with the beam launched vertically upward toward the open sky. A carriage mounted on a utility pole is used to position the radiation monitor probe or antenna under test (AUT) in the center of this beam. A set of three rectangular open-end waveguides is available to cover 100 to 500 MHz, each having a two-to-one aspect ratio and a height of 2 meters. The AUT or hazard meter probe is placed in the beam center of the OEG launcher. The distance between the

Figure 3. Detected output of a 5 cm dipole transfer probe as a function of field
intensity and signal frequency.

31

Figure 4. Instrumentation for generating a known electromagnetic field near a pyramidal horn to calibrate and evaluate an rf radiation monitor.

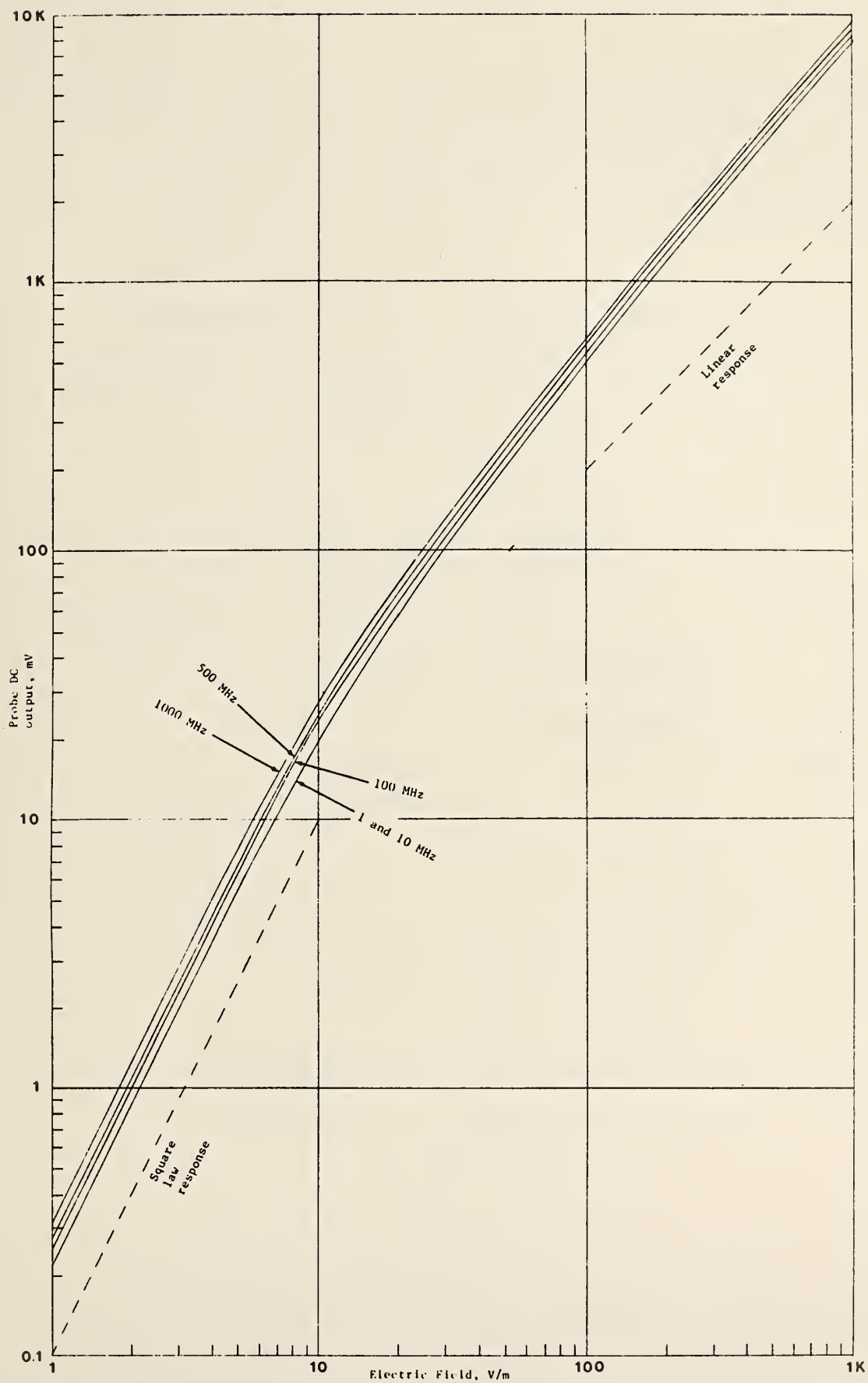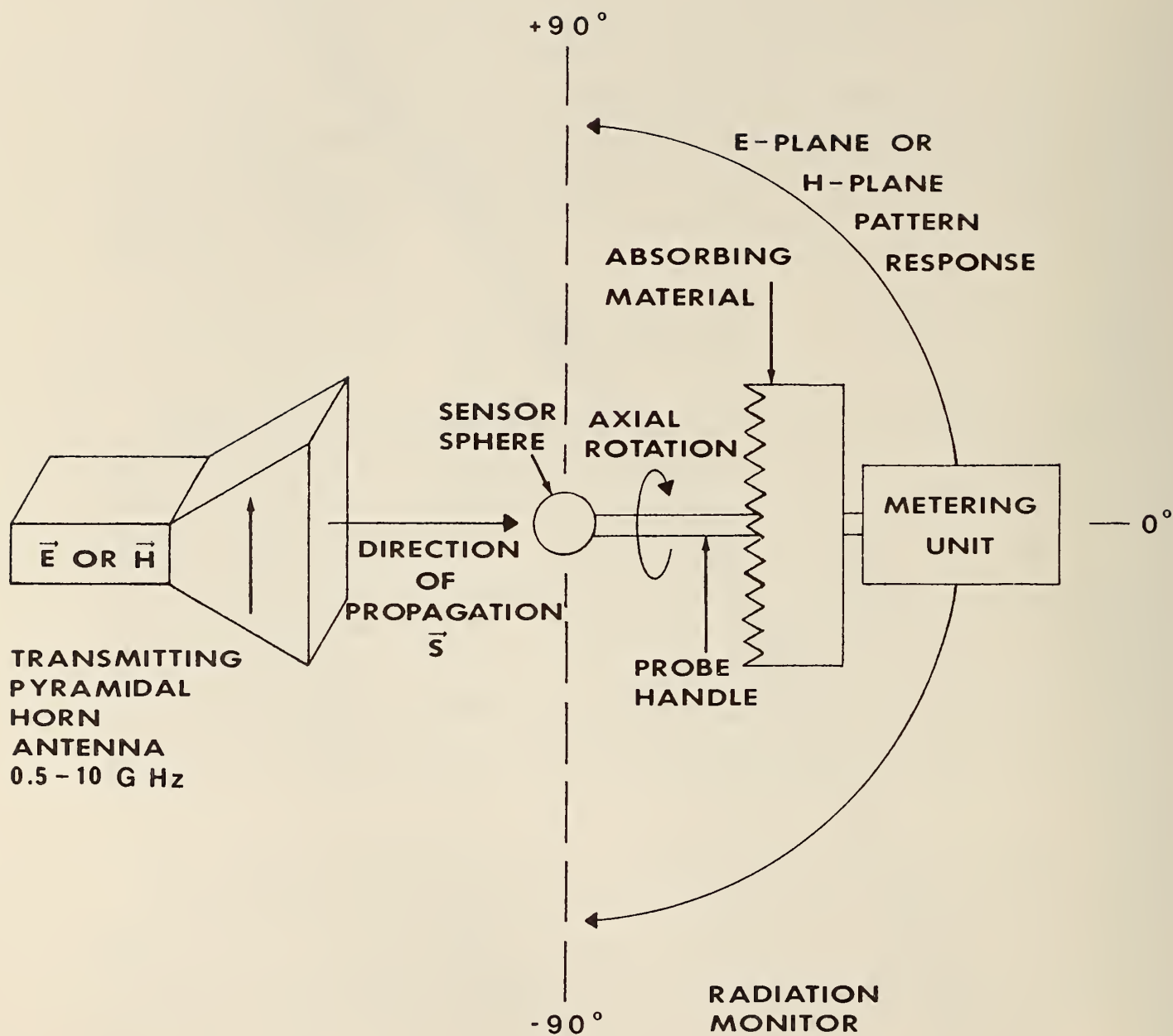transmitting aperture and the calculated field point is adjustable (at NBS) up to 7 meters above the waveguide flange. The on-axis field intensity can be calculated in terms of the net power delivered to the transmitting OEG and the measured gain of the OEG launcher determined by a technique similar to those used for pyramidal horns [3 and 9 to 14].

2.4 Pyramidal horn antennas used in an anechoic chamber, 500 MHz to 10 GHz

The approach used at NBS to establish a standard field at frequencies above 500 MHz is to calculate the radiated field intensity in the near zone of standard-gain horn antennas. These antennas consist of a series of rectangular pyramidal horns. Figure 4 shows a sketch of the instrumentation used to calibrate the amplitude-versus-frequency response of a radiation monitor or to evaluate the various pattern responses.

It would be possible to calibrate an rf radiation monitor in far-zone, plane-wave fields [15 and 16]; however, the transmitter power levels required to produce intense fields (up to 10 mW/cm^2 or higher) would generally exceed 1 kW. An alternative approach is used at NBS in which lower power rf sources are adequate. A simple equation for accurately calculating the field strength close to a horn aperture will be given later. However, a brief discussion of near- vs. far-zone effects is presented first.

Plane-wave conditions exist in the far zone of a transmitting antenna. The E and H field vectors are orthogonal to each other, and both are perpendicular to the direction of propagation. In addition, the ratio of the magnitudes (E/H) is a constant given by the free-space wave impedance (Z_o); that is:

$$Z_o \equiv (E/H) \text{ of free space} \simeq 377 \text{ ohms.} \tag{6}$$

In this case E and H also have a definite relation to the average power density given by:

$$S_o = \frac{E^2}{Z_o} = Z_o H^2 \tag{7}$$

Equation (7) is not necessarily valid for conditions other than a single plane wave. It is important to remember that the usual commercial radiation monitor does not actually measure power density, even though the dial indication is in units of mW/cm^2. Yet, taking some liberties with technical exactness, it is possible to convert a measured E or H field to an "equivalent" plane-wave power density. However, this common practice is not necessarily valid.

One way to avoid the confusion of power density units would be for the American National Standards Institute (ANSI) to state the maximum permissible field values in terms of the quantity actually measured; namely, E field in V/m or H field in A/m. For isotropic probes having three mutually orthogonal sensors, the total field magnitude is measured in terms of orthogonal field components by the following equations:

$$E_{total} = \sqrt{E_x^2 + E_y^2 + E_z^2} \quad \text{and} \quad H_{total} = \sqrt{H_x^2 + H_y^2 + H_z^2} \quad (8)$$

The total field as defined by equation (8) is also called the Hermitian magnitude of E or H. It is closely related to the electric or magnetic field energy density. The familiar power density or Poynting vector, however, is not directly relatable to the energy density except for a simple field structure such as a plane wave.

If electromagnetic fields always occurred in simple plane-wave configurations, the question of which physical quantity to measure and how to relate this quantity to biological effects would be more easily answered. The regions very close to radiating systems are most likely to approach hazardous levels. Unfortunately, they are also characterized by complicated field structure including reactive (stored) and propagating fields, multipath reflections, standing and traveling waves, irregular phase surfaces, and unknown field polarization.

In addition to the ambiguity of using power density units, a complication arises when calculating field strength very close to a transmitting antenna, known as near-zone gain reduction. Unlike a field traveling in a waveguide, the electromagnetic field across a horn aperture has a somewhat spherical (rather than planar) wavefront. The phase at the rim of the horn lags that at the center, causing a nonequiphase front across the aperture, which reduces the effective gain in the near-field (Fresnel) region. A further reduction occurs, even for an equiphase aperture, due to the difference in distance between the various elements in the radiating aperture and the on-axis field point in question. Both of these "defects" reduce the power density to less than that predicted by the simple far-zone, inverse-square relation of a distant point source. In the far-zone (Fraunhofer) region of an antenna, plane-wave conditions will exist, and:

34

$$S = \frac{PG}{4\pi d^2} \tag{9}$$

where:

    S = On-axis power density of the radiated field, W/m^2,

    P = Power delivered to the transmitting antenna, W,

    G = Gain of the antenna, and

    d = Distance from the antenna aperture to the field point, m.

A computer program was written at NBS for the effective gain of a pyramidal horn at any distance. It is used so that high-level standard fields can be produced with low-power transmitters. It involves an integration of the amplitude and phase contribution from all the aperture elements of the transmitting antenna. An approximation, in terms of Fresnel integrals, was compared with this direct numerical integration and found to agree within ± 0.1 dB. The Fresnel integrals are useful for solving many problems in optics and fields near aperture antennas. Unfortunately, the integrals cannot be evaluated easily without a computer. Graphical constructions and tables of Fresnel integrals are sometimes employed, but both are tedious to use. Mathematical approximations have also been given for the Fresnel integrals; some of these involve infinite series expansions and others, a combination of trigonometric and algebraic functions. However, recently a short paper was published by E. V. Jull [17] which gives tables of values for near-zone gain reduction factors of a pyramidal horn. His technique begins with an equation for the far-zone gain of a rectangular in-phase aperture. Then two separate factors, R_H and R_E, are calculated for the gain reduction due to the H-plane and E-plane flare of the horn.

The author has generated simple polynomial expressions, similar to the various algebraic equations which have been published for approximating the Fresnel integrals, for determining these R_H and R_E factors with a calculator. The pertinent horn dimensions used in the equations are shown in figure 5, where the dimensions have been normalized to wavelengths by letting:

$$A = \frac{a}{\lambda} , \quad B = \frac{b}{\lambda} , \quad L_H = \frac{\ell_H}{\lambda} , \quad L_E = \frac{\ell_E}{\lambda} , \text{ and } D = \frac{d}{\lambda} . \tag{10}$$

Here:

    a, b, ℓ_H and ℓ_E = Horn dimensions, meters,

    d = Distance in front of the horn aperture to the field point, meters, and
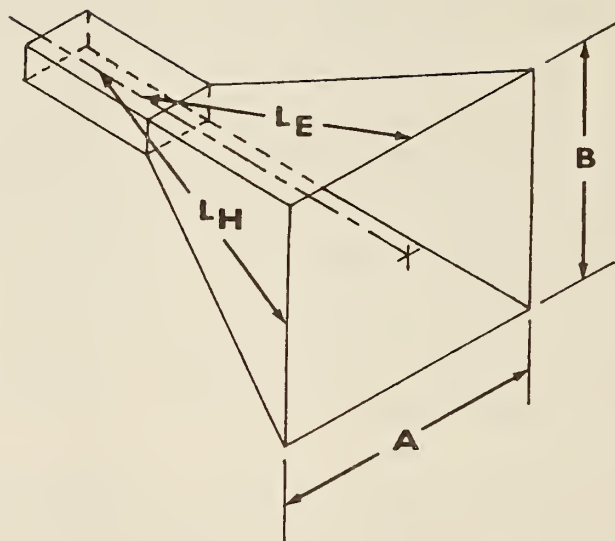
    λ = Free-space wavelength, meters.

35

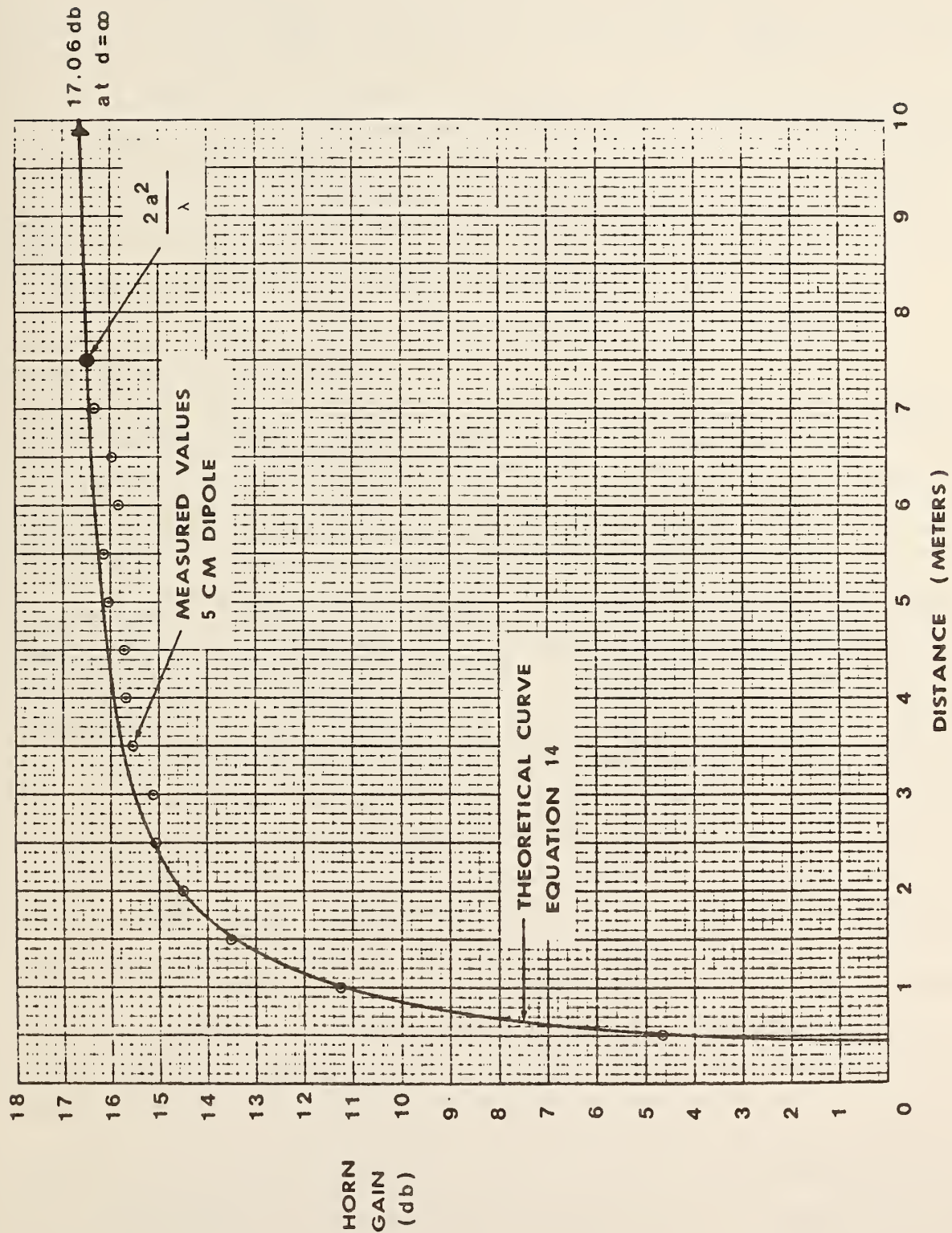Figure 5. Sketch of a pyramidal horn. All dimensions shown are in wavelengths.

Figure 6. Near-zone antenna gain of an SA 12-0.5 pyramidal horn at 750 MHz.

37

After defining:

$$\alpha = A^2 \left[\frac{1}{L_H} + \frac{1}{D} \right] \quad \text{and} \quad \beta = B^2 \left[\frac{1}{L_E} + \frac{1}{D} \right], \tag{11}$$

the two gain reduction factors R_H and R_E, in dB, are:

$$R_H = (0.01\alpha)(1 + 10.19\alpha + 0.51\alpha^2 - 0.097\alpha^3)$$
(Due to H-plane flare of horn) $\tag{12}$

$$R_E = (0.1\beta^2)(2.31 + 0.053\beta)$$
(Due to E-plane flare of horn). $\tag{13}$

Finally, the theoretical gain of the horn (near zone or far zone) is given by:

$$\text{GAIN, dB} = 10 \log(AB) + 10.08 - R_H - R_E. \tag{14}$$

The first two terms of equation (14) represent the gain of an in-phase aperture. For a sectoral horn, either R_H or R_E would be zero. The calculated values of R_H and R_E, using equation (14) for pyramidal horns, were found to agree with reference [17] within 0.05 dB for R_H < 5 dB and R_E < 6 dB, assuming $D > L_H$ and $D > L_E$. The calculated gain values given in NRL Report 4433, reference [18], for the 15-cm band horn were compared with equation (14) at frequencies of 1.6, 2.0, 2.4, and 2.8 GHz, using Brauns near-zone correction curves. The distances involved were 1.2 m, 1.8 m, 2.4 m, and ∞. The largest discrepancy found for any of the 16 comparisons was less than 0.1 dB. The average value of the differences between the NRL report and the calculations of equation (14) was only 0.001 dB.

The above approach was also tested experimentally at two frequencies using two different standard-gain horns covering the frequency range of 450 to 1100 MHz. The horns were first calibrated at NBS by the well-known, three-antenna method [10, 11, 12], and these gains were compared with that given by equation (14). The distance used was about 5 meters. The gain difference between the experimental determination and the theoretical value was 0.02 dB at 470 MHz and 0.21 dB at 850 MHz.

Another near-zone gain calibration of the large pyramidal horn (1.225 x 0.
m aperture) was performed at 750 MHz in order to compare experimental results w.
those calculated from equation (14). Figure 6 gives a graph of the data obtaine
as a function of distance from the horn flange. As can be seen, the agreement
between the measured near-zone values and the theoretical equation was within
0.5 dB for all distances checked up to 7 meters above the horn flange.

For calibrating a radiation monitor, the on-axis field intensity of the
transmitting horn is calculated in terms of the net power delivered to the
pyramidal horn, using equation (9). The proper gain value to use for any
distance is obtained from equation (14). The overall uncertainty in the 0.5 to
10 GHz frequency range is estimated to be within 0.5 dB.

3.   Summary and Conclusions

The method used at NBS for calibrating an rf radiation monitor involves
inserting the probe in a field of known magnitude. The optimum instrumentation
to use for generating this field depends on the frequency and required accuracy.
Up to 300 MHz a TEM cell is convenient since it produces a uniform electromagneti
field. Both the E and H field strengths can be calculated in terms of the plate
spacing and measured voltage (or power and cell characteristic impedance). This
known field can then be used to calibrate a radiation hazard meter or a small
transfer probe.

In the 300 to 1000 MHz range a series of rectangular waveguide transmission
lines is used for a calibrating field. The E and H magnitudes can be calculated
approximately in terms of the guide dimensions, power flow and frequency. However
the uncertainty of the calculated field is relatively large and it is necessary to
check the amplitude and uniformity by using a small transfer probe which is known
to be flat vs frequency across the 300 to 1000 MHz band. Another approach now bei
evaluated at an outdoor field site, for generating high-level fields in the 100 to
500 MHz range, makes use of large open-end waveguide launchers. This technique is
required only for larger antennas and probes which would cause perturbation of the
field inside a TEM cell or waveguide chamber.

Calibrating fields above 500 MHz are generated in a new anechoic chamber at
NBS, using a series of standard-gain pyramidal horns. Intense fields can be
produced very close to the antenna aperture, even with low power transmitters.
Simple algebraic equations are given for accurately calculating these near-zone

39

fields. The procedure involves a computation of the intensity produced by an in-phase aperture and then applying two near-zone correction factors. The values of these gain reduction factors depend on frequency, horn dimensions and the distance to the field point.

It is concluded that radiation monitors (and other antennas) can easily be calibrated over the entire frequency range of 10 kHz to 10 GHz with an uncertainty less than ± 0.5 dB. It is possible to produce high level fields (greater than 200 V/m) using only low-power rf sources (less than 50 W).

4. References

[1] M. L. Crawford, "Generation of standard EM fields using TEM transmission cells," IEEE Trans. Elec. Compat., Vol. EMC-16, pp. 189-195 (Nov. 1974).

[2] G. A. Skaggs, "High frequency exposure chamber for radiobiological research," NRL Report 2218, Naval Research Laboratory (Feb. 1971).

[3] R. C. Baird, "Methods of calibrating microwave hazard meters," Proc. of symposium on Biologic effects and health hazards of microwave radiation, Warsaw, Poland, pp. 228-236 (Oct. 1973).

[4] M. L. Crawford, "Generation of standard EM fields for calibration of power density meters, 20 kHz to 1000 MHz," NBS Interagency Report, NBSIR 75-804, 40 pages (Jan. 1975).

[5] R. R. Bowman, "Some recent developments in the characterization and measurement of hazardous electromagnetic fields," Proc. of symposium on Biologic effects and health hazards of microwave radiation, Warsaw, Poland, pp. 217-227 (Oct. 1973).

[6] P. S. Ruggera, "E- and H-field instrumentation and calibration below 500 MHz," Proc. of symposium on Biological effects of electromagnetic waves, USNC/URSI meeting, Boulder, Colo., pp. 281-296 (Dec. 1976).

[7] E. Aslan, "Simplify leakage probe calibration," Microwaves, pp. 52-54, 57 (Dec. 1975).

[8] D. Woods, "Standard intensity electromagnetic field installation for calibration of radiation hazard monitors from 400 MHz to 40 GHz," Non-ionizing radiation, Vol. 1, pp. 9-17 (June 1969).

[9] R. R. Bowman, "Field strength above 1 GHz: measurement procedures for standard antennas," Proc. IEEE, Vol. 55, pp. 981-990 (June 1967).

[10] W. H. Kummer and E. S. Gillespie, "Antenna measurements--1978," Proc. IEEE, Vol. 66, pp. 483-507 (April 1978).

[11] "Microwave antenna measurements," Edited by J. S. Hollis, T. J. Lyon, and L. Clayton, Jr., Scientific Atlanta, Inc., Chapter 8, "Measurement of gain," pp. 8-1 to 8-29 (July 1970).

[12] A. C. Newell, R. C. Baird and P. F. Wacker, "Accurate measurement of antenna gain and polarization at reduced distances by an extrapolation technique," IEEE Trans. Ant. & Prop., Vol. AP-21, pp. 418-431 (July 1973).

[13] "Electromagnetic horn antennas," Edited by A. W. Love, IEEE Press, selected reprints prepared under sponsorship of the IEEE Ant. & Prop. Society, 453 pages (1976).

[14] "Calibration technique replaces large antenna measurement ranges," Communications Designer's Digest, pp. 30-31 (Dec. 1969).

[15] H. I. Bassen and W. A. Herman, "Precise calibration of plane-wave microwave power density using power equation techniques," IEEE Trans. Microwave Theory and Techniques, Vol. MTT-25 (Aug. 1977).

[16] M. Swicord, H. Bassen, W. Herman, J. Duff and J. Bing, "Methods and instrumentation for the evaluation and calibration of microwave survey instruments," Proc. of symposium on Biological effects of electromagnetic waves, USNC/URSI meeting, Boulder, Colo. pp. 297-309 (Dec. 1976).

[17] E. V. Jull, "Finite-range gain of sectoral and pyramidal horns," Electronic Letters, Vol. 6, pp. 680-681 (Oct. 15, 1970).

[18] W. T. Slayton, "Design and calibration of microwave antenna gain standards," NRL Report 4433, Naval Research Laboratory (Nov. 9, 1954).

Appendix B

Donaldson, E. E.; Free, W. R.; Robertson, D. W.; Woody, J. A. "Field measurements made in an enclosure."

Field Measurements Made in an Enclosure

ERNEST E. DONALDSON, MEMBER, IEEE, WILLIAM R. FREE, MEMBER, IEEE,
DOUGLAS W. ROBERTSON, SENIOR MEMBER, IEEE, AND JIMMY A. WOODY, MEMBER, IEEE

Abstract—This paper presents a survey of radiated emission and susceptibility measurement methods which can be employed to evaluate the electromagnetic interference (EMI) characteristics of electronic systems. The paper reviews conventional anechoic-chamber and shielded-enclosure-measurement methods, as well as alternate methods which have been developed to circumvent measurement problems associated with radiated measurements in conventional shielded enclosures. Alternative methods presented include hooded antennas, mode perturbation, statistical sampling, transverse electromagnetic (TEM) cells, and other techniques such as parallel-plates, low-Q-enclosures, and long-wire-antennas. A qualitative comparison of each technique in terms of advantages and limitations is also given.

I. INTRODUCTION

THE ACHIEVEMENT of electromagnetic compatibility (EMC) in electronic systems is highly dependent upon the availability of accurate and reliable measurement techniques for defining and controlling system electromagnetic interference (EMI) characteristics. Over the last two decades, considerable effort has been directed to the development of better EMI measurement techniques. In particular, emphasis has been placed on test methods for performing radiated emission and susceptibility measurements which provide a valid description of system EMC/EMI performance in actual operating environments.

There are three common test environments which are employed for radiated emission and susceptibility measurements: open-field, shielded-anechoic-chamber, and shielded-enclosure. Each of these environments has advantages and disadvantages for radiated measurements, both technical and economical. Open-field measurements constitute a fairly straightfoward approach to evaluating system EMI performance, but require a field measurement site, provide no isolation between the test setup and external environment, and are subject to weather conditions. The shielded anechoic chamber will simulate an open-field environment while providing isolation between the measurement setup and external environment. However, anechoic-chamber costs can become prohibitive, particularly as size requirements increase. A shielded enclosure will satisfy isolation requirements but can produce measurement problems due to multiple reflections, resonances, distortion of radiated fields, and changes in the emission and susceptibility characteristics of systems under test. However, primarily because of economic considerations, the shielded enclosure is widely used to perform radiated type measurements, and efforts to develop improved EMI measurement methods have revolved about the shielded enclosure test environment.

This paper briefly summarizes current measurement methods which are employed in performing radiated type EMI measure-

ments, and provides a qualitative comparison of the advantages and limitations of each technique. These methods include: 1) anechoic chambers; 2) shielded enclosures; 3) hooded antennas; 4) mode perturbation; 5) statistical samples; 6) TEM cell; and 7) other methods such as parallel-plates, long-wire-antennas, and low-Q-enclosures.

II. MEASUREMENT METHODS

A. Anechoic Chamber

A shielded anechoic chamber [1], [2] represents the best approach for performing indoor radiated electromagnetic field measurements. This type chamber provides a nearly free-space test volume isolated from the outside environment. A good quality shielded enclosure should provide 100 dB or more of attenuation over the 10-kHz to 20-GHz frequency range. Hence, signals present in the outside environment will have little effect on measurements made in the chamber, and signals radiated in the chamber during testing are contained within the chamber and thus will not interfere with external operations. Also, a shielded anechoic chamber eliminates the need for FCC approval to radiate, and can reduce the possibility of compromising classified radiation characteristics. The anechoic material mounted on the inside walls, floor, and ceiling of the shielded enclosure absorbs the energy radiated inside the enclosure and provides a nearly reflection-free volume for performing measurements. The disadvantages associated with shielded anechoic chambers are the high cost of the chamber and the low-frequency performance limitations of currently available anechoic materials. A rule-of-thumb estimate of shielded anechoic chamber cost is $15 to $25 per cubic foot of interior usable space (not including the interior volume occupied by the anechoic material) for typical laboratory size enclosures. The cost per cubic foot tends to decrease as the chamber size increases, but the total cost is quite high for any size enclosure.

In general, the anechoic material must be at least one-quarter wavelength thick for any appreciable absorption of radiated energy to take place. An exception is ferrite absorbing material; however, the cost of the material is so high (approximately $100 per square foot) that it is not considered economically feasible for anechoic chamber designs. Since wavelength is inversely proportional to frequency, the thickness of the anechoic material must be increased as the low-frequency limit is decreased. For example, to obtain any appreciable absorption at 100 MHz, the anechoic material would have to be at least 30 in thick, and at 50 MHz the material would have to be 60 in thick. As the thickness of the anechoic material increases, there are three related factors which limit the low-frequency threshold of anechoic chambers: 1) the cost increases; 2) the size of the shielded enclosure must increase to retain the same test volume; and 3) it becomes more difficult to mount the material and prevent sagging of the pyramids. For these

reasons, most existing anechoic chambers have low frequency limits of 200 MHz or higher. A few large chambers have 100-MHz low-frequency thresholds.

It is not possible to specify the absolute accuracy of measurements made in a shielded anechoic chamber [3] without specifying the test setup in some detail, since the measurement accuracy is dependent on several test parameters, including:

1) location of the test setup in the chamber; in particular, distance from the internal surface of the chamber;
2) directivity of transmitting and/or receiving antennas;
3) separation between source and receptor;
4) frequency; and
5) reflectivity of the anechoic material.

In addition, the accuracy is dependent upon the magnitude of the energy being measured relative to the maximum energy being radiated in the chamber. This can be illustrated by considering an antenna pattern measurement being made in an anechoic chamber with a reflectivity level of 40 dB. On boresight, where measurements of maximum energy levels are being performed, reflections will have little effect on measurement results. Thus maximum errors on the order of 0.1 dB can be expected. However, at points on the pattern which are below the maximum, reflected energy can significantly influence measurement results. For example, at a level of −30 dB relative to the beam maximum, a maximum error of 3.3 dB is possible. It should be pointed out that a similar situation exists on outdoor ranges due to reflections and the background interference environments which exist on the ranges.

B. Shielded Enclosures

A large percentage of indoor radiated electromagnetic-field measurements are made in shielded enclosures without anechoic material on the inside surfaces of the enclosure. The shielded enclosure provides a high degree of isolation from the electromagnetic environment and local sources of interference. However, the reflections from the enclosure walls significantly affect any radiated measurements made in the enclosure. Measurement results are extremely sensitive to the size and shape of the enclosure, the location of the test setup in the enclosure, the spacing between the equipment under test and the test antenna, and the presence and location of personnel and test equipment in the enclosure.

A typical measurement setup in a shielded enclosure is illustrated in Fig. 1. The diagram also illustrates some of the multiple signal paths which exist with this measurement configuration. It is apparent from the figure that a great deal of radiated energy is reflected into the receiving antenna by the enclosure walls. This energy would not be present if the measurement setup was in the open-field or in an anechoic chamber. It is also apparent from the figure that the phase of a signal arriving at the antenna over any given reflection path relative to the phase of the signal arriving at the antenna over the desired signal path will be influenced by the frequency of the signal, the size of the enclosure, the location of the measurement setup in the enclosure, and the spacing between the radiating source and the antenna.

If the majority of the reflected energy arriving at the receiving antenna over all of the reflection paths is of the proper phase to cause a cancellation with energy arriving at the antenna over the desired signal path, the measurement result will be less than would have been obtained in the open-field or in an anechoic chamber. By the same token, if the majority of the reflected
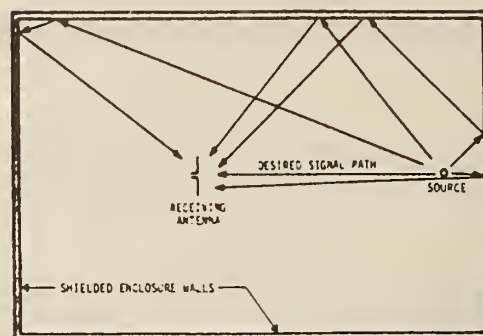

Fig. 1. Diagram of a typical measurement setup in a shielded enclosure showing multiple-signal paths.
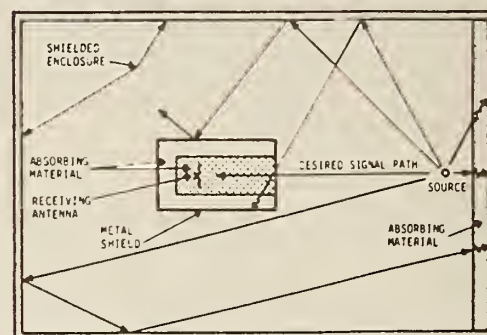

Fig. 2. Diagram of a hooded-antenna measurement setup in a shielded enclosure.

energy is of the proper phase to add to the energy arriving at the antenna over the desired signal path, the measurement result will be greater than would have been obtained in the open field or in an anechoic chamber. When the magnitude of the reflected energy is equal to or greater than the magnitude of the desired signal path energy, very large errors may be encountered.

Results from experimental investigations [4]–[6] have shown that errors as great as ±40 dB are possible in radiated measurements made in shielded enclosures at frequencies greater than 50 MHz. Results from these investigations have also shown that a change of one-half inch in the spacing between the test antenna and the equipment under test could change measurement results approximately 15 dB. It is obvious that measurements made under these conditions are of little value and the possibility of correlating these measurements with measurements made in the open-field is small.

C. Hooded-Antenna Technique

A search for a technique which would reduce the multipath reflections in shielded enclosures without the cost, fabrication, and space disadvantages associated with an anechoic chamber led to the development of the hooded antenna technique [4]-[6]. This concept, illustrated in Fig. 2, involves shielding the test antenna in all but the desired signal direction by means of a metal hood. The inside of the hood is lined with an anechoic material to reduce reflections from the hood to the test antenna. The shielded enclosure wall behind the equipment under test is also covered with absorbing material to prevent reflections on or near the desired signal path. The concept of the hooded antenna differs little from the concept of an anechoic chamber. The absorber-lined walls of the hood, together with the absorber-lined enclosure wall opposite the

46

aperture of the hood, look essentially the same to the test antenna as the six absorber-lined walls of an anechoic chamber. The edge diffraction around the aperture of the hood may be minimized by extending shaped absorbing material beyond the edge of the hood shield.

Two hooded antennas covering the frequency range from 200 MHz to 12 GHz have been fabricated and evaluated. A UHF hooded antenna designed to operate over the 200 to 1500-MHz frequency range consists of a balanced log-conical antenna and a cylindrical hood 24 in in diameter and 49 in long. The hood was fabricated with 1/8-in sheet aluminum and was lined with Eccosorb® NZ-1 absorbing material. This is a ferrite absorbing material, approximately 1 in thick, with good reflectivity characteristics from 200 MHz to 15 GHz. A microwave-hooded antenna designed to operate over the 1-to 12-GHz frequency range consists of a microwave log-conical antenna and a cylindrical hood 8 inches in diameter and 19.5 in long. This hood was also lined with NZ-1 absorbing material. The use of these hooded antennas in a shielded enclosure with one wall covered with absorbing material reduced the errors in "boresight" measurements from ±40 dB to ±3 dB. Subsequent investigations indicated that planar cavity-backed spiral antennas with shorter hoods gave equivalent results [6], [7]. As discussed for the anechoic chamber, the accuracy of radiated measurements made in a shielded enclosure with the hooded antenna technique is dependent on various test parameters and the magnitude of the energy being measured relative to the maximum energy being radiated in the enclosure.

D. Mode Perturbation

Because of convenience and economy, acoustical engineers have historically used reverberation chambers as an alternative to anechoic chambers for the measurement of sound power output [8]-[10]. Subjective experience with echoes led to early recognition that the reflective nature of the reverberation chambers precluded measurement of the radiated sound intensity at specific ranges or angular orientations. In order to provide a degree of field uniformity in the measurement area, Sabine [11] introduced the concept of placing a moving reflector within the chamber. Since then other investigators have developed techniques based on rotating field perturbators and/or microphone-source movements. As a result, significant improvements in energy density uniformity were obtained.

1) Stirred Mode: Recognition of a degree of similarity between electromagnetic field measurements and the approach of acoustical engineers to sound field measurements in reverberation chambers has led to adoption of room perturbation concepts for electromagnetic measurements in shielded enclosures. In one approach [12], [13], a combination of mode and spatial perturbation is obtained by rotating a probe antenna and a large reflecting surface within the enclosure. In effect, the perturbator "tunes" the enclosure through many resonant modes at the test frequency.

As the perturbator varies the room mode structure, the measured electric field will pass through a maximum value (E_{max}) for each sequentially excited mode. Since the losses remain relatively constant, E_{max} will exhibit considerable consistency from mode to mode and its value can be readily determined. E_{max} is related to the power radiated (P_{rad}) by the source by $P_{rad} = k(\omega) E_{max}^2$ where $k(\omega)$ is a measured calibration quantity for each specific room. Each enclosure can be calibrated for the frequency range of interest by driving an omnidirectional antenna with a CW source, setting the radiated

power with a directional wattmeter, and recording E_{max} for each calibration point.

The technique has been found to be suitable for frequencies slightly above the first resonant frequency of a room (approximately 35 MHz for a 3m × 6m × 6m enclosure) to over 1 GHz. The source or equipment under test (EUT) can be arbitrarily located at any point within the enclosure except in close proximity to the walls.

The field perturbation technique provides for simple and straightforward determination of the radiated power, but, for many cases of interest (specifications and standards) the field intensity at a specified range is required. A good approximation to the field intensity (E_0) for open-field conditions can be obtained from P_{rad} by assuming hemispheric radiation and by use of the relation

$$E_0 = \frac{\sqrt{60 P_{rad}}}{R} \text{ V/m} \tag{1}$$

where P_{rad} is in watts and the distance in meters (R) is larger than $\lambda/6$ at the frequency of interest.

The method has been tested for both simple and complicated sources and the calculated field intensities based on the enclosure measurements have consistently been within ±6 dB of open-field values from 45 MHz to 1 GHz.

A similar radiation measurement approach [14]-[17] is based on the use of two large rotating vanes, each rotating at uncorrelated speeds of approximately 1.0 to 2.0 r/s around axes perpendicular to adjacent walls. When a radiating source is introduced into the enclosure and the vanes activated, the field within the enclosure is perturbed in both time and space. If the resultant field is sampled by means of a test antenna and a detector with a low-pass filter for removing the vane rotational components, the measured field will exhibit considerable uniformity. Field uniformity to within ±0.5 dB has been obtained from 1 to 18 GHz for any antenna orientation and for any location of the source or test antenna within the working area of the enclosure. Of course the electric field rapidly falls to zero near the metallic walls as the boundary conditions are satisfied. Again, a room calibration coefficent curve, $k(\omega) = P_{rad}/E_{avg}^2$, can be plotted for the frequency range of interest. Once the curve is obtained, a single measurement of the field at any point in the room will suffice for determination of the radiated power of other equipments at given frequencies.

The similarity of the two approaches is evident with the difference in the E_{max} of the first case and the E_{avg} above being accommodated within each of the empirically established curves. Also, the reported results indicate that the 45-MHz to 1-GHz frequency range for the first case complements the 1-GHz to 18-GHz range of the second. The parameters which define the frequency range limits have not been determined, but they are undoubtedly related to the perturbator and room dimensions in terms of test frequency wavelength.

A number of factors related to perturbed mode enclosures measurements should be noted. The technique is relatively insensitive to differences in the spectral content of the radiations from the reference source and the EUT because the losses (skin current, etc.) in an individual enclosure are nearly constant for small frequency differences. However, the technique requires an inherent assumption that the total power radiated into, and dissipated within, the enclosure is equal to that which would be radiated by the EUT under free space or operational conditions. In a related sense, the use of a calibration curve for a specific enclosure requires the assump-
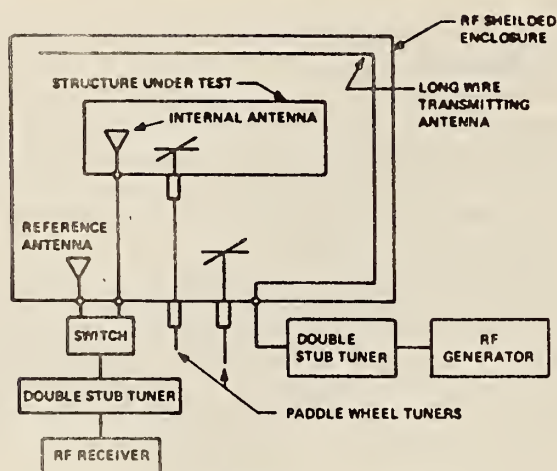
Fig. 3. MIL-STD-1377 type test setup.

Fig. 4. Sample statistical descriptions of case emission and case susceptibility.

tion that the losses within the enclosure remain the same for each EUT configuration tested. Some quantitative data directed to bounding the above two assumptions has been reported [18], but as yet the significance of the assumptions has not been determined. It is conceivable that an empirically determined calibration factor could be obtained for individual enclosures which would permit comparison of EUT radiated power in an enclosure to that in a free space or anechoic chamber environment.

In spite of the assumptions and the limited quantitative data reported to date, the reverberation enclosure technique does provide an attractive concept for a simple and repeatable shielded enclosure measurement technique for the determination of radiated power.

2) Tuned Mode: A shielded-enclosure measurement technique which involves mode tuning rather than mode stirring was developed by Jarva [19] and has been incorporated into MIL-STD-1377 (Navy) [20, 21] as a test method for measuring the shielding effectiveness of cables, connectors, enclosures, and filters over the frequency range of 1 to 10 GHz. This technique involves placing the component or equipment to be tested inside a multimoded, tuned shielded enclosure in which paddle wheel tuners are used to redistribute the energy within the enclosure. A typical test setup is shown in Fig. 3.

To determine shielding effectiveness, the equipment to be tested is placed within the enclosure and the enclosure is energized at specific frequencies of interest via the long-wire input antenna. The paddle wheel tuners are then adjusted to maximize the power coupled through the test specimen equipment to the external receiver. Because the equipment under test is subjected to a composite field pattern, both in position and polarity, many local maxima are possible as the tuners are moved. The largest local maxima is indicative of the intrinsic shielding effectiveness of the test specimen equipment. Comparison of this value with the maximum power coupled to the receiver via the unshielded reference antenna yields the shielding effectiveness of the test specimen.

The MIL-STD-1377 type test method has several advantages as a shielding effectiveness test technique. Elaborate test equipment is not necessary, and testing can be performed with an enclosure only slightly larger than the equipment under test. Test techniques are relatively simple, and experience to date indicates that measurements are repeatable within a few decibel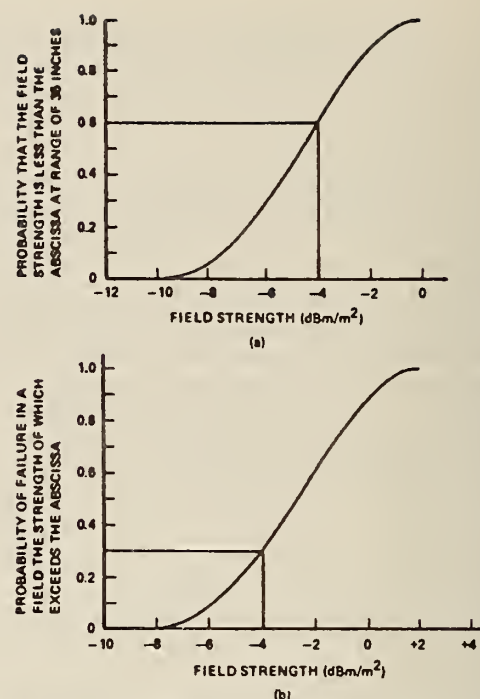s. A basic limitation of the technique is that its use is restricted to frequencies above a few hundred megahertz in order to obtain a sufficient number of modes.

Efforts are currently underway to modify the MIL-STD-1377 type test method to permit its use in performing radiated emissions and susceptibility type measurements [22].

E. Statistical Sampling

It is often necessary to predict, using measured case emission and case susceptibility data, the mutual interference between electromagnetic emitters and receptors. Current techniques for collecting the necessary data involve emission or susceptibility measurements made at a fixed point with respect to the equipment case orientation, or at a point at which the maximum case emission or susceptibility level is detected. Both of these techniques have definite disadvantages with regard to mutual interference predictions. Measurements made at either selected fixed points around an equipment case or at the point of maximum emission or susceptibility are not adequate for defining emission or susceptibility levels at the infinitude of other case orientations. To account for all possible emitter-case to receptor-case orientations which may exist in a typical equipment lash-up would seemingly require that emission and susceptibility levels be measured in a three-dimensional pattern centered around an equipment case. Unfortunately, this approach would lead to an infinite number of measurements to completely describe case emission or susceptibility levels.

Another approach which has been investigated involves a statistical description of case emission and case susceptibility [23]-[28]. The concept of this approach is illustrated in Fig. 4. Fig. 4(a) illustrates a probability distribution function statistically describing the strength of a three-dimensional radiated field at a given frequency which might surround a particular culprit case. The function shows the probability that the field strength at any point 35 in from the center of the case would be less than any given level if the case were randomly oriented in three space. Fig. 4(b) shows a corresponding prob-
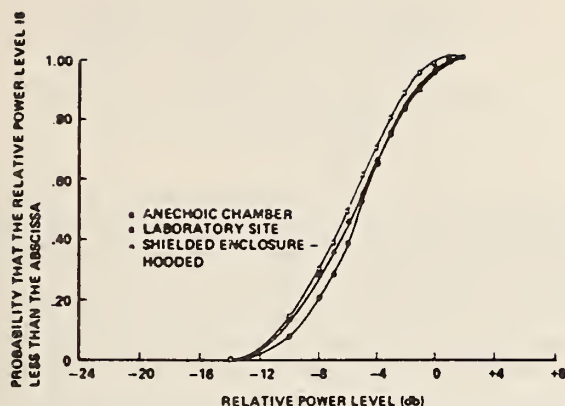
48

Fig. 5. Average cumulative distributions for a simulated source in three environments.

Fig. 6. Geometry of TEM cell.

NOTE: CENTER PLATE IS SUPPORTED WITH DIELECTRIC RODS AND SPACERS

ability distribution function statistically describing the susceptibility of a particular victim case in a radiated field of the same frequency. Here, the function yields the probability that the victim case will fail in a field the strength of which exceeds any given level if the case is randomly oriented in three space.

The probability of mutual interference can be predicted from the data of Fig. 4. For example, in Fig. 4(b), the probability of a failure by a case in a field corresponding to a level of -4 dBm/m^2 is 0.3. If the culprit is at a range of 35 in, the probability of a field corresponding to a level of at least -4 dBm/m^2 at the victim case is 0.6. Therefore, the joint probability of a failure is given by the product, $0.3 \times 0.6 = 0.18$.

In the above example, a 35-in separation between source and receptor cases was assumed for purposes of illustration. The probability of mutual interference at a separation of other than 35 in can be calculated by appropriately modifying the field strength levels of Fig. 4(a) using the distance/inverse-square law for radiated fields. Also, where the sample calculation assumed only one interference frequency, the probability of mutual interference can be determined for any number of interferences frequencies.

A power distribution measurement technique for statistically describing case emissions in the manner indicated in Fig. 4(a) has been evaluated [23]. An experiment was conducted in which measurements were made on simulated culprit sources to determine probability distribution functions for the source emissions. This experiment consisted of statistically describing the three-dimensional radiated fields about each of the sources at different frequencies under three different environmental conditions: an anechoic chamber, a typical work location in a laboratory, and a shielded enclosure. Shielded-enclosure measurements were made using the hooded antenna technique previously described.

Fig. 5 shows the probability distribution functions established from measurements at one frequency for one simulated source in the anechoic chamber, laboratory, and shielded enclosure. The distribution functions were expressed in terms of relative power levels for purposes of convenience in illustrating the characteristics of the functions; conversion to absolute levels of field strength can be accomplished through the use of appropriate calibration factors. The data of Fig. 5 and data recorded on other simulated sources and at other frequencies show that the power distribution measurement technique can be used to obtain highly repeatable radiated emission measurements in a laboratory and/or shielded enclosure that routinely lie within
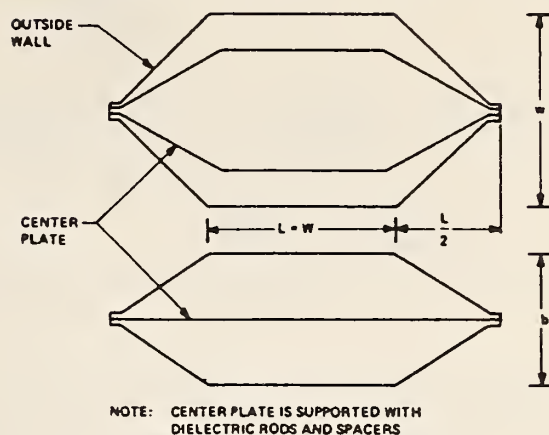
± 1.5 dB of corresponding values measured in a free-space or anechoic chamber environment.

Used in conjunction with appropriate statistical descriptions of case susceptibility, case emission data accumulated with the power distribution measurement technique could be used to predict directly the probability of electromagnetic compatibility (or incompatibility) in actual field equipment lash-ups. Although not yet reduced to practice, the concept of statistical based measurements of case emission and case susceptibility represents a potentially significant method for defining mutual interference between emitters and receptors.

F. TEM Cell

The transverse electromagnetic (TEM) cell is an expanded coaxial transmission line operated in the TEM mode. As shown in Fig. 6, it consists of a rectangular metallic box enclosing a flat-plate center conductor. The TEM cell provides shielded enclosure isolation but does not introduce the reflection problems associated with the conventional shielded enclosure. The TEM mode field characteristics between the center plate and either the top or bottom wall of the cell are used to establish a relatively uniform TEM field for susceptibility testing or to couple the EUT's emissions to the cell's measurement ports.

The geometry of the TEM cell is designed based on the following considerations [29]-[33]:

1) maximum usable test area;
2) maximum upper frequency limit;
3) maximum uniformity of the field characteristics; and
4) maximum cell mismatch or VSWR (50-Ω system).

These design considerations are functions of the cell's dimensions above and below the center plate ($b/2$, W, and L as shown in Fig. 6) and, therefore, are related to each other. The maximum dimensions of the EUT must be less than 1/3 of $b/2$, W, and L to keep the field perturbations in the cell within acceptable limits. Also, to prevent multimoding effects the upper frequency limit must be less than the lowest order TE mode (TE$_{10}$) cutoff frequency (f_{c10}), where

$$f_{c10} = \frac{3 \times 10^8}{2W}. \tag{2}$$

Thus as the cell's dimensions are increased to accommodate larger EUT's, the upper frequency limit of the cell decreases proportionally. Tests have shown that the optimum geometry
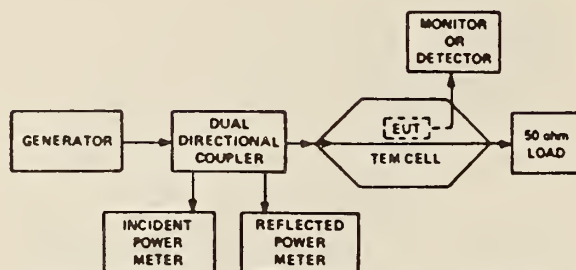
Fig. 7. Susceptibility test configuration using TEM cell from 1 MHz to f_{c10}.

Fig. 8. Emission test configuration using TEM cell.

for maximum test area and maximum test frequency is one in which b equals W. With this geometry, the E-field uniformity in the usable test area is within ±2 dB. Modifying the cell geometry by reducing b to 0.6 W, i.e., reducing the usable test area, improves the E-field uniformity such that the variations in the relative E-field are less than ±1 dB.

A typical TEM cell test setup for susceptibility testing above 1 MHz is shown in Fig. 7. The EUT is placed midway between the outer wall and the center plate of the cell. The E-field in the cell is given by the following equation:

$$E_c = \frac{\sqrt{P_n R_z}}{b/2} \tag{3}$$

where

E_c magnitude of the E-field in the cell,
P_n net power flowing through the cell,
R_z real part of the cell's characteristics impedance, and
$b/2$ distance between the cell's outer wall and center plate.

For frequencies below 1 MHz, the dual directional coupler and power meters in Fig. 7 are replaced with a voltage monitor tee and an RF voltmeter. The E-field in the cell is then given by the following equation:

$$E_c = \frac{V_c}{b/2} \tag{4}$$

where V_c is the measured voltage at the input port of the cell. An error analysis of this susceptibility measurement technique indicates that the uncertainty of the value of E_c is less than ±2 dB depending on the EUT's perturbation of the field in the cell.

Emission measurements have been made as shown in Fig. 8, based on the assumption of reciprocity [29], [33]. The emissions of the EUT are coupled to the TEM mode of the cell and propagated to the cell's ports. The RF energy at the measurement port of the cell was used to determine the relative (as a function of frequency) emissions of the EUT based on the receiver characteristics and the impedance and coupling properties of the cell.

When an EUT is placed in a TEM cell, its radiation resistance is changed relative to its free-space radiation resistance. Thus to determine the absolute magnitude of the EUT's emissions relative to free space, a correction factor must be applied. Theoretical and experimental investigations [31], [32] have been conducted to determine this correction factor for electrically small dipoles in a TEM cell. This correction factor can be applied to emissions from equipments that can be modeled as electrically small (dimensions much less than a wavelength) dipoles with a resulting estimated uncertainty in the measured

E-field of less than 5 dB. Correction factors for larger EUT's have not been determined and the absolute magnitude of such equipment's emissions relative to free space cannot be determined from TEM cell measurements. However, work in improving the TEM cell is presently being conducted [33].

The TEM cell offers several advantages in measuring the susceptibility and emission characteristics of small equipments and devices. It is portable, simple to build, and can be used from dc to f_{c10} to provide fields from 10 μV/m to 500 V/m. The cell's construction cost is lower than conventional anechoic chambers and shielded enclosures, and it is a relatively accurate (1–2 dB) susceptibility test chamber. Because of its TEM mode of operation, the cell has a linear phase response from dc to near f_{c10} and can thus be used for swept frequency measurements.

The major limitations of the TEM cell are: 1) the inverse proportionality between its size and the upper frequency limit; 2) the restriction on EUT size imposed by cell dimensions; and 3) the inaccuracy of the emission measurements on devices that are not electrically small.

G. Other Methods

Various methods, other than those previously discussed, which are used for making susceptibility and/or emission measurements include long-wire-antenna, parallel-plate, and low-Q-enclosure methods.

1) Long-Wire Antenna: The long-wire-antenna method involves a wire suspended on insulators between two opposite walls of a conventional shielded enclosure as shown in Fig. 9. This method is generally used for making susceptibility measurements at frequencies below 30 MHz. The wire is installed along the longest dimension of the enclosure and at a distance from the ceiling between one-fourth and one-third the interior height of the enclosure [34]. In a manner similar to the TEM cell, the enclosure operates in the TEM mode with the wall as the outer conductor. Therefore, the termination resistances are chosen to match the characteristic impedances of the concentric feed-line and the antenna, respectively [34], [35]. The EUT is located on a ground plane in the center of the enclosure and directly under the center of the long-wire antenna. The field intensity (E_d) at the EUT location is given in microvolts per meter by the following equations:

$$E_d = \frac{1}{K_d} E_l \tag{5}$$

and

$$\frac{1}{K_d} = \frac{2.36 \times 10^3}{Z_l} \left(\frac{1}{d} + \frac{1}{2d_1 - d} - \frac{1}{2d_2 + d} \right) \tag{6}$$

where

E_l voltage in μV to the input of the concentric line,
K_d attenuation factor,
Z_l characteristic impedance of the line, and
$d, d_1,$ and d_2 distances in meters as shown in Fig. 9.
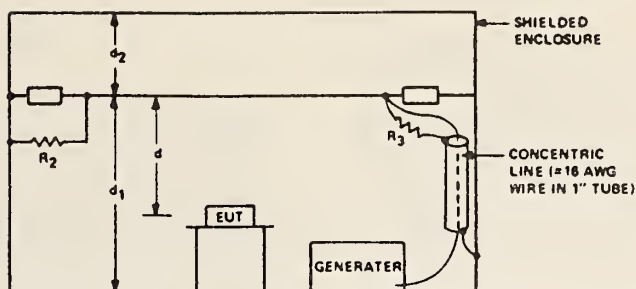
Fig. 9. Long-wire antenna test chamber.

	Cost	Accuracy	Complexity	Frequency Range	Field Intensity Limit	Sensitivity (5)	Test Time	Data Reduction Requirement	Calibration Requirements	Isolation	EUT Size Range	Proximity Effects	Operator Skill	Concurrence with Theory
Anechoic Chamber	H	H	L	H	H	M(6)	M	L	M	H	H	M	M	H
Shielded Enclosure	M	L(1)	L	H	H	H(6)	M	L	H(1)	H	H	H	M	L
Hooded Antenna	M	H	M	H	H	M(6)	M	L	M	H	H	L	M	H
Stirred Mode	M	M	M	H	H	M(6)	L	M	L	H	H	L	L	H
Tuned Mode (2)	M	M	M	H	H	H	L	L	L	H	H	L	L	H
Statistical Sample	L	H	H	H	H	M(6)	H	H	M	H(4)	H	L	H	H
TEM Cell	L	H(3)	L	L	M	H	L	M	M	H	L	L	L	M
Long-wire Antenna	M	H(3)	L	L	H	H	L	M	M	H	H	H	M	H
Parallel Plate	L	H(3)	L	L	M	H	L	M	M	L	L	L	L	H
Low-Q Enclosure	H	M	L	H	H	M(6)	M	L	M	H	M	M	M	H

Key:

H High
M Moderate
L Low

Notes:

1. Invalid measurement method.
2. Susceptibility measurements only.
3. Shielding effectiveness measurements only.
4. High in anechoic chamber and shielded enclosure, but low in laboratory.
5. For emission measurements, the ratio of field intensity to sampled power. For susceptibility measurements, the ratio of field intensity to input power.
6. Function of antenna gain.

Fig. 10. Qualitative comparison measurement of methods.

The long-wire antenna test chamber can accommodate relatively large EUT's. It provides isolation from the ambient electromagnetic environment and can develop relatively high field intensities. Also, the long-wire antenna is simple and can be installed in a shielded enclosure in a short period of time. The major limitation of the long-wire antenna test configuration is the upper frequency limit of approximately 30 MHz.

2) Parallel Plate: Parallel-plate structures are widely used for making susceptibility measurements up to approximately 30 MHz [34]. A common structure consists of two parallel plates 24-in wide and up to 18-in separation [36]. The length of the plates is normally 10 ft although there is no maximum limit on the length other than practical considerations. The ends of the parallel-plate structure are terminated with matched loads so that it operates in the TEM mode. A generator is connected to one end to drive the line and a receiver or RF voltmeter is connected to the other end to measure the voltage between the plates (V). The magnitude of the field intensity between the plates (E) is given by $E = V/h$, where h is the separation distance between the plates. The EUT is placed between the parallel

plates and its operation is monitored for malfunction or degradation of performance. This structure is capable of providing fields up to several hundred volts per meter with the only practical limitation being the power rating of the terminating resistors.

The parallel-plate technique has several disadvantages. First, the size of the EUT is limited by plate separation. Equipment dimensions which approach the plate separation distance will substantially perturb the TEM field. When large perturbations exist in the field, accurate calculations of the field intensities can no longer be obtained from the equation $E = V/h$ (this effect is the same as when a large EUT is placed in a TEM cell). Another disadvantage is that the parallel-plate structure is not truly a shielded enclosure. Thus, the EUT is exposed to the ambient electromagnetic environment and the structure itself radiates electromagnetic fields.

3) Low-Q Enclosures: Low-Q (lossy wall) enclosures are a modified form of the conventional shielded enclosure in which nonmetallic lossy walls of low reflectivity are used to reduce reflections and attenuate wall coupling. Two investigations of

the feasibility of low-Q enclosures have been conducted. The first investigation [37] consisted of coating the inside walls of a conventional shielded enclosure with a lossy material. This material reduced the Q of the enclosure and, thereby, reduced the ±40-dB measurement errors in conventional enclosures by more than 20 dB over the 20- to 200-MHz frequency range. The lossy material was a mixture of graphite and spackling compound with a resulting conductivity of 1.0 mho/m. This lossy wall approach, even though promising, has been evaluated only in scaled models of full-sized enclosures.

The second investigation [29] of low-Q enclosures evaluated the use of an underground room or tunnel as a shielded enclosure. The tunnel walls were solid granite with a relative permittivity of 6. It was found that if the tunnel was sufficiently deep, adequate isolation from the ambient electromagnetic environment could be obtained. Also, measurements indicate that the ±40 dB measurement errors in conventional shielded enclosures can be reduced to less than ±5 dB in the low-Q tunnel over the 20 to 100 MHz frequency range. The major disadvantage of performing measurements in low-Q tunnels is their limited accessibility.

III. Conclusions

Each of the measurement methods presented has merits as well as limitations in terms of its application to a particular measurement requirement. Fig. 10 provides a qualitative comparison of the different methods as a function of various measurement parameters. The ordinate tabulates the measurement methods presented, whereas the abscissa lists the parameters selected to permit measurement method comparisons.

As an example of the manner in which Fig. 10 was derived, consider radiated emission or susceptibility measurements performed in an anechoic chamber. Relative to other methods, anechoic chamber measurements are high cost because of the required shielded enclosure, anechoic material, and measurement instrumentation. The accuracy, frequency range, EUT size range, and field intensity levels which can be achieved are high, limited primarily by such factors as instrumentation and anechoic material characteristics and chamber size. Furthermore, shielded anechoic chamber measurements provide high isolation between the measurement environment and the external environment and have a well established theoretical basis. The operator skill, test time, and calibration requirements for anechoic-chamber measurements are moderate, as are proximity effects (effects of equipment, personnel, etc.) on measurement accuracy. Also, the measurement sensitivity is moderate, i.e., equipment emissions can be measured at moderately low levels and the field intensity necessary to measure equipment susceptibility can be attained with sources of moderate power. Anechoic chamber measurements are relatively simple and straightforward (low complexity and generally yield a direct measurement result with little or no data reduction required.

It is to be noted that Fig. 10 is intended only to provide a broad qualitative comparison of the various measurement methods based on selected measurement parameters. The selection and use of a specific method for a particular application may depend upon measurement parameters not listed in the figure or other factors. For example, the availability of a particular method (facilities, instrumentation, etc.) may be the overriding factor in the selection of a method for a new measurement task. Also, measurement methods may be dictated by contractual requirements.

References

[1] S. Galahan, "Understanding microwave absorbing materials and anechoic chambers," *Microwaves*, Pt. I, Dec. 1969; Pt. II, Jan. 1970; Pt. III, Apr. 1970; Pt. IV, May 1970.

[2] W. H. Emerson, "Electromagnetic wave absorbers and anechoic chambers through the years," *IEEE Trans. Antennas Propagat.*, vol. AP-21, pp. 484–489, July 1973.

[3] J. Appel-Hansen, "Reflectivity level of radio anechoic chambers," *IEEE Trans. Antennas Propagat.*, vol. AP-21, pp. 490–498, July 1973.

[4] W. R. Free, "Radiated EMI measurements in shielded enclosures," in *IEEE Electromagn. Compat. Symp. Rec.*, pp. 43–53, 1967.

[5] W. R. Free *et al.*, "Electromagnetic interference measurement methods—shielded enclosure," Tech. Rep. ECOM-02381-F, Contract DA28-034, AMC-02381 (E), Dec. 1967.

[6] W. R. Free and C. W. Stuckey, "Electromagnetic interference methodology, communication equipment," Tech. Rep. ECOM-0189-F, Contract DAAB07-68-C-0189, Oct. 1969.

[7] J. C. Toler and J. A. Woody, "An analysis of errors in radiated EMC measurements," in *Proc. of the 2nd Symp. Technical Exhibition on Electromagnetic Compatibility* (Montreux, Switzerland) pp. 199-204, June 28-30, 1977.

[8] R. Waterhouse, "Noise measurement of reverberant rooms," *J. Acoust. Soc. Amer.*, vol. 50, no. 4, pp. 931–934, Oct. 1973.

[9] J. Tichy and P. K. Baade, "Effects of rotating diffusers and sampling Techniques on sound-pressure averageing in reverberation rooms," *J. Acoust. Soc. Amer.*, vol. 56, no. 1, pp. 137–142, July 1976.

[10] C. E. Ebbing and G. C. Maling, Jr., "Reverberation room qualifications for determination of sound power of sources of discrete frequency sound," *J. Acoust. Soc. Amer.*, vol. 54, no. 4 pp. 935-941, Oct. 1973.

[11] W. B. Sabine, *Collected Papers on Acoustics*. New York: Dover Publications, 1964.

[12] H. A. Mendez, "A new approach to electromagnetic field strength measurements in shielded enclosures," in *WESCON Tech. Papers*, Session 19, 1968.

[13] ——, "Meaningful EMC measurements in shielded enclosures," presented at 1969 IEEE Int. Symp. Electromagnetic Compatibility, Asbury Park, NJ, June 17-19, 1969.

[14] P. Corona *et al.*, "Use of a reverberating enclosure for measurements of radiated power in the microwave range," *IEEE Trans. Electromagn. Compat.*, vol. EMC-18, pp. 54–59, May 1976.

[15] P. Corona and Latmiral, "Evaluation and use of the reverberating chamber," presented at 1st National Meeting of Applied Electromagnetism, National Committee for Engineering Sciences and Architecture of the National Research Council, Instituto Universatario Navale, Naples, Italy, 1976.

[16] E. Paolini and L. Picciolo, "Measuring technique for assessing interference radiations produced from industrial scientific and medical (ISM) apparatus at microwaves," in *IEEE Int. Electromagnetic Compatibility Symp. Record*, pp. 279-287, June 1973.

[17] H. Anderson, Litton Microwave Products, Minneapolis, MN, personal communication.

[18] P. Corona *et al.*, "Performance of a reverberating enclosure for power measurements in the microwave range," in *Proc. 2nd Symp. and Technical Exhibition on Electromagnetic Compatibility* (Montreux, Switzerland), pp. 419-423, June 28-30, 1977.

[19] W. Jarva, "Shielding tests for cables and small enclosures in the 1 to 10 GHz range," *IEEE Trans. Electromagn. Compat.*, vol. EMC-12, Feb. 1970.

[20] MIL-STD-1377 (Navy), "Effectiveness of cable, connector, and weapon enclosure shielding and filters in precluding hazards of electromagnetic radiation to ordnance; measurement of," Aug. 20, 1971.

[21] J. D. Lee, "MIL-STD-1377 Versus MIL-STD-285 Microwave Shielding Effectiveness measurements," in *IEEE Int. Symp. Rec. on Electromagnetic Compatibility*, Oct. 7-9, 1975.

[22] J. R. Cummings, "Translational electromagnetic environment chamber, A new method for measuring radiated susceptibility and emissions," in *IEEE Electromagnetic Compatibility Symp. Rec.*, pp. 4A1e1-4A1e5, 1975.

[23] C. W. Stuckey and J. C. Toler, "Statistical determination of electromagnetic compatibility," *IEEE Trans. Electromagn. Compat.*, vol. EMC-9, pp. 27-34, Sept. 1967.

[24] C. W. Stuckey *et al.*, "Statistical Description of Near Zone Spurious Emissions," Georgia Institute of Technology, Atlanta, Georgia, Technical Report AFAL-TR-67-37, Contract AF 33 (615)-3329, February 1967.

[25] J. C. Toler and C. W. Stuckey, "The power distribution measurement technique—A method for measuring radiated fields from equipment cases," presented at the 20th meeting of the SAE Electromagnetic Compatibility Committee, Wright-Patterson Air Force Base, OH, May 1967.

[26] R. C. Johnson, "Mutual gain of radar search antennas," in *Proc. 9th Tri-Service Conf. Electromagnetic Compatibility*, 1963.

[27] R. D. Wetherington *et al.*, "Analysis of some near zone microwave antenna patterns recorded by the Naval Ordnance Test Station," Georgia Institute of Technology, Atlanta, GA, Tech. Rep., Contract NOrd-16189, 1958.

[28] M. W. Long, "Wide angle radiation measurements," in *Proc. 6th Conf. on Radio Interference Reduction and Electronic Compatibility*, 1960.

[29] M. L. Crawford, "Techniques for measurement of electromagnetic radiation and susceptibility of electronic equipment," in *Proc. 1st Int. Symp. and Technical Exhibition on EMC* (Montreux, Switzerland), pp. 38–44, 1975.

[30] ——, "Generation of standard EM fields using TEM transmission cells," *IEEE Trans. Electromagn. Compat.*, vol. EMC-16, pp. 189–195, Nov. 1974.

[31] J. C. Tippett and D. C. Chang, "Radiation characteristics of electrically small devices in a TEM transmission cell," *IEEE Trans. Electromagn. Compat.*, vol. EMC-18, pp. 134–140, Nov. 1976.

[32] M. L. Crawford, "Experimental evaluation of the radiation characteristics of dipole sources enclosed in a TEM transmission cell," in *Conf. Precision Electromagnetic Measurements Digest*, pp. 57–59, 1976.

[33] ——, "Improved techniques and instrumentation for EMC measurements," in *IEEE Int. Electromagnetic Compatibility Symp. Rec.*, pp. 369–371, 1976.

[34] MIL-STD-462, Notice 3, "Electromagnetic interference characteristics, measurement of," Feb. 9, 1971.

[35] D. R. J. White, "Electromagnetic interference and compatibility, vol. 4, EMI test instrumentation and systems," Don White Consultants, Inc., Germantown, MD, p. 4.7, para. 4.2, 1971.

[36] B. E. Roseberry and R. B. Schulz, "A parallel-strip line for testing RF susceptibility," *IEEE Trans. Electromagn. Compat.*, vol. EMC-7, pp. 142–150, June 1965.

[37] W. R. Free *et al.*, "Electromagnetic field probes," Georgia Institute of Technology, Atlanta, GA, Research and Development Tech. Rep. ECOM-0306-F, Contract DAAB07-71-C-0306, Mar. 1973.

Appendix C

Crawford, M. L. "Generation of standard EM fields using TEM transmission cells."

Reprinted from IEEE Trans. Electromagn. Compat. EMC-16(4):189-195; 1974 November.

Generation of Standard EM Fields Using TEM Transmission Cells

MYRON L. CRAWFORD

Abstract—A new technique developed at the National Bureau of Standards (NBS) for establishing standard, uniform, electromagnetic (EM) fields in a shielded environment is described. The technique employs transverse electromagnetic (TEM) transmission cells that operate as 50 Ω impedance-matched systems. A uniform TEM field is established inside a cell at any frequency of interest below that for which higher order modes begin to propagate. Standard field strength levels from 10 μV/m to 500 V/m can be established with uncertainties of less than 1.0 dB to 2.0 dB inside the NBS cells for frequencies from dc to 500 MHz. The cells are especially useful for calibrating EM radiation hazard meters, for emission and susceptibility testing of small to medium sized equipment, and for special low level calibration of very sensitive field strength meters.

I. INTRODUCTION

THE proliferation of electronic/electromechanical systems in our environment is causing a rapid rise in the level and number of potential interfering signals. Compatible operation of such systems in the presence of electromagnetic (EM) interference is a function of their EM susceptibility, the ability to accurately measure and control it, and/or to effectively shield against it.

A number of techniques exist for establishing known, uniform levels of electromagnetic energy for susceptibility testing over limited frequency ranges and for limited applications [1]–[3]. For example, high level fields can be generated quite accurately above a few hundred megahertz using standard gain horns and below a few megahertz using parallel plate lines. Both these techniques are widely used, but suffer a major disadvantage; they radiate electromagnetic energy into the surrounding space which may interfere with the measurements, be hazardous to the operator, or interfere with other experiments being conducted within transmission range.

The technique described in this paper contains the EM field inside the transmission cell. It is extremely broad band in frequency, being limited only by the waveguide multimode frequency associated with the cell size. Construction costs of the cells are minimal and the use of expensive anechoic chambers or shielded enclosures are unnecessary. The cells can be used to establish known field strength levels from 10 μV/m to 500 V/m with uncertainties less than 1.0 dB to 2.0 dB (depending on frequency). The cells are especially useful for calibrating EM radiation hazard monitors, for equipment emissions and susceptibility testing, and for special low-level sensor calibrations.

II. DESCRIPTION, DESIGN, AND EVALUATION OF THE TEM CELLS

The design of the cells was patterned somewhat after a large cell constructed for the USAF School of Aerospace Medicine at Brooks AFB [4]. The NBS cells were designed as shielded chambers for EM susceptibility and emissions testing of test specimens, and for calibration of EM field probes. A cross sectional view of a typical cell is shown in Fig. 1. The cell consists of a section of rectangular coaxial transmission line tapered at each end to adapt to standard coaxial connectors. The line and tapered transitions have a nominal characteristic impedance of 50 ohms along their length to insure minimum voltage standing wave ratios (VSWR). The EM field is developed inside the cell when RF energy is coupled to the line from a transmitter connected at the cell input port. A matched 50 ohm termination is connected to the output port. The fields inside the cell are monitored using special electric and magnetic field probes designed and constructed by NBS [5]. A differential power measuring system, designed by NBS [6] for measuring energy absorbed from the cell by test subjects, can also be used to determine the field strength if the cell's impedance is known.

Experience with the Brooks AFB cell showed that at frequencies for which only the principal wave (TEM mode) propagates through the cell, a reasonably uniform electric field could be generated. The main limitation of their cell was its large size, restricting its usefulness to frequencies below 50 MHz. A series of smaller cells were developed at NBS to increase this range up to 500 MHz. The major design considerations were:

1) maximize usable test cross sectional area;
2) maximize upper useful frequency limit;
3) minimize cell impedance mismatch or voltage standing wave; and
4) maximize uniformity of EM field pattern characteristic of the cell.

The cells were designed using experimental modeling and the approximate equation for the characteristic impedance of shielded strip line [4]

$$z_0 \simeq \frac{94.15}{(\epsilon_r)^{1/2}\left[\dfrac{w}{b(1-t/b)} + \dfrac{C''}{0.0885\epsilon_r}\right]} \quad \text{(ohms)} \quad (1)$$

where ϵ_r is the relative dielectric constant of the medium between the conductors, C_f' is the fringing capacitance in
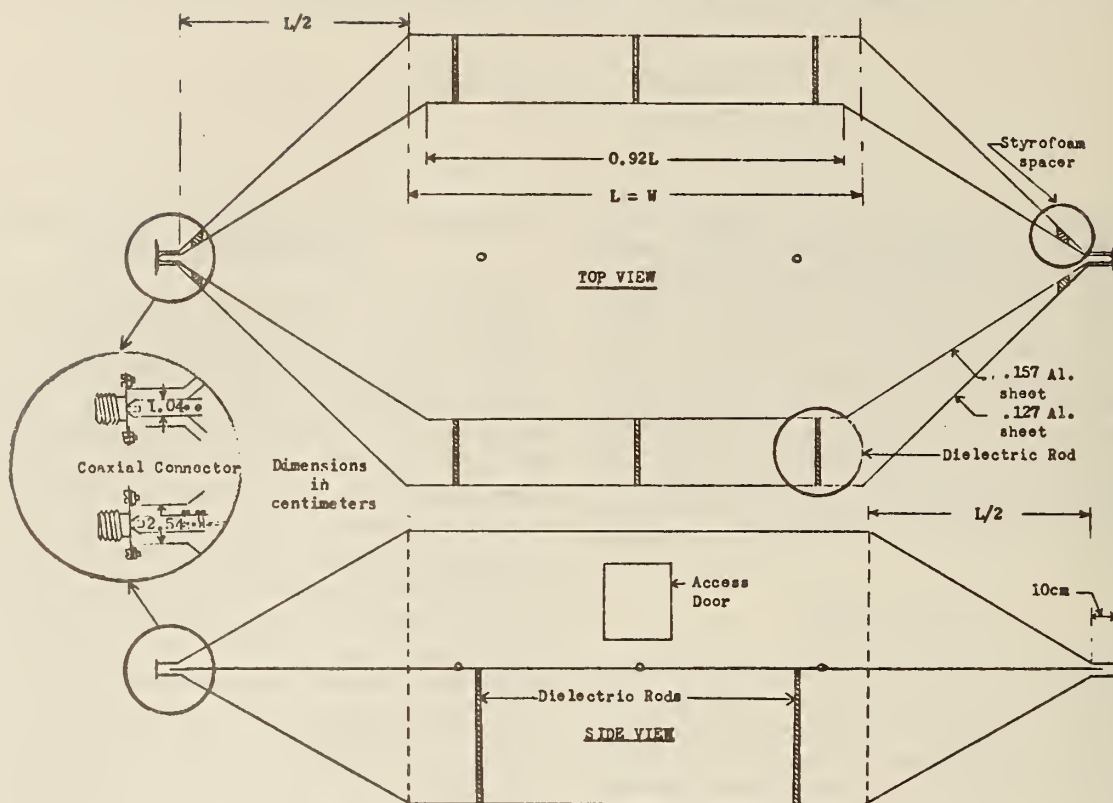
Fig. 1. Design for rectangular TEM transmission cell.

Fig. 2. Shielded strip line.

Fig. 3. Cross sectional view of optimum geometry of rectangular transmission line for maximum test area and frequency.

Fig. 4. Cross sectional view of rectangular transmisison line with improved E field uniformity.
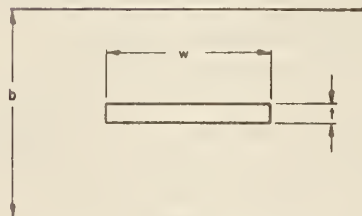
picofarads per centimeter, and w, b, and t are shown in Fig. 2.

The problem of modifying the shielded strip line into a "rectangular coaxial" line was primarily one of determining experimentally the value of C_f'. This was done using a time domain reflectometer (TDR) to evaluate small scale models of cells with the cross sectional geometry shown in Figs. 3 and 4. C_f' was found to be approximately equal to 0.087 pF/cm, respectively. Dimensions for b were determined from the design criterion that as much as 1/3 [1] of the volume between the septum and outer plates can be occupied by the equipment under test (EUT) to meet design considerations 1, 3, and 4. Once b was calculated, an experimental estimate of C_f' determined, and an available metal thickness t selected, w can be calculated from (1), assuming a nominal 52 ohms for the line characteristic impedance. (Fifty-two ohms

[1] The one third factor is considered a maximum. The impedance loading effect from inserting the EUT should not exceed a few ohms if a reasonable VSWR and EM field perturbation is to be maintained.
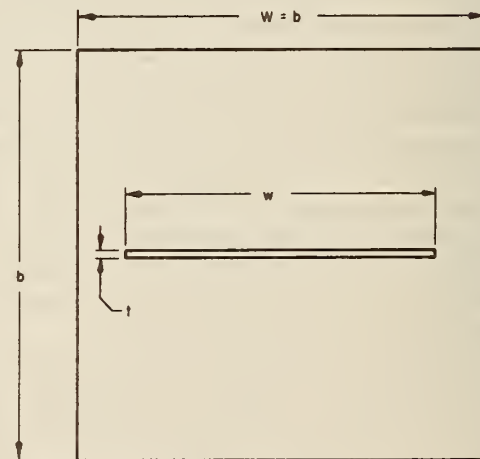
TABLE 1
TEM CELL DIMENSIONS

	Square Cell (Fig. 3)				Rectangular Cell (Fig. 4)			
Cutoff/ Multimode Frequency (MHz)	Plate Separation b (cm)	w (cm)	t (cm)	C'_f (pF/cm)	Plate Separation b (cm)	w (cm)	t (cm)	C'_f (pF/cm)
100	150	123.83	.157	.087	90	108.15	.157	.053
300	50	41.28	.157	.087	30	36.05	.157	.053
500	30	24.77	.157	.087	18	21.83	.157	.053
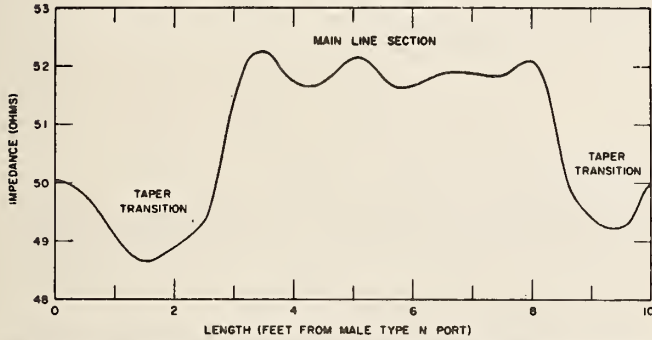
Fig. 5. Time domain reflectometer trace of distributed impedance of empty cell. (Form factor Fig. 3.)

Fig. 6. Port input VSWR of empty cell. (Form factor Fig. 3.)

was chosen to allow for some impedance loading effect when inserting the EUT inside the cell.) Table 1 gives the dimensions for constructing the two cell forms with specified upper frequency limits. The TDR was then used to make refinements by trimming w until the proper characteristic impedance was obtained.

The cross section of Fig. 3 is used at high frequencies where maximum cell size is limited and requires some compromise in electric field uniformity. The cross section of Fig. 4 achieves greater field uniformity at the cost of vertical test space restriction. Fig. 5 gives a typical TDR trace of the distributed impedance along the length of a cell of Fig. 3 cross section, and Fig. 6 shows the VSWR as seen at the cell's input and output ports.

MAPPING THE FIELDS INSIDE THE CELLS

Measurements were made using a calibrated short dipole to probe the electric field inside the empty cells. The variations in relative field strength versus position were determined in the longitudinal, transverse, and vertical directions within the cells. The electric field E is essentially vertically polarized in the region near the center of the cells and gradually becomes horizontally polarized as one moves in the horizontal direction toward the gap at the side. Both vertical and horizontal components of E were measured at each point to determine the total electric field, $E = (E_v^2 + E_H^2)^{1/2}$ where E_v and E_H are in phase. The electric field distributions for each form factor are shown in Figs. 7 and 8. The electric field in the test regions shown is primarily vertically polarized or $E_v \gg E_H$. The relative field distribution is independent
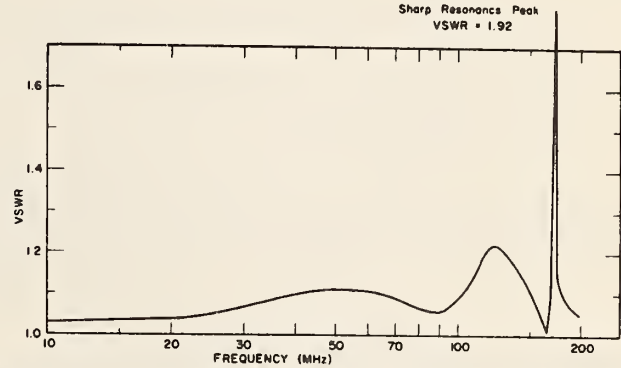
of the magnitude of the test field used and the frequency so long as the frequency is less than the first order TE mode (TE_{10}) cutoff frequency given by the following equation:

$$(f_c)_{10} = c/2W. \qquad (2)$$

The equation for determining the cutoff frequency for any higher order mode in general is given by

$$(f_c)_{m,n} = \frac{c(b^2m^2 + W^2n^2)^{1/2}}{2bW} \qquad (3)$$

For (2) and (3), c is the velocity of propagation of light $\simeq 3.0 \times 10^8$ m/s, b and W are as shown on Figs. 3 and 4 and m and n are integers related to the half sine variations of the field in the vertical and transverse directions. If higher order modes are allowed to propagate, the field configuration, which is the vector sum of each contributing mode, no longer has the simple pattern shown in Figs. 7 and 8. Thus higher order modes would greatly complicate interpretation of the measured results of the cell.

Variations in the electric field strength for the empty cells were less than 2 dB for the cross section of Fig. 3 and less than 1 dB for the cross section of Fig. 4 over the area typically occupied by the EUT. Inserting the EUT shorts out part of the electric field due to the metal in the case and increases the field strength proportional to the percentage cross section occupied. Fig. 9 shows an example of the results of inserting a solid metal case inside a cell of the form factor shown in Fig. 3. This case occupied 1/3 the vertical separation between the upper wall and
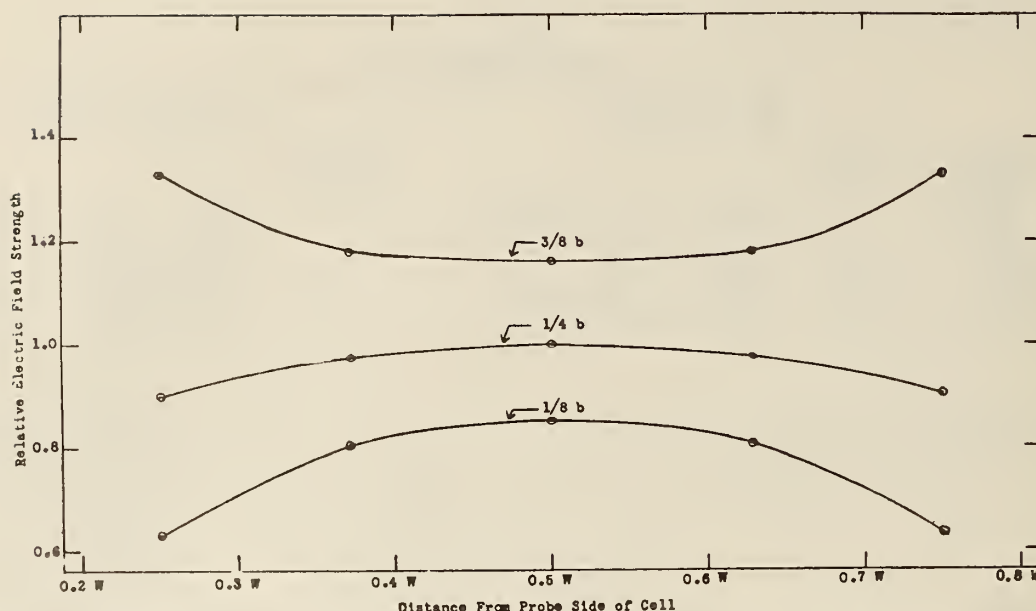
Fig 7. Relative electric field distribution inside cell. Cross sectional cut through upper half at center of cell. (Form factor Fig. 3.)
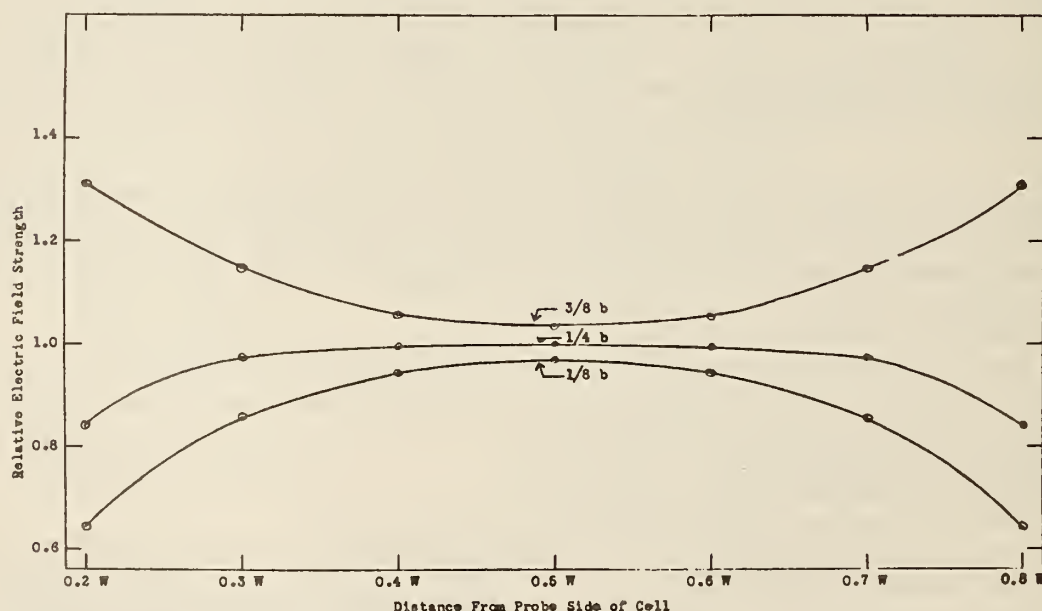

Fig. 8. Relative electric field distribution inside cell. Cross sectional cut through upper half at center of cell. (Form factor Fig. 4.)

the septum or center conductor and increased the field strength 3 dB and 6 dB, respectively, in the regions directly above and below the case. This increase in field strength for a constant test input power must be taken into account when determining the absolute test field, and occurs if significant cross section within the cell is occupied by the EUT.

III. STANDARDIZATION OF THE FIELD INSIDE THE CELLS

The absolute electric field strength E_v at the cell's center between the upper wall and the center conductor is determined using the equation

$$E_v = (P_n R_c)^{1/2}/d \qquad (4)$$

where P_n is the net power flowing through the cell, R_c is the real part of the cell's complex characteristic impedance, and d is the separation distance between the cell's upper wall and its center plate or septum.

A brief discussion of the sources of error is given below. The total fractional error ΔE_v in determining the absolute field strength E_v inside the cell is given as

$$\Delta E_v \simeq | \tfrac{1}{2}(\epsilon_R + \epsilon_P) + \epsilon_d + \epsilon_E | \qquad (5)$$

where $\epsilon_P = \Delta P_n/P_n$, $\epsilon_R = \Delta R_c/R_c$, $\epsilon_d = \Delta_d/d$, and ϵ_E is the error due to the nonuniformity of E_v determined experimentally by mapping the field distribution in the test region of the cell. Equation (5) was derived by substituting $P_n' = | P_n + \Delta P_n |$, $R_c' = | R_c + \Delta R_c |$, and
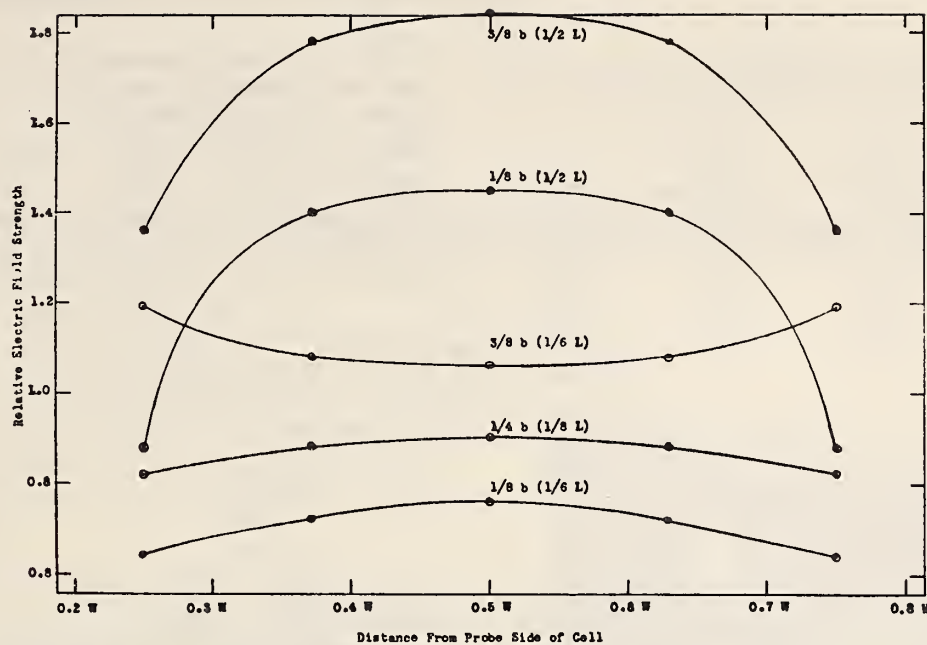
Fig. 9. Relative electric field distribution inside cell with metal case mounted in center of upper half space. Cross sectional cuts at center and off end of case.

$d' = |d + \Delta d|$ into (4) and adding ϵ_E (obtained from E field mapping). Higher order terms contributing to small errors were then dropped in the derivation to arrive at (5).

The error ϵ_P, in determining P_n, is due to uncertainties in coupler calibration, absolute measurement of RF power on the side arm of the coupler, and impedance mismatch between the cell, coupler, RF source, and cell termination. If a precision calibrated coupler and power meter are used and the cell and its termination are impedance matched (VSWR $\leq$ 1.05), ϵ_P should be less than $\pm 5\%$.

The error ϵ_R in determining R_c is a function of the measurement accuracy of the TDR and the impedance loading of the EUT inside the cell. If the EUT occupies a small portion ($\leq 1/5$) of the cross section of the cell, ϵ_R will be small ($\leq 3\%$), and is typically neglected in the calculation of E_v. For larger EUT's (occupying up to 1/3 the cross section of the cell) the impedance loading effect must be determined with the TDR and used to correct R_c when using (4) to calculate E_v. ϵ_R for these cases can be much larger but typically would be less than 10% if the EUT is centered inside the cell. Exceeding the 1/3 load factor is not recommended.

Determining ϵ_E is more difficult. Introducing the EUT inside the cell perturbs the electric field distribution as described in the section on field mapping. This loading factor (increase in E) is determined using the small calibrated probes referred to earlier. If the size of the EUT is less than the 1/5th factor and if care is taken to properly orient or eliminate interconnecting leads to the EUT, ϵ_E can be reduced to less than 6% for cells with the form factor of Fig. 3. Larger EUT's would necessitate measurement of the field distribution around the EUT and a resulting higher estimate of ϵ_E.

TABLE 2
SUMMARY OF MEASUREMENT ERRORS

| Source of Error | Percent Uncertainty | |
	Form Factor Fig. 4	Form Factor Fig. 3
a) Absolute measurement of incident RF power on the side arm of coupler	± 3.0	± 3.0
b) Coupler calibration	± 2.0	± 2.0
ϵ_P, total error in determination of RF power passing through cell	± 5.0	± 5.0
c) Real part of cell complex impedance ϵ_R	± 3.0	± 3.0
d) Cell plate separation ϵ_d	± 1.0	± 1.0
e) Nonuniformity of electric field inside cell ϵ_E	± 6.0	±20.0
maximum field strength error	±11.0 <± 1.0 dB	±25.0 <± 2.0 dB

$$\Delta E_v \sim |\tfrac{1}{2}(0.03 + 0.05) + 0.01 + \underset{(0.20)}{0.06}| \times 100$$

The sources of errors for the two form factors are summarized in Table 2.

IV. APPLICATIONS

The block diagrams for making EM susceptibility measurements using the cell are shown in Fig. 10. The EUT is mounted inside the cell in the desired orientation with the interconnecting leads/cables and power cord extended through a side or end wall of the cell, as required. The orientation, size, and type (shielded or unshielded) of interconnecting leads and power cord of the EUT can have a large effect upon the equipment's susceptibility. Tests can be performed with the leads oriented for minimum or maximum field coupling while making the
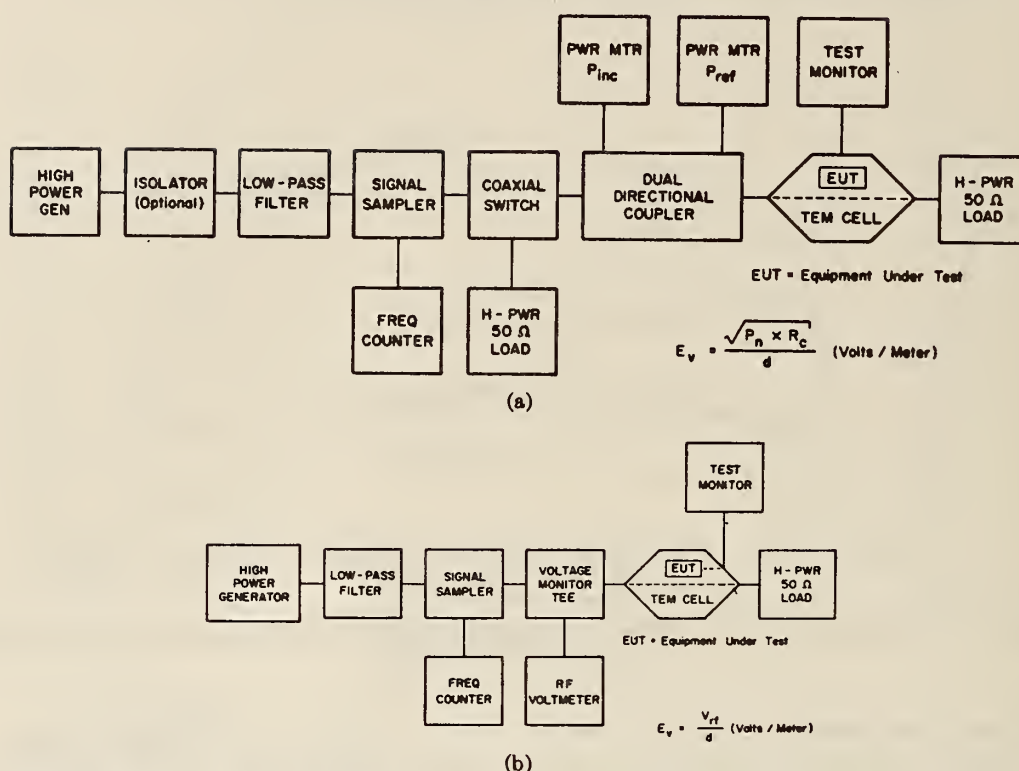
Fig. 10. Block diagrams of system for susceptibility testing of equipment.

susceptibility measurements, thus providing data for evaluating the lead contributions to the overall EUT susceptibility. Minimum lead interaction with the test field is achieved by orienting them in a direction perpendicular to the E field and by properly shielding them. Maximum interaction is achieved by allowing the unshielded leads to sag inside the cell and/or by aligning with the polarization of the test field (leads through top of cell). The susceptibility level for the EUT is determined at frequencies from 1 MHz to the cell multimode frequency by means of the block diagram of Fig. 10(a). The generator output is progressively increased until the EUT's normal operation is noticeably affected. The test field can be further increased until the EUT fails if failure tests are required.

The cells can also be used to calibrate various field detection devices such as hazard probes, field sensors, or small field intensity meters. In this type of operation the device being calibrated is placed inside the cell in a uniform field region. The standard test field is determined by the procedure outlined in Section III, and the field intensity indicated by the instrument is compared with the known value of the standard test field.

Measurements below 1 MHz are made using a voltage monitor tee and RF voltmeter as shown in Fig. 10(b), because directional couplers are not available at these lower frequencies. Directional couplers and power meters are used above 1 MHz because of the ability to monitor impedance variations in the system when installing

EUT's inside the cell and orienting them for various tests.

Swept measurements can be made for a fixed orientation of the EUT and its cables using the block diagrams of Fig. 10(a) or (b) assuming the circuit components remain matched over the desired frequency range and have acceptable frequency bandwidth characteristics. When using the system of Fig. 10(b), the input voltage to the cell is monitored directly and (4) becomes,

$$E_v = V_c/d \qquad (6)$$

where V_c is the measured input voltage to the cell and is equivalent to $V_c = (P_n R_c)^{1/2}$. The error analysis then involves evaluating the uncertainty in measuring V_c as compared to P_n and R_c, and at the frequencies indicated for these tests, the errors would be about equivalent.

Pulsed RF susceptibility measurements can also be made by replacing the signal source and monitor/detector with an appropriate pulse generator, sampler, and detector (oscilloscope). The exposure level standardization would be similar to that outlined in Section III, but would involve determining the calibration measurement accuracy of the detector, the sampling (coupling) accuracy, and the time domain response of the cell. Additional work needs to be done in this area but it is believed that measurements using pulses with frequency components less than 500 MHz could be made.

The measurement systems shown in Fig. 10(a) and (b) have been used to calibrate or determine the EM sus-

ceptibility of a number of test items. Examples are calibration and evaluation of radiation hazard probes and meters (both NBS and commercial types); calibration of small E field sensors; calibration of small field strength meters and sensitive receivers; susceptibility of fire alarms (smoke detectors) for malfunction and false alarm indication; equipment cable susceptibility (shielded and unshielded); and evaluation of RF conductance/interference on high resistance dc transmission lines.

Intercomparison of the standardized field strength data obtained using the cells with data taken using calibrated probes (calibrated with parallel plate lines and in a uniform field over a large ground screen) indicate excellent agreement, i.e., well within the uncertainties attributed to the different techniques. Table 3 presents a sample of these results at 15 MHz.

V. SUMMARY AND CONCLUSIONS

The objective of the work described in this paper was to develop an alternate technique for making susceptibility measurements of electronic equipment at frequencies up to 500 MHz. Tasks included designing and constructing the cells, optimizing the field distribution and usable test area inside the cells, evaluating the characteristics of the cell and measurement system, and performing susceptibility measurements on typical electronic equipment. The technique offers a unique way of determining not only EUT susceptibility to CW RF fields but also EUT susceptibility to pulsed RF fields. The cells can also be used to determine relative (as a function of frequency) levels of radiated emissions from electronic equipment by using the cell's inverse coupling characteristic with 50 ohm impedance-matched RF detectors connected to the input and/or output ports [7]. However, more work is needed to determine if these radiation measurements can be interpreted quantitatively.

The real advantage of using TEM transmission cells for making susceptibility or emissions measurements is the elimination of background interference without the introduction of measurement problems associated with shielded or anechoic enclosures. Furthermore, no EM fields are generated external to the cell and the cells produce uniform and readily determined fields. Shielded enclosures on the other hand reflect the emitted energy from their walls in such a complicated manner that prediction of the enhancement or interference of the desired signal is extremely difficult. Measurements using the cell are simple to make and require a minimum of detection equipment, e.g., no additional antennas are required.

The main handicap of the cell is its size limitation due to multimoding at higher frequencies. The largest cell at NBS can accomodate equipment 8 in by 19 in by 25 in at frequencies up to about 150 MHz. Smaller cells useful at frequencies up to 500 MHz have much less usable test space. Fig. 11 shows a photograph of the large NBS cell.

TABLE 3
INTERCOMPARISON ON NBS CELLS WITH PARALLEL PLATE LINE
AT 16 MHz USING 10 cm DIPOLE PROBE

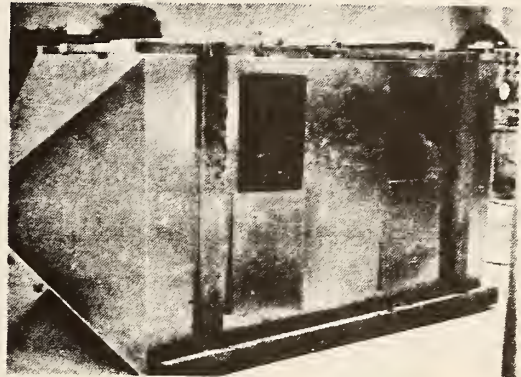| Probe Output Voltage	NBS 0.6 m by 1.0 m Cell E_v(V/m)	NBS 1.2 m by 1.2 m Cell E_v(V/m)	Parallel Plate Line E_v(V/m)
0.1	21.3	21.5	27.0
0.3	34.5	34.8	32.0
0.3	47.2	47.6	47.0
0.5	71.0	71.5	71.5
1.0	127.0	127.5	131

Fig. 11. Photograph of NBS rectangular TEM transmission cell.

VI. RECOMMENDATIONS FOR FUTURE WORK

Additional work is needed to solve the problems of size limitation of the cells, to evaluate the loading effects of large equipment inside the cells, to determine possible mode suppression and alteration techniques, and to derive the mathematics of cell modal coupling. The error analysis included in this report is rough and needs further refinement.

Only limited susceptibility measurements have been made using the cells. Additional measurements should be made with other pieces of equipment to establish the degree of generality of the method.

REFERENCES

[1] V. P. Musil, "Generating High-Intensity Electromagnetic Fields for Radiated-Susceptibility Test," *IEEE EMC Symp. Rec.*, Seattle, Wash., pp. 185–194, July 1968.
[2] B. E. Roseberry and R. B. Schulz, "A Parallel-Strip Line For Testing RF Susceptibility," *IEEE Trans. Electromagn. Compat.*, vol. EMC-7, pp. 142–150, June 1965.
[3] R. R. Bowman and W. E. Jessen, "Calibration Techniques for RAMCOR Densiometer Antennas," NBS Rep., unpublished, Dec. 1970.
[4] G. A. Skaggs, "High Frequency Exposure Chamber for Radiobiological Research," NLR Memo. Rep. 2218, Feb. 1971.
[5] F. M. Greene, "Design and Calibration of E and H Field Probes for HF Band Application," *Proc. Dep. Defense Electromagnetic Res. Workshop*, Washington, D.C., pp. 50–76, Jan. 1971.
[6] M. L. Crawford, C. A. Hoer, and E. L. Komarek, "RF Differential Power Measurement System for the Brooks AFB Electromagnetic Radiation Hazards Experiment," NBS Rep. unpublished, Apr. 1971.
[7] M. L. Crawford, "Measurement of Electromagnetic Radiation from Electronic Equipment using TEM Transmission Cells," NBSIR 73–306, Feb. 1973.

Appendix D

Tippet, J. C.; Chang, D. C. "Radiation characteristics of dipole sources located inside a rectangular, coaxial transmission line."

Nat. Bur. Stand. (U.S.) NBSIR 75-829; 1976 January.

NBSIR 75-829

RADIATION CHARACTERISTICS OF DIPOLE SOURCES LOCATED INSIDE A RECTANGULAR, COAXIAL TRANSMISSION LINE

John C. Tippet
David C. Chang
University of Colorado

CONTENTS

69

FOREWORD

This report describes theoretical analyses of Transverse Electromagnetic (TEM) Transmission cells developed at the National Bureau of Standards. The effort is part of a program sponsored by the Electronic Systems Division, Hanscom Air Force Base, under Contract number Y75-917 with the National Bureau of Standards (NBS). The purpose of this effort is to evaluate the use of TEM cells for measuring total RF power radiated by a small electronic device.

The theoretical analyses were developed by staff from the University of Colorado under contract with NBS. Myron L. Crawford of the Electromagnetics Division was the technical monitor for NBS and Charles E. Wright of the Electronics Systems Division was the technical monitor for the Air Force. The period of performance covered by this report extends from May 1975 to October 1975.

Results of these analyses include expressions for the capacitance and characteristic impedance of a cell, the electric field distribution inside a cell, and the radiation resistance of electric and magnetic dipoles in a cell. These results are prerequisite to determining the radiation characteristics of a device under test relative to its operational environment or to its operation in a free space environment.

RADIATION CHARACTERISTICS OF DIPOLE SOURCES LOCATED INSIDE
A RECTANGULAR, COAXIAL TRANSMISSION LINE

When making EMC measurements inside a shielded enclosure, the radiation characteristics of the device being tested changes. In this report the change in radiation resistance of dipole sources located inside a National Bureau of Standards TEM transmission cell is determined. In many cases a practical device can be modeled by dipole sources. In these cases, the analysis allows one to predict the device's radiation characteristics in other environments, e.g., free space.

Key words: EMC measurements; radiation resistance; rectangular coax; shielded strip line; TEM cell.

1. INTRODUCTION

There are currently many researchers interested in developing a method of measuring the radiated EM emissions and EM susceptibility of electronic equipment [1]. At the National Bureau of Standards work is progressing on the design and experimental evaluation of a TEM transmission cell for this purpose. A typical NBS cell consists of a section of rectangular coaxial transmission line tapered at each end to connect to standard 50 Ω coaxial line as shown in figure 1.
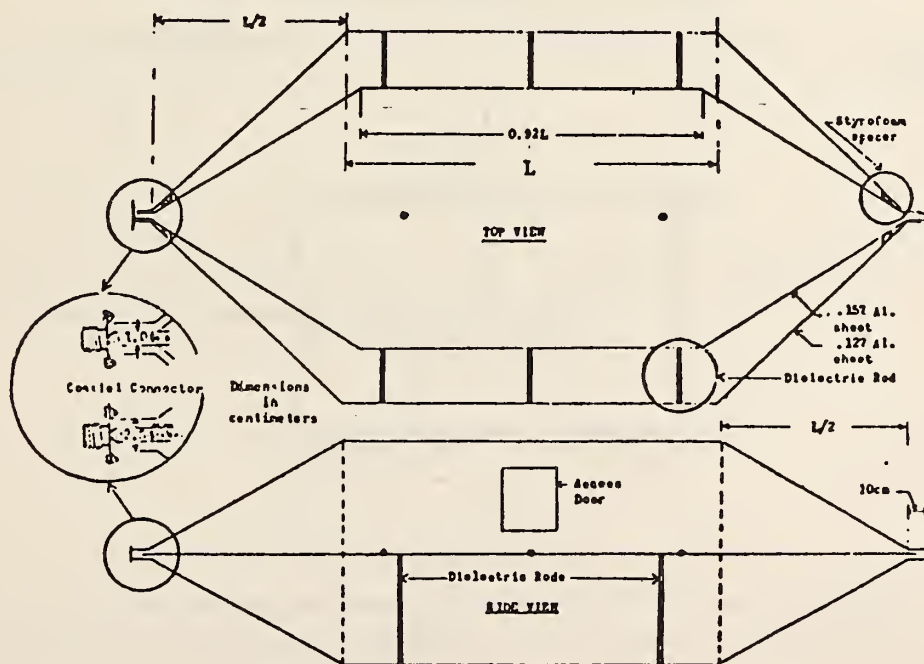
Figure 1. Design for rectangular TEM transmission cell.

To minimize reflections, the cell is designed to have a nominal characteristic impedance of 50 Ω. The description, design, and evaluation of these cells is described in reference [2].

In order to interpret the measurements made in this cell, a knowledge of the propagating TEM mode is required. This report contains a theory for calculating some basic properties of the TEM mode. These include: 1) capacitance; 2) characteristic impedance; and 3) electric field distribution inside the cell.

Once we possess a basic knowledge of the TEM mode, we can study the radiation characteristics of some simple sources located inside the cell. Since these characteristics will not be the same as if the source were located in free space, we need to determine the effect the TEM cell has on the radiation resistance of the source. This will allow measurements made in the TEM cell to be correctly interpreted for sources in other environments such as free space.

The power radiated by and the radiation resistance of both electric and magnetic dipoles located in the TEM cell are derived and compared to their values in free space. We indicate how these expressions can be used to determine both the magnitudes and directions of the respective dipoles through measurements made in the TEM cell.

2. PARAMETERS CHARACTERIZING A TEM CELL

The TEM cell is basically a rectangular, coaxial transmission line as shown in figure 2.

Figure 2. Cross-section of a TEM cell.

In order to understand how an electromagnetic wave can be guided by this structure, a brief review of the results from standard transmission line theory is presented.

Any multi-conductor system, of which the TEM cell is one, can propagate at least one TEM mode. This mode has many unique properties, not the least of which is that it has no lower cut-off frequency. That is, the TEM mode can propagate through the guide at frequencies all the way 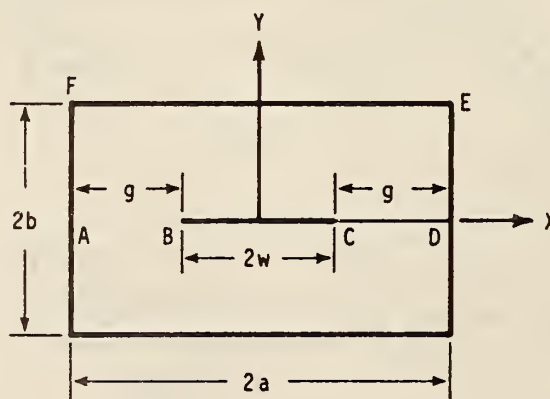down to DC. Another characteristic property of the TEM mode (as its name implies) is that the electric and magnetic field components of this mode lie totally in the transverse plane (i.e., $E_z = H_z = 0$). In the transverse plane, the electric field satisfies Laplace's equation: $\nabla_t^2 \bar{E} = 0$, which in the case of the TEM cell reduces to: $(\frac{\partial^2}{\partial x^2} + \frac{\partial^2}{\partial y^2})\bar{E}(x,y) = 0$. This means that the transverse field distribution can be obtained from the solution of a related static problem. The magnetic field is easily obtained from the electric field as

$$\hat{\bar{H}}^\pm = \pm \frac{\bar{a}_z \times \hat{\bar{E}}^\pm}{\eta_o} \tag{2.1}$$

where

$$\hat{\bar{E}}^\pm = \bar{E}(x,y)e^{jwt \mp \gamma z};$$

$$\hat{\bar{H}}^\pm = \bar{H}(x,y)e^{jwt \mp \gamma z};$$

$$\eta_o = \sqrt{\frac{\mu_o}{\epsilon_o}};$$

μ_o is the magnetic permeability;

ϵ_o is the dielectric permittivity;

γ is the propagation constant;

and $\bar{a}_z$ is a unit vector in the z direction.

The total fields are then given by:

$$\bar{E} = \text{Re}[\hat{\bar{E}}^+ + \hat{\bar{E}}^-] \tag{2.2}$$

and

$$\bar{H} = \text{Re}[\hat{\bar{H}}^+ + \hat{\bar{H}}^-] \tag{2.3}$$

Many times, it is desirable to characterize TEM waves in terms of the voltage and current on the line instead of the field quantities, $\bar{E}$ and $\bar{H}$. The voltage and current are given by the following equations:

$$\hat{V}(z) = \hat{V}_m^+ e^{-\gamma z} + \hat{V}_m^- e^{\gamma z} \tag{2.4}$$

$$\hat{I}(z) = \hat{I}_m^+ e^{-\gamma z} + \hat{I}_m^- e^{\gamma z} \tag{2.5}$$

where

$$\hat{V}_m^\pm = - \int_p \hat{\bar{E}}^\pm \cdot \overline{d\ell} \tag{2.6}$$

and

$$\hat{I}_m^\pm = \oint_\ell \hat{\bar{H}}^\pm \cdot \overline{d\ell} \tag{2.7}$$

p is any path connecting the two conductors in a constant cross-sectional plane, and ℓ is a closed path encircling the inner conductor. $\hat{V}_m$ and $\hat{I}_m$ are related by a constant which is called the characteristic impedance, Z_0 of the line, and is given by:

$$Z_0 = \pm \frac{\hat{V}_m^{\pm}}{\hat{I}_m^{\pm}} = \pm \frac{\hat{V}_m^{\pm}}{\oint_{\ell} \frac{\bar{a}_z \times \hat{\bar{E}}^{\pm}}{\eta_0} \cdot \overline{d\ell}} \tag{2.8}$$

Thus, eq. (2.5) may be written:

$$\hat{I}(z) = \frac{\hat{V}_m^{+}}{Z_0} e^{-\gamma z} - \frac{\hat{V}_m^{-}}{Z_0} e^{\gamma z} \tag{2.9}$$

If one measures the amplitudes of the forward and backward voltage waves, $\hat{V}_m^{\pm}$, then, with a knowledge of the characteristic impedance, eqs. (2.4) and (2.9) determine the voltage and current anywhere on the line.

The characteristic impedance, Z_0, can also be expressed in terms of the distributed capacitance per unit length of the transmission line, C_0 as follows:

$$Z_0 = \frac{1}{v \, C_0} \tag{2.10}$$

where $v = \dfrac{1}{\sqrt{\mu_0 \epsilon_0}}$ is the phase velocity.

Thus, a knowledge of the distributed capacitance, C_0, completely determines the characteristic impedance.

The capacitance of the TEM cell can be obtained analytically using the method of conformal transformation. The details of the analysis are contained in Appendix A where it is shown that the capacitance per unit length, C_0, is given by:

$$\frac{C_0}{\epsilon_0} = 2 \frac{K(\lambda)}{K(\lambda')} \tag{2.11}$$

where $K(\lambda)$ and $K(\lambda')$ are complete elliptic integrals of the first kind of modulus λ and λ' respectively [3]. λ' is termed the complementary modulus and is related to λ by:

$$\lambda' = [1 - \lambda^2]^{\frac{1}{2}} \tag{2.12}$$

The modulus, λ', is given by:

$$\lambda' = k' \left(\frac{sn \, \xi}{cn \, \xi} \right)^2 \tag{2.13}$$

where $\xi = mg$ and $sn \, \xi$ and $cn \, \xi$ are Jacobian elliptic functions of modulus k [4]. As shown in figure 2, $g = a-w$ is the width of the gap between the center septum

76

and the side wall. k' is the complementary modulus to k defined analogously to eq. (2.12), and m is given by:

$$m = \frac{K(k')}{b} \tag{2.14}$$

k, and thus, k' can be determined from the requirement that:

$$\frac{K(k)}{K(k')} = \frac{2a}{b} \tag{2.15}$$

where $K(k)$ and $K(k')$ are complete elliptic integrals of the first kind of modulus k and k' respectively. We note that in reference [5] the value of k^2 is tabulated for a given ratio, $K(k')/K(k)$.

Using eq. (2.10), the characteristic impedance is then found to be:

$$\frac{Z_o}{\eta_o} = \frac{1}{2} \frac{K(\lambda')}{K(\lambda)} \tag{2.16}$$

where η_o is the intrinsic impedance of free space. Equations (2.11) and (2.16) are exact but are not easy to use. There is an efficient algorithm [6], however, for evaluating numerically the complete elliptic integrals appearing in eqs. (2.11) and (2.16); it is contained in Appendix C. In the next section, approximate formulas are derived for the capacitance and characteristic impedance.

3. APPROXIMATE EXPRESSIONS FOR THE CAPACITANCE AND CHARACTERISTIC IMPEDANCE

In view of the complete elliptic integrals appearing in the formulas in the last section, it is desirable to investigate the possibility of obtaining formulas which do not involve special functions, but nevertheless, yield numerical results sufficiently accurate to be of practical engineering use. We hope to obtain a formula which expresses the capacitance in terms of the dimensions, a, b, and w of the TEM cell, and which can thus be used to design TEM cells with a given characteristic impedance.

Since eqs. (2.11), (2.15), and (2.16) all involve ratios of complete elliptic integrals, the following approximation is particularly useful [7].

$$\frac{K(\delta)}{K(\delta')} \simeq \frac{1}{\pi} \ln\left[2 \frac{1 + \sqrt{\delta}}{1 - \sqrt{\delta}} \right] \qquad (\delta^2 > \tfrac{1}{2}) \tag{3.1}$$

Using eq. (3.1) we can write approximate expressions for eqs. (2.15) and (2.11) respectively as follows:

$$\frac{2a}{b} \simeq \frac{1}{\pi} \ln\left[2 \frac{1 + \sqrt{k}}{1 - \sqrt{k}} \right] \qquad (k^2 > \tfrac{1}{2}) \tag{3.2}$$

$$\frac{C_o}{\varepsilon_o} \simeq \frac{2}{\pi} \ln\left[2 \frac{1 + \sqrt{\lambda}}{1 - \sqrt{\lambda}} \right] \qquad (\lambda^2 > \tfrac{1}{2}) \tag{3.3}$$

Equations (3.2) and (3.3) may be written alternatively as follows:

$$\frac{4a}{b} \approx \frac{2}{\pi} \ln[2(1+\sqrt{k})^2(1+k)] - \frac{2}{\pi} \ln(1-k^2) \tag{3.4}$$

$$\frac{C_o}{\epsilon_o} \approx \frac{2}{\pi} \ln[2(1+\sqrt{\lambda})^2(1+\lambda)] - \frac{2}{\pi} \ln(1-\lambda^2) \tag{3.5}$$

Subtracting eq. (3.4) from eq. (3.5) we obtain:

$$\frac{C_o}{\epsilon_o} - \frac{4a}{b} \approx \frac{2}{\pi} \ln\left(\frac{k'^2}{\lambda'^2}\right) + \frac{2}{\pi} \ln\left\{ \left(\frac{1 + \sqrt{\lambda}}{1 + \sqrt{k}}\right)^2 \left(\frac{1 + \lambda}{1 + k}\right) \right\} \tag{3.6}$$

and substituting from eq. (2.13):

$$\frac{C_o}{\epsilon_o} \approx 4\left[\frac{a}{b} + \frac{2}{\pi} \ln\left(\frac{cn\ \xi}{sn\ \xi}\right)\right] + \frac{2}{\pi} \ln\left\{ \left(\frac{1 + \sqrt{\lambda}}{1 + \sqrt{k}}\right)^2 \left(\frac{1 + \lambda}{1 + k}\right) \right\} \tag{3.7}$$

In eq. (3.2), the restriction that $k^2 > \frac{1}{2}$ is equivalent to requiring $\frac{b}{2a} < 1$, since when $k^2 = \frac{1}{2}$, $K(k') = K(k)$. If we make the somewhat more stringent requirement that $\frac{b}{a} < 1$, which is equivalent to $k^2 > .97$, then eq. (3.7) may be further simplified by noting that for $k \approx 1$, $cn\ \xi \approx sech\ \xi$; $sn\ \xi \approx tanh\ \xi$, and $\xi \approx \frac{\pi g}{2b}$. Thus,

$$\frac{C_o}{\epsilon_o} \approx 4\left[\frac{a}{b} - \frac{2}{\pi} \ln\left(\sinh \frac{\pi g}{2b}\right)\right] - \frac{\Delta C}{\epsilon_o} \tag{3.8}$$

where

$$\frac{\Delta C}{\epsilon_o} = \frac{2}{\pi} \ln\left\{ \left(\frac{1 + \sqrt{k}}{1 + \sqrt{\lambda}}\right)^2 \left(\frac{1 + k}{1 + \lambda}\right) \right\} \tag{3.9}$$

An alternate form of eq. (3.8) may be obtained by using the following identity:

$$\sinh\left(\frac{\pi g}{2b}\right) = \frac{e^{(\pi g/2b)}}{[1 + \coth\left(\frac{\pi g}{2b}\right)]} \tag{3.10}$$

with the result: $?o = \frac{\sim}{C_o/c_o}$

$$\frac{C_o}{\epsilon_o} \approx 4\left[\frac{w}{b} + \frac{2}{\pi} \ln\left(1 + \coth \frac{\pi g}{2b}\right)\right] - \frac{\Delta C}{\epsilon_o} \tag{3.11}$$

In this form, it is easy to identify the first term in eq. (3.11) as the plate capacitance between the center septum and the horizontal walls, and the second term as the fringing capacitance between the edges of the septum and the side walls. For large gaps, the fringing term approaches $\frac{8}{\pi} \ln 2$, as expected [8].

78

It is interesting to note that the term in the square brackets in eq. (3.11) is the identical formula given by T.-S. Chen [8] and originally derived by S.B. Cohn [9]. Cohn's formula was derived assuming that the width of the center septum, 2w, was very large compared to the plate separation, 2b. This is equivalent to assuming that the two edges of the septum do not interact. ΔC, then in eq. (3.11) can be interpreted as a correction term needed to account for the interaction between the two edges. From eq. (3.9) it can be seen that ΔC will be negligibly small if λ is near one (or λ' is near zero) since k is near one. From eq. (2.13) λ'^2 is given approximately by:

$$\lambda'^2 \simeq k'^2 \sinh^4\left(\frac{\pi g}{2b}\right) \tag{3.12}$$

It can be seen from eq. (3.12) that for small gaps, λ' is always much less than one. By using the approximate expression for the modulus, k given by G.M. Anderson [10], it can be shown that for large gaps eq. (3.12) further reduces to:

$$\lambda'^2 \simeq e^{-2\pi \frac{w}{b}} \tag{3.13}$$

From eq. (3.13) it can easily be verified that λ' will be negligibly small, and hence ΔC may be neglected if:

$$\frac{w}{b} \geq \frac{1}{2} \tag{3.14}$$

From eq. (3.3) we have the restriction that $\lambda^2 > \frac{1}{2}$ or equivalently $\lambda'^2 < \frac{1}{2}$. From eq. (3.13) it can be seen that $\lambda'^2 < \frac{1}{2}$ if:

$$\frac{w}{b} \geq \frac{1}{2\pi} \ln 2 \simeq 0.1 \tag{3.15}$$

So for the range: $\frac{1}{10} < \frac{w}{b} < \frac{1}{2}$, ΔC is not negligible and must be calculated using eqs. (3.9), (3.13), and $k \cong 1$.

Using eq. (2.10), the characteristic impedance is found to be:

$$Z_0 \cong \frac{\eta_0}{4\left[\frac{a}{b} - \frac{2}{\pi} \ln\left(\sinh \frac{\pi g}{2b}\right)\right] - \frac{\Delta C}{\varepsilon_0}} \tag{3.16}$$

Thus we have obtained approximate expressions for the capacitance and characteristic impedance of the TEM cell. These are given in eqs. (3.8), (3.9), and (3.16). Due to the limitations of the approximations, these formulas are valid for $a/b \geq 1$ and $\frac{w}{b} \geq \frac{1}{2\pi} \ln 2$. The approximate formula for the capacitance given in eq. (3.8) is plotted in figure 3 with a dashed line for $\Delta C = 0$. The exact formula using eqs. (2.11), (2.13), and (2.15) is plotted using a solid line. The two curves agree almost identically except where $w/b < \frac{1}{2}$. This discrepancy can be attributed, however, to the ΔC term which was neglected.
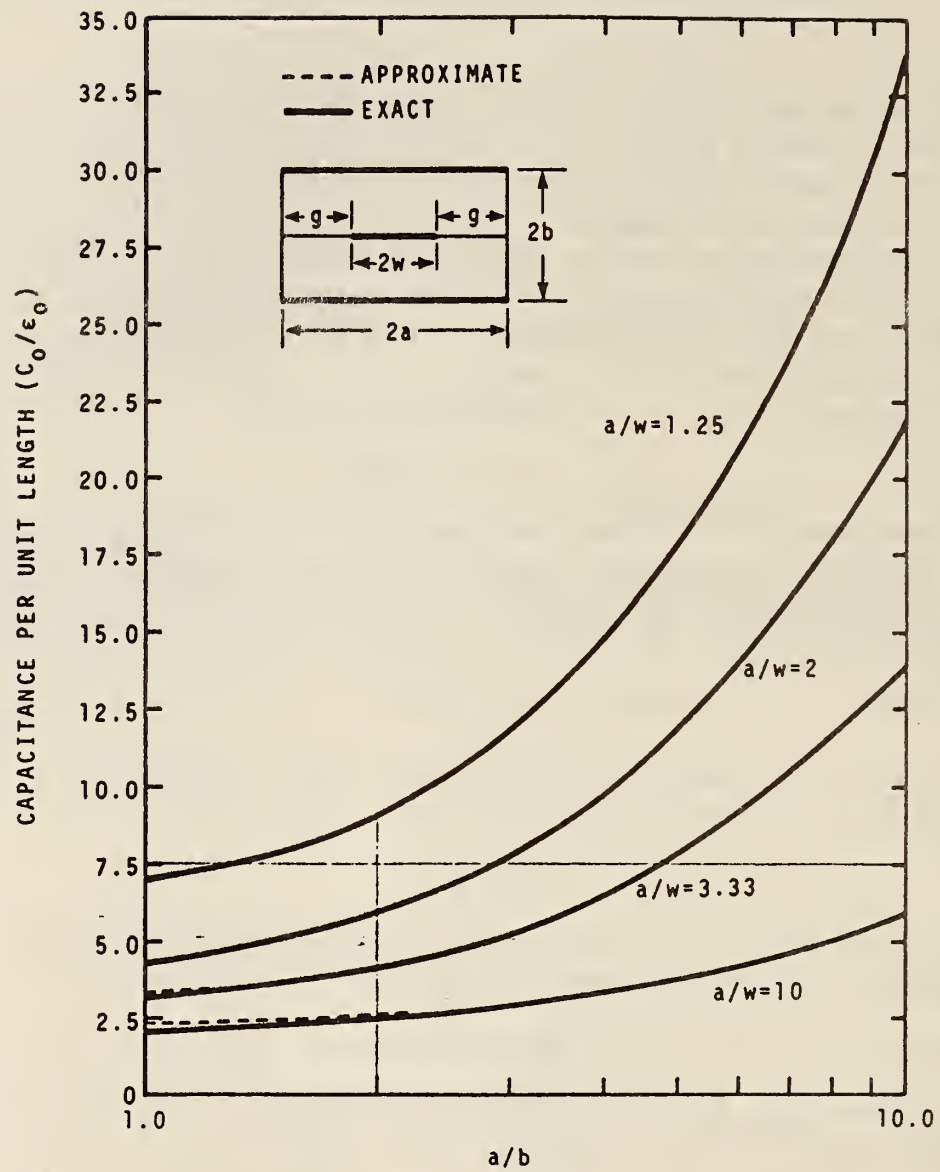
79

Figure 3. Capacitance per unit length of a TEM cell.

4. RADIATION RESISTANCE OF ELECTRIC AND MAGNETIC DIPOLES IN A TEM CELL

The power carried by the TEM mode of a transmission line that is excited by an elementary electric dipole is given by [11]:

$$P_e = \frac{|A^+|^2 \; V^2}{Z_o} \qquad (4.1)$$

where A^+ is the excitation factor;

          V is a unit voltage;

and Z_o is the characteristic impedance.

From Green's theorem, A^+ is given by:

$$A^+ = -\frac{Z_o}{2V^2} \int_\tau \overline{J} \cdot \overline{E}^{(-)} \; dv' \qquad (4.2)$$

where $\overline{J}$ is the source current density;

         $\overline{E}^{(-)}$ is the electric field of the negative (-z) propagating wave;

and τ is the volume enclosing all sources.

Since our source is an electric dipole, the volume integral in eq. (4.2) reduces to:

$$\int_\tau \overline{J} \cdot \overline{E}^{(-)} \; dv' = E_o(x_o, y_o, z_o) \; I \; \ell_{eff} \; \cos \theta \qquad (4.3)$$

where (x_o, y_o, z_o) is the source point;

         θ is the angle between the dipole and the electric field at the source point;

       ℓ_{eff} is the effective dipole length;

         I is the magnitude of the dipole current;

and E_o is the magnitude of the electric field at the source point.

Using eqs. (4.2) and (4.3), eq. (4.1) can be written as:

$$P_e = Z_o \left[\ell_{eff} \; \frac{E_o I \cos \theta}{2V} \right]^2 \qquad (4.4)$$

If, instead of an electric dipole, our source were a magnetic dipole, then following a similar analysis, the radiated power is given by

$$P_m = Z_o \left[\frac{2\pi A}{\lambda_o} \cdot \frac{E_o I_m \cos \phi}{2V} \right]^2 \qquad (4.5)$$

where λ_o is the wavelength;

    $A = \pi r^2$ is the area of the loop representing the magnetic dipole;

      I_m is the equivalent magnetic current;

and ϕ is the angle between the loop normal and the magnetic field at the source point.

In order to determine the change in the radiation characteristics of the source, we will calculate the ratio of the radiation resistance inside the cell to that in free space. The free space radiation resistances of electric and magnetic dipoles are given in reference [12] as:

$$R_e = \frac{2\pi}{3} \, \eta_o \left(\frac{\ell_{eff}}{\lambda_o}\right)^2 \tag{4.6}$$

$$R_m = \frac{\pi}{6} \, \eta_o \left(\frac{2\pi r}{\lambda_o}\right)^4 \tag{4.7}$$

From eqs. (4.4) and (4.5), the radiation resistances inside the guide are given by:

$$R_e' = \frac{P_e}{I^2} = 2 Z_o \left(\ell_{eff} \, \frac{E_o \cos \theta}{2V}\right)^2 \tag{4.8}$$

$$R_m' = \frac{P_m}{I_m^2} = 2 Z_o \left(\frac{2\pi A}{\lambda_o} \, \frac{E_o \cos \phi}{2V}\right)^2 \tag{4.9}$$

If we define the following, normalized parameters:

$$Z_o' = \frac{Z_o}{\eta_o} \tag{4.10}$$

$$\tilde{E} = \frac{E_o}{V/b} \tag{4.11}$$

then the ratios, Q_e and Q_m, of the radiation resistances are respectively:

$$Q_e = \frac{R_e'}{R_e} = 3\pi Z_o' \left|\frac{\tilde{E} \cos \theta}{k_o b}\right| \tag{4.12}$$

$$Q_m = \frac{R_m'}{R_m} = 3\pi Z_o' \left|\frac{\tilde{E} \cos \phi}{k_o b}\right| \tag{4.13}$$

where $k_o = 2\pi/\lambda_o$. Thus, in order to determine the "correction factors," Q_e and Q_m, which determine the change in the radiation characteristics of dipole sources inside a TEM cell as compared to free space, we need to know the squared magnitude of the electric field E_o, at the dipole location. An analytical expression for the electric field squared is shown in Appendix B as:

$$E_o^2 = \left(\frac{Vm'}{K(\alpha')}\right)^2 \left|\frac{dn^2(m'z)}{sn^2(m'w) - sn^2(m'z)}\right| \tag{4.14}$$

82

where

$$\alpha' = [1 - \alpha^2]^{\frac{1}{2}}; \tag{4.15}$$

$$\alpha = sn(m'w,k); \tag{4.16}$$

$$\frac{a}{b} = \frac{K(k)}{K(k')}; \tag{4.17}$$

$$m' = \frac{K(k)}{a}; \tag{4.18}$$

and

$$z = x + iy;$$

where x and y indicate the location of the dipole as measured from the center of the TEM cell in the transverse plane. Thus, $\tilde{E}$ in eqs. (4.12) and (4.13) is given by:

$$\tilde{E} = \left(\frac{bm'}{K(\alpha')}\right) \left| \frac{dn^2(m'z)}{sn^2(m'w) - sn^2(m'z)} \right|^{1/2} \tag{4.19}$$

We further note that eqs. (4.12) and (4.13) are very similar. In fact, if we were to average $\cos \theta$ and $\cos \phi$ they would be identical. That is,

$$<Q_e> = <Q_m> \equiv Q_o/(k_o b)^2 \tag{4.20}$$

where

$$Q_o = \frac{3\pi}{4} Z_o' \tilde{E}^2 \tag{4.21}$$

So that the same correction factor can be applied whether the dipole is electric or magnetic. It is interesting to note that this is the same result obtained by D.M. Kerns in his analysis of dipoles located in an ordinary coaxial line [13]. His result for the correction factor also contains the same $(1/frequency)^2$ dependence, but the constant Q_o which contains the geometrical constants characteristic of the particular transmission line (through Z_o), is different. Equation (4.20) is plotted in figure 4 and shows how the radiation resistance is
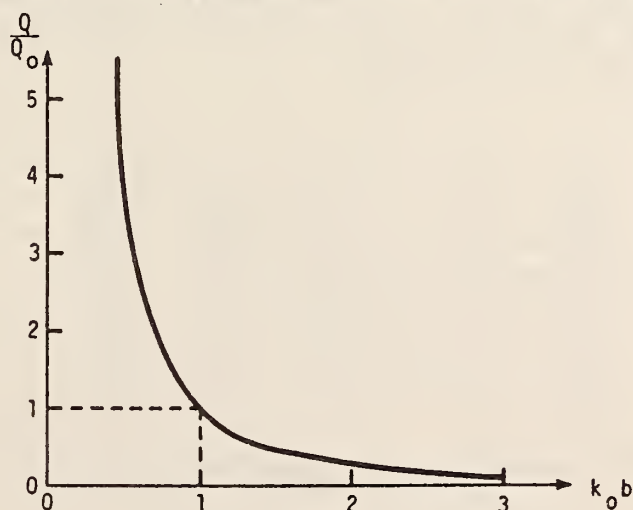
Figure 4. Correction factor as a function of frequency.

83

reduced as the frequency is increased. Values of Q_o are included in tables 1-2 for dipoles located at various places inside a TEM cell. Each table corresponds to a different TEM cell geometry.

Table 1

Q_o, the ratio of the radiation resistance inside the TEM cell to that in free space for $k_o b = 1$. Dimensions of the TEM cell: a = 25 cm, b = 25 cm, w = 20.64 cm.

y(cm)						
y=b→25	0.220	0.205	0.158	0.091	0.027	0.000
20	0.236	0.222	0.181	0.119	0.057	0.031
15	0.248	0.277	0.255	0.217	0.172	0.150
10	0.357	0.365	0.390	0.435	0.482	0.497
5	0.432	0.460	0.567	0.866	1.507	1.696
0	0.465	0.503	0.665	1.281	14.322	4.216
	0	5	10	15	20	25	x(cm)

                                                     x=w   x=a

Center of
TEM cell

Table 2

Q_o, the ratio of the radiation resistance inside the TEM cell to that in free space for $k_o b = 1$. Dimensions of the TEM cell: a = 25 cm, b = 15 cm, w = 18.025 cm.

y(cm)						
y=b→15	0.303	0.291	0.247	0.159	0.051	0.000
12	0.307	0.297	0.259	0.177	0.071	0.020
9	0.318	0.314	0.294	0.238	0.140	0.087
6	0.332	0.336	0.350	0.367	0.291	0.217
3	0.344	0.356	0.412	0.622	0.642	0.403
0	0.349	0.364	0.441	0.901	1.262	0.512
	0	5	10	15	20	25	x(cm)

Center of
TEM cell

5. SUMMARY AND CONCLUDING REMARKS

We have calculated in this report the exact capacitance and characteristic
impedance of a TEM cell, as given by eqs. (2.11) and (2.16). In addition,
approximate formulas given by eqs. (3.8), (3.9), and (3.16) were obtained
which agree very closely with the exact results. Finally, the electric field
distribution of the TEM mode, given by eq. (4.14), was obtained analytically
and was used to derive expressions for the radiation resistance of simple dipoles
located inside a TEM cell as given in eqs. (4.8) and (4.9). These expressions,
when compared to their free-space counterparts, allows one to evaluate the
change in the radiation characteristics of those sources which can be modeled
by dipoles when located inside the TEM cell as compared to free-space.

How can these results be used to interpret measurements made on a practical
source radiating inside a TEM cell, such as a piece of electronic equipment?
When can a practical source be modeled by a collection of elementary dipoles?
If the source can be modeled by a collection of dipoles, how can we determine
the magnitudes and directions as well as the type (electric or magnetic) of the
dipoles which represent the source? These are all questions which should be
asked, and which, as yet, have not been completely answered. We will, however,
indicate some of the problems and some ideas that might be used to solve them.

When we model the source by a dipole, we are assuming that the source is
"electrically small"; that is, its dimensions are small compared to the operating
wavelength. The useful upper frequency limit of the TEM cells used at NBS is
typically 100 MHz. At this frequency the wavelength is 3 meters, so that the
dimensions of most electronic equipment will be only a fraction of a wavelength
and can therefore be modeled by dipoles.of both electric and magnetic type.
This means, of course, that we are not interested in determining where leaks
occur from a piece of equipment since we have assumed a "point" source.

Assume, now, that we have a collection of electric and magnetic dipoles
all operating in phase at the same frequency, which is under our control. By
superposition, all of the electric dipoles can be combined into one equivalent
electric dipole. Similarly, all of the magnetic dipoles can be combined into
an equivalent magnetic dipole. We would like to be able to determine the magni-
tudes and directions of these equivalent dipoles. From eqs. (4.4) and (4.5) the
total power radiated is given by:

$$P = P_e + P_m = Z_o \left(\frac{E_o}{2V}\right)^2 \left((\ell_{eff} \, I \cos \theta)^2 + \left(\frac{2\pi A I_m \cos \phi}{\lambda_o}\right)^2\right) \qquad (5.1)$$

At low frequencies, eq. (5.1) is dominated by the first term, so that $P \approx P_e$. At high frequencies, the second term dominates, and $P \approx P_m$. Therefore, by judiciously choosing the frequency, we can make the source appear as if it were either an electric or magnetic dipole. Whether or not we have chosen a frequency such that the source appears as a single type of dipole and not a "hybrid" dipole should be verified by measuring the power as a function of frequency over a narrow frequency band. The electric dipole will exhibit a characteristic that is independent of frequency, whereas the characteristic of the magnetic dipole will increase as the square of the frequency. If we are not able to adjust the frequency so that the source appears as only one type of dipole, then we will have to take measurements at two selected frequencies and fit the data to eq. (5.1); so that even in this case, the separation of the contributions from the electric and magnetic dipoles is not a problem.

Now assume that we are able to obtain a single dipole source by adjusting the frequency. By measuring the power, we can determine the magnitude of the dipole moment times the cosine of some angle; $(\ell_{eff} I) \cos \theta$ for the electric dipole, and $(A I_m) \cos \phi$ for the magnetic dipole. In order to separate the angular dependence from the dipole magnitude we can perform the following experiment.

(1) Rotate the source until the radiated power is zero, thus aligning the electric or magnetic dipole perpendicularly to the respective field.

(2) Rotate the source about the longitudinal axis of the TEM cell (z-axis). If the power radiated does not remain zero, return the source to its original position.

(3) Rotate the source slightly about the x axis for magnetic dipoles or the y axis for electric dipoles.

(4) Repeat steps (2) and (3) until the radiated power remains zero upon rotation about the z-axis.

(5) The dipole is then aligned along the z-axis.

Thus, we can rotate the electric or magnetic dipole 90° around the x or y axis respectively, and obtain $\cos \theta = 1$ or $\cos \phi = 1$. With the dipole so oriented, we can measure the magnitude of the dipole moment by measuring the power radiated.

The procedure just described is more complicated if we have both an electric and a magnetic dipole. In this case, we may not be able to obtain a null in the power by rotating the source. By taking measurements as a function of frequency and rotation angle of the source, however, we can separate the contributions from both the electric and magnetic dipoles, as well as their respective orientations. Thus, having found the equivalent dipoles that represent the source, we are able to predict the radiation characteristics of the source in free space. It should also be noted that in this report we have addressed ourselves to the problem of radiated emissions testing of electrically small devices; by reciprocity, however, the results are applicable also to the problem of susceptibility testing.

The usefulness of the technique just described hinges on the validity of the following assumptions that were made initially. (1) The equivalent dipoles that represent the source have dipole moments that are constants, independent of frequency. (2) The directions of the dipoles are not a function of frequency. (3) The electric and magnetic dipoles operate in phase at the same frequency, and (4) the operating frequency is under our control. These assumptions will now be examined.

In order to understand why it seems reasonable to model a practical source by an equivalent electric and magnetic dipole operating in phase at the same frequency, we will borrow some of the results from the theory of excitation of waveguides by small apertures [14]. We will consider a practical source to consist of an electrically small conducting box housing low-frequency AC circuits. The box can have numerous apertures through which electromagnetic energy may radiate; however, we restrict these apertures to be small compared to the size of the conducting box. The coupling through a small aperture can be modeled by replacing the aperture by an equivalent electric and magnetic dipole. The magnitude of the electric dipole is proportional to the normal electric field that would be present at the aperture assuming the aperture is replaced by a perfect conductor. Similarly, the magnitude of the magnetic dipole is proportional to the tangential magnetic field that would exist at the aperture. It seems reasonable to assume that at the apertures no normal electric fields would exist, since this would imply that a net accumulation of charge would exist inside the box. However, there could exist tangential magnetic fields as a result of any current loops in the circuitry. Thus, we will model the apertures by magnetic dipoles only. These dipoles will induce currents and charges on the outside surface of the conducting box, which can, in turn, be modeled by an equivalent electric dipole and a magnetic dipole. These dipoles will obviously not have magnitudes that are independent of frequency; however, at each frequency, the relationship between the magnitude of the electric and magnetic dipole will remain fixed, if we assume that the box contains only one source which induces both dipoles. Since the box is electrically small and contains only one source, the equivalent dipoles will also operate in phase. By the same argument, their directions will not be a function of frequency. Therefore, we can separate the contribution to the total power radiated from each dipole as described previously by measuring the power radiated at two selected frequencies. Since in some cases we do not have the operating frequency under our control, this will not always be possible unless our source radiates at more than one frequency, or we know a priori from physical grounds that the source can be modeled by only one type of dipole.

6. REFERENCES

[1] Adams, J.W., Electromagnetic Interference Measurement Program at the National Bureau of Standards, USNC/URSI, Commissions I-VIII, Annual Meeting, p. 33 (Oct. 20-23, 1975).

[2] Crawford, M. L., Generation of standard EM field using TEM transmission cells, IEEE Trans. on Electromagnetic Compatibility, EMC-16, No. 4 (Nov. 1974).

[3] Bowman, F., Introduction to Elliptic Functions with Applications, Chapter II (Dover Publ. Inc., New York, 1961).

[4] Ibid., Chapter I.

[5] Abramowitz and Stegun, Eds., Handbook of Mathematical Functions, 5th Ed., p. 612 (Dover Publ. Inc., New York, 1968).

[6] Ibid., Sec. 17.6, p. 598.

[7] Whittaker, E.T. and Watson, G.N., A Course of Modern Analysis, 4th Ed., p. 486 (Cambridge Univ. Press, 1969).

[8] Chen, T.-S., Determination of the capacitance, inductance, and characteristic impedance of rectangular lines, IRE Trans. on MTT, MTT-8, No. 5, 510-519 (Sept. 1960).

[9] Cohn, S.B., Shielded coupled-transmission line, IRE Trans. on MTT, MTT-3, No. 5, 29-38 (Oct. 1955).

[10] Anderson, G. M., The calculation of the capacitance of coaxial cylinders of rectangular cross-section, AIEE Trans., 69, pt. II, 728-731 (1950).

[11] Collin, R.E., Field Theory of Guided Waves, pp. 200-204 (McGraw-Hill, New York, 1960).

[12] Ramo, Whinnery and Van Duzer, Fields and Waves in Communication Electronics, pp. 645, 657 (Wiley, New York, 1967).

[13] Kerns, D.M., unpublished work (Aug. 1965).

[14] Collin, R.E., op cit., pp. 285-302.

[15] Walker, M., The Schwarz-Christoffel Transformation and Its Applications -- A Simple Exposition (Dover Publ. Inc., New York, 1964).

[16] Bowman, F., op cit., p. 58.

[17] Bowman, F., op cit., p. 57.

[18] Churchill, R.V., Complex Variables and Applications, 2nd Ed., p. 209 (McGraw-hill, New York, 1960).

[19] Abramowitz and Stegun, op cit., Sec. 17.6, p. 598, Sec. 16.4, p. 571.

[20] Abramowitz and Stegun, op cit., Sec. 16.21, p. 575.

APPENDIX A
Calculation of the Capacitance of a TEM Cell

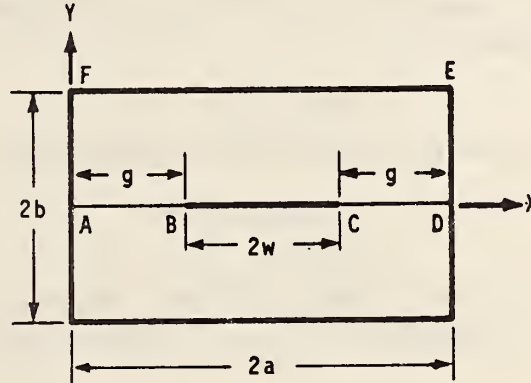A cross-section view of the TEM cell is shown in figure 5 with an x-y coordinate system superimposed.

Figure 5. Cross-section of a TEM cell.

The center septum of width 2w is located symmetrically inside the cell of height 2b and width 2a and is assumed to have negligible thickness. In addition, the septum is located a distance g from each vertical side wall and is embedded in a homogeneous dielectric of permittivity, ε_o. For convenience, some key points in the cell have been labeled A through F. The reason for choosing an unsymmetrically located coordinate system is to facilitate obtaining the approximate formula for the capacitance given in section 3.

To determine the capacitance, the method of conformal transformation will be used, whereby the structure in figure 5 is transformed into a simpler configuration whose capacitance is already known. Since it is well known that capacitance is invariant under a conformal transformation, the formula obtained will also be applicable to the TEM cell.

Since we have symmetry with respect to the septum, we will calculate the capacitance between the upper plate, A-F-E-D and the center septum B-C. The total capacitance is then twice this figure, since we have effectively two capacitors in parallel. The region A-D-E-F may be mapped into the upper-half of a complex t-plane via the Schwarz-Christoffel transformation [15] which, due to symmetry, can be expressed in terms of Jacobian elliptic functions. The transformation is given by [16]:

$$mz = \int_o^t \frac{dt}{[4t(1-t)(1-k^2t)]^{\frac{1}{2}}} \qquad (A.1)$$

or alternatively by:

$$t = sn^2(mz,k) \qquad (A.2)$$

89

where sn is a Jacobian elliptic function of modulus, k;

$$m = \frac{K(k')}{b};$$ (A.3)

and

$$z = x + iy.$$ (A.4)

Here $K(k)$ and $K(k')$ are complete elliptic integrals of the first kind of moduli k and k' respectively and:

$$k' = [1 - k^2]^{\frac{1}{2}}$$ (A.5)

The modulus k can be determined from the requirement that:

$$\frac{K(k)}{K(k')} = \frac{2a}{b}$$ (A.6)

Under the transformation given by eq. (A.2), the region, A-D-E-F, in the z-plane is mapped into the upper half of the t-plane as shown in figure 6.
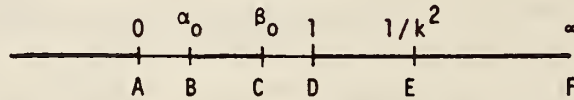
Figure 6. Complex t-plane.

Using eq. (A.2) and elliptic function identities, α_o and β_o can be calculated as:

$$\alpha_o = sn^2 mg = sn^2 \xi$$ (A.7)

$$\beta_o = sn^2 m(2a-g) = cn^2 \xi/dn^2 \xi$$ (A.8)

where

$$\xi \equiv mg$$ (A.9)

nd cn and dn are also Jacobian elliptic functions all of which have modulus, k. For convenience, we now make an intermediate transformation from the t-plane to a complex u-plane defined by:

$$u = \frac{\beta_o}{t}\left[\frac{t - \alpha_o}{\beta_o - \alpha_o}\right]$$ (A.10)

The u-plane is shown in figure 7.

90
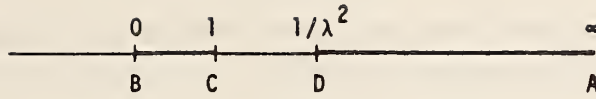
Figure 7. Complex u-plane.

λ in figure 7 can be found using eq. (A.10) and substituting t = 1. Thus:

$$\frac{1}{\lambda^2} = \beta_o \left| \frac{1 - \alpha_o}{\beta_o - \alpha_o} \right| \tag{A.11}$$

Substituting for α_o and β_o from eq. (A.7) and eq. (A.8), we obtain:

$$\lambda^2 = \frac{cn^2\xi - sn^2\xi \; dn^2\xi}{cn^2\xi [1-sn^2\xi]} \tag{A.12}$$

Using elliptic function identities, eq. (A.12) reduces to:

$$\lambda^2 = 1 - k'^2 \left(\frac{sn \; \xi}{cn \; \xi} \right)^4 \tag{A.13}$$

and defining a complementary modulus, λ' as:

$$\lambda' = [1 - \lambda^2]^{\frac{1}{2}} \tag{A.14}$$

We have from eqs. (A.13) and (A.14):

$$\lambda' = k' \left(\frac{sn \; \xi}{cn \; \xi} \right)^2 \tag{A.15}$$

In the final transformation, we map the upper half of the u-plane into a rectangular region in a complex χ-plane. The transformation is given by:

$$u = sn^2 (\chi, \lambda) \tag{A.16}$$

and the χ-plane is shown in figure 8.

Figure 8. Complex χ-plane.

91
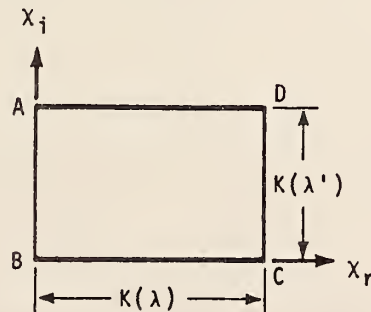
From figure 8, it is evident that the capacitance is just given by the ordinary parallel plate capacitor formula, that is:

$$C = \frac{\epsilon_o A_o}{d} \qquad (A.17)$$

where A_o is the cross-sectional area;

      d is the plate spacing;

and ϵ_o is the permittivity of free space.

Substituting for A_o and d in terms of $K(\lambda)$ and $K(\lambda')$ we obtain:

$$\frac{C}{\epsilon_o} = \frac{K(\lambda)}{K(\lambda')} \qquad (A.18)$$

where C is now interpreted as the capacitance per unit length. Therefore, the total capacitance of the TEM cell per unit length is just twice that given by eq. (A.18).

$$\frac{C_o}{\epsilon_o} = 2 \frac{K(\lambda)}{K(\lambda')} \qquad (A.19)$$

APPENDIX B

Calculation of the Electric Field Distribution
Inside a TEM Cell

In order to evaluate eqs. (4.12) and (4.13), we need to calculate the magnitude of the electric field, E_o, inside the guide. This is most easily done using a different coordinate system as well as a Schwarz-Christoffel transformation similar to that used in Appendix A. A cross-section view of the TEM cell is shown in figure 9 with a symmetrical x-y coordinate system superimposed.
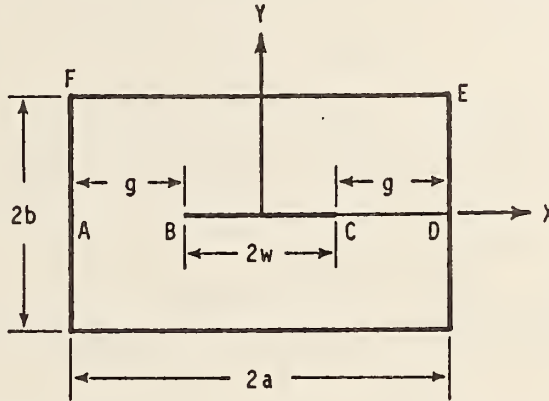
Figure 9.   Cross-section of a TEM cell.

The region A-D-E-F can be mapped into the upper-half of a complex t_o-plane via the following transformation [17]:

$$t_o = sn(m'z,k) \qquad (B.1)$$

where

$$m' = \frac{K(k)}{a} = \frac{K(k')}{b} \qquad (B.2)$$

Note that this transformation is not the same as the one used in Appendix A to solve for the capacitance, since a different coordinate system was used. The symbols used in this appendix should not be confused with those in Appendix A.

The complex t_o-plane is shown in figure 10.
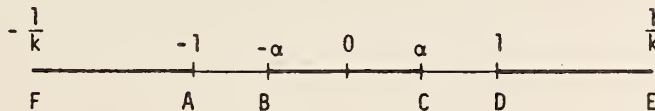
Figure 10.   Complex t_o-plane.

93

From eq. (B.1), α is given by:

$$\alpha = sn(m'w,k) \tag{B.3}$$

For convenience, we now make an intermediate transformation from the t_0-plane to a complex u_0-plane defined by:

$$u_0 = t_0/\alpha \tag{B.4}$$

The u_0-plane is shown in figure 11.
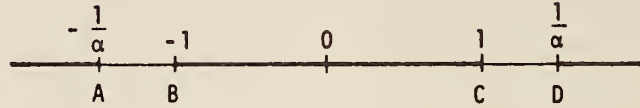
Figure 11.   Complex u_0 plane.

Finally, we map the upper-half of the u_0-plane into a complex χ_0-plane defined by:

$$u_0 = sn(\chi_0,\alpha) \tag{B.5}$$

The χ_0-plane is shown in figure 12.
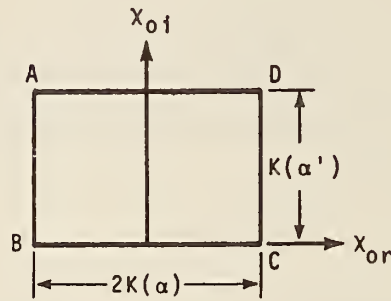
Figure 12.   Complex χ_0-plane.

In order to calculate the electric field, we must find the complex potential, F, which is given by [18]:

$$F = \phi(\chi_0) + i\psi(\chi_0) \tag{B.6}$$

where $\phi(\chi_0)$ is the potential function;

   $\psi(\chi_0)$ is the stream function;

and   F satisfies the Cauchy-Riemann equations.

In addition the potential $\phi(\chi_0)$ must satisfy the following boundary conditions:

   $\phi(\chi_0) = 0$ on BC

and $\phi(\chi_0) = V$ on AD.

94

It is easily verified that the following solution satisfies all of the above requirements:

$$\phi(\chi_o) = \frac{V\chi_{oi}}{K(\alpha')} \tag{B.7}$$

and

$$\psi(\chi_o) = -\frac{V\chi_{or}}{K(\alpha')} \tag{B.8}$$

where

$$\chi_o = \chi_{or} + i\chi_{oi}$$

The electric field, E, is defined by:

$$E = -\nabla\phi = -\left(\frac{\partial}{\partial x}\phi + i\frac{\partial}{\partial y}\phi\right)$$

$$= -\left(\frac{\partial}{\partial x}\phi - i\frac{\partial}{\partial x}\psi\right) = \frac{d}{dz}F^* \tag{B.9}$$

The real part of E gives the x-component of the electric field, and the imaginary part of E gives the y-component of the electric field. $\frac{dF}{dz}$ may be calculated as follows:

$$\frac{dF}{dz} = \frac{dF}{d\chi_o}\frac{d\chi_o}{du_o}\frac{du_o}{dt_o}\frac{dt_o}{dz} \tag{B.10}$$

Using eq. (B.1) and eq. (B.4) through eq. (B.8), $\frac{dF}{dz}$ may be evaluated as:

$$\frac{dF}{dz} = \frac{-iVm'}{K(\alpha')}\frac{dn(m'z)}{[P_o(z)]^{\frac{1}{2}}} \tag{B.11}$$

where

$$P_o(z) = [sn^2(m'w) - sn^2(m'z)] \tag{B.12}$$

Thus, the magnitude-squared of the electric field, E_o^2 is given by:

$$E_o^2 = \left(\frac{Vm'}{K(\alpha')}\right)^2 \left|\frac{dn^2(m'z)}{sn^2(m'w) - sn^2(m'z)}\right| \tag{B.13}$$

It is easy to see from eq. (B.13) that for $z = \pm w$, E_o^2 goes to infinity as expected from the edge condition.

Equation (B.11) was evaluated numerically for some typical TEM cell
geometries and used to calculate the x and y components of the electric field,
as well as the magnitude and polarization angle of the electric field defined by:

$$\theta = \arctan\left|\frac{E_y}{E_x}\right| \qquad (B.14)$$

These results are included in tables 3 through 10 where all field quantities
have been normalized to V/b. In addition, the relative electric field distri-
bution is plotted in figure 13. The top graph in that figure contains experi-
mental data measured by M.L. Crawford [2] for comparison.
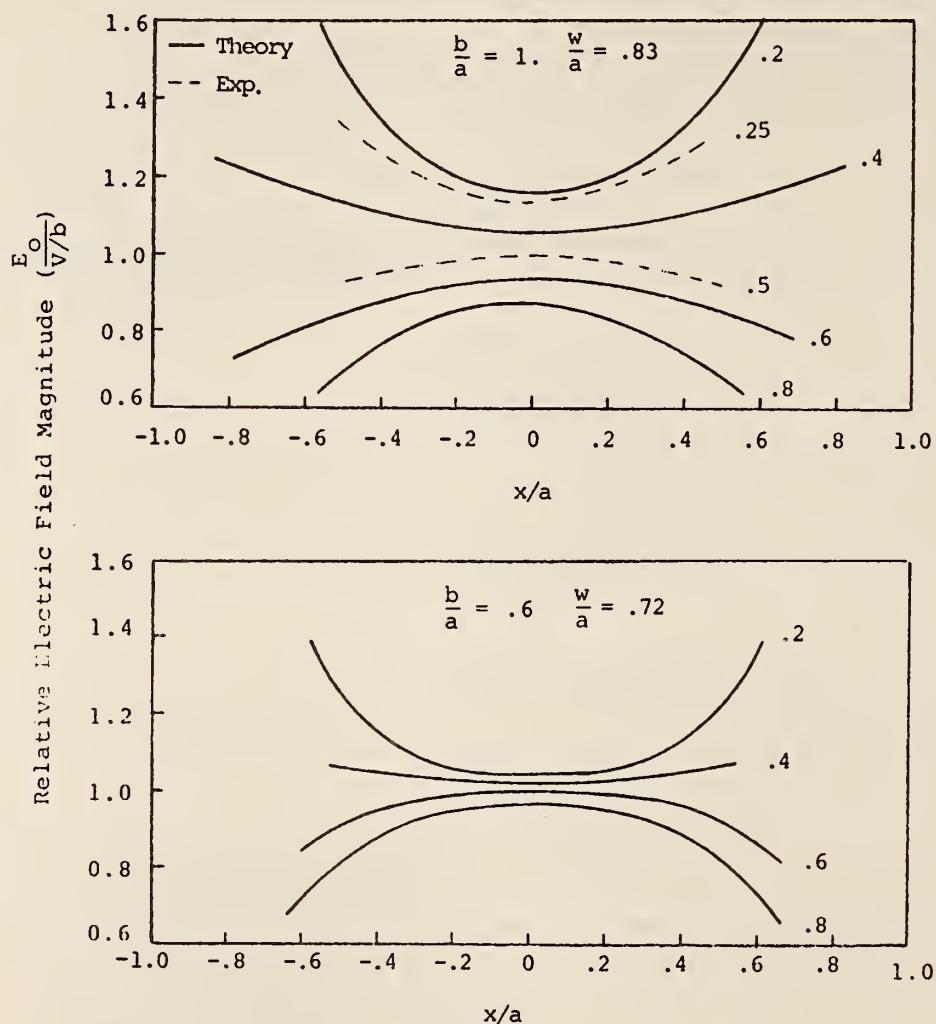
Figure 13. Relative electric field distribution inside a TEM
cell. Parameter indicates distance from the
center septum (y/b).

Table 3

x-component of the electric field in a TEM cell of dimensions:
a = 25 cm, b = 25 cm, w = 20.64 cm normalized to V/b.

y(cm)

y=b→25	0.000	0.000	0.000	0.000	0.000	0.000
20	0.000	0.060	0.129	0.208	0.278	0.307
15	0.000	0.108	0.245	0.422	0.600	0.680
10	0.000	0.127	0.311	0.620	1.029	1.237
5	0.000	0.090	0.248	0.647	1.684	2.285
0	0.000	0.000	0.000	0.000	0.000	3.603
	0	5	10	15	20	25 x(cm)

x=w x=a

Center of
TEM cell

Table 4

y-component of the electric field in a TEM cell of dimensions:
a = 25 cm, b = 25 cm, w = 20.64 cm normalized to V/b.

y(cm)

y=b→25	0.824	0.793	0.698	0.530	0.289	0.000
20	0.853	0.825	0.736	0.568	0.315	0.000
15	0.935	0.917	0.852	0.699	0.410	0.000
10	1.049	1.052	1.051	0.977	0.652	0.000
5	1.153	1.186	1.298	1.499	1.343	0.000
0	1.196	1.245	1.431	1.986	6.640	0.000
	0	5	10	15	20	25 x(cm)

x=w x=a

Center of
TEM cell

Table 5

Magnitude of the electric field in a TEM cell of dimensions:
a = 25 cm, b = 25 cm, w = 20.64 cm normalized to V/b.

y(cm)

y=b→25	0.824	0.793	0.698	0.530	0.289	0.000
20	0.853	0.827	0.747	0.605	0.420	0.307
15	0.935	0.924	0.886	0.817	0.727	0.680
10	1.049	1.060	1.096	1.157	1.218	1.237
5	1.153	1.189	1.321	1.633	2.154	2.285
0	1.196	1.245	1.431	1.986	6.640	3.603
	0	5	10	15	20	25	x(cm)
					x=w	x=a	

Center of
TEM cell

Table 6

Polarization angle of the electric field in degrees in a TEM
cell of dimensions: a = 25 cm, b = 25 cm, w = 20.64 cm.

y(cm)

y=b→25	90.00	90.00	90.00	90.00	90.00	--
20	90.00	85.86	80.05	69.89	48.54	00.00
15	90.00	83.27	73.97	58.89	34.35	00.00
10	90.00	83.14	73.50	57.60	32.36	00.00
5	90.00	85.64	79.20	66.67	38.56	00.00
0	90.00	90.00	90.00	90.00	90.00	00.00
	0	5	10	15	20	25	x(cm)
					x=w	x=a	

Center of
TEM cell

Table 7

x-component of the electric field in a TEM cell of dimensions:
a = 25 cm, b = 15 cm, w = 18.025 cm normalized to V/b.

y(cm)	0	5	10	15	20	25
y=b→15	0.000	0.000	0.000	0.000	0.000	0.000
12	0.000	0.024	0.067	0.143	0.220	0.249
9	0.000	0.040	0.121	0.284	0.462	0.517
6	0.000	0.043	0.141	0.410	0.763	0.817
3	0.000	0.028	0.101	0.440	1.247	1.112
0	0.000	0.000	0.000	0.000	1.969	1.254

x(cm)

Center of TEM cell

x=w   x=a

Table 8

y-component of the electric field in a TEM cell of dimensions:
a = 25 cm, b = 15 cm, w = 18.025 cm normalized to V/b.

y(cm)	0	5	10	15	20	25
y=b→15	0.966	0.946	0.872	0.698	0.394	0.000
12	0.972	0.956	0.890	0.724	0.411	0.000
9	0.989	0.981	0.944	0.807	0.464	0.000
6	1.010	1.015	1.028	0.979	0.557	0.000
3	1.028	1.046	1.120	1.311	0.645	0.000
0	1.035	1.058	1.164	1.664	0.000	0.000

x(cm)

Center of TEM cell

x=w   x=w

Table 9

Magnitude of the electric field in a TEM cell of dimensions:
a = 25 cm, b = 15 cm, w = 18.025 cm normalized to V/b.

y(cm)

	0	5	10	15	20	25
y=b→15	0.966	0.946	0.872	0.698	0.394	0.000
12	0.972	0.956	0.892	0.738	0.466	0.249
9	0.989	0.982	0.951	0.856	0.655	0.517
6	1.010	1.016	1.038	1.062	0.945	0.817
3	1.028	1.046	1.125	1.383	1.404	1.112
0	1.035	1.058	1.164	1.664	1.969	1.254

x(cm): 0, 5, 10, 15, 20 (x=w), 25 (x=a)

Center of
TEM cell

Table 10

Polarization angle of the electric field in degrees in a TEM
cell of dimensions: a = 25 cm, b = 15 cm, w = 18.025 cm.

y(cm)

	0	5	10	15	20	25
y=b→15	90.00	90.00	90.00	90.00	90.00	--
12	90.00	88.58	85.68	78.80	61.76	00.00
9	90.00	87.66	82.70	70.61	45.12	00.00
6	90.00	87.60	82.20	67.26	36.15	00.00
3	90.00	88.48	84.82	71.43	27.36	00.00
0	90.00	90.00	90.00	90.00	90.00	00.00

x(cm): 0, 5, 10, 15, 20 (x=w), 25 (x=a)

Center of
TEM cell

Numerical Evaluation of Complete Elliptic Integrals and Jacobian Elliptic Functions

The method used to evaluate elliptic functions and elliptic integrals is given in reference [19], a summary of which follows. Assuming that the modulus of the particular function desired is k, we begin by defining the following:

$$a_o = 1 \qquad b_o = k' \qquad c_o = k \qquad (C.1)$$

Then we set up an Arithmetic-Geometric Mean (AGM) table defined recursively as follows:

$$a_1 = \frac{1}{2}(a_o + b_o) \qquad b_1 = (a_o b_o)^{\frac{1}{2}} \qquad c_1 = \frac{1}{2}(a_o - b_o)$$

$$a_2 = \frac{1}{2}(a_1 + b_1) \qquad b_2 = (a_1 b_1)^{\frac{1}{2}} \qquad c_2 = \frac{1}{2}(a_1 - b_1)$$

$$\cdot \qquad\qquad\qquad \cdot \qquad\qquad\qquad \cdot$$
$$\cdot \qquad\qquad\qquad \cdot \qquad\qquad\qquad \cdot$$
$$\cdot \qquad\qquad\qquad \cdot \qquad\qquad\qquad \cdot$$

$$a_N = \frac{1}{2}(a_{N-1} + b_{N-1}) \qquad b_N = (a_{N-1} b_{N-1})^{\frac{1}{2}} \qquad c_N = \frac{1}{2}(a_{N-1} - b_{N-1})$$

Stopping at n = N when $c_N = 0$ to the degree of accuracy required.

The complete elliptic integral K(k) is then given by:

$$K(k) = \frac{\pi}{2a_N} \qquad (C.2)$$

The Jacobian elliptic functions, $sn(\xi)$, $cn(\xi)$, and $dn(\xi)$ can be determined by calculating ϕ_N in degrees where

$$\phi_N = 2^N a_N \xi \frac{180°}{\pi} \qquad (C.3)$$

and then computing recursively, ϕ_{N-1}, ϕ_{N-2}, $\cdots$ ϕ_1, ϕ_o by using:

$$\sin(2\phi_{n-1} - \phi_n) = \frac{c_n}{a_n} \sin \phi_n \qquad (C.4)$$

The Jacobian elliptic functions are then given by:

$$sn(\xi, k) = \sin \phi_o \qquad (C.5)$$

$$cn(\xi, k) = \cos \phi_o \qquad (C.6)$$

$$dn(\xi, k) = \frac{\cos \phi_o}{\cos(\phi_1 - \phi_o)} \qquad (C.7)$$

In eqs. (C.5) through (C.7), the argument, ξ, was assumed to be real. If the argument is complex then the following formulas from reference [20] can be used.

$$sn(\xi,k) = \frac{s \cdot d_1 + ic \cdot d \cdot s_1 \cdot c_1}{c_1^2 + k^2 \cdot s^2 \cdot s_1^2} \qquad (C.8)$$

$$cn(\xi,k) = \frac{c \cdot c_1 - is \cdot d \cdot s_1 \cdot d_1}{c_1^2 + k^2 \cdot s^2 \cdot s_1^2} \qquad (C.9)$$

$$dn(\xi,k) = \frac{d \cdot c_1 \cdot d_1 - ik^2 \cdot s \cdot c \cdot s_1}{c_1^2 + k^2 \cdot s^2 \cdot s_1^2} \qquad (C.10)$$

where

$$\xi = \xi_r + i\xi_i$$

and

$$s = sn(\xi_r,k) \qquad s_1 = sn(\xi_i,k')$$

$$c = cn(\xi_r,k) \qquad c_1 = cn(\xi_i,k')$$

$$d = dn(\xi_r,k) \qquad d_1 = dn(\xi_i,k')$$

Two Fortran subroutines, AGM and SNCNDN, were used to perform the calculations described in this appendix. When AGM(K) is called, the AGM table described above is defined. SNCNDN(X,SN,CN,DN) can then be called with real argument X to return the functions desired. A copy of these subroutines follows.

```
      SUBROUTINE AGM(K)
      COMMON A(20),B(20),C(20),L
      REAL K
      A(1)=1.
      B(1)=SQRT(1.-K*K)
      C(1)=K
      DO 10 I=2,20
      A(I)=.5*(A(I-1)+B(I-1))
      B(I)=SQRT(A(I-1)*B(I-1))
      C(I)=.5*(A(I-1)-B(I-1))
      IF(C(I).LT.1.E-6) GOTO 30
   10 CONTINUE
      PRINT 20
   20 FORMAT(1X,*AGM FAILED TO CONVERGE IN 20 ITERATIONS*)
   30 L=I
      RETURN
      END
```

```
      SUBROUTINE SNCNDN(X,SN,CN,DN)
      COMMON A(20),B(20),C(20),L
      DIMENSION P(20)
      P(L)=A(L)*X*2.**(L-1)
      I=L
   10 P(I-1)=.5*(ASIN((C(I)/A(I))*SIN(P(I)))+P(I))
      I=I-1
      IF(I.NE.0) GOTO 10
      SN=SIN(P(1))
      CN=COS(P(1))
      DN=CN/COS(P(2)-P(1))
      RETURN
      END
```

U.S. DEPT. OF COMM. BIBLIOGRAPHIC DATA SHEET	1. PUBLICATION OR REPORT NO. NBSIR 75-829	2. Gov't Accession No.	3. Recipient's Accession No.

4. TITLE AND SUBTITLE	5. Publication Date
RADIATION CHARACTERISTICS OF DIPOLE SOURCES LOCATED INSIDE A RECTANGULAR, COAXIAL TRANS-MISSION LINE	January 1976
	6. Performing Organization Code 276.00

7. AUTHOR(S) John C. Tippet and David C. Chang	8. Performing Organ. Report No. NBSIR 75-829

9. PERFORMING ORGANIZATION NAME AND ADDRESS	10. Project/Task/Work Unit No. 2768281
NATIONAL BUREAU OF STANDARDS DEPARTMENT OF COMMERCE WASHINGTON, D.C. 20234	11. Contract/Grant No.

12. Sponsoring Organization Name and Complete Address (Street, City, State, ZIP)	13. Type of Report & Period Covered
Same as Item 9.	
	14. Sponsoring Agency Code

15. SUPPLEMENTARY NOTES

16. ABSTRACT (A 200-word or less factual summary of most significant information. If document includes a significant bibliography or literature survey, mention it here.)

When making EMC measurements inside a shielded enclosure, the radiation characteristics of the device being tested changes. In this report the change in radiation resistance of dipole sources located inside a National Bureau of Standards TEM transmission cell is determined. In many cases a practical device can be modeled by dipole sources. In these cases, the analysis allows one to predict the device's radiation characteristics in other environments, e.g., free space.

17. KEY WORDS (six to twelve entries; alphabetical order; capitalize only the first letter of the first key word unless a proper name; separated by semicolons) EMC measurements; radiation resistance; rectangular coax; shielded strip line; TEM cell.

18. AVAILABILITY ☒ Unlimited	19. SECURITY CLASS (THIS REPORT)	21. NO. OF PAGES
☐ For Official Distribution. Do Not Release to NTIS	UNCLASSIFIED	33
☐ Order From Sup. of Doc., U.S. Government Printing Office Washington, D.C. 20402, SD Cat. No. C13	20. SECURITY CLASS (THIS PAGE)	22. Price
☒ Order From National Technical Information Service (NTIS) Springfield, Virginia 22151	UNCLASSIFIED	$3.75

Appendix E

Kanda, M. "Electromagnetic field distortion due to a conducting rectangular cylinder in a transverse electromagnetic cell."

Electromagnetic-Field Distortion Due to a Conducting Rectangular Cylinder in a Transverse Electromagnetic Cell

MOTOHISA KANDA, MEMBER, IEEE

Abstract—This paper deals with the distortion effects in a TEM cell resulting from loading by the object under test. To insure that higher order modes are ruled out as contributing factors, a brief discussion of the cutoff frequencies of these modes is presented. The paper then proceeds to a theoretical and experimental analysis of the loading effects. In the theoretical analysis for the loading effects, i.e., the electromagnetic-field distortion caused by an object under test in a TEM cell, the frequency-domain integral equation for the magnetic field, or equivalently, the current density on the surface of a perfectly conducting cylinder in a parallel-plate waveguide, is solved by the method of moments to predict the degree of magnetic-field distortion.

The experimental investigations are performed by mounting a number of electrically small half loops on the surface of the conducting cylinder in a TEM cell. The loading effects in terms of magnetic-field distortion are analyzed as the ratio of one of the object dimensions (height) to the separation distance between the inner conductor and the ground plane of the TEM cell. Also, the response of an electrically small loop to both the magnetic and electric components of the electromagnetic field is used to measure the phase relation between the magnetic and electric fields, which in turn can be used to determine the degree of degradation of the TEM mode due to the presence of the conducting cylinder. These theoretical and experimental results are compared with the available quasi-electrostatic results.

Key Words—Electromagnetic compatibility (EMC), Green's function, integral equation, linear equation, method of moments, parallel-plate waveguide, quasi-electrostatic, TEM cell.

I. INTRODUCTION

THE STUDY of electromagnetic compatibility (EMC) (including the electric and biological effects due to electromagnetic (EM) radiation) and EM calibration require accurate measurement techniques for defining EM interference (EMI) characteristics. Thus, fully enclosed, rectangular, transverse electromagnetic (TEM) transmission lines with thin inner conductors are often used for generating standard known test fields. In all cases, it is desirable that only the dominant TEM mode should propagate. Thus the limitations of these structures are discussed in this paper in terms of the higher order modes and the loading effects. First, presented below is a brief discussion of the modal considerations based on existing theory. Results are presented which upper bound the frequency to which the TEM cell should be limited in order to suppress the higher order modes. Then, the loading effects, i.e., the electromagnetic-field distortions caused by an object
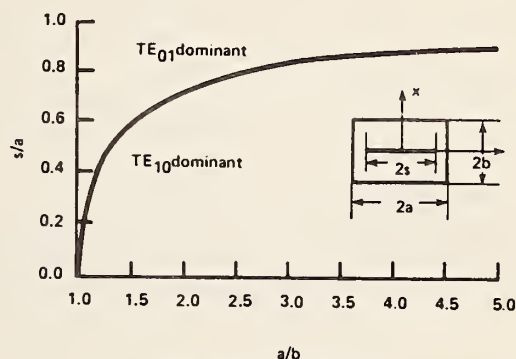
Fig. 1. Curve of equal TE_{01} and TE_{10} cutoff frequencies for a transverse electromagnetic cell.

under test in a TEM cell, are treated in detail giving analysis and experimental support.

II. MODE SUPPRESSION

The higher order mode cutoff frequencies of the rectangular TEM cell have been well studied by many workers [1]–[4]. In a rectangular hollow waveguide, the dominant mode is always the TE_{10} mode as long as the width exceeds the height. However, the same conclusion does not hold for the rectangular line with an inner conductor, even if its thickness is infinitesimally small. In fact, it is found [1], [2], [4] that, depending on the width of the inner conductor and the size of the TEM cell, the cutoff frequency of the TE_{01} mode can be much lower than that of the TE_{10} mode as illustrated in Fig. 1. While the cutoff frequency of the TE_{10} mode is simply calculated from

$$f_c = \frac{1}{2\sqrt{\mu\epsilon}} \sqrt{\frac{m^2}{a} + \frac{n^2}{b}} \Bigg|_{\substack{m=1 \\ n=0}} = \frac{1}{2a\sqrt{\mu\epsilon}} \qquad (1)$$

the cutoff frequencies of the TE_{01} mode are much more involved and have been calculated by many workers [1]–[4] as shown in Fig. 2. Let us consider, for example, a typical 50-Ω TEM cell having a width of $a = 1$ m, and a height of $b = 0.6$ m, and a width of inner conductor of $s = 0.72$ m. While the cutoff frequency of the TE_{10} mode is 150 MHz, the cutoff frequency of the TE_{01} mode is approximately 135 MHz, according to Fig. 2. It can also be shown that the cutoff frequencies of all TM modes of a TEM cell are always higher than
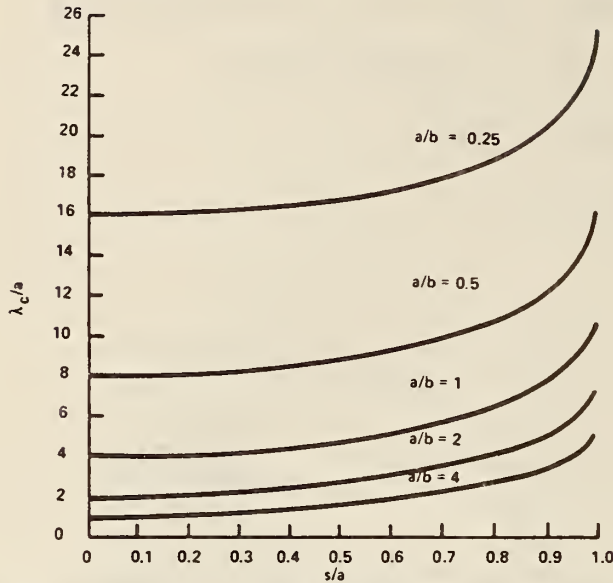
Fig. 2. Normalized TE_{01} cutoff wavelength for a transverse electromagnetic cell.
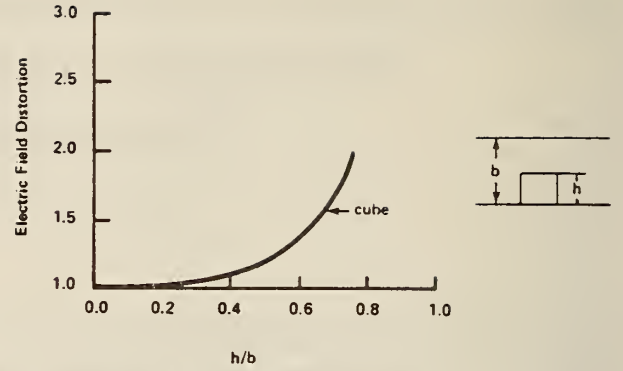

Fig. 3. Electromagnetic-field distortion due to a metallic cube in a transverse electromagnetic cell (electrostatic approximation).

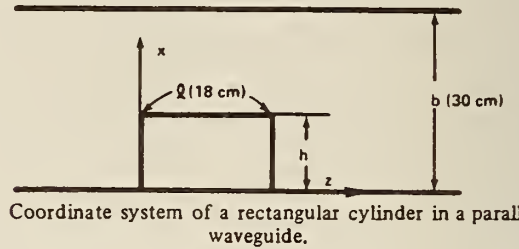Fig. 4. Coordinate system of a rectangular cylinder in a parallel-plate waveguide.

those of their hollow-waveguide counterparts. Thus, the dominant cutoff frequency (i.e., the lowest) is either the TE_{01} mode or the TE_{10} mode. It is interesting to note that the cutoff frequency of the TE_{01} mode decreases as the gap between the inner conductor and the wall of the TEM cell becomes narrower. This phenomenon has also been observed in a ridge waveguide [5] and is associated with the infinite-gap capacitance.

III. LOADING EFFECTS

In EMC measurements, an object under test is placed inside a TEM cell. The field from the TEM-mode incident upon the scattering object is identical to that of a plane wave in free space. However, the scattered field produced by the object in the TEM cell is different from the scattered field produced by the object in free space because of multiple reflections from the TEM-cell walls, or equivalently, because of the mutual coupling between the object and the TEM cell.

Placing a test object in a TEM cell is equivalent to introducing a capacitive discontinuity. For low frequencies, where the transverse dimensions of the object are negligible compared to the wavelength, the discontinuity due to the object is a pure capacitive reactance, and may be regarded as the fringing capacitance of the corresponding electrostatic problem. Under this assumption, the ratio of the electric-field strength near the metal object in the TEM cell to the unperturbed electric-field strength at the same location in a pure TEM mode has been calculated by Meyer [6] and is shown in Fig. 3.

In the theoretical analysis of the loading effects, i.e., the electromagnetic-field distortion caused by an object under test in a TEM cell, the frequency-domain integral equation for the magnetic field, or equivalently, the current density on the surface of a perfectly conducting cylinder in a parallel-plate waveguide, is solved by the method of moments to predict the degree of magnetic-field distortion. For the purpose of mathematical tractability, a parallel-plate waveguide is used to

model a TEM-cell structure. The results given in this paper are for the magnetic-field strength on the surface of the cylinder. Other related quantities, such as the electric-field strength and the Poynting vector, can be readily derived from the surface current by use of Maxwell's equations.

A. Theory

The problem of determining the electromagnetic field scattered by a perfectly-conducting rectangular cylinder has been studied by many workers [7]-[9]. The coordinate system used to analyze the current density on the surface of the rectangular cylinder in a parallel-plate waveguide is shown in Fig. 4. The source of the TEM wave is a delta-function voltage source of the form

$$M = y V_0(\omega)\delta(z - z_0) \qquad (2)$$

where V_0 is the magnitude of an equivalent voltage source located at the source location z_0. Since there is no variation in the y-direction and the voltage source has only a y-component, we will have a scalar wave equation in H_y, i.e.,

$$\nabla^2 H_y + k^2 H_y = j\omega\epsilon M_y \cdot \qquad (3)$$

where $\nabla^2 = (\partial^2/\partial x^2) + (\partial^2/\partial z^2)$ and k is the free-space wavenumber. The boundary condition is that the tangential E field be zero on all of any reflecting conducting surfaces, i.e.,

$$\frac{\partial H_y}{\partial n} = 0 \qquad (4)$$

where $n = x$ and z.

The solution of (3) may be found through the Green's

Function technique

$$\nabla^2 G(r, r') + k^2 G(r, r') = -\delta(x - x')\delta(z - z'). \quad (5)$$

Multiplying (3) by $G(r, r')$, (5) by $H_y(r')$, subtracting the two results, and integrating over the free-space volume v

$$\int_v [G(r, r')\nabla^2 H_y(r') - H_y(r')\nabla^2 G(r, r')] \, dv'$$

$$= j\omega\epsilon \int_v G(r, r')M_y(r') \, dv'$$

$$+ \int_v H_y(r')\delta(x - x')\delta(z - z') \, dv'. \quad (6)$$

Evaluating the second integration of the right-hand side of (6) and using Green's theorem on the left-hand side, we get

$$\int_s \left[G(r, r')\frac{\partial H_y(r')}{\partial n'} - H_y(r')\frac{\partial G(r, r')}{\partial n'} \right] ds'$$

$$= j\omega\epsilon \int_v G(r, r')M_y(r') \, dv' + H_y(r). \quad (7)$$

On the perfectly conducting surface s of the rectangular cylinder, we set the boundary condition as

$$\frac{\partial H_y(r')}{\partial n'} = 0. \quad (8)$$

Equation (7) then reduces to

$$H_y(r) = -j\omega\epsilon \int_v G(r, r')M_y(r') \, dv'$$

$$- \int_s H_y(r')\frac{\partial G(r, r')}{\partial n'} \, ds' \quad (9)$$

where s indicates the surface of the rectangular cylinder. The first term on the right-hand side of (9) corresponds to the incident field, and the second term to the scattered field. The known incident magnetic field is given by

$$H^{\text{inc}}(x, z) = -j\omega\epsilon \int_0^\infty \int_0^b V_0\delta(z' - z_0)$$

$$\cdot G(x, z; x', z') \, dx' \, dz'$$

$$= \frac{\omega\epsilon}{k} V_0 e^{jkz_0} \cos kz. \quad (10)$$

Equation (9) is an integral equation which can be solved for $H_y(r)$ once Green's function $G(r, r')$ is obtained.

The Green's function is the solution of (5). By imposing the proper boundary condition for the parallel-plate waveguide, i.e.,

$$\frac{\partial G}{\partial x} = 0 \quad (11)$$

at $x = 0$ and $x = b$, one finds

$$G(x, z; x', z') = \frac{j}{2kb} [e^{jk(z+z')} + e^{jk|z - z'|}]$$

$$+ \frac{j}{b} \sum_{n=1}^\infty \frac{\cos\dfrac{n\pi x}{b} \cos\dfrac{n\pi x'}{b}}{\Gamma_n}$$

$$\cdot [e^{j\Gamma_n(z+z')} + e^{j\Gamma_n|z - z'|}] \quad (12)$$

where

$$\Gamma_n = \sqrt{k^2 - \left(\frac{n\pi}{b}\right)^2} \quad (13)$$

Once the Green's function is obtained and the source is specified, (9) can be solved by the method of moments. The technique used is discussed briefly below. A detailed discussion on this subject is given by Harrington [10].

The unknown H_y is expanded in terms of a set of known basis functions f_i with unknown coefficients α_i, i.e.,

$$H_y = \sum_{i=1}^n \alpha_i f_i. \quad (14)$$

Substituting (14) into (9) we obtain

$$\sum_{i=1}^n \alpha_i \left[f_i(x, z) + \int_{s'} f_i(x', z')\frac{\partial G(x, z; x', z')}{\partial n'} \, ds' \right]$$

$$= H^{\text{inc}}(x, z). \quad (15)$$

Equation (15) is a single equation with n unknowns α_i. To create at least n linear equations, a set of testing functions w_j is introduced, and the inner products (integral over the surface) of both sides of (15) for each w_j are set equal. The result is a set of linear equations of the form

$$[Z][I] = [V] \quad (16)$$

where the matrix element Z_{ij} is given by

$$Z_{ij} = \int_s \left[f_i(r) + \int_{s'} f_i(r')\frac{\partial G(r, r')}{\partial n'} \, ds' \right] w_j(r) \, ds \quad (17)$$

and the column matrix element V_j is given by

$$V_j = \int_s H^{\text{inc}}(r)w_j(r) \, ds. \quad (18)$$

The unknown coefficients α_j are found by solving the matrix (16). The expression for H_y is then given by (14).

B. Theoretical and Experimental Results

A number of electrically small half-loops whose diameters are 1.5 cm are mounted transversely across a perfectly con-
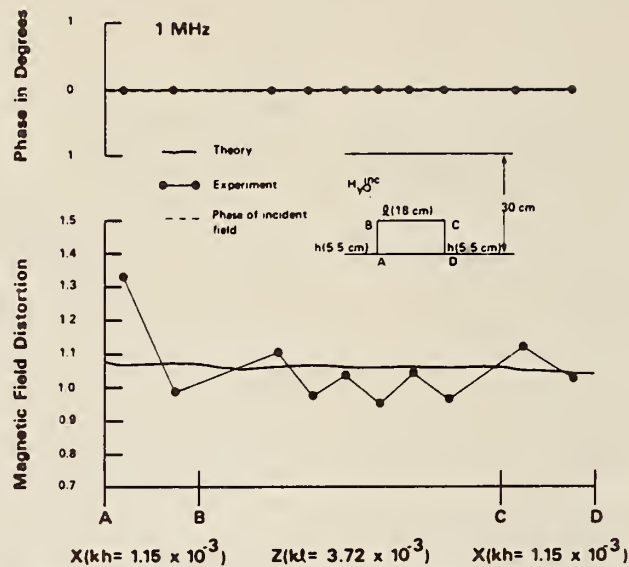
Fig. 5. Magnetic-field distortion along path ABCD due to a conducting cylinder (width l = 18 cm, height h = 5.5 cm) in a transverse electromagnetic cell at 1 MHz.

ducting rectangular cylinder. The cylinder is placed in a TEM cell which acts approximately as a parallel-plate waveguide. A vector voltmeter is used to measure both the magnitude and phase of the magnetic-field strength and therefore the current density on the surface of the cylinder. In the theoretical analysis, the frequency-domain integral equation for the magnetic field on the surface of the cylinder in a parallel-plate waveguide given in Section III-A is solved by the method of moments. Other related quantities, such as the electric-field strength and the Poynting vector, can be readily derived from the surface current by use of Maxwell's equations.

In this part of the paper, the loading effects due to the conducting rectangular cylinder in a TEM cell are indicated in terms of the magnetic-field distortion, which is defined as the ratio of the magnetic-field strength on the surface of the cylinder in a TEM cell to that at the same position in an empty TEM cell. The separation distance of the parallel-plate waveguide, i.e., the distance between the center conductor and the ground plane in the TEM cell, is chosen to be 30 cm. Three different conducting rectangular cylinders are used, all of which have the same widths of 18 cm, but have different heights of 5.5 cm, 15 cm, and 18 cm. The magnetic-field distortion and the corresponding phase are shown in Figs. 5–10 for frequencies from 1 MHz and 100 MHz. The phase reference is taken to be at the center of the top of the cylinder ($x = h$ and $z = l/2$). Figs. 11 and 12 show the magnetic-field distortion at the center of the top of the cylinder as the ratio of its height to the separation distance of the TEM cell. For a comparison, the electric-field distortion due to a metal cube reported by Meyer [6] is also shown in these figures. In general, it is found that the magnetic-field distortion due to a perfectly-conducting rectangular cylinder is quite small, and much less than the electric-field distortion reported by Meyer [6].

In order to confirm the result by Meyer [6], an electrically small dipole is mounted on the center of the top of the perfectly-conducting rectangular cylinder. The electric-field distortion (defined as the ratio of electric field at the surface

Fig. 6. Magnetic-field distortion along path ABCD due to a conducting cylinder (width l = 18 cm, height h = 5.5 cm) in a transverse electromagnetic cell at 100 MHz.

of the cylinder to that at the same position in an empty TEM cell) is shown in Fig. 13 as a function of the ratio of the cylindrical height to the separation distance of the parallel-plate waveguide. Fig. 13 indicates that the electric-field distortion is much larger than that predicted by Meyer [6]. The discrepancy may be due to the fact that the Meyer calculation is based on the quasi-electrostatic approximation.

When the conducting rectangular cylinder is placed in the TEM cell, the scattered field produced by the cylinder can be far different from the original incident TEM mode. In order to determine the degree of degradation of the TEM mode due to the presence of the cylinder, the response of an electrically small loop to both the magnetic and electric components of an

110
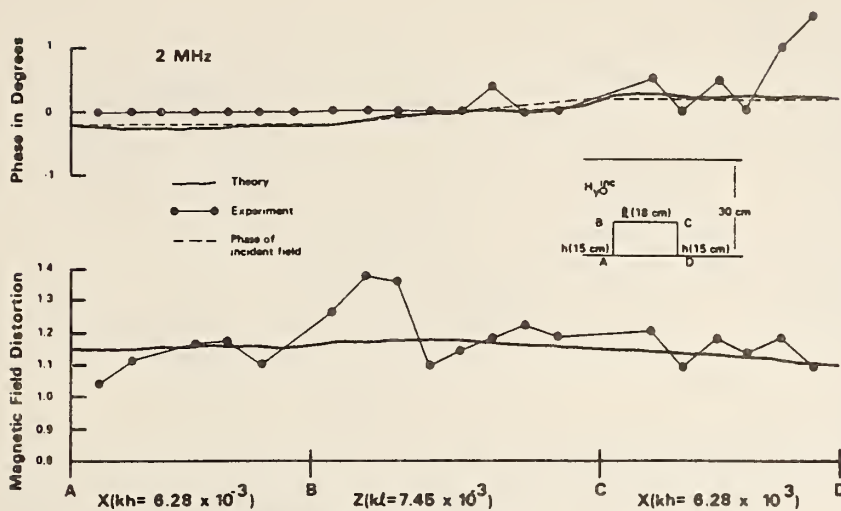
Fig. 7. Magnetic-field distortion along path ABCD due to a conducting cylinder (width l = 18 cm, height h = 15 cm) in a transverse electromagnetic cell at 2 MHz.
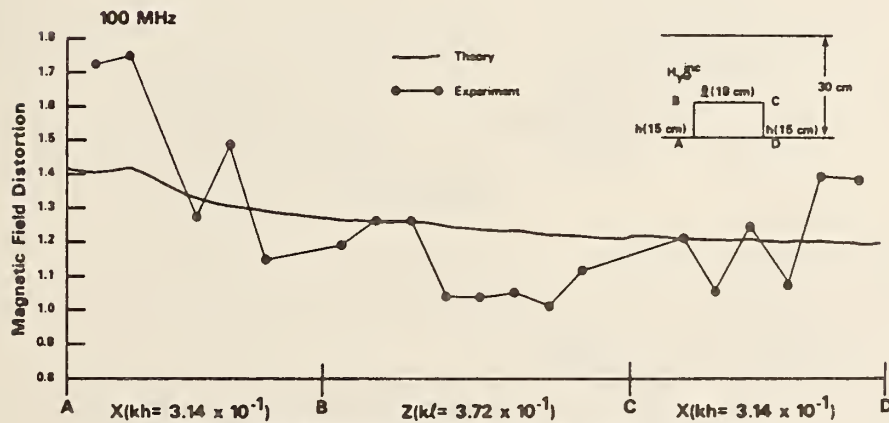
Fig. 8. Magnetic-field distortion along path ABCD due to a conducting cylinder (width l = 18 cm, height h = 15 cm) in a transverse electromagnetic cell at 100 MHz.
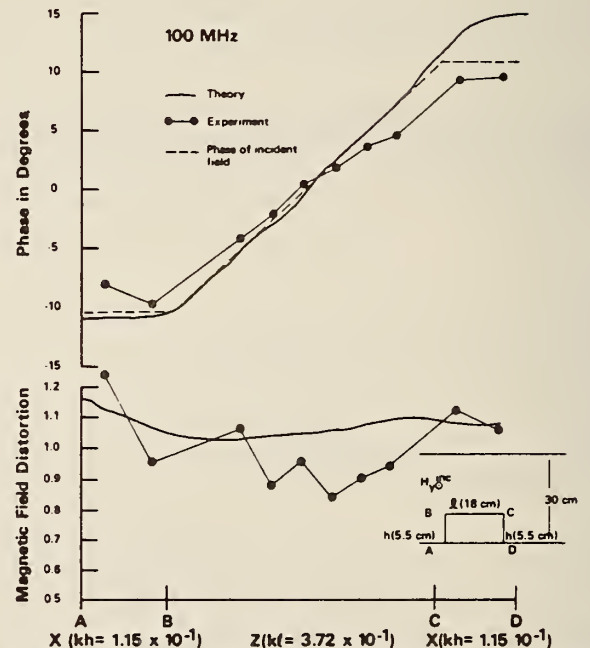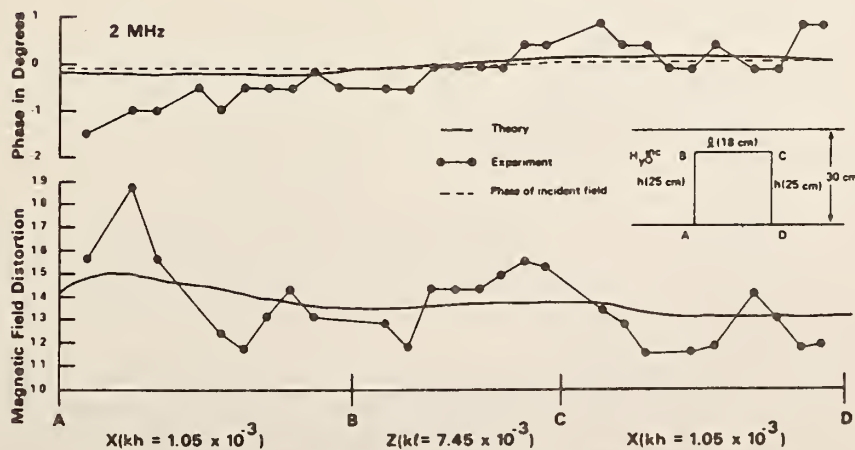

Fig. 9. Magnetic-field distortion along path ABCD due to a conducting cylinder (width l = 18 cm, height h = 25 cm) in a transverse electromagnetic cell at 2 MHz.

111
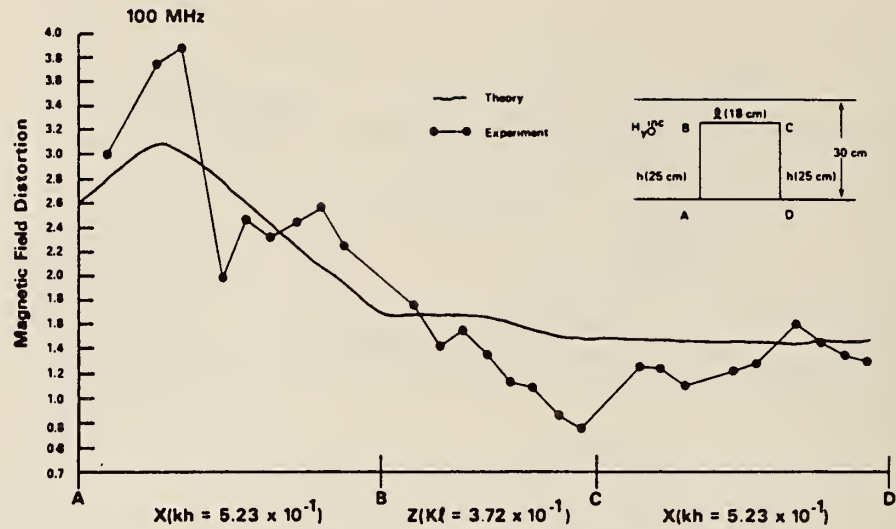
Fig. 10. Magnetic-field distortion along path ABCD due to a conducting cylinder (width l = 18 cm, height h = 25 cm) in a transverse electromagnetic cell at 100 MHz.
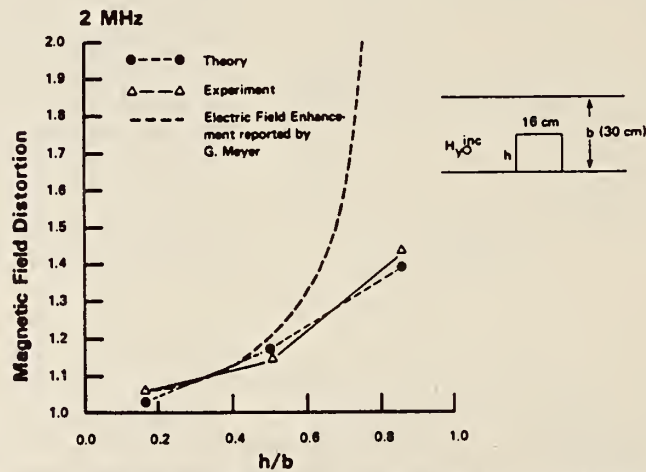
Fig. 11. Magnetic-field distortion at the center of a top of the cylinder versus the ratio of its height to the separation distance of the parallel-plate waveguide at 2 MHz.
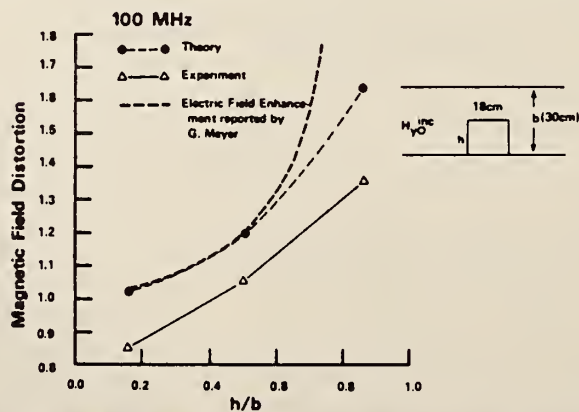
Fig. 12. Magnetic-field distortion at the center of the top of the cylinder versus the ratio of its height of the separation distance of the parallel-plate waveguide at 100 MHz.
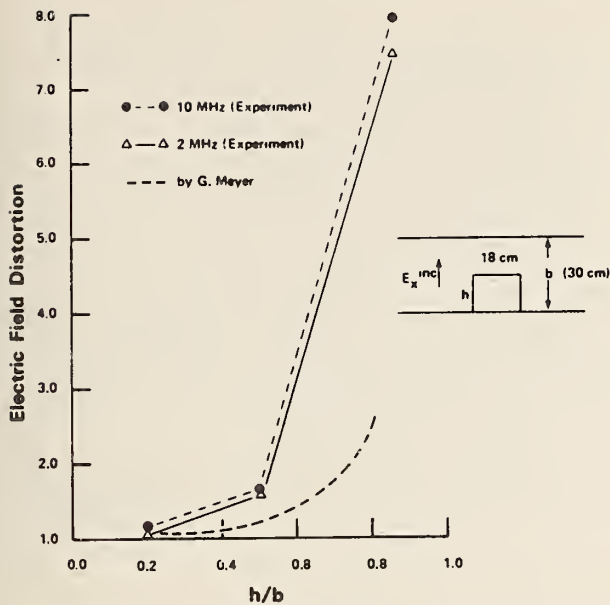
Fig. 13. Electric-field distortion at the center of the top of the cylinder versus the ratio of its height to the separation distance of the parallel-plate waveguide.
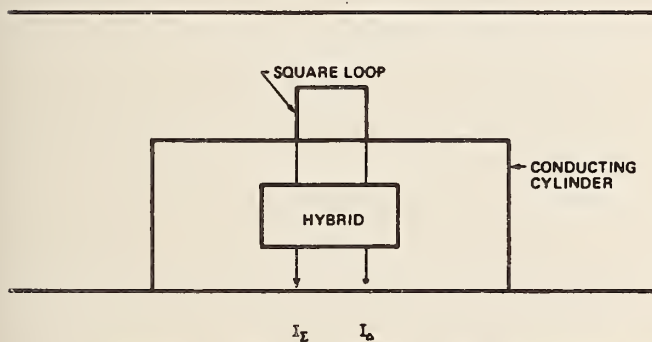
Fig. 14. Simultaneous electric- and magnetic-field measurements using a doubly loaded electrically small loop.

electromagnetic field is examined. Consider the loop loaded at each of the diametrically opposite points as shown in Fig. 14. One can show that the sum of the two load currents I_Σ is given by [11]

$$I_\Sigma = K_h H_y \qquad (19)$$

and their difference I_Δ is given as

$$I_\Delta = K_e E_x \qquad (20)$$

where K_h and K_e are, respectively, the loop sensitivity constants for magnetic and electric fields. These formulas clearly show that the use of the sum current gives a measure of the magnetic field, whereas that of its difference gives a measure of the electric field.

While the magnetic and electric fields are normally in phase for the pure TEM mode, the presence of the perfectly conducting rectangular cylinder in the TEM cell will cause a distortion, and thus a phase degradation of the TEM mode around the cylinder. The phase degradation of the TEM mode thus obtained is shown in Fig. 15 as a function of the ratio of
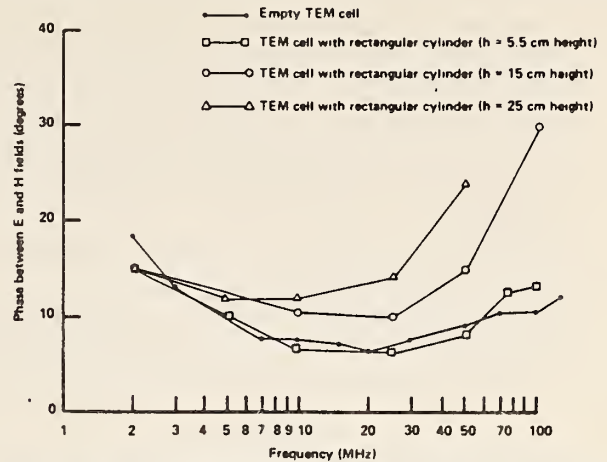
Fig. 15. Phase degradation of the TEM mode versus the ratio of the cylinder height to the separation distance between the center conductor and the ground plane in the TEM cell.

the cylinder height to the separation distance of the TEM cell. It is very interesting to note that the phase degradation at the center of the cylinder increases as the frequency approaches the cutoff frequency of the TE_{01} mode, and also as the height of the cylinder becomes large compared to the separation of the parallel-plate waveguide. The phase degradation observed at the low frequencies around 2 MHz is not well understood, but is probably due to the experimental problems caused by the vector voltmeter and the hybrid junction used in the experiments.

IV. CONCLUSIONS

This paper discussed the loading effects of the TEM cell, i.e., the electromagnetic-field distortion caused by a metal object placed in a TEM cell. In the theoretical analysis the frequency-domain integral equation for the magnetic-field strength on the surface of a perfectly conducting cylinder in a parallel-plate waveguide was solved by the method of moments to obtain the degree of magnetic-field distortion. The results given in the paper are for the magnetic-field strength on the surface of the cylinder. Other related quantities, such as the electric-field strength and the Poynting vector can be readily derived from the surface current by use of Maxwell's equations.

The experimental investigations were performed by mounting a number of electrically small half-loops on the surface of a conducting cylinder placed in a TEM cell. The loading effects in terms of magnetic-field distortion were expressed as a function of the ratio of the object height to the separation distance between the inner conductor and the ground plane of the TEM cell. Also, the response of an electrically small loop to both the magnetic and electric components of an electromagnetic field was used to measure the phase relation between the magnetic and electric fields, which in turn was used to assess the degree of degradation of the TEM mode due to the presence of the perfectly conducting cylinder. These theoretical and experimental results were compared with the available quasi-electrostatic results.

REFERENCES

[1] W. Brackelmann, D. Landmann, and W. Schlosser, *Die Grenzfrequenzen von hoheren Eigenwellen in Streifenleitungen AEU,* vol. 21, pp. 112–120, Mar. 1967.

[2] L. Gruner, "High order modes in rectangular coaxial wave-guides," *IEEE Trans. Microwave Theory Tech.*, vol. MTT-15, pp. 483–485, Aug. 1967.

[3] R. Mittra, and T. Itoh, "A new technique for the analysis of the dispersion characteristics of microstrip lines," *IEEE Trans. Microwave Theory Tech.*, vol. MTT-19, pp. 47–56, Jan. 1971.

[4] J. C. Tippet, "Modal Characteristics of Rectangular Coaxial Transmission Line," Ph.D. thesis, Univ. Colorado, Boulder, CO, June 1978.

[5] S. Ramos and J. R. Whinnery, *Fields and Waves in Modern Radio*, 2nd ed. New York: Wiley, 1953.

[6] G. Meyer, "Application of a broadband measuring line in field immunity testing, in *2nd Symp. Tech. Exhibition Electromagn. Compat.*, Montreux, Switzerland, June 1977, pp. 241–46.

[7] K. Mei and J. G. Van Blade, "Low-frequency scattering by rectangular cylinders," *IEEE Trans. Antennas Propagat.*, vol. AP-11, pp. 52–56, Jan. 1963.

[8] K. K. Mei and J. G. Van Bladel, "Scattering by perfectly conducting rectangular cylinders," *IEEE Trans. Antennas Propagat.*, vol. AP-11, pp. 185–192, Mar. 1963.

[9] M. G. Andreasen, "Comments on scattering by conducting rectangular cylinders," *IEEE Trans. Antennas Propagat.*, vol. AP-12, pp. 235–236, Mar. 1964.

[10] R. F. Harrington, *Field Computation by Moment Methods.* New York: Macmillan, 1968.

[11] H. Whiteside and R. W. P. King, "The loop antenna as a probe," *IEEE Trans. Antennas Propagat.*, vol. AP-19, pp. 291–297, May 1964.

Appendix F

Spiegel, R. J.; Joines, W. T.; Blackman, C. F.; Wood, A. W. "A method for calculating electric and magnetic fields in TEM cells at ELF."

Reprinted from IEEE Trans. Electromagn. Compat. EMC-29(4):265-272; 1987 November.

A Method for Calculating Electric and Magnetic Fields in TEM Cells at ELF

R. J. SPIEGEL, MEMBER, IEEE, W. T. JOINES, MEMBER, IEEE, C. F. BLACKMAN, AND A. W. WOOD

Abstract—A method is presented whereby the electric and magnetic field distributions within rectangular-strip transmission lines (TEM cells) can be calculated. Quasi-static approximations are employed, thereby restricting the validity of the results to operational frequencies well below the cell cutoff frequency. The method is illustrated by calculating the fields within an existing structure used in biological experimentation. Where possible, calculations are compared with measured data.

Key Words—TEM cells, rectangular-strip lines, Crawford cells, quasi-static solution, electric field, magnetic field.

Index Code—A3d.

I. INTRODUCTION

RECTANGULAR-STRIP transmission lines, commonly termed TEM or Crawford cells, have found increasing use for exposing biological objects to electromagnetic (EM) radiation [1]–[4]. Their most popular configuration consists of a center conductor (septum) surrounded by a rectangular-shaped shield; these structures are commercially available in a wide variety of sizes. Other "open" versions consist of a conductor-over-ground plane, or a conductor sandwiched between two ground planes. In general, it is desirable to operate these cells using exposure frequencies well below the cell cutoff frequency [5], [6], i.e., the frequency at which higher order modes begin to propagate. When operated below cutoff and terminated in its characteristic impedance, a propagating TEM field can be generated within the cell structure. This TEM field approximates a plane wave, and, consequently, reasonably well-defined and uniform fields exist over a central portion of the cell.

Because of the inherent simplicity of the structure relative to design and construction, several research laboratories have built customized cells suitable to their requirements. However, very few researchers have either modeled or measured the electric and magnetic field distributions within their exposure volume. Rather, it has generally been assumed that the electric (E) field strength at the center of the cell, midway between plates, is determined by dividing the voltage applied to the center conductor by the conductor-to-shield separation distance. It is further assumed that the magnetic (H) field component is equal to the E field intensity divided by 377 Ω. Of course, the rationale for the E field calculation is based on the premise of a parallel-plate capacitor configuration. The H field determination relies on plane-wave propagation in free space, where, according to theory, the E and H fields are related by the intrinsic impedance of free space, i.e., 377 Ω.

For many applications, these rather rough calculations will suffice. However, it is certainly desirable to have much more information relative to the E and H field distributions within the cell. This can be achieved by measurement, but the process is lengthy and can be difficult or impossible in small cells. Additionally, especially at low frequencies (< 100 kHz), accurate field measurement is difficult due to probe lead interference.

This research presents a relatively simple method whereby the E and H fields can be calculated inside the cell. Quasi-static methods are employed, which consequently restrict the calculations to frequencies below the cell cutoff frequency. The E field distribution in a TEM cell exposure system is determined by numerical means, under the assumption that essentially no axial variation of the fields occurs down the length of the cell (at least in the volume of the cell utilized for object placement). An integral equation is formulated in terms of the line charge density over the transverse contour of the cell. This integral equation is solved by moment-method procedures for the line-charge density, and the E field distribution is subsequently calculated. The H field distribution is determined from the vector potential where the integral is evaluated analytically from knowledge of the current distribution on the center conductor and outer shield.

II. ELECTRIC AND MAGNETIC FIELD DISTRIBUTIONS

A general formulation of the EM field distribution inside a TEM cell is beyond the scope of this analysis. Rather, for the reason that most TEM cells are operated well below the cell upper frequency limit (cutoff frequency), quasi-static approximations are used to calculate the internal field (E and H) distribution. Basically, the quasi-static approximation is based on the premise that the dimensions of the cell are much smaller than the wavelength of the field produced by the cell current distribution. Further, it is also tacitly assumed that the distance from the source (current distribution) to field points (location where object is placed) is very small (relative to the wavelength). Under these conditions, the scalar and vector potentials can be approximated by [7]

$$\phi(\vec{r}) \approx \frac{1}{\epsilon_0} \int \rho(\vec{r}') G(\vec{r}, \vec{r}') \, dV \tag{1}$$

and

$$\bar{A}(\bar{r}) \approx \mu_0 \int \bar{J}(\bar{r}')G(\bar{r}, \bar{r}') \, dV \tag{2}$$

respectively, where

$\bar{J}$ current distribution,
ρ charge distribution,
G Green's function,
$\bar{r}$ field point,
$\bar{r}'$ source point,
ϵ_0 $= 8.85 \times 10^{-12}$ F/m, and
μ_0 $= 4\pi \times 10^{-7}$ H/m.

With these provisions imposed, the resulting oscillating E and H fields are identical to static fields, except for the time-dependence factor of exp $(j\omega t)$, with ω being the angular frequency. Thus, the E and H fields are given by

$$\bar{E} = -\nabla \phi \tag{3}$$

and

$$\bar{H} = \frac{1}{\mu_0} \nabla \times \bar{A}. \tag{4}$$

With tapered transitions at each end, the rectangular-shaped cell can be adapted to standard coaxial connectors. These tapers, along with a matched terminal impedance, help in providing a good electrical match between source and cell, thereby ensuring minimal voltage standing-wave ratios. Consequently, there is very little axial variation of the field along the cell (in the direction of EM propagation), and the E and H distributions essentially vary only over the transverse plane of the cell. A two-dimensional analysis is thereby warranted, with the Green's function expressed as [7]

$$G(\bar{r}, \bar{r}') = (1/2\pi) \ln (1/\sqrt{(x-x')^2 + (y-y')^2}) \tag{5}$$

where the coordinate (x, y) denotes the field point and (x', y') locates the source point in the transverse plane.

A. Electric Field Distribution

First consider the determination of the E field distribution. A general solution for the potential produced by a surface-charge distribution ρ is then a superposition of ϕ due to all elements of charge $\rho dx' dy'$, or

$$\phi(x, y) = \frac{1}{2\pi\epsilon_0} \iint \rho(x', y') \ln$$

$$\cdot (1/\sqrt{(x-x')^2 + (y-y')^2}) \, dx' \, dy' \tag{6}$$

where the integration is over the cross section of the TEM cell, including the septum. The boundary conditions are

$$\phi(x, y) = 0 \text{ over the cell walls}$$

$$\phi(x, y) = V \text{ over the septum.}$$

Because the charge density is 0 everywhere except over the cell walls and septum, as defined by contours C_1 and C_2 in
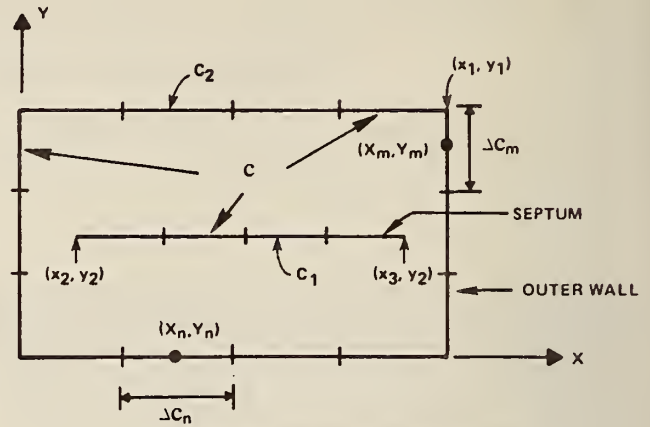
Fig. 1.   TEM cell segmentation used in the computer program.

Fig. 1, the surface integral of (6) becomes a line integral. Substituting the boundary conditions into (6) results in the following integral equation:

$$V = \frac{1}{2\pi\epsilon_0} \int_C \rho(x', y') \ln (1/\sqrt{(x-x')^2 + (y-y')^2}) \, dc' \tag{7}$$

where $V = 0$ when the integration is performed over contour C_2, $C = C_1 + C_2$, and it is now understood that ρ is a line-charge density.

Equation (7) can be solved for ρ by using well-known moment-method procedures [8]. The numerical procedure consists of dividing the contour C into N small segments ΔC_n, as illustrated in Fig. 1; ρ is assumed to be constant over each segment. This allows the integral (7) to be approximated by a set of linear, algebraic equations from which the ρ's associated with each segment can be determined by inverting the matrix equation. Details of the moment-method solution can be found in Appendix A.

In order to determine the accuracy of this formulation, calculations were performed for a TEM cell designed according to National Bureau of Standards (NBS) specifications [9]. The insert in Fig. 2 contains the cross-sectional dimensions of the cell; longitudinal dimensions are immaterial for this study since it is assumed that no axial variation of the fields occurs down the length of the cell. Calculations for the E field distribution were made by dividing the contour of the cell, including the septum, into 145 segments, each 1 cm in length. Fig. 2 is a graph of the calculated results for the magnitude of the total E field normalized with respect to the electric field at the central position ($x = 15$ cm, $y = 7.5$ cm and $x = 15$ cm, $y = 22.5$ cm in the lower and upper half of the cell, respectively). Measured values [9] are also included in the graph. As shown, the calculated values agree quite well with the measured values.

To further illustrate the technique, Fig. 3 contains plots of the magnitude of both the vertical (E_y) and horizontal (E_x) components of the E field strength for a TEM cell used in calcium-ion efflux experiments [1]–[4]. This cell is fairly small (refer to Fig. 3 for dimensions) and was custom-made

Fig. 2. Comparison of calculated results with measured values in an NBS TEM cell.

[1]. The E field is plotted horizontally across the cell for constant vertical positions. The y positions ($y = 1.53$, 2.0, and 2.47 cm or $y = 6.47$, 6.0, and 5.53 cm) represent scans through the volume occupied by the biological samples. No E fie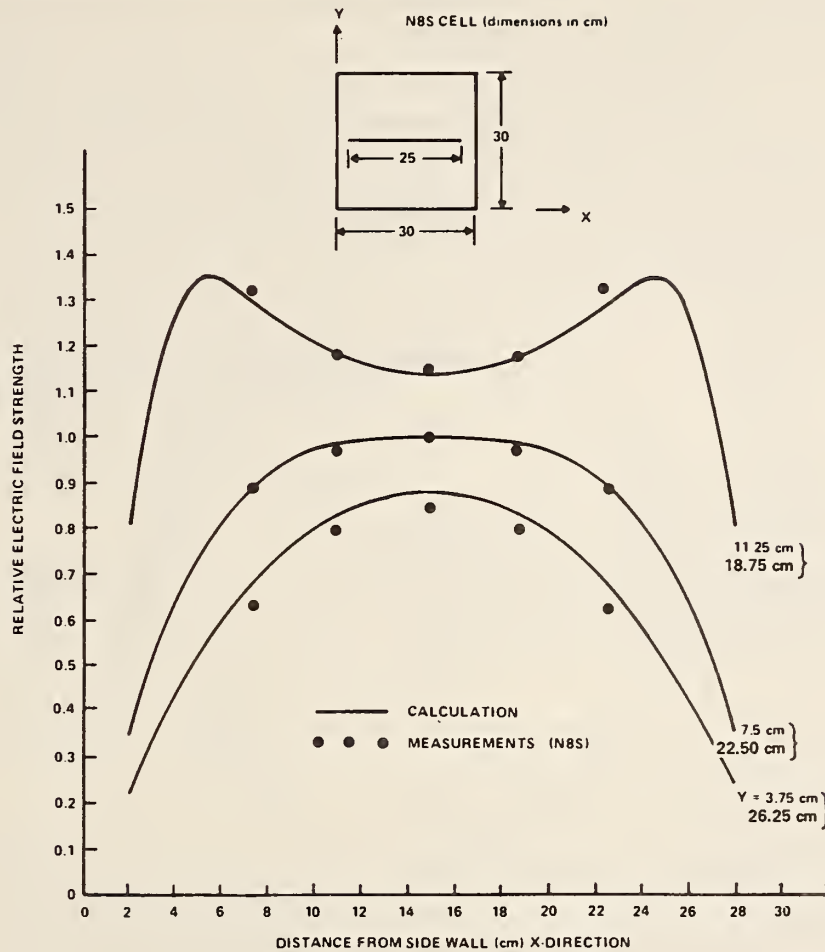ld measurements were made in this cell because its small size precluded the use of available probes. However, based on the excellent agreement obtained with the NBS cell, little useful information would have been obtained by this exercise. Note that the field strength is essentially in the vertical direction near the center of the cell, and the horizontal component gradually becomes dominant toward the side walls. Also, the field distribution is relatively flat near the center of the cell. The field strength was calculated for a voltage of 4.16-V peak applied to the cell septum.

B. Magnetic Field Distribution

The H field is easier to determine than the E field. This is a result of the fact that the current distribution can be determined from knowledge of the charge distribution. However, as will be demonstrated below, this approach leads to inconsistencies when the frequency approaches the static case. Therefore, at lower frequencies another method is presented.

With the cell terminated in its characteristic impedance, a traveling wave with a propagation constant β exists in the cell. The equation of conservation of charge for a surface current J is given by

$$\nabla \cdot \vec{J} = -j\omega\rho \qquad (8)$$

where ρ is the surface-charge density previously discussed. Neglecting transverse current flow, one can show that the flow of surface current down the cell is related to the surface charge via

$$J_z = (\omega/\beta)\rho. \qquad (9)$$

The substitution of (9) into (2) shows that the vector potential is identical to the scalar potential, except that the magnitude is different by the factor $(\epsilon_0\mu_0\omega)/\beta$. This difference means that from (3) and (4), the H field is related to the E field according to

$$\vec{H} = (\vec{E} \times \hat{a}_z)(\epsilon_0\omega/\beta) \qquad (10)$$

where $\hat{a}_z$ is a unit vector in the axial (z) direction. Thus, the E field distributions of Figs. 2 and 3 also represent the H field distributions when the proper scaling factor and vector component conversions are applied through (10).

It should be pointed out that there is a small transverse current flow in the cell as a result of the nonuniform charge distribution (e.g., the edge of the septum produces a very large charge buildup). From Maxwell's equations, this current flow

119
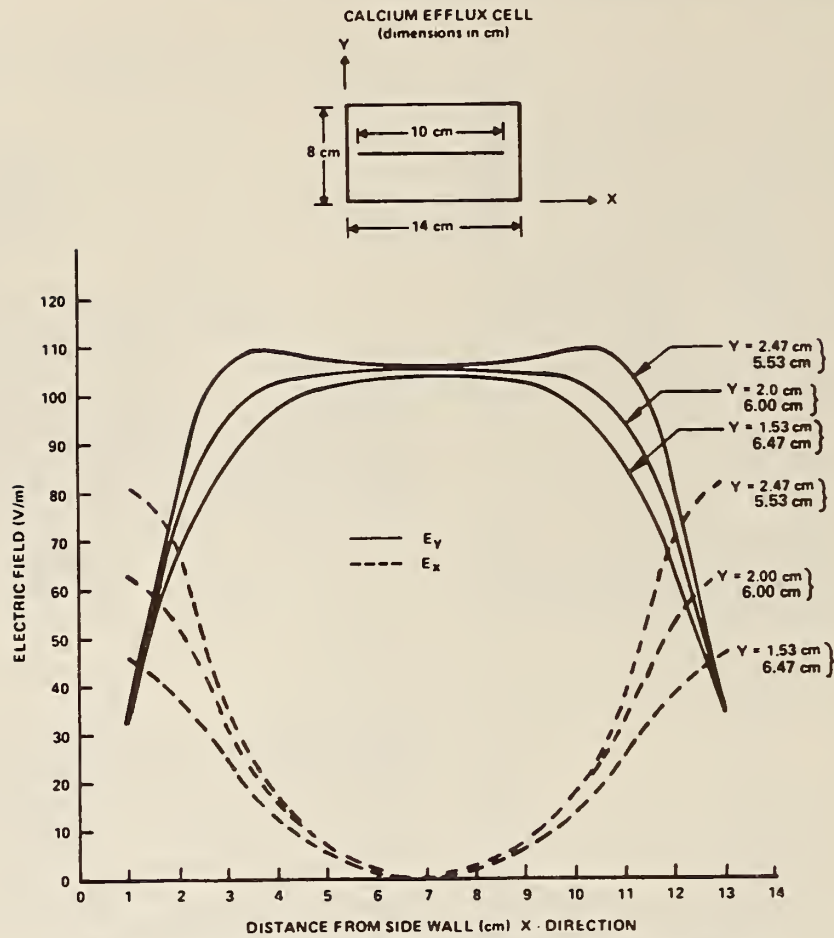
Fig. 3. Electric field distribution for both the horizontal (E_x) and vertical (E_y) components.

would produce axial fields. However, in the central portion of the cell, measurements [10], [11] have shown these components to be minimal, and they can therefore be neglected for this discussion.

To determine the scaling factor requires knowledge of β. From transmission-line theory, a well-known expression for the complex propagation constant is

$$\gamma = j\omega(LC)^{1/2}[1 - (RG)/(LC\omega^2) - j(G/(C\omega) + R/(L\omega))]^{1/2}$$

$$(11)$$

where

$L = (\mu_0 h)/W$ = inductance/unit length,
$C = (\epsilon_0 W)/h$ = capacitance/unit length,
$G = (\sigma_0 W)/h$ = shunt conductance/unit length,
$R = 2/(\sigma_c Wt)$ = resistance/unit length,
h height between the septum and shield,
t thickness of septum,
W equivalent width of septum (including correction for fringing field),
σ_0 conductivity of free space $\approx 1 \times 10^{-14}$ S/m, and
σ_c conductivity of metal (aluminum) = 3.72×10^7 S/m.

For higher frequencies (below cutoff) and low-loss cells (small R and G), the smallness of the imaginary term allows

the propagation constant to be given by

$$\beta \approx \omega(LC)^{1/2} = \omega(\mu_0\epsilon_0)^{1/2}. \qquad (12)$$

Since $G/(\omega C) = \sigma_0/(\omega\epsilon_0) \approx 1.8 \times 10^{-5}/f$, at lower frequencies (but above $f = 0$) $G/(\omega C) \ll 1$ and (11) may be expressed as

$$\gamma = j\omega(LC)^{1/2}[1 - (jR)/(L\omega)]^{1/2}. \qquad (13)$$

Upon separation of the real and imaginary parts of (13), it is possible to show

$$\beta = \omega(LC)^{1/2}[0.5(1 + \sqrt{1 + R^2/(L\omega)^2})]^{1/2}. \qquad (14)$$

Notice that (14) becomes proportional to $\omega^{1/2}$ as the frequency approaches the static case ($\omega = 0$), and consequently equals zero when ω equals zero. This is also consistent with the exact value $\gamma = (RG)^{1/2} = $ real number in (11) at $\omega = 0$, or $\beta = 0$.

The foregoing analysis, however, cannot be utilized to determine the H field for arbitrarily small frequencies because (10) approaches zero as ω goes to zero. This, of course, makes no sense because a cell terminated in its characteristic impedance, say 50 Ω, has a current flow given by

$$I = V/50. \qquad (15)$$

Thus, another technique must be used for frequencies below a

yet undetermined frequency and the static case. The approach taken here is described below.

It is possible to determine [7] the surface current distribution on a thin metallic plate for a current injected at one point contact and removed at another. With the electrodes separated a given distance, the current pattern takes the approximate shape of the septum of a TEM cell. Because the plate can be cut along a line of current, the current distribution on the TEM cell septum likewise takes the same form. For electrode separation distances that correspond to the length of a TEM cell, it is easy to show that the current distribution in the central portion of the septum is essentially uniform. Likewise, the nature of the boundary conditions and the geometry of the outer shield of the cell suggest that its current distribution is also uniform.

Therefore, the current distribution on C_2 (shield) can be represented as

$$\vec{J} = \hat{a}_z \frac{I}{L_2} \delta(l - l') \qquad (16)$$

and on C_1 (septum) by

$$\vec{J} = -\hat{a}_z \frac{I}{L_1} \delta(l - l') \qquad (17)$$

where

L_1 total length of C_1,
L_2 total length of C_2, and
$\delta(l - l')$ Dirac delta function evaluated on either C_1 or C_2.

Writing (2) in component form yields

$$H_x = \frac{\partial}{\partial y} \int_C J_z(\vec{r}') G(\vec{r}, \vec{r}') \, dc' \qquad (18)$$

$$H_y = -\frac{\partial}{\partial x} \int_C J_z(\vec{r}') G(\vec{r}, \vec{r}') \, dc' \qquad (19)$$

where J_z is given by either (16) or (17), depending on whether the integral is evaluated over C_1 or C_2. The Green's function is again expressed according to (5). Appendix B presents more detail on the evaluation of the integrals associated with (18) and (19).

Fig. 4 contains the results for the previously described TEM cell, where the current flow in the cell is determined from (15) with $V = 4.16$. As before, the magnitude of the field is plotted for horizontal scans across the cell for constant vertical positions. The field pattern is as expected: the H_x component is relatively constant in the center of the cell and falls off rapidly near the edge of the septum, while H_y is zero in the center of the cell and becomes larger near the side walls.

III. DISCUSSION AND CONCLUSIONS

A technique for numerically computing the E and H field distributions inside TEM cells has been described. The method is based on quasi-static approximations, and is consequently valid for cells that are operated well below their cutoff

frequency value. The E field determination relies on moment-method procedures, whereas analytical techniques can be used for the H field calculation. Both methods are implementable on small personal computers.

It does not appear that a technique for calculating H field distributions within TEM cells has previously appeared in the literature. Therefore, the data presented herein are novel. Because of a similar paucity of measured data, the numerical results could not be compared with accepted measurements.

A further interesting result of this study is the observation that the standard method for determination of the magnetic field via

$$E/H = Z_0 \qquad (20)$$

where

$$Z_0 = \text{wave impedance} = (\mu_0/\epsilon_0)^{1/2} = 377 \ \Omega$$

is valid only for higher frequencies in the cell. This fact is demonstrated by the data contained in Table I for the TEM cell previously utilized for the determination of the E and H field distributions. The column headed by the words "Transmission-Line Theory" represents the wave impedance according to

$$E/H = Z_0/[0.5(1 + \sqrt{1 + R^2/(L\omega)^2})]^{1/2} \qquad (21)$$

which is easily determined from a consideration of (14) and the wave equation for transmission lines. Note that E/H does not equal Z_0 until the frequency becomes approximately 1 kHz. The other column contains the value for E/H in the center of the cell as determined via quasi-static theory. It only contains one value because the theory is based on static current and charge distributions under the assumption that the results are valid for nonzero frequencies when the corresponding wavelengths are large compared to the cell dimensions. Note also that the quasi-static results are equal to the transmission-line data around 100 Hz. This indicates that, for frequencies above this point, the wave impedance predicted by (21) is most likely the most valid result. Finally, recent experimental results [11] tend to support these results. For the cells tested, E/H was on the order of 300 Ω for frequencies less than 200 Hz. Above 200 Hz, E/H tended to rise, and 377 Ω was achieved for frequencies in excess of 1 or 2 kHz.

APPENDIX A

EVALUATION OF MATRIX ELEMENTS

The solution to (7) in the text was accomplished by using well-known moment-method procedures [8] in which pulse functions were used for basis functions and delta functions were used for testing. The basic procedure consists of partitioning the contour of Fig. 1 into N small segments and assuming that ρ is constant over each segment. The nth segment will be denoted by ΔC_n and the position of the midpoint of each segment, by (x_n, y_n). By requiring that (7) be satisfied at each (x_n, y_n), it is possible to show that the integral equation can be approximated by a set of linear, algebraic equations that can be cast in matrix form as

$$[V_m] = [G_{mn}][\rho_n] \qquad (A1)$$

TEM CELL (NOT TO SCALE)
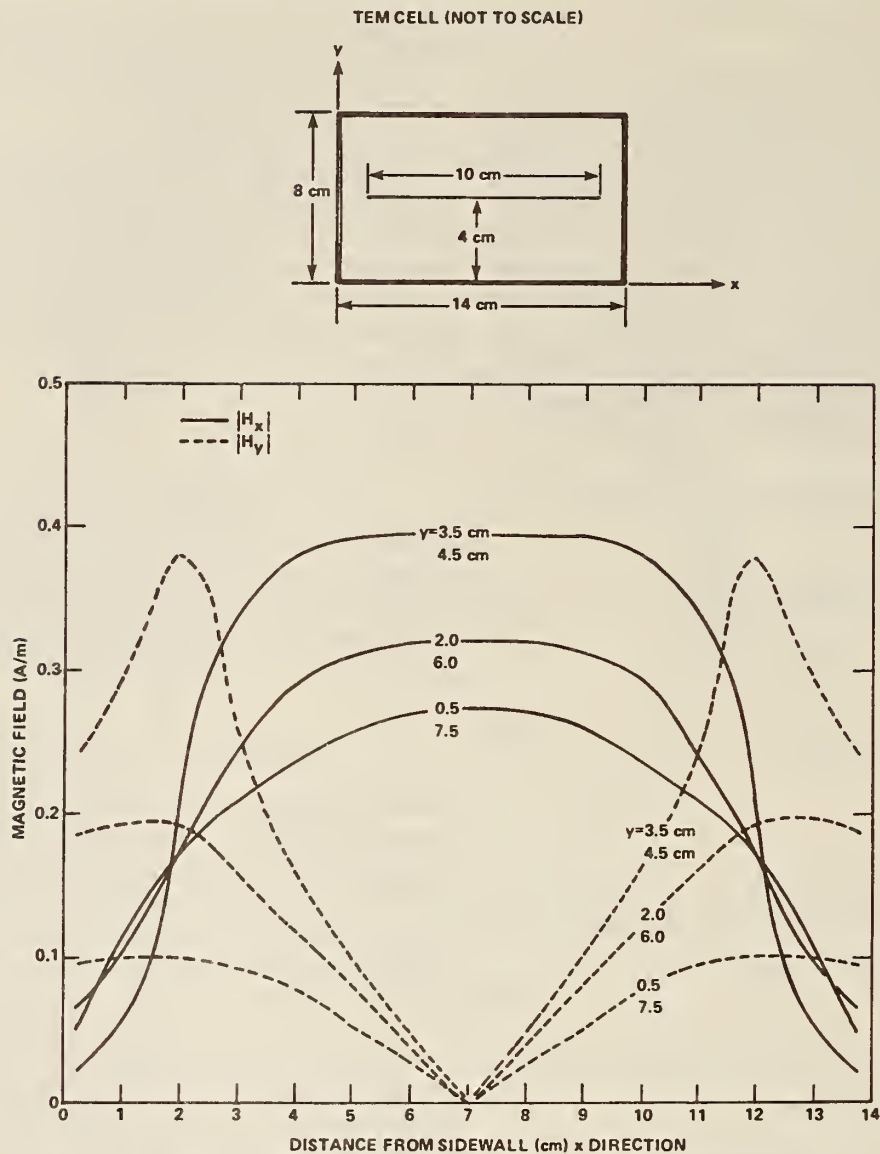
Fig. 4.   Magnetic field distribution for both the horizontal (H_x) and vertical (H_y) components.

TABLE I
CALCULATED WAVE IMPEDANCES FOR A TEM CELL

FREQUENCY [Hz]	WAVE IMPEDANCE [Ω]	
	Transmission-Line Theory	Quasi-static Theory
0	0	325
1	50	
10	160	
100	340	
1000	377	

where

$$G_{mn} = \frac{1}{2\pi\epsilon_0} \int_{\Delta C_n} \ln\left(\frac{1}{\sqrt{(x_m - x')^2 + (y_m - y')^2}}\right) dc'. \quad \text{(A2)}$$

The unknowns $[\rho_n]$ can be determined by inverting the matrix equation. Usually, however, it is numerically more efficient not to calculate the inverse of the $[G_{mn}]$ matrix, but to solve the system of equations by employing a Gauss–Jordon elimination method in which the matrix is triangularized and the unknowns are determined by systematic elimination.

When $m = n$, this approach implies that the field point (x_m, y_m) lies on the integration contour. Consequently, the integral of (A2) is singular because there are a finite number of points where $x_m = x'$ and $y_m = y'$ simultaneously. In a physical sense, the diagonal elements G_{nn} represent the potential at the center of each ΔC_n due to a unit charge over its length. Centering the coordinate system on the segment ΔC_n allows (A2) to be written as

$$G_{nn} = \frac{1}{2\pi\epsilon_0} \lim_{\eta \to 0} \left[\int_{-\Delta C_n/2}^{-\eta} \ln\left(\frac{1}{c}\right) dc \right.$$

$$\left. + \int_{\eta}^{\Delta C_n/2} \ln\left(\frac{1}{c}\right) dc \right] \quad \text{(A3)}$$

where the singularity at $c = 0$ has been excluded from the integration by surrounding it with an infinitesimally small interval, and after the integration is performed, by collapsing the interval to 0. Performing the indicated integration yields

$$G_{nn} = \frac{\Delta C_n}{2\pi\epsilon_0} \left(1 - \ln \frac{\Delta C_n}{2} \right). \quad (A4)$$

Off-diagonal elements are treated by assuming the charge on ΔC_n is a point charge and by using

$$G_{mn} = \frac{\Delta C_n}{2\pi\epsilon_0} \ln \left(\frac{1}{\sqrt{(x_m - x_n)^2 + (y_m - y_n)^2}} \right). \quad (A5)$$

If more accuracy is desired, then (A2) can be numerically or analytically integrated.

Once the potential has been determined, the electric field distribution can be calculated by expressing the electric field as the gradient of the potential and then integrating the result. The resultant expressions for E_x and E_y are

$$E_x = \frac{1}{2\pi\epsilon_0} \sum_{n=1}^{N} \rho_n \Delta C_n \frac{(x - x_n)}{(x - x_n)^2 + (y - y_n)^2} \quad (A6)$$

and

$$E_y = \frac{1}{2\pi\epsilon_0} \sum_{n=1}^{N} \rho_n \Delta C_n \frac{(y - y_n)}{(x - x_n)^2 + (y - y_n)^2}. \quad (A7)$$

Note that, in (A6) and (A7), the numerical integration associated with the integrals was achieved by merely adding the contributions from each of the elements of charge $\rho_n \Delta C_n$.

APPENDIX B

EVALUATION OF MAGNETIC FIELD INTEGRALS

The evaluation of the integrals associated with (18) and (19) in the text is straightforward, albeit tedious. First, consider (18) evaluated over a horizontal surface; the integral becomes

$$H_x = \frac{I}{L} \int_0^a \int_0^b \delta(y' - b) \frac{\partial}{\partial y} G(\vec{r}, \vec{r}') \, dy' \, dx' \quad (B1)$$

where $y' = b$ defines the horizontal surface and L is the length of the surface. Performing the indicated differential operation on the Green's function yields

$$\frac{\partial G}{\partial y} = -(y - y')/[(x - x')^2 + (y - y')^2]2\pi. \quad (B2)$$

The substitution of (B2) into (B1) and subsequent integration produces

$$H_x = -I(y - b)/(2\pi L) \int_0^a dx'/[(x - x')^2 + (y - b)^2]. \quad (B3)$$

It is easy to show that (B3) gives

$$H_x = I/2\pi L \, [\tan^{-1} (x - a)/(y - b) - \tan^{-1} x/(y - b)]. \quad (B4)$$

Now (18) is evaluated over a vertical surface, i.e.,

$$H_x = \frac{I}{L} \int_0^b \int_0^a \delta(x' - a) \frac{\partial}{\partial y} G(\vec{r}, \vec{r}') \, dx' \, dy' \quad (B5)$$

where $x' = a$ defines the vertical surface. Performing the indicated integration over the x' coordinate yields

$$H_x = \frac{I}{2\pi L} \int_0^b \frac{\partial}{\partial y} \ln [1/\sqrt{(x - a)^2 + (y - y')^2}] \, dy'. \quad (B6)$$

From the functional form of the Green's function, it is possible to show that $\partial y = -\partial y'$. This knowledge allows (B6) to be integrated easily, with the result given by

$$H_x = \frac{I}{2\pi L} \ln [\sqrt{(x - a)^2 + (y - b)^2}/\sqrt{(x - a)^2 + y^2}]. \quad (B7)$$

The H_y component can be determined in exactly the same fashion as H_x. However, the derivative is performed on the Green's function in the x direction (see (19)). Consequently, the result for the H_y component from a vertical surface is given by (B4), while the horizontal surface contribution is obtained via (B7). In other words, the contributions from both types of surfaces are reversed from the previous case.

From this information, it is possible to determine the resultant H_x and H_y components inside the TEM cell by superposition. The result is

$$H_x = \frac{I}{2\pi L_2} [\tan^{-1} (x - x_1)/(y - y_1) - \tan^{-1} x/(y - y_1)$$

$$+ \tan^{-1} (x - x_1)/y - \tan^{-1} (x/y)] + \frac{I}{2\pi L_3}$$

$$\cdot [\ln (\sqrt{(x - x_1)^2 + (y - y_1)^2}/\sqrt{(x - x_1)^2 + y^2})$$

$$+ \ln (\sqrt{x^2 + (y - y_1)^2}/\sqrt{x^2 + y^2})] + \frac{I}{2\pi L_1}$$

$$\cdot [\tan^{-1} (x - x_2)/(y - y_2) - \tan^{-1} (x - x_3)/(y - y_2)]$$

$$(B8)$$

$$H_y = \frac{-I}{2\pi L_2} [\ln (\sqrt{(x - x_1)^2 + (y - y_1)^2}/\sqrt{x^2 + (y - y_1)^2})$$

$$+ \ln (\sqrt{(x - x_1)^2 + y^2}/\sqrt{x^2 + y^2})] - \frac{I}{2\pi L_3}$$

$$\cdot [\tan^{-1} (y - y_1)/x - \tan^{-1} (y/x)$$

$$+ \tan^{-1} (y - y_1)/(x - x_1) - \tan^{-1} y/(x - x_1)] + \frac{I}{2\pi L_1}$$

$$\cdot \ln (\sqrt{(x - x_3)^2 + (y - y_2)^2}/\sqrt{(x - x_2)^2 + (y - y_2)^2}).$$

$$(B9)$$

The parameters x_1, x_2, x_3, y_1, and y_2 are defined in Fig. 1,

while L_2 and L_3 define the lengths of the horizontal and vertical sections of the shield, respectively. As before, L_1 is the transverse length of the septum.

REFERENCES

[1] C. F. Blackman *et al.*, "Induction of calcium-ion efflux from brain tissue by radio-frequency radiation: Effects of modulation frequency and field strength," *Radio Sci.*, vol. 14, no. 6S, pp. 93–98, 1979.

[2] C. F. Blackman *et al.*, "Induction of calcium-ion efflux from brain tissue by radio-frequency radiation: Effects of sample number and modulation frequency on the power-density window," *Bioelectromagnetics*, vol. 1, pp. 35–43, 1980.

[3] C. F. Blackman, S. G. Benane, W. T. Joines, M. A. Hollis, and D. E. House, "Calcium-ion efflux from brain tissue: Power-density vs internal field-intensity dependencies at 50-MHz RF radiation," *Bioelectromagnetics*, vol. 1, pp. 277–283, 1980.

[4] C. F. Blackman, W. T. Joines, and J. A. Elder, "Calcium-ion efflux in brain tissue by radiofrequency radiation," in *Biological Effects of Nonionizing Radiation*, K. H. Illinger, Ed. Washington, DC: Amer. Chem. Soc., 1981, pp. 299–314.

[5] D. A. Hill, "Bandwidth limitations of TEM cells due to resonances," *J. Microwave Power*, vol. 18, pp. 182–195, 1983.

[6] C. M. Weil, W. T. Joines, and J. B. Kinn, "Frequency range of large-scale TEM mode rectangular strip lines," *Microwave J.*, vol. 24, pp. 93–100, 1981.

[7] J. Van Bladel, *Electromagnetic Fields.* New York: McGraw-Hill, 1964, pp. 126 and 274.

[8] R. F. Harrington, *Field Computation by Moment Methods.* New York: Macmillan, 1968.

[9] M. L. Crawford, "Generation of standard EM fields using TEM transmission cells," *IEEE Trans. Electromagn. Compat.*, vol. EMC-16, pp. 189–195, 1974.

[10] D. A. Hill, "Human whole-body radiofrequency absorption studies using a TEM-cell exposure system," *IEEE Trans. Microwave Theory Tech.*, vol. MTT-30, pp. 1847–1854, 1982.

[11] A. W. Wood, W. T. Joines, and C. F. Blackman, "The characteristics of transverse electric and magnetic field (TEM) cells at extremely low frequencies," *Bioelectromagnetics*, to be published.

Appendix G

Gruner, L. "Higher order modes in rectangular coaxial waveguides."

Higher Order Modes in Rectangular Coaxial Waveguides

A precise determination of the characteristic impedance of rectangular coaxial waveguides has been recently undertaken by Cruzan and Garver [1] and it is well known that these structures have many applications in the design of shielded striplines, varactor mounts, etc. While their operation is, in general, confined to the TEM mode, there are instances when higher-order modes must be taken into account; the effect of the latter on striplines has been studied by Oliner [2], but there appears to be no record of a similar investigation applicable to rectangular coaxial waveguides.

In what follows, a symmetrical structure will be considered, i.e., the centers of the inner and outer conductors will be assumed to coincide. Furthermore, reference will be made to TE_{mn} and TM_{mn} modes to conform with standard notation for single-ridge waveguides [3] as well as rectangular waveguides.

Inspection of Fig. 1 shows that when the subscripts m or n or both are even, the planes of symmetry MN or KL or both are electric walls and the field pattern may be deduced from that of the corresponding single-ridge waveguide. On the other hand, the $TE_{2n+1,2m+1}$ and $TM_{2n+1,2m+1}$ ($n = 0, 1, 2, \cdots,$

$m = 0, 1, 2, \cdots$) mode patterns cannot be studied in this manner. Furthermore, while the TE_{n2} modes in ridge waveguides have been very adequately studied [3], [6], published information concerning other modes is either incomplete or not available.

The solution of the problem may be readily accomplished (without recourse to finite difference methods) using a procedure due to Butcher [4] as well as Collins and Daly [5].

Thus, in order to determine the cutoff frequencies of $TM_{2n+1,2m+1}$ modes, it is necessary to solve the wave equation for the cross section TLBNPF (Fig. 1) subject to the boundary conditions which require the longitudinal component of the electric field intensity E_z to vanish along PFT and LBN while the normal derivative $\partial E_z/\partial n$ is equal to zero along PN and TL. Furthermore, it is advantageous [5] to divide the cross section into two rectangular areas and to match the fields along the boundary FF'. Using subscripts 1 and 2 to refer to the cross sections TLBF' and PFF'N, respectively, we find that

$$E_{z1} = \sum_r \phi_{1r} \sinh p_{1r} \left(\frac{x}{a} - \frac{1}{2} \right)$$
$$\cdot \sin \frac{r\pi y}{b} \qquad 0 < y < \frac{b}{2}$$
$$r = 1, 3, 5, \cdots, \text{odd} \quad (1)$$

$$E_{z2} = \sum_m \phi_{2m} \cosh p_{2m} \frac{x}{a} \sin \frac{m\pi y}{d}$$
$$0 < y < d \qquad d \neq 0$$
$$m = 1, 2, 3, \cdots \quad (2)$$

where

$$p_{2m}^2 = -k^2 a^2 + \left(\frac{m\pi a}{d} \right)^2$$

$$p_{1r}^2 = -k^2 a^2 + \left(\frac{r\pi a}{b} \right)^2 \quad k = \frac{2\pi}{\lambda_c} \quad (3)$$

and λ_c represents the cutoff wavelength. Continuity of E_z along the boundary implies that $E_{z1} = E_{z2}$ when $x = s/2$, $s \neq a$; when the equation is multiplied by $\sin n\pi y/b$ and both sides integrated from 0 to $b/2$ we find that, noting the orthogonality properties of trigonometric functions,

$$\phi_{1n} \sinh p_{1n} \left(\frac{s}{2a} - \frac{1}{2} \right)$$
$$= \frac{4d}{b} \sum_m \phi_{2m} K_{m,n} \cosh p_{2m} \frac{s}{2a} \quad (4)$$

where

$$K_{m,n} = \frac{1}{d} \int_0^d \sin \frac{m\pi y}{d} \sin \frac{n\pi y}{b} dy. \quad (5)$$

Similarly, continuity of H_y along the boundary FF' requires that $\partial E_{z1}/\partial x$ be equated to $\partial E_{z2}/\partial x$ at $x = s/2$; when the resulting equation is multiplied by $\sin m\pi y/d$ and both sides integrated from 0 to d, we find that

$$\sum_r \phi_{1r} p_{1r} K_{mr} \cosh p_{1r} \left(\frac{s}{2a} - \frac{1}{2} \right)$$
$$= \frac{1}{2} \phi_{2m} p_{2m} \sinh p_{2m} \frac{s}{2a}. \quad (6)$$
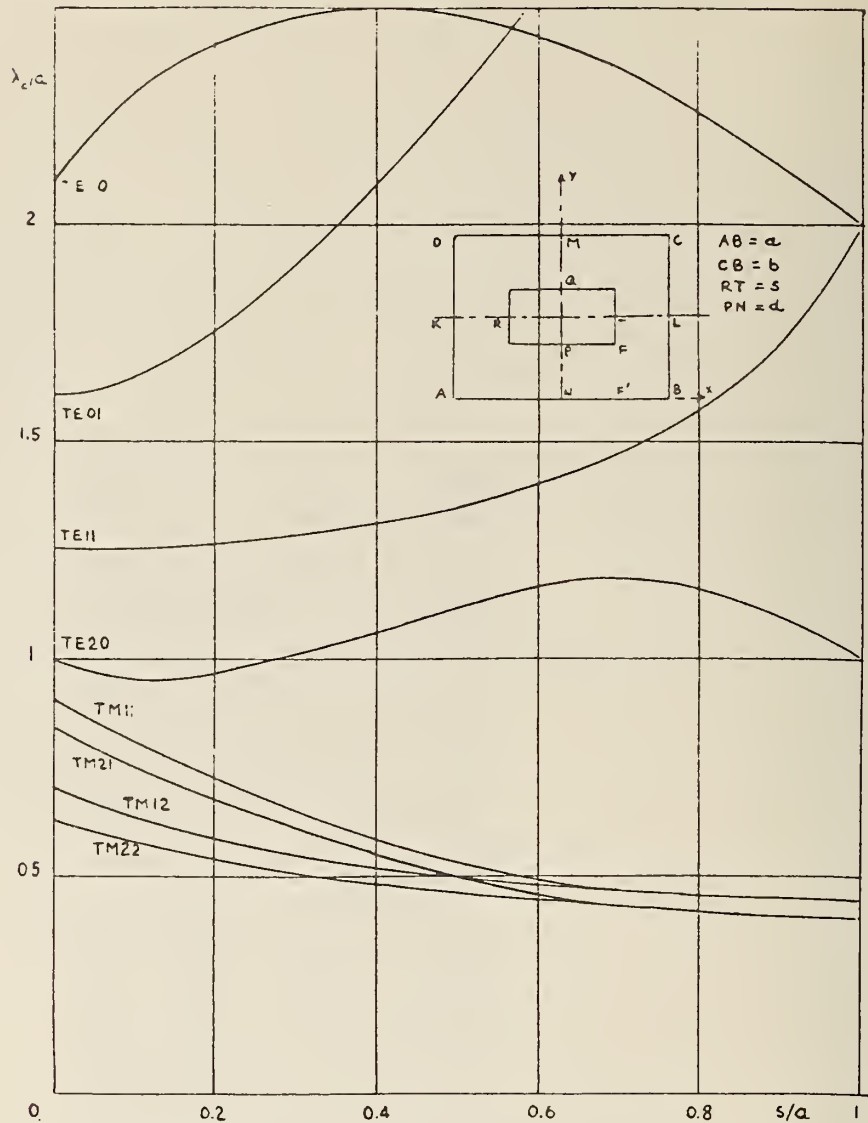
Fig. 1. Typical mode characteristics of rectangular coaxial waveguides ($b/a = 0.8$, $2d/b = 0.6$).

Eliminating ϕ_{2m} from (4) and (6) we have

$$\sum_{\substack{n=1,3 \\ \text{odd}}}^{\infty} \sum_{\substack{r=1,3 \\ \text{odd}}}^{\infty} \phi_{1r} a_{nr(ce)}$$
$$\cdot \cosh p_{1r} \left(\frac{1}{2} - \frac{s}{2a} \right) = 0 \quad (7)$$

where

$$a_{nr(ce)} = \frac{S d p_{1r}}{b}$$
$$\cdot \sum_{m=1}^{\infty} \frac{K_{mr} K_{mn} \coth p_{2m} \frac{s}{2a}}{p_{2m}}$$
$$+ \delta_{nr} \tanh p_{1r} \left(\frac{1}{2} - \frac{s}{2a} \right) \quad (8)$$

and $\delta_{nr} = 1$ if $n = r$ whereas $\delta_{nr} = 0$ otherwise. Equation (7) has a solution only if the determinant vanishes and the cutoff frequencies may be deduced by setting

$$\det[a_{nr(ce)}] = 0. \quad (9)$$

Let us designate $a_{nr(ee)}$ an expression obtained from (8) by letting the summation extend over all even n and r (commencing with $r = n = 2$);

similarly, let $a_{nr(ct)}$ refer to (8) subject to coth $p_{2m}(s/2a)$ being replaced by tanh $p_{2m}(s/2a)$, etc.

Then we find that the cutoff frequencies of various modes can be deduced by solving the following equations

$$TM_{2n+1,2m}: \det[a_{nr(ce)}] = 0 \quad (10)$$

$$TM_{2n,2m+1}: \det[a_{nr(ct)}] = 0 \quad (11)$$

$$TM_{2n,2m}: \det[a_{nr(et)}] = 0. \quad (12)$$

The cutoff frequencies of TE modes may be obtained in an analogous manner if the magnetic field intensity H_z in regions 1 and 2 is represented as suitable Fourier series and then the continuity of H_z and E_y is satisfied along the boundary FF'. Introducing a notation

$$b_{nr(ce)} = S \frac{d}{b p_{1r} \Delta_r}$$
$$\cdot \sum_{m=2}^{\infty} \frac{p_{2m} C_{rm} C_{mn} \coth p_{2m} \frac{s}{2a}}{\Delta_m}$$
$$+ \delta_{nr} \tanh p_{1r} \left(\frac{1}{2} - \frac{s}{2a} \right) \quad (13)$$

128

where

$$C_{mr} = \frac{1}{d} \int_0^d \cos\frac{r\pi y}{b} \cos\frac{m\pi y}{d} \, dy \quad (14)$$

$\Delta_m = 2$ if $m = 0$, $\Delta_r = 2$ if $r = 0$, and $\Delta_m = \Delta_r = 1$ otherwise and finally letting the subscripts o, e, c, and t have the same significance as applied to both a_{nr} and b_{nr} (but for the fact that even summation includes $r = n = 0$), we find that the cutoff frequencies of various modes may be deduced by solving the following equations

$$TE_{2n+1,2m+1}: \det[b_{nr(cc)}] = 0 \quad (15)$$
$$TE_{2n+1,2m}: \det[b_{nr(cs)}] = 0 \quad (16)$$
$$TE_{2n,2m+1}: \det[b_{nr(st)}] = 0 \quad (17)$$
$$TE_{2n,2m}: \det[b_{nr(st)}] = 0. \quad (18)$$

Evidently (10) to (12) and (16) to (18) may be used to study modes in single-ridge waveguides; (16) and (18) are, with some changes in notation, due to Collins and Daly [5].

It can be shown that the cutoff frequencies of all modes reduce to those of the rectangular waveguide as the dimensions of the inner conductor tend to zero. Thus, for example, for $TM_{2n+1,2m}$ modes we note that when $2d/b = 1$, then for all s (including $s = 0$) we have $p_{1r} = p_{2m}$, $K_{mr} = K_{mn} = \frac{1}{2}$ subject to $n = r = m$. Hence (10) reduces to

$$\left[\coth p_{1r}\frac{s}{2a} + \tanh p_{1r}\left(\frac{1}{2} - \frac{s}{2a}\right)\right]$$
$$\times \text{const.} = 0 \quad (19)$$

which has a solution

$$\coth\frac{p_{1r}}{2} = 0 \quad (20)$$

and hence

$$\lambda_c = 2 / \sqrt{\left(\frac{2n+1}{a}\right)^2 + \left(\frac{2m}{b}\right)^2}$$
$$n = 0, 1, 2, \cdots, \quad m = 1, 2, \cdots. \quad (21)$$

Equations (20) and (21) hold for $TE_{2n+1,2m}$ modes as well subject to $m = 0, 1, 2, \cdots$.

Similarly, when $TM_{2n,2m+1}$ and $TE_{2n,2m-1}$ modes are considered, we find that the plane $s = 0$ represents an electric wall and hence, for all values of $2d/b$, the determinant vanishes when

$$\tanh\frac{p_{1r}}{2} = 0 \quad (22)$$

and

$$\lambda_c = 2 / \sqrt{\left(\frac{2n}{a}\right)^2 + \left(\frac{2m+1}{b}\right)^2}. \quad (23)$$

With reference to the curves when $s = 0$, for the TE_{01} mode $\lambda_c/a = 1.6$ and for the TM_{21} mode $\lambda_c/a = 0.848$.

Furthermore, $TM_{2n,2m}$ and $TE_{2n,2m}$ modes have two planes of symmetry $s = 0$ and $2d/b = 1$ and hence (22) applies in conjunction with

$$\lambda_c = 2 / \sqrt{\left(\frac{2n}{a}\right)^2 + \left(\frac{2m}{b}\right)^2}. \quad (24)$$

Specifically, when $s = 0$, for the TE_{20} mode $\lambda_c/a = 1$ and for the TM_{22} mode $\lambda_c/a = 0.625$.

Finally, $TE_{2n+1,2m+1}$ and $TM_{2n+1,2m-1}$ modes have no planes of symmetry. When $s = 0$ and $2d/b = 1$ determinants (10) and (15) diverge; however, in practice when $2d/b = 1$, $b/a = 0.8$ and $s = 0.03$, numerical computations reveal

the presence of a root $\lambda_c/a = 1.249$ while for the rectangular waveguide corresponding to $s = 0$, $2d/b = 1$, we find that $\lambda_c/a = 1.249$ as well.

When $d = 0$ and $s = a$, the coaxial structure is transformed into two waveguides and the equations cannot be expected to hold in general.

However, a study of the field pattern suggests that when s approaches a, in the limit the ratio λ_c/a of a coaxial TE_{11} mode tends to that of a TE_{10} mode in a rectangular waveguide, viz., $\lambda_c/a = 2$; similarly, λ_c/a of the coaxial TE_{12} mode tends to that of a TE_{11} mode in a rectangular waveguide of reduced height (when $b/a = 0.8$, $2d/b = 0.6$, replacing b by $0.3b$ we find that $\lambda_c/a = 0.466$) etc. Numerical calculations confirm these conjectures.

The convergence with respect to m in both (8) and (13) is quite rapid and both expressions vary asymptotically as $O(m^{-3})$. Furthermore, the cutoff frequencies are primarily determined by a single diagonal term of $\det[a_{nr}]$ or $\det[b_{nr}]$ and a 3×3 determinant is likely to be adequate for most purposes.

It is of interest to note that the above procedure entails no approximations other than those inherent in the assumption that the walls are lossless. Normalized cutoff wavelength ratios λ_c/a obtained by Pyle [6] for the TE_{10} mode ($b/a = 0.45$) were compared with those obtained by the evaluation of 2×2 and 3×3 determinants of (16) and truncating the summation with respect to m after 8 terms. Typical results are shown below.

d/b	s/a	2×2 Determinant	3×3 Determinant	Reference [6]
0.2	0.2	3.769	3.920	3.985
0.2	0.9	2.892	2.916	2.961
0.8	0.2	2.121	2.140	2.163
0.8	0.9	2.051	2.051	2.057

Some λ_c/a characteristics of a rectangular coaxial waveguide (such that $b/a = 0.8$, $2d/b = 0.6$) are presented in Fig. 1.

An examination of these curves shows that as the frequency is increased and the propagation of higher-order modes becomes possible, the TE_{10} (TE_{01}) mode appears followed by the TE_{11} and TE_{20} modes (the TM_{11} mode precedes the TE_{20} mode for some combinations of $2d/b$ and s/a subject to the same aspect ratio $b/a = 0.8$); it also shows under what conditions two modes have the same cutoff frequency and hence velocity of propagation.

Acknowledgment

L. Gruner
Dept. of Elec. Engrg.
Monash University
Clayton, Victoria
Australia

References

[1] O. R. Cruzan and R. V. Garver, "Characteristic impedance of rectangular coaxial transmission lines," *IEEE Trans. Microwave Theory and Techniques*, vol. MTT-12, pp. 488–495, September 1964.
[2] A. A. Oliner, "Theoretical developments in symmetrical strip transmission line," in *Proc. of the Symp. on Modern Advances in Microwave Techniques*, vol. 4, Brooklyn, N. Y.: Polytechnic Press of the Polytechnic Institute of Brooklyn, 1954.
[3] S. Hopfer, "The design of ridged waveguides," *IRE Trans. Microwave Theory and Techniques*, vol. MTT-3, pp. 20–29, October 1955.
[4] P. N. Butcher, "A theoretical study of propagation along tape ladder lines," *Proc. IEE* (London), pt. B, vol. 104, pp. 169–176, March 1957.
[5] J. H. Collins and P. Daly, "Orthogonal mode theory of single-ridge waveguides," *J. Electronics and Control*, vol. 17, pp. 121–129, August 1964.
[6] J. R. Pyle, "The cutoff wavelength of the TE_{10} mode in ridged rectangular waveguide of any aspect ratio," *IEEE Trans. Microwave Theory and Techniques*, vol. MTT-14, pp. 175–183, April 1966.

Appendix H

Tippet, J. C.; Chang, D. C.; Crawford, M. L. "An analytical and experimental determination of the cutoff frequencies of higher order TE modes in a TEM cell."

Nat. Bur. Stand. (U.S.) NBSIR 76-841;1976 June.

AN ANALYTICAL AND EXPERIMENTAL DETERMINATION OF THE CUTOFF FREQUENCIES OF HIGHER-ORDER TE MODES IN A TEM CELL

John C. Tippet
David C. Chang

University of Colorado

and

Myron L. Crawford

Electromagnetics Division
Institute for Basic Standards
National Bureau of Standards
Boulder, Colorado 80302

CONTENTS

LIST OF FIGURES AND TABLES

FOREWORD

This report describes the theoretical and experimental determination of the cutoff frequency of the first higher-order mode for several TEM cells of differing geometry developed at the National Bureau of Standards (NBS). In addition, the field distribution of the first higher-order mode is found explicitly.

The effort is part of a program sponsored by the Electronics Systems Division, Hanscom Air Force Base, under contract number Y75-917 with NBS. The purpose of this effort is to evaluate the use of TEM cells for determining the radiated emission characteristics of small electronic devices.

The theoretical analyses were developed by staff from the University of Colorado under contract with NBS. The experimental work was performed at NBS. Myron L. Crawford of the Electromagnetics Division was the technical monitor for NBS and Charles E. Wright of the Electronics Systems Division was the technical monitor for the Air Force. The period of performance covered by this report extends from November 1975 to April 1976.

Results of this effort will be used to develop higher-order mode suppression or rejection techniques to increase the useful frequency range of a TEM cell.

AN ANALYTICAL AND EXPERIMENTAL DETERMINATION OF THE CUTOFF FREQUENCIES
OF HIGHER-ORDER TE MODES IN A TEM CELL

John C. Tippet, David C. Chang and Myron L. Crawford

ABSTRACT

In addition to the TEM mode, higher order TE and TM modes can propagate in a TEM cell. Since only the TEM mode is desired, the higher-order modes restrict the useful frequency range of the TEM cell. In this paper, the cutoff frequency of the first higher-order mode is obtained both analytically and experimentally for several TEM cells of differing geometry. The difference between the experimental and theoretical results is shown to be only a few percent. In addition the field distribution of the first higher-order mode is found explicitly.

Key words: Shielded strip line; TEM cell.

1. INTRODUCTION

In our previous report on the TEM cell, an effort was made to investigate the properties of the dominant TEM mode [1]. In this paper, the first few nigher-order TE modes in the TEM-cell will be studied. They are of interest since they determine the upper frequency limit below which only the TEM mode can propagate. Thus, knowledge of these modes may enable us to increase the useful frequency range of a TEM-cell, for example, by placing selectively absorbing material in the cell at locations where the effect is least on the propagation of the TEM mode.

As is obvious from the sketch shown in figure 1, the TEM cell can be viewed as a special case of a shielded strip line for which the strip is embedded in a homogeneous dielectric. Solutions leading to the cutoff frequencies of the higher-order modes in shielded strip line structures usually involve a numerical search for the roots of an infinite determinant obtained from a mode matching at the interface between the partial regions separated by the center septum in the cell. A problem arises, however, since the infinite determinant must be truncated in order to obtain numerical results. As Mittra has shown [2], the partitioning of the set of equations (i.e. the number of modes used in each of the partial regions) must be chosen in the correct ratio in order that the solution of the truncated set of equations converges to the correct value. In fact, an incorrect choice of the partitioning ratio leads to a violation of the edge condition [3].

In order to bypass the difficulties associated with relative convergence, an alternative approach was sought in this report. An integral-equation formulation for the electric field in the gap was found, and an approximate, but analytical solution of the integral equation was obtained using the assumption of a small gap between the center septum and side walls. (All of the TEM cells currently in use at NBS indeed have small enough gaps so that the analysis

applied.) This allows us to represent the cutoff frequency of the first higher order mode as a perturbation to the TE_{10} mode in a rectangular waveguide. The method developed in this paper is applicable to TEM cells for which the center septum is displaced vertically from its center position, and may also apply to TEM cells for which the regions above and below the center septum have different dielectric constants (i.e. a shielded strip line). In addition to the cutoff frequencies, the electric field distribution of the higher-order modes can be found explicitly.

In order to check our solution, we compared our results to those obtained by other authors [4,5,6]. In particular, Mittra and Itoh [4] used a singular-integral equation formulation. Their results reduce exactly to ours when a small gap approximation is used in their equations. However, the results obtained by Bräckelmann, et al. [5] and Bezlyudova [6] were not useful for comparison since their result for a zero-thickness septum reduces to the cutoff frequency of the unperturbed TE_{10} mode in a TEM cell, independent of the width of the center septum. If we regard the upper and lower regions of the TEM cell as two rectangular waveguides coupled through a small aperture, then the use of the so-called coupled mode theory predicts that two system modes (symmetric and anti-symmetric) can exist, both of which have approximately the same propagation constant. The symmetric mode is unaffected by the edge condition at the ends of the septum, while the anti-symmetric mode is more strongly affected by the width of the septum [7]. It is clear that the results of Bräckelmann et al. [5] and Bezlyudova [6] were intended for the symmetric mode. However, because the excitation of the TEM cell is basically of a TEM nature which yields an oppositely-directed electric field in the upper and lower regions of the cell, it is more relevant to obtain results corresponding to the anti-symmetric case.

The resonant frequency of the first higher-order perturbed mode was also obtained experimentally in this paper. Using the well-known relationship between the resonant frequency and the cutoff frequency, excellent agreement was obtained between the theoretically and experimentally measured resonant frequencies.

2. FORMULATION OF THE INTEGRAL EQUATION

A cross-section of a TEM cell with an off-center septum is shown in figure 1. The strip, of width $2w$, is located a distance g from each vertical sidewall and is assumed to have negligible thickness. In addition it is embedded in a homogeneous dielectric of permittivity, ε_o and permeability, μ_o. The outer wall of the cell, of width $2a$ and height $2b = b_1 + b_2$, and the strip are assumed to be perfect conductors. The region above the strip is designated region 1 while that below the strip is designated region 2.

We will attempt in this paper to obtain only the cutoff frequencies of the TE-type modes since the TE_{10} mode is usually the lowest order mode next to the dominant TEM-mode in the cell. For the TE modes it is well known that the fields in region 1 can be found in terms of an auxiliary scalar function, $\psi^{(1)}$, which satisfies the following relations.

$$(\nabla_t^2 + K^2)\psi^{(1)} = 0 \qquad \text{in } S_1, \text{ region 1} \qquad (1)$$

and

$$\partial_n \psi^{(1)} = 0 \qquad \qquad \text{on the metal walls, i.e.,} \qquad (2)$$
$$\text{B-C and A-F-E-D}$$

where

$$K^2 = k_o^2 - \gamma^2; \qquad (3)$$

$$k_o^2 = \omega^2 \mu_o \varepsilon_o = \left(\frac{2\pi}{\lambda}\right)^2 ; \qquad (4)$$

and we have assumed that the fields propagate as $e^{-i\omega t \pm i\gamma z}$. ∇_t^2 is the transverse Laplacian, which, for our geometry is given by $\partial^2/\partial x^2 + \partial^2/\partial y^2$, and ∂_n represents the outward normal derivative. ω is the angular frequency, λ is the wavelength, k_o is the wave number and γ is the propagation constant which is equal to zero at cutoff. In addition to (2), we will also require that $\partial_n \psi^{(1)}$ be nonzero in the gap regions, that is, A-B and C-D. If $\partial_n \psi^{(1)}$ were zero there also, then we could write the solution to (1) immediately as just an unperturbed rectangular waveguide mode unaffected by the presence of the center septum.

In terms of $\psi^{(1)}$, the field components in region 1 can be written as follows

$$\bar{H}_z = K^2 \psi^{(1)} \bar{a}_z \qquad (5)$$

and

$$\bar{E}_t = i\omega\mu_o \nabla_t (\psi^{(1)}) \times \bar{a}_z \qquad (6)$$

where $\bar{a}_z$ is a unit vector in the z-direction and ∇_t represents the transverse gradient $(\bar{a}_x \frac{\partial}{\partial x} + \bar{a}_y \frac{\partial}{\partial y})$.

In order to determine $\psi^{(1)}$, we will write it as a superposition of a complete set of basis functions $\psi_{mn}^{(1)}$ as follows

$$\text{In } S_1 \qquad \psi^{(1)} = \sum_{m,n} A_{mn}^{(1)} \psi_{mn}^{(1)} (x,y). \qquad (7)$$

$A_{mn}^{(1)}$ are the unknown amplitudes, and the basis functions, $\psi_{mn}^{(1)}$, must satisfy the following

$$(\nabla_t^2 + K_{mn}^{(1)^2})\psi_{mn}^{(1)} = 0 \qquad (8)$$

141

and

$$\partial_n \psi_{mn}^{(1)} = 0 \tag{9}$$

on ℓ_1, the boundary of S_1, i.e. A-B-C-D-E-F. It may appear that (7) is logically inconsistent since the basis functions, $\psi_{mn}^{(1)}$ satisfy (9) while their sum, $\Psi^{(1)}$ satisfies $\partial_n \Psi^{(1)} \neq 0$ in the gap regions. As shown by Friedman [8], however, $\Psi^{(1)}$ is discontinuous at $y = 0$ and thus the limit $y = 0$ and the sum in (7) cannot be interchanged. In other words, the requirement of $\partial_n \Psi \neq 0$ at the gap should be understood as applied to the plane $y = 0_+$ where $0_+ = \epsilon$ and $\epsilon \to 0$. The solution of (8) and (9) is obviously

$$\psi_{mn}^{(1)}(x,y) = \left[\frac{2}{ab_1}\right]^{\frac{1}{2}} \cos\left[\frac{m\pi}{2a}(x+a)\right]\cos\left[\frac{n\pi y}{b_1}\right] \tag{10}$$

with $K_{mn}^{(1)}$ given by

$$K_{mn}^{(1)} = \left[\left(\frac{m\pi}{2a}\right)^2 + \left(\frac{n\pi}{b_1}\right)^2\right]^{\frac{1}{2}} \tag{11}$$

and the normalization constant appearing in (10) is included for convenience.

Using the orthogonality properties of the basis functions, the amplitudes, $A_{mn}^{(1)}$, can be written as follows

$$A_{mn}^{(1)} = \Delta_m \Delta_n \int_{S_1} \Psi^{(1)}(x',y')\psi_{mn}^{(1)}(x',y') \, ds' \tag{12}$$

where

$$\Delta_i = \begin{cases} \frac{1}{2} & i = 0 \\ 1 & \text{otherwise.} \end{cases} \tag{13}$$

In order to find an alternative expression for the surface integral appearing in (12), we multiply (1) by $\psi_{mn}^{(1)}$ and (8) by $\Psi^{(1)}$. Subtracting the resulting equations and integrating over S_1, we obtain the following

$$(K_{mn}^{(1)^2} - K^2) \int_{S_1} \Psi^{(1)}\psi_{mn}^{(1)} \, ds = \int_{S_1} [\psi_{mn}^{(1)}\nabla_t^2\Psi^{(1)} - \Psi^{(1)}\nabla_t^2\psi_{mn}^{(1)}] \, ds. \tag{14}$$

Using the two-dimensional form of the divergence theorem and Green's second identity [9], the right-hand-side of (14) can be written as

$$\text{R.H.S.} = \oint_{\ell_1} [\psi_{mn}^{(1)}\partial_n\Psi^{(1)} - \Psi^{(1)}\partial_n\psi_{mn}^{(1)}] \, d\ell. \tag{15}$$

The second term in (15) is zero by virtue of (9). Thus the unknown amplitudes given in (12) reduce to

$$A_{mn}^{(1)} = \frac{\Delta_m \Delta_n}{(K_{mn}^{(1)^2} - K^2)} \oint_{\ell_1} \psi_{mn}^{(1)}\partial_n\Psi^{(1)} \, d\ell. \tag{16}$$

142

Because of (2), however, the line integral in (16) only contributes in the gap. Thus,

$$\oint_{\ell_1} \psi_{mn}^{(1)} \partial_n \psi^{(1)} \, d\ell = -\left(\int_{-a}^{-w} + \int_{w}^{a} \right) \psi_{mn}^{(1)}(x,0) \partial_y \psi^{(1)}(x,0) \, dx \tag{17}$$

since

$$\partial_n \psi^{(1)} = -\frac{\partial}{\partial y} \psi^{(1)} \quad \text{at } y = 0. \tag{18}$$

In order to combine the two integrations appearing in (17), we will consider two cases: (1) the odd modes for which $\psi^{(1)}(x,y) = -\psi^{(1)}(-x,y)$; and (2) the even modes for which $\psi^{(1)}(x,y) = \psi^{(1)}(-x,y)$. The following analysis will apply for the odd modes for which (17) can be written as

$$\oint_{\ell_1} \psi_{mn}^{(1)} \partial_n \psi^{(1)} \, d\ell = -\int_{w}^{a} \partial_y \psi^{(1)}(x,0) \, [\psi_{mn}^{(1)}(x,0) - \psi_{mn}^{(1)}(-x,0)] \, dx. \tag{19}$$

The term in the square brackets in (19) is zero if m is even. Thus (16) gives

$$A_{mn}^{(1)} = \begin{cases} \dfrac{2\Delta_n}{(K^2 - K_{mn}^{(1)\,2})} \displaystyle\int_{w}^{a} \partial_y \psi^{(1)}(x,0) \psi_{mn}^{(1)}(x,0) \, dx & (m=1,3,5,\ldots) \\[4mm] 0 & (m=0,2,4,\ldots). \end{cases} \tag{20}$$

Equation (20) can now be inserted into (7) which then determines the scalar function, $\psi^{(1)}$ in region 1 in terms of the unknown cutoff wave number, K, and an integration of the unknown electric field in the gap ($\partial_y \psi^{(1)}(x,0) \propto E_x(x,0)$). Thus

$$\psi^{(1)}(x,y) = 2 \sum_{p,n} \frac{\Delta_n}{(K^2 - K_{2p+1,n}^{(1)\,2})} \psi_{2p+1,n}^{(1)}(x,y) \int_{w}^{a} \partial_y \psi^{(1)}(x',0) \psi_{2p+1,n}^{(1)}(x',0) \, dx'$$

where p = 0, 1, 2, ... \hfill (21)

A similar relation can be written in region 2 by replacing all subscripts and superscripts 2 by 1 and by replacing y by -y. In the gap, we require continuity of H_z and E_x which is equivalent to requiring the following

$$\psi^{(1)}(x,0) = \psi^{(2)}(x,0) \qquad (w < x < a) \tag{22}$$

and

$$\partial_y \psi^{(1)}(x,0) = \partial_y \psi^{(2)}(x,0) \qquad (w < x < a). \tag{23}$$

When (22) and (23) are imposed on (21) and its equivalent expression in region 2, we obtain the following integral equation.

$$\int_{w}^{a} \partial_y \psi(x',0) G_0(x,x') dx' = 0 \qquad (w < x < a) \tag{24}$$

143

where

$$G_o(x,x') = \sum_{j=1}^{2} \sum_{p,n} \frac{\Delta_n}{(K^2 - K_{2p+1,n}^{(j)\ 2})} \psi_{2p+1}(x,0)\psi_{2p+1}(x',0) \qquad (25)$$

and we have dropped the superscript on $\partial_y\psi(x',0)$ since it is continuous across the gap as well as the subscript "n" on the basis functions since they are evaluated at y = 0. The Green's function given in (25) is singular at x = x'. Thus, as shown in [10, pp. 197-198] the integral equation (24) is to be interpreted in the principal value sense.

A similar expression can be obtained for the even modes. The resulting integral equation is identical to (24) if we replace G_o by G_e which is given as

$$G_e(x,x') = \sum_{j=1}^{2} \sum_{p,n} \frac{\Delta_p \Delta_n}{(K^2 - K_{2p,n}^{(j)2})} \psi_{2p}(x,0)\psi_{2p}(x',0). \qquad (26)$$

If the septum is located in the center of the TEM cell (i.e. $b_1 = b_2 = b$) then the summation on "j" in (25) and (26) can be dropped and replaced by the factor 2.

3. SMALL GAP APPROXIMATION FOR THE GREEN'S FUNCTIONS

The integral equation given in (24) could be solved numerically at this point using, for example, the moment method. In this method, the unknown function, $\partial_y\psi(x',0)$, can be approximated by an M-term Fourier series. Using the orthogonality properties of the basis functions, an M x M matrix equation ensues, and the requirement that the determinant vanish then determines the cutoff frequencies of the higher-order modes. However, since a strictly numerical technique does not furnish much insight as to how the cutoff frequencies change as the gap varies and may also lead to relative convergence difficulties [11], we will solve (24) by approximating the Green's function using a small gap assumption, i.e. Kg << 1. The solution to the approximate integral equation can then be obtained analytically.

In order to find an approximation for G_o, we note that the summation on "n" in (25) can be written as follows

$$\sum_{n=0} \frac{\Delta_n}{[K^2 - K_{2p+1,n}^{(j)\ 2}]} = \left(\frac{b_j}{\pi}\right)^2 \left(\frac{1}{2\alpha_{2p+1}^{(j)2}} - \sum_{n=1}^{\infty} \frac{1}{(n^2 - \alpha_{2p+1}^{(j)2})}\right) \qquad (27)$$

where

$$\alpha_{2p+1}^{(j)} \equiv \left(\frac{b_j}{\pi}\right)\left(K^2 - (2p+1)^2\left(\frac{\pi}{2a}\right)^2\right)^{\frac{1}{2}}. \qquad (28)$$

The summation on the right-hand-side of (27) is given as [12]

$$\sum_{n=1}^{\infty} \frac{1}{(n^2 - \alpha_{2p+1}^{(j)2})} = \frac{1}{2\alpha_{2p+1}^{(j)2}} - \frac{\pi}{2} \frac{1}{\alpha_{2p+1}^{(j)}} \cot(\pi \alpha_{2p+1}^{(j)}) \tag{29}$$

so that (27) reduces to

$$\sum_{n=0}^{\infty} \frac{\Delta_n}{[K^2 - K_{2p+1,n}^{(j)2}]} = \frac{b_j^2}{2\pi \alpha_{2p+1}^{(j)}} \cot(\pi \alpha_{2p+1}^{(j)}). \tag{30}$$

Thus, G_O given in (25) can be written as

$$G_O(x,x') = \sum_{j=1}^{2} \frac{b_j^2}{2\pi} \sum_{p} \frac{\cot(\pi\alpha_{2p+1}^{(j)})}{\alpha_{2p+1}^{(j)}} \psi_{2p+1}(x,0)\psi_{2p+1}(x',0). \tag{31}$$

The summation on "p" in (31) cannot be done in closed-form; however, we notice that for large "p"

$$\frac{\cot(\pi\alpha_{2p+1}^{(j)})}{\alpha_{2p+1}^{(j)}} \sim -\left(\frac{2a}{b_j}\right) \frac{1}{(2p+1)} \tag{32}$$

so that if we add and subtract the right-hand-side of (32) to G_O we obtain the following

$$G_O(x,x') = G_O^{(1)}(x,x') + G_O^{(2)}(x,x') \tag{33}$$

where

$$G_O^{(1)}(x,x') = \sum_{j=1}^{2} \frac{b_j^2}{2\pi} \left(-\frac{2a}{b_j}\right) \sum_{p} \frac{\psi_{2p+1}(x,0)\psi_{2p+1}(x',0)}{(2p+1)} \tag{34}$$

and

$$G_O^{(2)}(x,x') = \sum_{j=1}^{2} \frac{b_j^2}{2\pi} \sum_{p} \left[\frac{\cot(\pi\alpha_{2p+1}^{(j)})}{\alpha_{2p+1}^{(j)}} + \left(\frac{2a}{b_j}\right) \frac{1}{(2p+1)}\right] \psi_{2p+1}(x,0)\psi_{2p+1}(x',0). \tag{35}$$

The term in the square brackets in (35) now decays rapidly as p^{-2}. Hence, $G_O^{(2)}$ approaches a constant whenever $|x-x'| \to 0$. On the other hand, the terms involved in $G_O^{(1)}$ decay only as p^{-1} and thus will have a logarithmic singularity as $|x-x'| \to 0$. Therefore under the assumption of a small gap the dominant contribution to G_O will come from $G_O^{(1)}$.

Substituting for the basis functions from (10), and making the following change of variables

$$t = a - x \tag{36}$$

and

$$t' = a - x' \tag{37}$$

$G_o^{(1)}$ can be written as

$$G_o^{(1)}(t,t') = -\frac{2}{\pi} \sum_{p=0}^{\infty} \frac{2}{(2p+1)} \left\{ \cos\left[\frac{(2p+1)\pi(t+t')}{2a}\right] + \cos\left[\frac{(2p+1)\pi(t-t')}{2a}\right] \right\} \quad (38)$$

which can be summed as [13]

$$G_o^{(1)}(t,t') = \frac{2}{\pi}\left\{ \ln\ \tan\left[\frac{\pi}{4a}\ |t+t'|\right] + \ln\ \tan\left[\frac{\pi}{4a}\ |t-t'|\right] \right\}. \quad (39)$$

The largest value of $|t+t'|$ is 2g so that if we assume that $g/a << 1$ we can replace the tangents in (39) by their arguments and obtain

$$G_o^{(1)}(t,t') \simeq \frac{2}{\pi}\ \ln\left[\left(\frac{\pi}{4a}\right)^2\ |t^2-t'^2|\right] \quad \left(\frac{g}{a} << 1\right). \quad (40)$$

In order to obtain an approximate form for $G_o^{(2)}$ we notice that if we restrict attention to only the first few higher-order modes for which K is not too large, then the sum in (35) converges very rapidly, so rapidly in fact that the arguments of the cosines appearing in the basis functions in (35) remain close to zero. Thus, $G_o^{(2)}$ is essentially independent of x and x' for $gK \to 0$ and we can write

$$G_o^{(2)} \simeq \sum_{j=1}^{2} \frac{1}{\pi} \frac{b_j}{a} \sum_{p=0}^{\infty} \left[\frac{\cot(\pi\alpha_{2p+1}^{(j)})}{\alpha_{2p+1}^{(j)}} + \left(\frac{2a}{b_j}\right)\frac{1}{(2p+1)}\right]. \quad (41)$$

$$(2gK << 1) \quad (42)$$

Since we have assumed a small gap, it seems reasonable to represent the modes in the TEM cell as perturbations of rectangular waveguide modes; that is, we let

$$K^2 = K_{qr}^{(s)\,2} + \delta_{qr}^{(s)\,2} \qquad (q=1,3,5...) \qquad (r=0,1,2....) \qquad (s=1,2) \quad (43)$$

with

$$\delta_{qr}^{(s)} << K_{qr}^{(s)} \quad (44)$$

and $K_{qr}^{(s)}$ cannot be so large that (42) is violated. Then the main contribution to the summation in (41) occurs when $\alpha_{2p+1}^{(j)} \simeq n$ or when $K \simeq K_{2p+1,n}^{(j)}$. There may be more than one term for which this occurs since it is possible to have two or more rectangular waveguide modes with the same cutoff frequency. We will take, for example, q = 1 and r = 0 which corresponds to a perturbation of the TE_{10} mode in a rectangular waveguide which is the first higher-order mode that we would expect to appear. $K_{qr}^{(s)}$ does not depend on "s" in this case since r = 0, and only one term in (41) is dominant. For this case, $G_o^{(2)}$ can be written as

$$(G_o^{(2)})_{TE_{10}} \simeq \sum_{j=1}^{2} \left\{\left[\frac{\cot(b_j\delta_{10})}{a\delta_{10}} + \frac{2}{\pi}\right] + \frac{2}{\pi}\sum_{p=1}^{\infty}\frac{1}{(2p+1)}\left[1 - \coth\frac{\pi b_j}{2a}(2p+1)\right]\right\}. \quad (45)$$

146

The summation on "p" in (45) is very small compared to the dominant p = 0 term, so we will neglect it, subject to a consistency check when δ_{10} is determined. In any case the summation is rapidly convergent and can be evaluated numerically if needed. Thus,

$$(G_o^{(2)})_{TE_{10}} \simeq \frac{4}{\pi} + \frac{\cot b_1\delta_{10} + \cot b_2\delta_{10}}{a\delta_{10}}.$$ (46)

In the general case for non-degenerate odd modes, we obtain in a similar way

$$(G_o^{(2)})_{TE_{qr}^{(s)}} \simeq \sum_{j=1}^{2} \left\{ \left[\frac{\cot(b_j\xi_{qr}^{(s)})}{\xi_{qr}^{(s)}} + \frac{2}{\pi q} \right] + \frac{2}{\pi} \sum_{p=0}^{\infty} \frac{1}{(2p+1)} \left[1 - \coth \frac{\pi b_j}{2a}(2p+1) \right] \right\}$$

$$p \neq \frac{(q-1)}{2}$$ (47)

where

$$\xi_{qr}^{(s)} = \left[\left(\frac{n\pi}{bj}\right)^2 + \delta_{qr}^{(s)2} \right]^{\frac{1}{2}}.$$ (48)

The preceding analysis has dealt with the approximation of G_o. A similar analysis also applies for G_e, and we therefore only quote the results.

$$G_e^{(1)}(t,t') \simeq \frac{1}{\pi} \ln\left[\left(\frac{\pi}{a}\right)^2 |t^2-t'^2| \right]$$ (49)

and in the general case for non-degenerate even modes we obtain

$$(G_e^{(2)})_{TE_{qr}^{(s)}} \simeq \sum_{j=1}^{2} \left\{ \left[\frac{\cot(b_j\xi_{qr}^{(s)})}{\xi_{qr}^{(s)}} + \frac{2}{\pi q} \right] + \frac{2}{\pi} \sum_{p=1}^{\infty} \frac{1}{p} \left[1 - \coth \frac{\pi b_j p}{a} \right] + \frac{2}{\pi} \frac{\cot\left(\frac{q\pi b_j}{2a}\right)}{q} \right\}.$$

$$p \neq q/2$$ (50)

It is interesting to note that all of the dependence on position (through the variables t and t') is contained in $G_{o,e}^{(1)}$ while all of the dependence on the as yet undetermined K (through $\delta_{qr}^{(s)}$) is contained in $G_{o,e}^{(2)}$.

4. SOLUTION OF THE APPROXIMATE INTEGRAL EQUATION

4.1 Cutoff Frequencies of the Higher-Order Modes

Inserting the approximate form for G_o into (24) we obtain

$$\int_0^g f(t') \left\{ \frac{1}{\pi} \ln\left[\left(\frac{\pi}{4a}\right)^2 |t^2-t'^2| \right] + G_o^{(2)} \right\} dt' = 0$$ (51)

where

$$f(t') \equiv \partial_y \Psi(a-t',0).$$ (52)

147

If we make the following substitutions

$$u = \frac{\pi t}{4a};$$ (53)

$$u' = \frac{\pi t'}{4a};$$ (54)

$$u_o = \frac{\pi g}{4a};$$ (55)

$$A_o = \int_o^g g(t')\, dt;$$ (56)

$$h(u') \equiv f(\frac{4au'}{\pi});$$ (57)

then (51) reduces to

$$\int_o^{u_o} h(u')\, \ln |u^2 - u'^2|\, du' = -\frac{\pi^2}{4a} G_o^{(2)} A_o.$$ (58)

But the solution of (58) is known to be [14]

$$h(u') = \frac{C}{[u_o^2 - u'^2]^{\frac{1}{2}}}$$ (59)

where C is an arbitrary constant which is related to A_o defined in (56). Inserting (59) into (58) we obtain

$$\int_o^{u_o} \frac{C}{[u_o^2 - u'^2]^{\frac{1}{2}}} \ln |u^2 - u'^2|\, du' = \frac{-\pi^2}{4a} G_o^{(2)} A_o$$ (60)

which can be written alternatively as follows

$$\int_{-u_o}^{u_o} \frac{C}{[u_o^2 - u'^2]^{\frac{1}{2}}} \ln |u - u'|\, du' = \frac{-\pi^2}{4a} G_o^{(2)} A_o.$$ (61)

If we make the following substitutions

$$u = u_o \cos \theta$$ (62)

and

$$u' = u_o \cos \phi$$ (63)

then (61) reduces to

$$C \int_o^{\pi} \ln[u_o |\cos \theta - \cos \phi|] d\phi = \frac{-\pi^2}{4a} G_o^{(2)} A_o.$$ (64)

However, since [10, p. 171]

$$\ln |\cos \theta - \cos \phi| = -\ln 2 - 2 \sum_{m=1}^{\infty} \frac{1}{m} \cos m\theta \cos m\phi$$ (65)

148

(64) reduces to

$$\pi C \ln\left(\frac{u_o}{2}\right) = \frac{-\pi^2}{4a} G_o^{(2)} A_o. \tag{66}$$

A_o in (66) can be found in terms of C by changing variables and substituting (59) into (56) with the result that

$$A_o = 2aC. \tag{67}$$

Thus, (66) and (67) give

$$\frac{G_o^{(2)}}{2} + \frac{1}{\pi} \ln\left(\frac{u_o}{2}\right) = 0. \tag{68}$$

Substituting for $G_o^{(2)}$ and u_o from (46) and (55) respectively we obtain the following characteristic equation for the perturbed TE_{10} mode.

$$\frac{1}{2}[\cot b_1 \delta_{10} + \cot b_2 \delta_{10}] = \frac{a\delta_{10}}{\pi} [\ln(\frac{8a}{\pi g}) - 2]. \tag{69}$$

Provided that the remaining sum in (45) is indeed small under the small gap assumption, this is then the equation for determining δ_{10}. In particular, when the gap ratio (g/a) is much smaller than one, the perturbation solution can be obtained simply from the small argument expansion of the cotangent to yield

$$\delta_{10}^2 \simeq \frac{\pi b/a}{b_1 b_2 \ln(\frac{8a}{\pi g})} \tag{70}$$

and from (43) the cutoff wavenumber is then given by

$$K \simeq \left[\frac{\pi}{2a} + \frac{\pi b/a}{b_1 b_2 \ln(\frac{8a}{\pi g})}\right]^{\frac{1}{2}}. \tag{71}$$

It is of interest to point out that the form of K as given by (71) is essentially the same as the one obtained in [15] which treats a similar problem in which coupling occurs through only one aperture.

As a trial solution for any numerical or graphical search of the root of (69), we note that since the value of the cotangent can vary from ∞ to 0 when $b_1 \delta_{10}$ increases from 0 to $\pi/2$ (assuming $b_1 > b_2$), the expected solution therefore lies in the range where δ_{10} varies from 0 to $\pi/2b$, which is the midpoint between the unperturbed TE_{10} mode and the unperturbed TE_{20} mode. For g/a ratios from .01 to .3 and a/b ratios from .5 to 1, a nomographic solution of (69) was obtained which allows one to easily determine the cut-off wavelength graphically. This is included in figure 2.

The integral equation with G_e instead of G_o is identical if we replace "a" by a/4. Thus, for example, for the perturbed TE_{20} mode we obtain

$$\frac{1}{2}[\cot b_1 \delta_{20} + b_2 \delta_{20}] = \frac{a\delta_{20}}{4\pi}[\ln(\frac{2a}{\pi g}) - 2] \tag{72}$$

from which the perturbed cutoff wavenumber can be obtained as above.

149

4.2 Field Distribution of the Higher Order Modes

The field distribution of the higher-order modes can be obtained by substituting the aperture field found in (59) into (21), but first we can evaluate advantageously the unknown constant, C, in terms of the "voltage" drop across the gap. Substituting for $f(t')$ from (52) into (56) and realizing from (6) that

$$\partial_y \Psi(x',0) = \frac{E_x(x',0)}{i\omega\mu_o} \tag{73}$$

we obtain for A_o.

$$A_o = \frac{1}{i\omega\mu_o} \int_{a-g}^{a} E_x(x',0)dx' = \frac{iV}{\omega\mu_o} \tag{74}$$

where V is the potential difference across the gap. Thus, C in (67) is given as

$$C = \frac{iV}{2a\omega\mu_o} \tag{75}$$

and the aperture field from (59) can then be written as

$$h(u') = \frac{iV}{2a\omega\mu_o} [u_o^2 - u'^2]^{-\frac{1}{2}}. \tag{76}$$

Transforming the integration in (21) from x' to u' via (37) and (54) and inserting $h(u')$ from (76) we obtain

$$\int_w^a \partial_y \Psi^{(1)}(x',0)\Psi_{2p+1}^{(1)}(x',0)dx' = -\frac{2}{\pi}\left(\frac{2}{ab_1}\right)^{\frac{1}{2}}\left(\frac{iV}{\omega\mu_o}\right)\int_0^{u_o}\frac{\cos[(2p+1)2u']du'}{\sqrt{u_o^2 - u'^2}}, \tag{77}$$

but the integration in (77) is given as [16]

$$\int_0^{u_o}\frac{\cos[(2p+1)2u']du'}{\sqrt{u_o^2 - u'^2}} = \frac{\pi}{2} J_o[2(2p+1)u_o]$$

$$= \frac{\pi}{2} J_o[(2p+1)\frac{\pi g}{2a}] \tag{78}$$

where J_o is a Bessel function of order zero. Thus by analogy with (21) the fields in regions 1 and 2 can be written as

$$\Psi^{(j)}(x,y) = \left(\frac{4}{ab_j}\right)\left(\frac{iV}{\omega\mu_o}\right)\sum_{p,n}\frac{\Delta_n(-1)^P J_o[(2p+1)\frac{\pi g}{2a}]\sin[(2p+1)\frac{\pi x}{2a}]\cos(\frac{n\pi y}{b_j})}{(K^2 - K_{2p+1,n}^{(j)\,2})} \quad (j = 1,2). \tag{79}$$

The summation on "n" in (79) can be written as follows

$$\sum_{n=0}^{\infty}\frac{\Delta_n \cos\left(\frac{n\pi y}{b_j}\right)}{(K^2 - K_{2p+1,n}^{(j)\,2})} = \left(\frac{b_j}{\pi}\right)^2\left[\frac{1}{2\alpha_{2p+1}^{(j)\,2}} - \sum_{n=1}^{\infty}\frac{\cos\left(\frac{n\pi y}{b_j}\right)}{(n^2 - \alpha_{2p+1}^{(j)\,2})}\right] \tag{80}$$

150

where $\alpha_{2p+1}^{(j)}$ was defined in (28). The summation on the right-hand-side of (80) is given as [12]

$$\sum_{n=1}^{\infty} \frac{\cos\left(\frac{n\pi y}{b_j}\right)}{(n^2 - \alpha_{2p+1}^{(j)2})} = \frac{1}{2\alpha_{2p+1}^{(j)2}} - \frac{\pi}{2\alpha_{2p+1}^{(j)}} \frac{\cos\left[\left(\frac{y}{b_j}\mp 1\right)\pi\alpha_{2p+1}^{(j)}\right]}{\sin(\pi\alpha_{2p+1}^{(j)})} \tag{81}$$

so that (79) reduces to

$$\psi^{(j)}(x,y) = \left(\frac{2b_j}{\pi a}\right)\left(\frac{iV}{\omega\mu_o}\right) \sum_{p=0}^{\infty} \frac{(-1)^P J_o[(2p+1)\frac{\pi g}{2a}]\sin[(2p+1)\frac{\pi x}{2a}]}{\alpha_{2p+1}^{(j)}} \frac{\cos\left[\left(\frac{y}{b_j}\mp 1\right)\pi\alpha_{2p+1}^{(j)}\right]}{\sin(\pi\alpha_{2p+1}^{(j)})} . \tag{82}$$

From (28) and (43) we have that $\alpha_1^{(j)} \simeq \frac{b_j\delta_{10}}{\pi}$ for $r = 0$ so that restricting attention to the perturbed TE_{10} mode we have

$$\psi^{(j)}(x,y) \simeq \left(\frac{2}{a\delta_{10}}\right)\left(\frac{iV}{\omega\mu_o}\right) \frac{\cos[\delta_{10}(y\mp b_j)]}{\sin \delta_{10}b_j} \sin\left(\frac{\pi x}{2a}\right)$$

$$+ \left(\frac{2b_j}{\pi a}\right)\left(\frac{iV}{\omega\mu_o}\right) \sum_{p=1}^{\infty} \frac{(-1)^P J_o[(2p+1)\frac{\pi g}{2a}]\sin[(2p+1)\frac{\pi x}{2a}]}{\alpha_{2p+1}^{(j)}} \frac{\cos\left[\left(\frac{y}{b_j}\mp 1\right)\pi\alpha_{2p+1}^{(j)}\right]}{\sin(\pi\alpha_{2p+1}^{(j)})} . \tag{83}$$

Since the potential difference, V, is still arbitrary, we can normalize V in such a way that the amplitude of $\sin(\frac{\pi x}{2a})$ is unity with the result that

$$\psi^{(j)}(x,y) = \sin\left(\frac{\pi x}{2a}\right) + \frac{b_j\delta_{10}}{\pi} \frac{\sin \delta_{10}b_j}{\cos[\delta_{10}(y\mp b_j)]} Q \tag{84}$$

where

$$Q = \sum_{p=1}^{\infty} \frac{(-1)^P J_o\left[(2p+1)\frac{\pi g}{2a}\right]\sin\left[(2p+1)\frac{\pi x}{2a}\right]\cos\left[\left(\frac{y}{b_j}\mp 1\right)\pi\alpha_{2p+1}^{(j)}\right]}{\alpha_{2p+1}^{(j)} \sin(\pi\alpha_{2p+1}^{(j)})} \qquad (j = 1,2). \tag{85}$$

In this form the first term in (84) can be recognized as the dominant TE_{10} mode of a rectangular waveguide and the second term as a small perturbation. As $g/a \to 0$, $\delta_{10} \to 0$, and the perturbation term in (84) vanishes.

5. EXPERIMENTAL DETERMINATION OF THE RESONANT FREQUENCIES OF TEM CELLS

Measurements were made using an automatic network analyzer to determine the network scattering (S), parameters for a number of TEM cells as a function of frequency. These S-parameters comprise a total characterization of the cell as a two terminal network from which the cell's complex impedance, insertion loss, and resonant frequencies can be determined.

151

The operational details of the system used to make these measurements has been published [17] and are not repeated here. However, the test system's functional diagram is shown in figure 3. The system has three main sections, namely, source, measurement, and computer. The signal generator provides the RF power over the frequency range of interest (0.1 GHz and above) required to pre-calibrate the system and test the unknown device or the TEM cells. The frequency and level of the RF source is stabilized, level controlled, and pre-selected by command to the computer. The RF is applied to the device under test via the S-parameter test set. Then depending upon how S_1 and S_2 are set, the parameters S_{11}, S_{22}, S_{12}, or S_{21} are measured.

The "complex ratio detector" measures the amplitude ratio and phase difference between the reference and test channels. This information is digitized and routed to the computer via the instrument interface.

The computer then takes the S-parameter data and stores it either as calibration data, if measuring standards, or raw, corrected data if measuring the TEM cell. This data is then processed for correction and routed to the displays and to other computer peripherals.

Summarizing, the measurement sequence essentially is broken into two steps. The first is the preparation of the system through pre-calibration to make the desired measurement. The second is to measure, digitize, and store the S-parameter data in the computer and then convert, correct, and output the data in the desired form. Examples of data obtained for a typical TEM cell are given in figure 4. Resonant frequencies are indicated by the high VSWR. Note how narrow the bandwidth is for each resonance. This is indicative of the small RF losses within the cell's conductive walls and center plate and is an indication of the cell Q factor.

6. RESULTS AND CONCLUSIONS

In this section we will discuss the result obtained for the resonant frequency of the first higher-order, perturbed mode in a TEM cell with a symmetrically placed center septum via three different techniques; 1) the experimental measurement as described in the last section, 2) theoretical calculations based upon (69), and 3) a numerical result based upon an exact integral equation formulation as obtained from equation (58) in the work of Mittra and Itoh [4]. In both of the last two methods, the cutoff frequency, f_c, is actually calculated, and this must then be converted to the resonant frequency, f_{res}, via the following well known result

$$f_{res} = [f_c^2 + (\frac{c}{2d})^2]^{\frac{1}{2}} \qquad (86)$$

where

$$c = 1/\sqrt{\mu_o \epsilon_o} \; ; \qquad (87)$$

and d is the resonant length.

As shown in the figure included with table 1, the two ends of the TEM cell are tapered, so that the resonant length is not very well defined. As a first approximation, however, we will take the average overall length as the resonant length.

In order to find the zero of (69), a root-finder based upon the bisection method was used. This is contained in the Appendix. This same root-finder was also used to find the zeroes of Mittra and Itoh's equation (58), which for a symmetrically-placed center septum and a homogeneous dielectric filling reduces to the following for the TE modes

$$\left(1 - \frac{Y_1(0)}{\hat{k}_1} K_1\right) = 0 \tag{88}$$

where

$$K_1 = \alpha_2 = \frac{1}{2}(1 + \cos \frac{\pi w}{a}); \tag{89}$$

and

$$\frac{Y_1(0)}{\hat{k}_1} = \frac{S_1'(0) + 2d_1(0)E_1}{\hat{k}_1[S(0) - 2I_g]}. \tag{90}$$

The symbols in the above equations are defined in Mittra and Itoh's paper and in general must be evaluated numerically. However, for a small gap, it can be shown that the solution of (88) is given approximately by

$$S(0) - 2I_g = 0 \tag{91}$$

or just the denominator of (90) equal to zero. Note that $K_1 \to 0$ in (88) as $w \to a$. Furthermore (91) can be shown to reduce to our result given in (69) for $g/a \to 0$.

Shown in figure 5 are the calculated cutoff wavelengths computed via Mittra and Itoh's eq. (58) and our result, eq. (69) for two different TEM cell geometries. As expected, the two curves become indistinguishable for very small gaps. The w/a ratios of the TEM cells currently being used at NBS are all greater than 0.72. Thus figure 5 shows that only a few percent error occurs even for those cells with the largest gaps. It is also interesting to note that Mittra and Itoh's result predicts a cutoff wavelength given by that of the TE_{11} mode in the full cell for septum widths up to nearly half of the width of the cell.

153

Shown in table 1 are the calculated and experimentally measured resonant frequencies of the first higher-order, perturbed mode in nine different TEM cells used at NBS. The column labeled "Form Factor Group" refers to those cells which are scaled versions of one another. As can be seen, the largest percentage error between our approximate solution and the measured value is 6.4% for w/a = .72 or g/a = 0.28. For smaller gaps (w/a = .83) the percentage difference is typically 1%.

Thus we are able to predict the useful frequency range of a TEM cell within a few percent. Using the same technique, additional work needs to be done to extend our solution to TEM cells which have different dielectrics above and below the center septum, i.e., a shielded strip line. In addition, if we re-formulate the problem in terms of an integral equation for the current on the septum, then we should be able to obtain an equivalent form for small center septums, i.e., w/a << 1. The formulation of the problem for TM modes has yet to be accomplished. When this is completed, we should be able to look at the TEM mode solution (a degenerate TM mode) and obtain a formula for the charac-teristic impedance of a TEM cell with an off-center septum. Thus, the solution of the conventional strip-line problem can be obtained by the same technique described in this report.

7. REFERENCES

[1] Tippet, J.C. and D.C. Chang, "Radiation characteristics of dipole sources located inside a rectangular , coaxial transmission line," NBSIR 75-829 (Jan. 1976).

[2] Mittra, R, "Relative convergence of the solution of a doubly infinite set of equations," J. Res. Nat. Bur. Stand. (U.S.), 67D, (Radio Propagation) No. 2, 245-254 (March-April 1963).

[3] Jones, D.S., The Theory of Electromagnetism, pp. 566-569 (Pergamon Press, New York, N.Y., 1964).

[4] Mittra, R. and T. Itoh, "A new technique for the analysis of the dispersion characteristics of microstrip lines," IEEE Trans. on MTT, Vol. MTT-19, No. 1, 47-56 (Jan. 1971).

[5] Bräckelmann, W., D. Landmann, and W. Schlosser, "Die grenzfrequenzen von höheren eigenwellen in streifenleitungen," Arch. Elek. Ubertragungstech., Vol. 21, No. 3, 112-120 (March 1967).

[6] Bezlyudova, M.M., "Cutoff wavelength of waveguide-type oscillations in transmission lines having internal and external conductors of rectangular cross section," Radio Engineering and Electronic Physics, Vol. 8, No. 11 1727-1733 (Nov. 1963).

[7] Kopp, E.H., "Coupling between dissimilar waveguides," IEEE Trans. on MTT, Vol. MTT-16, No. 1, 6-11 (Jan. 1968).

[8] Friedman, B., Principles and Techniques of Applied Mathematics, p. 271 (Wiley, New York, N.Y., 1956).

[9] Jackson, J.D., Classical Electrodynamics, p. 15 (Wiley, New York, N.Y., 1962).

[10] Lewin, L., Theory of Waveguides (Newnes-Butterworths, London, 1975).

[11] Mitta, R., T. Itoh, and T.-S. Li, "Analytical and numerical studies of the relative convergence phenomenon arising in the solution of an integral equation by the moment method," IEEE Trans. on MTT, Vol. MTT-20, No. 2, 96-104 (Feb. 1972).

[12] Collin, R.E., Field Theory of Guided Waves, p. 581 (McGraw-Hill, New York, N.Y., 1960).

[13] Jolley, L.B.W., Summation of Series, pp. 96, 97 (Dover Publ. Inc., New York, N.Y., 1961).

[14] Chang, D.C., "Equivalent-circuit representation and characteristics of a radiating cylinder driven through a circumferential slot," IEEE Trans. on Antennas and Propagation, Vol. AP-21, No. 6, 792-796 (Nov. 1973).

[15] Voytovich, N.N., B.Z. Katsenelenbaum, and A.N. Sivov, "The excitation of a two-dimensional metal cavity with a small opening (slotted cylinder)," Radio Engineering and Electronic Physics, Vol. 19, No. 12, 8-17 (Dec. 1974).

[16] Gradshteyn, I.S. and I.M. Ryzhik, Table of Integrals Series and Products, p. 419 (Academic Press, New York, N.Y., 1965).

[17] Rytting, D.K. and S.N. Sanders, "A system for automatic network analysis," Hewlett-Packard Journal, Vol. 21, No. 6, 2-10 (Feb. 1970).

```
      SUBROUTINE ROOT(A,B,F,X,JMAX,E,E1)

C     THIS SUBROUTINE USES THE BISECTION METHOD TO SOLVE FOR ONE ODD
C     ROOT OF F(X) = 0 ON THE INTERVAL (A,B).  THE FUNCTION PASSED
C     THROUGH F MUST BE DECLARED EXTERNAL IN ALL CALLING PROGRAMS.  E IS
C     INTERVAL OF UNCERTAINTY DESIRED FOR THE ROOT, AND MUST BE SMALLER
C     THAN THE STARTING INTERVAL, W = B-A.  THE NUMBER OF BISECTIONS IS
C     DETERMINED BY NMAX = LN(W/E)/LN(2).  AFTER BISECTING, THE FUNCTION
C     VALUE IS COMPARED TO E1.  IF ABS(F(X0)) > E1 THEN THE SUBROUTINE
C     PRINTS: DISCONTINUITY AT X = X0.  A RANDOM SEARCH OCCURING JMAX
C     TIMES IS USED TO LOOK FOR A CHANGE OF SIGN IF SIGN(F(A)) =
C     SIGN(F(B)).

      REAL LN2
      DIMENSION Y(3)

C     QUESTION: DOES F(A) = 0.

      Y1=F(A)
      IF(Y1.NE.0.) GOTO 10
      X=A
      GOTO 80

C     QUESTION: DOES F(B) = 0.

   10 Y2=F(B)
      IF(Y2.NE.0.) GOTO 20
      X=B
      GOTO 80

C     QUESTION: ARE THE SIGNS OF F(A) AND F(B) DIFFERE

   20 I1=SIGN(1.,Y1)
      I2=SIGN(1.,Y2)
      W=B-A
      IF(I1.NE.I2) GOTO 60

C     SEARCH FOR A CHANGE IN SIGN.

      DO 30 J=1,JMAX
      X=A+RANF(0.)*W
      I3=SIGN(1.,F(X))
      IF(I3.NE.I1) GOTO 50
   30 CONTINUE
      PRINT 40
   40 FORMAT(1X*NO CHANGE OF SIGN FOUND*/)
      RETURN
   50 B=X

C     DETERMINE NUMBER OF BISECTIONS

   60 LN2=0.693147181
      NMAX=ALOG(W/E)/LN2+1.
      Y(2+I1)=A
      Y(2-I1)=B

C     BEGIN BISECTION

      DO 70 N=1,NMAX
      X=(Y(1)+Y(3))/2.
      Y3=F(X)
      IF(Y3.EQ.0.) GOTO 80
      I3=SIGN(1.,Y3)
   70 Y(2+I3)=X
   80 IF(ABS(F(A)).LE.E1) GOTO 85

C     CONVERGENCE TO A DISCONTINUITY

      PRINT 82,X
   82 FORMAT(1X*DISCONTINUITY AT X = *E12.4/)
      RETURN

C     CONVERGENCE TO A ROOT

   85 PRINT 90,X
   90 FORMAT(1X*ONE ODD ROOT AT X = *E12.4/
      RETURN

      END
```
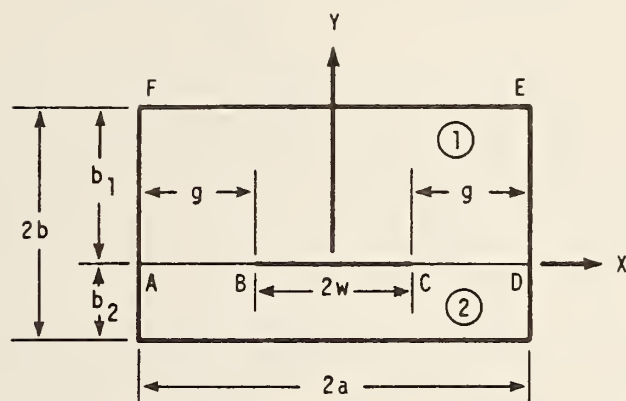
Figure 1. Cross-section of a TEM cell.
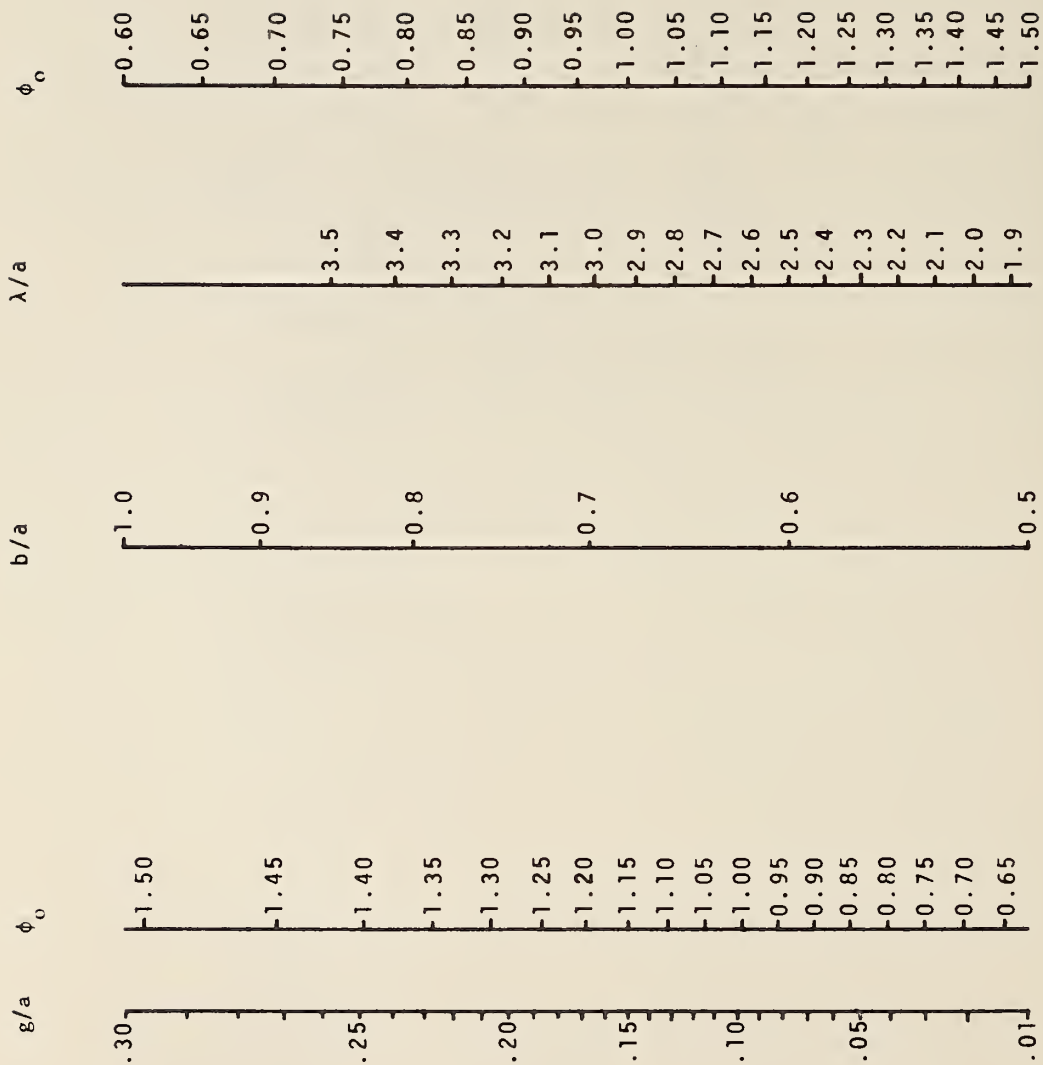
Figure 2. Nomograph for determining the cutoff wavelength of the first higher-order perturbed mode in a TLM cell given the ratios g/a and b/a.
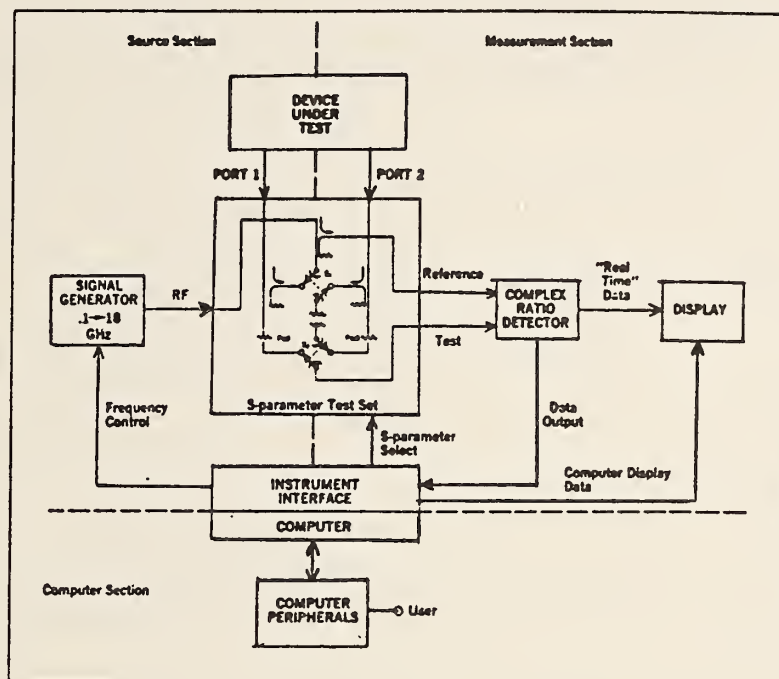
Figure 3. Functional diagram of an automatic network analyzer (ANA) system.
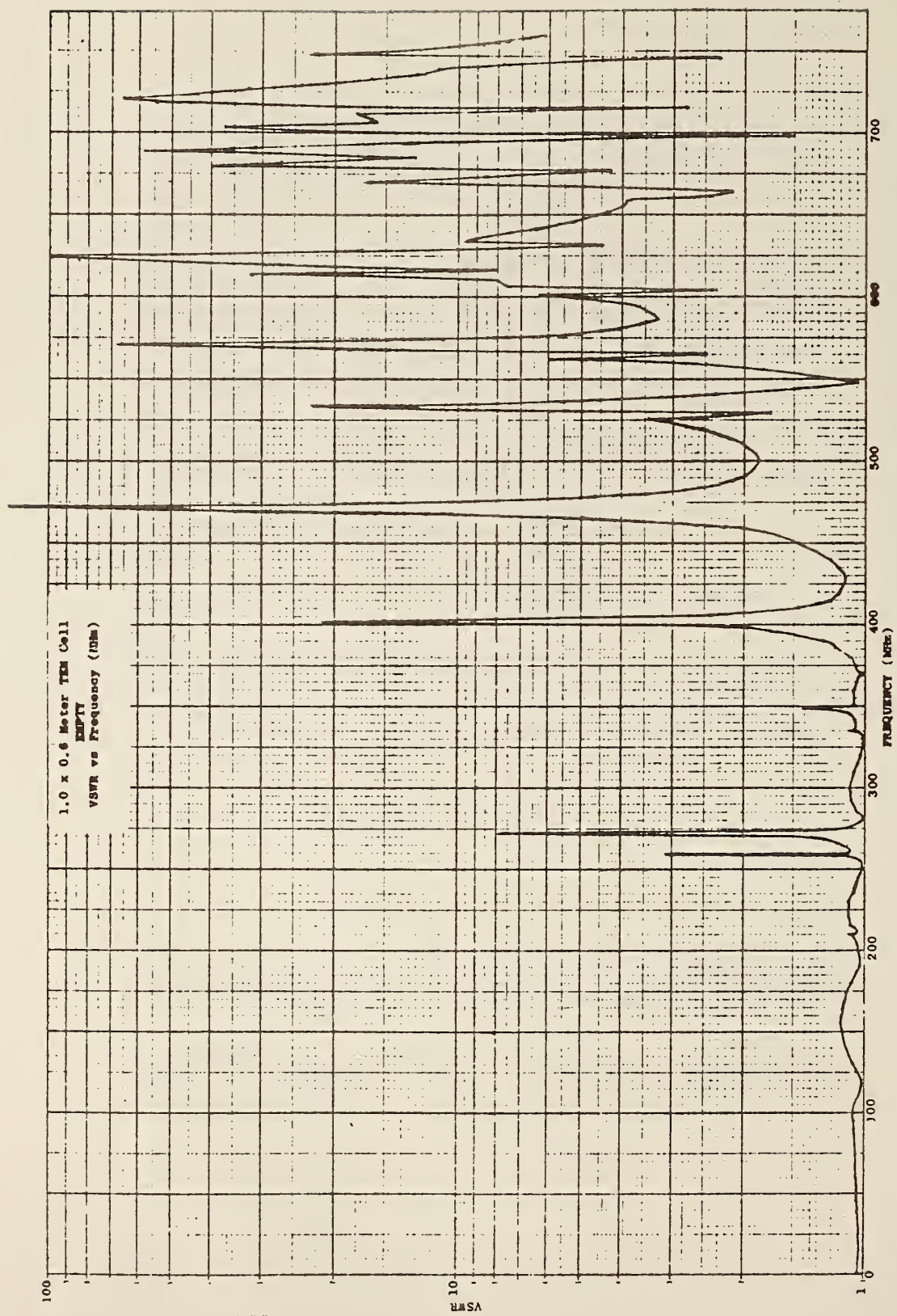
Figure 4. Typical data obtained from an automatic network analyzer.
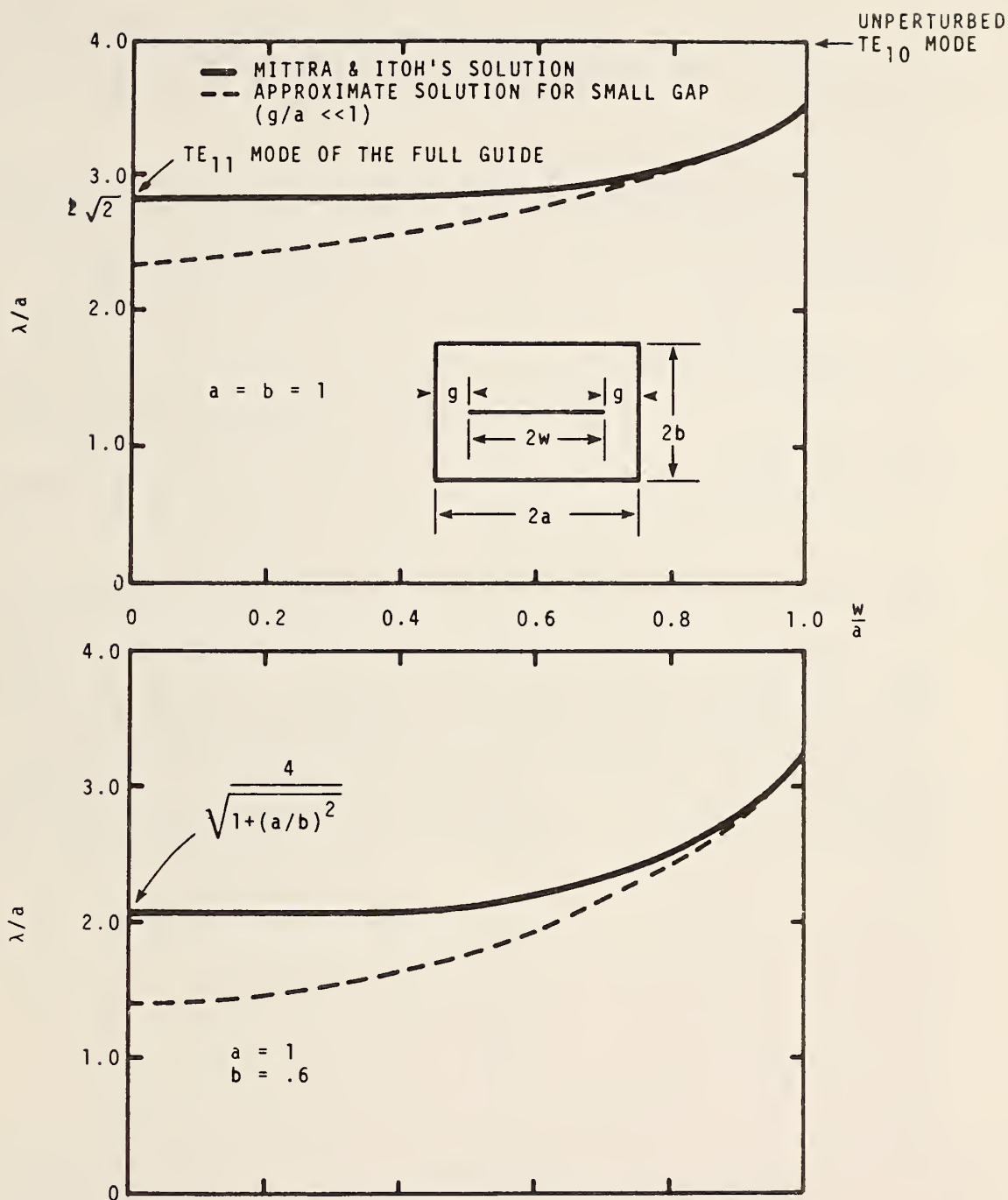
Figure 5. Comparison of Mittra and Itoh's exact solution and our approximate solution for the cutoff wavelength of the first higher-order perturbed mode in a TEM cell.

161

Table 1. Calculated and measured resonant frequencies of the first higher-order perturbed mode in nine different NBS TEM cells.

$$f_c \approx f_o \sqrt{1 + (2R_1\phi_o)^2}$$

where $\cot\phi_o = R_1[\ln R_2 - 2]\phi_o$; $f_o = \dfrac{c}{4a}$;

$R_1 = \dfrac{a}{b\pi}$; $R_2 = \dfrac{8a}{\pi g}$; and $\phi_o = b\delta_{10}$

$$f_{res} = \sqrt{f_c^2 + \left(\dfrac{c}{2d}\right)^2}$$
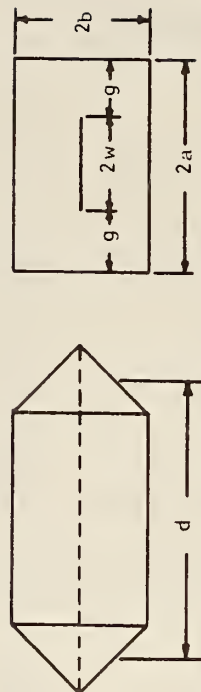
Cell number	2a (cm)	a/b	w/a	d/a	Form Factor Group	fc (MHz) Approx	Δfc %	fc (MHz) Mittra	fres (MHz) Approx	Δfres %	fres (MHz) Exp	Δfres %	fres (MHz) Mittra
1	600.	1.0	.83	3.0	I	32.4	1.25	32.0	36.4	-	-	-	36.1
2	25.4	1.0	.83	3.0	I	765.3	1.3	755.4	860.6	1.2	850.	.2	851.8
3	42.34	1.7	.72	3.0	II	639.0	6.5	599.8	681.3	6.1	640.	.7	644.6
4	50.	1.7	.72	3.0	II	541.4	6.6	508.1	577.2	6.4	540.	1.1	546.0
5	100.	1.7	.72	3.0	II	270.4	6.5	253.9	288.3	6.3	270.	1.1	272.9
6	30.	1.5	.76	3.0	III	813.1	4.3	779.6	878.8	-	-	-	847.9
7	90.	1.5	.76	3.0	III	270.1	4.2	259.2	292.1	2.4	285.	1.1	282.0
8	50.8	1.0	.83	4.75	IV	382.6	1.3	377.7	402.3	.6	400.	.6	397.6
9	121.92	1.0	.82	4.0	V	160.0	1.3	157.9	171.4	<1.4	169-172	<1.5	169.5

U.S. DEPT. OF COMM. BIBLIOGRAPHIC DATA SHEET	1. PUBLICATION OR REPORT NO. NBSIR 76-841	2. Gov't Accession No.	3. Recipient's Accession No.

4. TITLE AND SUBTITLE	5. Publication Date
An Analytical and Experimental Determination of the Cutoff Frequencies of Higher-Order TE Modes in a TEM Cell	July 1976
	6. Performing Organization Code 276.06

7. AUTHOR(S) John C. Tippet, David C. Chang, and Myron L. Crawford	8. Performing Organ. Report No.

9. PERFORMING ORGANIZATION NAME AND ADDRESS	10. Project/Task/Work Unit No. 2766281
NATIONAL BUREAU OF STANDARDS DEPARTMENT OF COMMERCE WASHINGTON, D.C. 20234	11. Contract/Grant No.

12. Sponsoring Organization Name and Complete Address (Street, City, State, ZIP)	13. Type of Report & Period Covered
Electronics Systems Division (AFSC) Hanscom Air Force Base, Mass. 01731	14. Sponsoring Agency Code

15. SUPPLEMENTARY NOTES

16. ABSTRACT (A 200-word or less factual summary of most significant information. If document includes a significant bibliography or literature survey, mention it here.)

In addition to the TEM mode, higher order TE and TM modes can propagate in a TEM cell. Since only the TEM mode is desired, the higher-order modes restrict the useful frequency range of the TEM cell. In this paper, the cutoff frequency of the first higher-order mode is obtained both analytically and experimentally for several TEM cells of differing geometry. The difference between the experimental and theoretical results is shown to be only a few percent. In addition the field distribution of the first higher-order mode is found explicitly.

17. KEY WORDS (six to twelve entries; alphabetical order; capitalize only the first letter of the first key word unless a proper name; separated by semicolons)

Shielded strip line; TEM cell.

18. AVAILABILITY ☒ Unlimited	19. SECURITY CLASS (THIS REPORT)	21. NO. OF PAGES
☐ For Official Distribution. Do Not Release to NTIS	UNCLASSIFIED	28
☐ Order From Sup. of Doc., U.S. Government Printing Office Washington, D.C. 20402, SD Cat. No. C13	20. SECURITY CLASS (THIS PAGE)	22. Price
☒ Order From National Technical Information Service (NTIS) Springfield, Virginia 22151	UNCLASSIFIED	$4.00

Appendix I

Tippet, J. C.; Chang, D. C. "Higher order modes in rectangular coaxial line with infinitely thin conductor."

Nat. Bur. Stand. (U.S.) NBSIR 78-873;1978 March.

NBSIR 78-873

HIGHER ORDER MODES IN RECTANGULAR COAXIAL LINE WITH INFINITELY THIN INNER CONDUCTOR

John C. Tippet
David C. Chang

Department of Electrical Engineering
University of Colorado

March 1978

CONTENTS

HIGHER ORDER MODES IN RECTANGULAR COAXIAL LINE
WITH INFINITELY THIN INNER CONDUCTOR

JOHN C. TIPPET, Student Member, IEEE, and

DAVID C. CHANG, Senior Member, IEEE

ABSTRACT

The singular integral equation approach is used to derive
the secular equations for both TE and TM waves in a rectangular
coaxial line with zero thickness inner conductor. Approximations
for the secular equations are found that reduce to simple expres-
sions in terms of well-known special functions (elliptic integrals).
When the strip width is exceedingly small or nearly equal to the
width of the outer conductor, closed form expressions for the cut-
off frequencies can be found by replacing the elliptic integrals
by their asymptotic forms for modulus either near zero or one.

Key words: Higher order modes; rectangular coaxial line; striplines.

I.   INTRODUCTION

In many applications involving rectangular coaxial waveguiding structures

an understanding of the propagation characteristics of higher order modes is

just as important as that of the fundamental TEM mode. One such application

is that of the so-called "TEM cell" which is used in some EMI measurement

systems [1]. This device consists of a section of rectangular coaxial line

which is used as a transducer for coupling EM energy from a device under

test into the TEM mode of the transmission line. The useful frequency range

of the TEM cell is limited by the cut-off frequencies of the higher order

modes. Thus, in order to design a cell for use over a specified frequency

range, these cut-off frequencies must be known.

The device analyzed in this paper consists of a zero thickness metal plate located inside a rectangular waveguide. The inner conductor may be offset vertically from its central position but is located symmetrically about the y-axis. Both the inner and outer conductor are perfectly conducting and the medium separating the two conductors is a homogeneous dielectric. A cross-sectional view of the rectangular line is shown in Fig. 1.

Although the transmission line properties of the TEM mode in these structures have been extensively studied, comparitively little work has been done in analyzing the higher order mode structure. One can find in the literature, however, this problem [2-4] as well as related problems, such as shielded strip lines [5-7], various coupling configurations [8-9], rectangular lines with thick inner conductors [10-13], and ridge waveguides [14-16] analyzed using a variety of techniques. These include functional equation techniques, finite difference techniques, mode matching techniques, integral equation techniques, and methods based on transmission line theory.

The purpose of this paper is to obtain a relatively simple, closed form expression for the characteristic equation for both TE and TM modes which is valid for arbitrary strip widths. Thus, very little computer programming is necessary to calculate the cut-off frequencies. In addition, approximate solutions for either small or large strip widths can be obtained without resorting to any numerical analysis. This is achieved by using the singular integral equation technique similar to that used in waveguide diaphragm problems [17]. This method has the advantage of handling the edge condition exactly and eliminates the problems encountered in any numerical solution associated with the discontinuities of the fields near the sharp edges of the inner conductor. More specifically, the problem is formulated using an integral equation--Green's function type of approach.

172

The singular part of the kernel of the resulting integral equation is extracted (as is done, e.g., in [18-20]) and the nonsingular part of the kernel that remains is expanding in terms of Chebyshev polynomials as suggested by [19].

II. FORMULATION

The cut-off frequencies of the higher-order modes of a rectangular coaxial line are just the eigenvalues K of the reduced wave equation

$$(\nabla^2 + K^2) \begin{pmatrix} H_z \\ E_z \end{pmatrix} = 0 \tag{1}$$

where

$$\nabla^2 = \partial^2/\partial x^2 + \partial^2/\partial y^2$$

and the unknowns satisfy the following boundary conditions on the metal walls

$$\partial_n H_z = 0$$

and

$$E_z = 0.$$

In the first case, H_z represents the z-component of the magnetic field of a TE mode; and in the second case, E_z represents the z-component of the electric field of a TM mode.

In order to solve this eigenvalue problem, we will convert (1) into an integral equation. This is accomplished by expanding $\begin{pmatrix} H_z \\ E_z \end{pmatrix}$ into a complete set of basis functions appropriate to each of the subregions above and below the strip (j=1,2, respectively), as

$$\begin{pmatrix} H_z^{(j)} \\ E_z^{(j)} \end{pmatrix} = \sum_{m,n} \begin{pmatrix} \overline{A}_{mn}^{(j)} & 0 \\ 0 & \overline{B}_{mn}^{(j)} \end{pmatrix} \begin{pmatrix} \psi_{mn}^{(j)} \\ \phi_{mn}^{(j)} \end{pmatrix} \qquad (j = 1,2)$$

where the $\bar{A}_{mn}^{(j)}$'s and $\bar{B}_{mn}^{(j)}$'s are as yet underminded coefficients.

For our geometry, $\psi_{mn}^{(j)}$ and $\phi_{mn}^{(j)}$ are just the TE and TM basis functions of a rectangular waveguide of height b_j, i.e.,

$$\psi_{mn}^{(j)}(x,y) = \left[\frac{2}{ab_j}\right]^{\frac{1}{2}} \cos\left[\frac{m\pi}{2a}(x+a)\right]\cos\left[\frac{n\pi y}{b_j}\right]$$

and

$$\phi_{mn}^{(j)}(x,y) = \left[\frac{2}{ab_j}\right]^{\frac{1}{2}} \sin\left[\frac{m\pi}{2a}(x+a)\right]\sin\left[\frac{n\pi y}{b_j}\right] \quad .$$

These basis functions also satisfy (1) but with known eigenvalues

$$K_{mn}^{(j)} = \left[\left(\frac{m\pi}{2a}\right)^2 + \left(\frac{n\pi}{b_j}\right)^2\right]^{\frac{1}{2}} \quad .$$

They do not, except in the rather trivial case of an unperturbed rectangular waveguide mode, satisfy the same continuity conditions as the unknowns $\begin{pmatrix} H_z \\ E_z \end{pmatrix}$ in the gap regions. We can still expand $\begin{pmatrix} H_z \\ E_z \end{pmatrix}$ in terms of these basis functions, however, since $\partial_n H_z$ or E_z need not be uniformly convergent at $y = 0$. In this case the limit $y \to 0$ cannot be taken inside the appropriate expansion. See [21] for a discussion of this phenomenon.

Using the orthogonality properties of the basis functions to solve for the unknown expansion coefficients, applying Green's theorem, and matching boundary conditions in the gap regions, results in the following integral equations for the TE and TM modes, respectively.

$$\int_w^a E_x(x',0)G^{TE}(x,x')dx' = 0 \tag{2}$$

and

$$P\int_w^a \partial_{x'}E_z(x',0)G^{TM}(x,x')dx' = 0 \quad . \tag{3}$$

174

where P denotes that the integral is to be interpreted in the principal value sense, $E_x(x,y) \propto \partial_y H_z(x,y)$, and the kernels G^{TE} and G^{TM} which contain the unknown eigenvalues K_{TE} and K_{TM} are given by

$$G^{TE}(x,x') = \sum_{j=1}^{2} \sum_{m,n} \Delta_m \Delta_n \frac{\psi_{mn}^{(j)}(x,0)\psi_{mn}^{(j)}(x',0)}{[K_{TE}^2 - K_{mn}^{(j)2}]} \qquad (4)$$

and

$$G^{TM}(x,x') = \sum_{j=1}^{2} \frac{\partial}{\partial y} \left\{ \sum_{m,n} \frac{K_{on}^{(j)}}{K_{mo}^{(j)}} \frac{\phi_{mn}^{(j)}(x,y)\psi_{mn}^{(j)}(x',0)}{[K_{TM}^2 - K_{mn}^{(j)2}]} \right\} \bigg|_{y=0} \qquad (5)$$

where

$$\Delta_i = \begin{cases} \dfrac{1}{2} & i = 0 \\ 1 & i > 0 \end{cases}.$$

The symmetry about the y-axis allows the integrations appearing in (2) and (3) to be written only over the one gap from $x = w$ to a and permits a decomposition of the TE and TM polarizations into even and odd modes. This is manifest in the summations on "m" in (4) and (5). For TE modes with odd symmetry, i.e., $H_z(x,y) = -H_z(-x,y)$, (4) is summed over odd values, while for TM modes with odd symmetry, i.e., $E_z(x,y) = -E_z(-x,y)$, (5) is summed over even values. The reverse is true for modes with even symmetry.

III. EXTRACTION OF THE SINGULAR PARTS OF THE KERNEL FUNCTIONS

The summations on "n" in (4) and (5) can both be summed exactly using the residue series technique [22]. The derivative in (5) can then be taken and when evaluated at $y = 0$ one finds

$$G^{TE}(x,x') = \sum_{j=1}^{2} \frac{b_j^2}{2\pi} \sum_m \frac{\Delta m \cot \pi \gamma_m^{(j)}}{\gamma_m^{(j)}} \psi_{mn}^{(j)}(x,0) \psi_{mn}^{(j)}(x',0) \qquad (6)$$

and

$$G^{TM}(x,x') = -\frac{\pi}{2} \sum_{j=1}^{2} \sum_m \frac{\Gamma_m^{(j)} \cot \pi \Gamma_m^{(j)}}{K_{mo}^{(j)2}} \partial_x \psi_{mn}^{(j)}(x,0) \psi_{mn}^{(j)}(x',0) \qquad (7)$$

where

$$\gamma_m^{(j)} = \frac{b_j}{\pi} [K_{TE}^2 - K_{mo}^{(j)2}]^{\frac{1}{2}} \qquad (8)$$

and

$$\Gamma_m^{(j)} = \frac{b_j}{\pi} [K_{TM}^2 - K_{mo}^{(j)2}]^{\frac{1}{2}} . \qquad (9)$$

Although the summations on "m" in (6) and (7) cannot be done in closed form, we can extract the singular part in each sum by replacing the coefficients in front of the basis functions by their asymptotic form for large "m", i.e.,

$$\frac{\cot \pi \gamma_m^{(j)}}{\gamma_m^{(j)}} \sim -\left(\frac{2a}{b_j}\right) \frac{1}{m}$$

and

$$\Gamma_m^{(j)} \cot \pi \Gamma_m^{(j)} \sim \left(\frac{b_j}{2a}\right) m .$$

The kernels will then consist of two parts, a singular part $\bar{G}$ which can be summed in closed form (see, e.g., [22]) and a correction series $\hat{G} = G - \bar{G}$. Recognizing that the summations on "m" are either over even or odd indices, four cases need to be considered. These are not independent, however, since it is easily verified that

176

$$\tilde{G}^{TM}(x,x') = \partial_x \tilde{G}^{TE}(x,x') \tag{10}$$

Thus, only the kernels for the TE polarization are needed, i.e.,

$$\tilde{G}^{TE}_{odd} = \frac{1}{\pi} \ln\left[\tan \frac{\pi}{4a}|t+t'|\tan \frac{\pi}{4a}|t-t'|\right] \tag{11}$$

and

$$\tilde{G}^{TE}_{even} = \frac{1}{\pi} \ln\left[4 \sin \frac{\pi}{2a}|t+t'|\sin \frac{\pi}{2a}|t-t'|\right] \tag{12}$$

where the following change of variables was introduced

$$t = a-x \tag{13}$$

and

$$t' = a-x'. \tag{14}$$

The singular kernels for the TM polarization can then be found using (10).

Although the correction series $\hat{G}$ cannot be summed in closed form, they are rapidly convergent and are given as

$$\hat{G}^{TE}(t,t') = \sum_m A_m \cos\left(\frac{m\pi t}{2a}\right)\cos\left(\frac{m\pi t'}{2a}\right) \tag{15}$$

and

$$\hat{G}^{TM}(t,t') = \sum_m B_m \sin\left(\frac{m\pi t}{2a}\right)\cos\left(\frac{m\pi t'}{2a}\right) \tag{16}$$

where

$$A_m = \sum_{j=1}^{2} \frac{b_j}{a\pi}\left(\frac{\Delta m \cot \pi\gamma_m^{(j)}}{\gamma_m^{(j)}} + \left(\frac{2a}{b_j}\right)\frac{(1-\delta_{mo})}{m}\right) \tag{17}$$

$$B_m = \sum_{j=1}^{2} \frac{-2}{mb_j}\left(\Gamma_m^{(j)}\cot\pi\Gamma_m^{(j)} - \left(\frac{b_j}{2a}\right)m\right) \tag{18}$$

177

and δ_{mo} is the Kroneker delta defined as

$$\delta_{mo} = \begin{cases} 1 & m = 0 \\ 0 & m \neq 0 \end{cases} \quad .$$

IV. SOLUTION OF THE SINGULAR INTEGRAL EQUATIONS

Having extracted the singular parts of both kernels we can move the nonsingular correction series to the right-hand sides of both integral equations and treat these terms as forcing terms. Since the singular parts of the kernels of (2) and (3) are related according to (10), it is convenient to differentiate (2) with respect to x. Both equations will then be of the same canonical form. In terms of the new variables defined in (13) and (14), (2) and (3) can be rewritten as follows

$$P \int_0^g U(t') \tilde{G}^{TM}(t,t')dt' = \int_0^g U(t') \partial_t \hat{G}^{TE}(t,t')dt' \tag{19}$$

and

$$P \int_0^g V(t') \tilde{G}^{TM}(t,t')dt' = -\int_0^g V(t') \hat{G}^{TM}(t,t')dt' \tag{20}$$

where

$$U(t') \equiv E_x(x',0)$$

and

$$V(t') \equiv \partial_{x'} E_z(x',0)$$

Equations (19) and (20) are both singular integral equations. The standard form of the singular integral equation, however, has integration limits -1 and +1 respectively. These limits can be achieved through the use of the Schwinger transformation [17]

178

$$\cos\left(\frac{\pi t'}{a}\right) = \alpha+\beta u \qquad (21)$$

and

$$\cos\left(\frac{\pi t}{a}\right) = \alpha+\beta v \qquad (22)$$

where

$$\alpha = \frac{1}{2}\left[\cos\left(\frac{\pi g}{a}\right) + 1\right]$$

and

$$\beta = \frac{1}{2}\left[\cos\left(\frac{\pi g}{a}\right) - 1\right] \quad .$$

Defining

$$T_v[F(u)] \equiv \frac{1}{\pi}P\int_{-1}^{1}\frac{F(u)du}{u-v}$$

and transforming to the new variables u and v defined in (21) and (22) we find that (19) and (20) can be rewritten in standard form as

$$T_v[F_{ij}(u)] = H_{ij}(v) \qquad (i,j = 1,2) \qquad (23)$$

where

$$F_{11}(u) = U(t')\cos\left(\frac{\pi t'}{2a}\right)\bigg/\sin\left(\frac{\pi t'}{a}\right)$$

$$F_{12}(u) = U(t')\bigg/\sin\left(\frac{\pi t'}{a}\right)$$

$$F_{21}(u) = V(t')\cos\left(\frac{\pi t'}{2a}\right)\bigg/\sin\left(\frac{\pi t'}{a}\right)$$

$$F_{22}(u) = V(t')\bigg/\sin\left(\frac{\pi t'}{a}\right)$$

$$H_{11}(v) = \int_{0}^{g}U(t')\partial_t\hat{G}^{TE}(t,t')dt'\bigg/2\sin\left(\frac{\pi t}{2a}\right)$$

$$H_{12}(v) = \int_{0}^{g}U(t')\partial_t\hat{G}^{TE}(t,t')dt'\bigg/\sin\left(\frac{\pi t}{a}\right)$$

$$H_{21}(v) = -\int_{0}^{g}V(t')\hat{G}^{TM}(t,t')dt'\bigg/2\sin\left(\frac{\pi t}{2a}\right)$$

and

$$H_{22}(v) = -\int_{0}^{g}V(t')\hat{G}^{TM}(t,t')dt'\bigg/\sin\left(\frac{\pi t}{a}\right) \quad .$$

In (23) the subscript "i" refers to the type of mode, TE or TM respectively, and the subscript "j" refers to the type of symmetry, odd or even respectively.

As shown in [17] (23) can be inverted exactly for the unknown $F_{ij}(v)$ as

$$F_{ij}(v) = \frac{1}{\sqrt{1-v^2}} \{C_{ij} - T_v[\sqrt{1-u^2}\ H_{ij}(u)]\} \qquad (24)$$

where the C_{ij}'s are constants to be determined.

In order to make use of (24) we need to express H_{ij} in terms of u. The most convenient expansion to use is one in terms of Chebyshev polynomials of the second kind U_n. In terms of these polynomials H_{ij} can be written as

$$H_{ij}(u) = \sum_{n=0}^{\infty} P_{ij,n}\ U_n(u) \qquad (25)$$

where the $P_{ij,n}$'s are expansion coefficients to be determined.

To express F_{ij} as a function of v we can use the following identity [23]

$$T_v[\sqrt{1-u^2}\ U_n(u)] = -T_{n+1}(v) \qquad (26)$$

where T_n is the Chebyshev polynomial of the first kind.

Thus, F_{ij} is given as

$$F_{ij}(v) = \frac{1}{\sqrt{1-v^2}} \{C_{ij} + \sum_{n=0}^{\infty} P_{ij,n} T_{n+1}(v)\}\ . \qquad (27)$$

V. DERIVATION OF THE SECULAR EQUATIONS

In order to complete the solution given in (27) we need to evaluate the unknown constants C_{ij} and $P_{ij,n}$. We begin by first expressing C_{ij} in terms of the $P_{ij,n}$'s. For the TM polarization this is accomplished by requiring

$$\int_w^a \partial_{x'} E_z(x',0)dx' = E(a,0) - E(w,0) = 0. \tag{28}$$

For the TE polarization, we substitute the solution given in (27) back into the undifferentiated form of the integral equation, i.e., eq. (2). As shown in Appendix 1, one then finds for C_{ij} the following

$$C_{ij} = -\frac{1}{R_{ij,0}} \sum_{m=0}^{\infty} R_{ij,m+1} \, P_{ij,m} \tag{29}$$

where

$$R_{11,m} = I_{11,m} - \frac{\pi}{4\Delta_m} \sum_{n=m}^{\infty} A_{2n+1} \, P_{mn}$$

$$R_{12,m} = I_{12,m} + \frac{\pi}{2\Delta_m} \sum_{n=m}^{\infty} A_{2n} q_{mn}$$

$$R_{21,m} = I_{21,m}$$

and

$$R_{22,m} = 0 \quad (m > 0) \quad .$$

I_{11}, I_{12}, and I_{21} are three canonical integrals, the recursion formulae for which, are derived in Appendix II. For modes with odd symmetry, the integrals I_{11} and I_{12} can be expressed in terms of complete elliptic integrals of modulus $\sqrt{\alpha}$ for the TE polarization and $\sqrt{-\beta}$ for the TM polarization, while for modes with even symmetry, I_{12} contains no special functions.

p_{mn} and q_{mn} are the coefficients of the following expansions

$$\frac{\cos(2n+1)\left(\frac{\pi t'}{2a}\right)}{\cos\left(\frac{\pi t'}{2a}\right)} = \sum_{m=0}^{n} p_{mn} \ T_m(u)$$

and

$$\cos\left(\frac{n\pi t'}{a}\right) = \sum_{m=0}^{n} q_{mn} \ T_m(u) \quad .$$

We are now in a position to substitute our solution for F_{ij} (expressed solely in terms of the unknown $P_{ij,n}$'s), back into the definition of the H_{ij}'s defined in (23). Upon matching coefficients of $U_n(v)$ we then obtain an infinite set of equations for the unknown $P_{ij,n}$'s. Setting the determinant of the coefficients to zero we obtain the secular equation from which K can be determined. The details of this procedure are outlined in Appendix III. Four infinite sets of equations are derived of which the following for the odd TM polarization is representative.

$$P_{22,m} = \frac{a\beta}{2} \sum_{n=m}^{\infty} \sum_{k=0}^{n} B_{2n+2} \ s_{mn} \ q_{k+1,n+1} \ P_{22,k} \qquad (30)$$

where s_{mn} is the coefficient in the following expansion

$$\frac{\sin[(n+1)\frac{\pi t}{a}]}{\sin\left(\frac{\pi t}{a}\right)} = \sum_{m=0}^{n} s_{mn} \ U_m(v) \quad .$$

Equation (30) is the simplest of the four equations given in Appendix III since $C_{22} = 0$ for this case only. Fortunately, however, these equations can be greatly simplified. In most cases, only a few of the A_m's or B_m's, given respectively in (15) and (16), are significant, and thus the infinite matrix equations given in Appendix III reduce to equations of very small order. The number

of A_m's or B_m's that we must keep depends upon the number of higher order modes that we allow to propagate. We can see from (8) or (9) that once "m" becomes large enough so that $K_{mo} > K_{TE}$ or K_{TM}, respectively, then $\gamma_m^{(j)}$ or $\Gamma_m^{(j)}$ becomes imaginary. The cotangents then in (15) or (16) can be replaced by hyperbolic cotangents and thus the succeeding A_m's or B_m's become negligibly small. Thus, we can truncate our infinite matrix equation to a finite one at the sacrifice of being able to calculate all of the higher order modes. We will only find those modes for which K_{TE} or $K_{TM} \lesssim K_{Mo}$ where we have truncated the matrix to one of the finite order M.

In many applications (e.g., [24]) one is only interested in the first few higher order modes. This method is especially applicable for finding these modes since we can usually truncate the matrices to matrices of order one. In this case, (30) reduces to

$$1 = \frac{a\beta^2}{2} B_2 \tag{31}$$

since $s_{00} = 1$ and $q_{11} = \beta$. Substituting for B_2 from (16) we then find the following secular equation for the odd TM modes

$$\sum_{j=1}^{2} \frac{a\Gamma_2^{(j)}}{2b_j} \cot \pi \Gamma_2^{(j)} = 1 - \frac{1}{\beta^2} \tag{32}$$

where $\Gamma_2^{(j)}$ was defined in (8). Similarly, for the even TM modes we find

$$\sum_{j=1}^{2} \frac{a\Gamma_1^{(j)}}{b_j} \cot \pi \Gamma_1^{(j)} = \frac{2E - \alpha K}{2E - (1+\alpha)K} \qquad (\text{mod } \sqrt{-\beta}) \tag{33}$$

183

for the odd TE modes,

$$\sum_{j=1}^{2} \frac{b_j \cot \pi \gamma_1^{(j)}}{4a\gamma_1^{(j)}} = \frac{(1-\beta)K-2E}{2E+\beta K} \qquad (\text{mod } \sqrt{\alpha}) \qquad (34)$$

and for the even TE modes,

$$\sum_{j=1}^{2} \frac{b_j \cot \pi \gamma_0^{(j)}}{2a\gamma_0^{(j)}} = -\ln(-\beta) \qquad (35)$$

In (34) and (35) for the TE modes we have also made an additional approximation in neglecting all of the A_n's except A_1 and A_0 respectively in expressing C_{1j} in terms of the $P_{1j,n}$'s through (29).

The roots of the secular equations given in (32) through (34) were found using a simple bisection method. These data were then plotted in Figs. 2-4 which are graphs of the cutoff wavelengths of the first higher-order modes as a function of strip width. In these figures we have made the simplifying assumption that the strip is symmetrically located, i.e., $b_1 = b_2 = b$, and the mode designation refers to the limiting value to which the cut-off frequency reduces as the strip width goes to zero ($\beta \rightarrow -1$).

We have not plotted a similar curve from the data of the solution of (35). This equation shows an anomalous behavior for small gap. In this case $\gamma_0^{(j)}$ must tend to zero in order to balance the logarithmic divergence which occurs when $\beta \rightarrow 0$. Since $K_{TE} \propto \gamma_0^{(j)}$ we thus have a mode with no low-frequency cut-off. This is not the TEM mode, however, since it only exists in the limit of zero gap. Bräckelmann, et al [11] have also observed this phenomenon in their analysis of a rectangular line with finite thickness inner conductor.

184

VI. CONCLUSIONS

In addition to the higher-order modes whose cut-off wavelengths are plotted in Figs. 2-4, there are also some higher-order modes which are unperturbed by the presence of the inner conductor. If $b_1 = b_2 = b$, these modes are just the $TE_{m,2n}$ and $TM_{m,2n}$ modes of the full guide of cross-section $2a \times 2b$. Alternatively, we can view this system as two rectangular sub-waveguides of cross-section $2a \times b$ which are coupled through the gap. The sub-waveguide modes can then be combined to form a system mode of the entire structure which is either symmetric with respect to the inner conductor (i.e., $E_y(x,y) = E_y(x,-y)$ or antisymmetric. As found also in [27] only the symmetric combination is unperturbed by the presence of the inner conductor. If the inner conductor is offset then there exists fewer unperturbed modes.

Since the perturbed modes reduce to rectangular waveguide modes in the limit of either zero strip width ($\beta \to -1$) or zero gap ($\beta \to 0$) we can obtain approximate solutions for the cut-off wavelengths by replacing the cotangents and elliptic integrals in (32) to (34) by their asymptotic forms for beta either near 0 or -1. One can then find that the cut-off frequencies are perturbed as follows. For small strip widths

$$\delta^2_{TM_{11}} \propto 1/\ell n \left(\frac{8a}{\pi w}\right)$$

$$\delta^2_{TM_{21}} \propto \left(\frac{w}{a}\right)^2$$

and

$$\delta^2_{TE_{11}} \propto \left(\frac{w}{a}\right)^2$$

while for small gaps one finds

$$\delta^2_{TM_{11}} \propto \left(\frac{g}{a}\right)^2$$

$$\delta^2_{TM_{21}} \propto \left(\frac{g}{a}\right)^4$$

and

$$\delta^2_{TE_{11}} \propto 1/\ell n \left(\frac{8a}{\pi g}\right)$$

where

$$K^2 - K^2_{unperturbed} \equiv \pm \left(\frac{\delta}{b}\right)^2 \quad .$$

The significance of the logarithmic perturbation of the cut-off wavelength of the TE_{11} mode for small gap and the TM_{11} mode for small strip width is apparent in Figs. 3 and 4. For any finite gap width or strip width, respectively, the perturbation is quite significant. Thus, in contrast to the other cases for which the perturbation is algebraic, the cut-off frequencies are not accurately predicted by their unperturbed values. This same type of logarithmic or algebraic behavior was found by [8] in an analysis of a related problem of two rectangular waveguides coupled through a longitudinal slot.

In reference [11] are plotted similar curves for the case of a thick center conductor. The curves show the same qualitative behavior as a function of strip width. In particular, the cut-off wavelength of the TE_{11} mode for a small gap tends to be that of a "coaxial TE_{10} mode" in each sub-waveguide.

Although we have only presented the numerical results for a one-term approximation to the secular equations, higher-order solutions can be easily found, since the canonical integrals needed in the computation of the matrix elements are given recursively. For example, if we keep two of the B_m's in the expression for the secular equation for the odd TM mode, (30) reduces to

186

$$\left(1 - \frac{a\beta^2}{2} B_2\right) \left(1 - \frac{a\beta^4}{2} B_4\right) = 0 \quad . \tag{36}$$

The first term in (36) gives the same roots as we found earlier in our one-term approximation as given in (31). In addition, however, we have an extra term which gives rise to additional higher-order modes. One can see how continuing this process would ultimately recover all of the higher-order modes.

VII. ACKNOWLEDGMENTS

VIII. REFERENCES

[1] Crawford, M. L., Generation of standard EM fields using TEM transmission cells, IEEE Trans. Electromagnetic Compatibility, vol. EMC-16, pp. 189-195 (Nov. 1974).

[2] Belousova, L. I., and Sal'nikova, L. P., Computation of the cutoff frequencies of higher order modes in shielded symmetric stripline, Radiotekhnika (Khar'kov), No. 17, pp. 72-76 (1971).

[3] Shestopalov, V. P., The Method of Riemann--Hilbert Problems in the Theory of Diffraction and Propagation of Electromagnetic Waves, Izdat. Khar'kov. University (1971).

[4] Belousova, L. I., and Sal'nikova, L. P., Higher wave modes in a shielded nonsymmetrical strip line, Radio Eng. and Elect. Physics, Vol. 16, No. 7, pp. 1199-1202 (July 1971).

[5] Lerer, A. M., and Mikhalevskii, V. S., Using paired integral equations in certain problems involving the diffraction of waveguide modes by bodies of finite size, Radiophys. Quantum Electron., vol. 18, pp. 859-865 (1975).

[6] Mittra, R., and Itoh, T., A new technique for the analysis of the dispersion characteristics of microstrip lines, IEEE Trans. Microwave Theory Tech., vol. MTT-19, No. 1, pp. 47-56 (Jan. 1971).

[7] Davies, J. B., and Corr, D. G., Computer analysis of the fundamental and higher-order modes in single and coupled microstrip, Electronics Letters, Vol. 6, No. 25, pp. 806-808 (Dec. 1970).

[8] Garb, Kh. L., and Fridberg, I. Sh., Dispersional properties of a Rectangular waveguide, loaded in half-space by a narrow slot, in a wall of finite thickness, Radio Eng. and Elect. Physics. Vol. 19, No. 1 (1974).

188

[9]   Voytovich, N. N., Katsenelenbaum, B. Z., and Sivov, A. N., The excitation
      of a two-dimensional metal cavity with a small opening (slotted
      cylinder), Radio Eng. and Elect. Physics, Vol. 19, No. 12, pp. 8-17
      (Dec. 1974).

[10] Bezlyudova, M. M., Cut-off wavelength of waveguide-type oscillations in
      transmission lines having internal and external conductors of rectangular
      cross section, Radio Eng. and ELect. Physics, Vol. 8, No. 11, pp. 1727-
      1733 (Nov. 1963).

[11] W. Bräckelmann, D. Landmann and W. Schlosser, Die Grenzfrequenzen von
      Höheren Eigenwellen in Streifenleitungen, Arch Elek. Ubertragungstech.,
      Vol. 21, No. 3, pp. 112-120 (Mar. 1967).

[12] Gruner, L., Higher order modes in rectangular coaxial waveguides, IEEE
      Trans. MTT, Vol. MTT-15, No. 8, pp. 483-485 (Aug. 1967).

[13] Bräckelmann, W., Wellentypen auf der Streifenleitung mit rechteckigem
      Schirm, Arch. Elek. Ubertragungstech., Vol. 21, No. 12, pp. 641-647
      (1967).

[14] Pyle, J. R., The cutoff wavelength of the TE_{10} mode in ridged rectangular
      waveguide of any aspect ratio, IRE Trans. Microwave Theory Tech., Vol.
      MTT-14, No. 4, pp. 175-183 (April 1966).

[15] Collins, J. H., and Daly, P., Orthogonal mode theory of single ridge
      waveguide, J. Electronics and Control, vol. 17, pp. 121-129 (Aug. 1964).

[16] Cohn, S. B., Properties of ridge wave guide, Proc. IRE, pp. 783-788
      (Aug. 1947).

[17] Lewin, L., Theory of Waveguides, London: Newnes-Butterworths (1975).

[18] Chang, D. C., Equivalent-circuit representation and characteristics of
      a radiating cylinder driven through a circumferential slot, IEEE Trans.
      Ant. Prop. Vol. AP-21, No. 6, pp. 792-796 (Nov. 1973).

[19] Gladwell, G. M. L., and Coen, S., A Chebyshev approximation method for microstrip problems, IEEE Trans. MTT, vol. MTT-23, No. 11, pp. 865-870, (Nov. 1975).

[20] Chang, W., and Otto, D. V., Current distributions on electrically thick tubular antennas of limited length, Int. J. Electronics, Vol. 39, No. 4, pp. 393-413 (Apr. 1975).

[21] Friedman, B., Principles and Techniques of Applied Mathematics, New York: Wiley, p. 271 (1956).

[22] Collin, R. E., Field Theory of Guided Waves, New York: McGraw-Hill (1960).

[23] Tricomi, F.G., Integral Equations, New York: Interscience (1957).

[24] Tippet, J. C., Chang, D. C., and Crawford, M. L., An analytical and experimental determination of the cutoff frequencies of higher-order TE modes in a TEM cell, National Bureau of Standards Internal Report NBSIR 76-841 (June 1976).

[25] Gradshteyn, I. S., and Ryzhik, I. M., Table of Integrals Series and Products, New York: Academic Press (1965).

[26] Byrd, P. F., and Friedman, M. D., Handbook of Elliptic Integrals for Engineers and Physicists, Berlin: Springer-Verlag (1954).

[27] Kopp, E. H., Coupling between dissimilar waveguides, IEEE Trans. on MTT, Vol. MTT-16, No. 1, pp. 6-11 (Jan. 1968).

APPENDIX 1. EXPRESSION FOR C_{ij} IN TERMS OF $P_{ij,n}$

We begin with the odd TM Polarization and transform (28) into an equation in terms of u as follows

$$\int_w^a \partial_{x'} E_z(x',0)dx' = \int_0^g V(t')dt' = \int_{-1}^1 F_{22}(u)du = 0 \qquad (1.1)$$

If we now substitute for $F_{22}(u)$ from (27), we obtain

$$C_{22} \int_{-1}^1 \frac{du}{\sqrt{1-u^2}} = - \sum_{n=o}^\infty P_{22,n} \int_{-1}^1 \frac{T_{n+1}(u)du}{\sqrt{1-u^2}} \quad . \qquad (1.2)$$

The right-hand side of (1.2) vanishes because of the orthogonality property of the Chebyshev polynomials, i.e., [25]

$$\int_{-1}^1 \frac{T_m(u) \ T_n(u)du}{\sqrt{1-u^2}} = \frac{\pi}{2\Delta_m} \delta_{mn} \qquad (1.3)$$

where

$$\Delta_m = \begin{cases} \frac{1}{2} & m=0 \\ 1 & m>0 \end{cases}$$

Thus,

$$C_{22} = 0 \quad . \qquad (1.4)$$

For the even TM Polarization, we transform (1.1) into an equation in terms of a new variable χ defined as

$$\chi = \cos\left(\frac{\pi t'}{2a}\right) \qquad (1.5)$$

to obtain

$$\int_w^a \partial_{x'} E_z(x',0)dx' = 2\int_0^g F_{21}(u)\sin\left(\frac{\pi t'}{2a}\right)dt' = \frac{4a}{\pi}\int_{\sqrt{\alpha}}^1 F_{21}\left(\frac{2\chi^2-1-\alpha}{\beta}\right)d\chi=0.$$

If we now substitute for F_{21} from (27) we obtain

$$\int_{\sqrt{\alpha}}^1 \frac{C_{21}d\chi}{\sqrt{(1-\chi^2)(\chi^2-\alpha)}} = -\sum_{n=0}^\infty P_{21,n}\int_{\sqrt{\alpha}}^1 \frac{T_{n+1}\left(\frac{2\chi^2-1-\alpha}{\beta}\right)d\chi}{\sqrt{(1-\chi^2)(\chi^2-\alpha)}}$$

since

$$\sqrt{1-u^2} = -\frac{2}{\beta}\sqrt{(1-\chi^2)(\chi^2-\alpha)}$$

Defining $I_{21,n}$ as

$$I_{21,n} = \int_{\sqrt{\alpha}}^1 T_n\left(\frac{2\chi^2-1-\alpha}{\beta}\right)\frac{d\chi}{\sqrt{(1-\chi^2)(\chi^2-\alpha)}}$$

we find for C_{21} the following

$$C_{21} = -\frac{1}{I_{21,0}}\sum_{n=0}^\infty P_{21,n} I_{21,n+1} \tag{1.6}$$

Now for the odd TE polarization we transform (2) into an equation in terms of t and t', and without loss of generality, evaluate the resulting equation at $t = 0$ to obtain

$$\int_0^g U(t')\tilde{G}^{TE}(0,t')dt' = -\int_0^g U(t')\hat{G}^{TE}(0,t')dt' . \tag{1.7}$$

The left-hand side (L.H.S.) of (1.7) can be transformed into an equation in terms of the variable χ defined in (1.5) as follows

$$\tilde{G}(0,t') = \frac{1}{\pi}\ln\tan^2\frac{\pi t'}{4a} = \frac{1}{\pi}\ln\left(\frac{1-\chi}{1+\chi}\right) .$$

Thus,

$$\text{L.H.S.} = \frac{2}{\pi} \int_0^g F_{11}(u) \ln\left(\frac{1-\chi}{1+\chi}\right) \sin\left(\frac{\pi t'}{2a}\right) dt' = \frac{4a}{\pi^2} \int_{\sqrt{\alpha}}^1 F_{11}\left(\frac{2\chi^2-1-\alpha}{\beta}\right) \ln\left(\frac{1-\chi}{1+\chi}\right) d\chi$$

If we now substitute for F_{11} from (27) we obtain

$$\text{L.H.S.} = \frac{2a}{\pi^2} \int_{\sqrt{\alpha}}^1 \frac{\ln\left(\frac{1+\chi}{1-\chi}\right) d\chi}{\sqrt{(1-\chi^2)(\chi^2-\alpha)}} \left\{ C_{11} + \sum_{n=0}^{\infty} P_{11,n} T_{n+1}\left(\frac{2\chi^2-1-\alpha}{\beta}\right) \right\} . \qquad (1.8)$$

Defining $I_{11,n}$ as

$$I_{11,n} = \frac{1}{\pi} \int_{\sqrt{\alpha}}^1 T_n\left(\frac{2\chi^2-1-\alpha}{\beta}\right) \ln\left(\frac{1+\chi}{1-\chi}\right) \frac{d\chi}{\sqrt{(1-\chi^2)(\chi^2-\alpha)}}$$

we see that (1.8) reduces to

$$\text{L.H.S.} = \frac{2a\beta}{\pi} \left[C_{11} I_{11,0} + \sum_{n=0}^{\infty} P_{11,n} I_{11,n+1} \right] \qquad (1.9)$$

Now the right-hand side (R.H.S.) of (1.7) can be written in terms of u as follows

$$\text{R.H.S.} = -\int_0^g F_{11}(u) \frac{\sin\left(\frac{\pi t'}{a}\right)}{\cos\left(\frac{\pi t'}{2a}\right)} \sum_{n=0}^{\infty} A_{2n+1} \cos\left[(2n+1)\frac{\pi t'}{2a}\right] dt' =$$

$$= \frac{a\beta}{\pi} \sum_{n=0}^{\infty} A_{2n+1} \int_{-1}^1 F_{11}(u) \frac{\cos\left[(2n+1)\frac{\pi t'}{2a}\right]}{\cos\left(\frac{\pi t'}{2a}\right)} du.$$

If we now make use of the following expansion in terms of Chebyshev polynomials of the first kind T_m

193

$$\frac{\cos[(2n+1)\frac{\pi t'}{2a}]}{\cos(\frac{\pi t'}{2a})} = \sum_{m=0}^{n} P_{mn} T_m(u) \tag{1.10}$$

and substitute for $F_{11}(u)$ from (27) we find the following

$$R.H.S. = \frac{a\beta}{\pi} \sum_{n=0}^{\infty} \sum_{m=0}^{n} A_{2n+1} P_{mn} \int_{-1}^{1} \frac{T_m(u)du}{\sqrt{1-u^2}} [C_{11} + \sum_{k=0}^{\infty} P_{11,k} T_{k+1}(u)] . \tag{1.11}$$

The integrations in (1.11) can be evaluated by using the orthogonality relation given in (1.3) and thus (1.11) reduces to

$$R.H.S. = a\beta \sum_{n=0}^{\infty} A_{2n+1} [P_{on}C_{11} + \frac{(1-\delta_{no})}{2} \sum_{k=1}^{n} P_{11,k-1} P_{kn}] \tag{1.12}$$

where δ_{no} is the Kroneker delta. Finally (1.9) and (1.12) when equated and solved for C_{11} gives

$$C_{11} = \frac{-\left(\sum_{n=0}^{\infty} P_{11,n} I_{11,n+1} - \frac{\pi}{4} \sum_{n=0}^{\infty} A_{2n+1}(1-\delta_{no}) \sum_{k=1}^{n} P_{11,k-1} P_{kn}\right)}{\left(I_{11,0} - \frac{\pi}{2} \sum_{n=0}^{\infty} A_{2n+1} P_{on}\right)} . \tag{1.13}$$

For the even TE polarization we again start with (1.7), but we transform the left-hand side of that equation into an equation in terms of u as follows

$$\tilde{G}^{TE}(0,t') = \frac{1}{\pi} \ell n[(-2\beta)(1+u)]$$

Thus,

$$L.H.S. = -\frac{a\beta}{\pi^2} \int_{-1}^{1} F_{12}(u)\ell n[(-2\beta)(1+u)]du .$$

194

If we now substitute for $F_{12}(u)$ from (27) we obtain

$$\text{L.H.S.} = -\frac{a\beta}{\pi^2} \int_{-1}^{1} \frac{\ln[(-2\beta)(1+u)]du}{\sqrt{1-u^2}} \; [C_{12} + \sum_{n=0}^{\infty} P_{12,n} \; T_{n+1}(u)] \;. \quad (1.14)$$

Defining $I_{12,n}$ as

$$I_{12,n} = \frac{1}{\pi} \int_{-1}^{1} \frac{T_n(u)\ln(1+u)}{\sqrt{1-u^2}} \; du + \delta_{no} \; \ln(-2\beta)$$

we see that (1.14) reduces to

$$\text{L.H.S.} = -\frac{a\beta}{\pi} \; [C_{12} \; I_{12,0} + \sum_{n=0}^{\infty} P_{12,n} \; I_{12,n+1}] \;. \quad (1.15)$$

Now the right-hand side of (1.7) can be written in terms of u as follows

$$\text{R.H.S.} = -\int_{0}^{g} F_{12}(u) \; \sin\left(\frac{\pi t'}{a}\right) \sum_{n=0}^{\infty} A_{2n} \; \cos\left(\frac{n\pi t'}{a}\right) dt' =$$

$$= \frac{a\beta}{\pi} \sum_{n=0}^{\infty} A_{2n} \int_{-1}^{1} F_{12}(u) \; \cos\left(\frac{n\pi t'}{a}\right) du.$$

If we now make use of the following expansion

$$\cos\left(\frac{n\pi t'}{a}\right) = \sum_{m=0}^{n} q_{mn} \; T_m(u)$$

and substitute for $F_{12}(u)$ from (27) we find the following

$$\text{R.H.S.} = \frac{a\beta}{\pi} \sum_{n=0}^{\infty} \sum_{m=0}^{n} A_{2n} \; q_{mn} \int_{-1}^{1} \frac{T_m(u)du}{\sqrt{1-u^2}} \; [C_{12} + \sum_{k=0}^{\infty} P_{12,k} \; T_{k+1}(u)] . \quad (1.16)$$

195

Again, the integrations in (1.16) can be evaluated using the orthogonality

relation given in (1.3) to obtain

$$\text{R.H.S.} = a\beta \sum_{n=0}^{\infty} A_{2n} \left[q_{on} C_{12} + \frac{(1-\delta_{no})}{2} \sum_{k=1}^{n} P_{12,k-1} q_{kn} \right] \qquad (1.17)$$

Finally (1.15) and (1.17) when equated and solved for C_{12} gives

$$C_{12} = - \frac{\left[\sum_{n=0}^{\infty} P_{12,n} I_{12,n+1} + \frac{\pi}{2} \sum_{n=0}^{\infty} A_{2n} (1-\delta_{no}) \sum_{k=1}^{n} P_{12,k-1} q_{kn} \right]}{\left(I_{12,0} + \pi \sum_{n=0}^{\infty} A_{2n} q_{on} \right)} \qquad . (1.18)$$

Equations (1.4), (1.6), (1.13) and (1.18) can all be expressed in one

equation as

$$C_{ij} = - \frac{1}{R_{ij,0}} \sum_{m=0}^{\infty} R_{ij,m+1} P_{ij,m}$$

where

$$R_{11,m} = I_{11,m} - \frac{\pi}{4\Delta_m} \sum_{n=m}^{\infty} A_{2n+1} P_{mn}$$

$$R_{12,m} = I_{12,m} + \frac{\pi}{2\Delta_m} \sum_{n=m}^{\infty} A_{2n} q_{mn}$$

$$R_{21,m} = I_{21,m}$$

and

$$R_{22,m} = 0 \quad (m > 0)$$

APPENDIX 2. EVALUATION OF THE CANONICAL INTEGRALS

The canonical integrals appearing in (29) are defined by

$$I_{11,n} = \frac{1}{\pi} \int_{\sqrt{\alpha}}^{1} T_n\left(\frac{2\chi^2 - 1 - \alpha}{\beta}\right) \ell n\left(\frac{1+\chi}{1-\chi}\right) \frac{d\chi}{\sqrt{(1-\chi^2)(\chi^2-\alpha)}}$$

$$I_{12,n} = \frac{1}{\pi} \int_{1}^{1} \frac{T_n(u)\ell n(1+u)}{\sqrt{1-u^2}} \, du + \delta_{no}\ell n(-2\beta)$$

and

$$I_{21,n} = \int_{\sqrt{\alpha}}^{1} T_n\left(\frac{2\chi^2 - 1 - \alpha}{\beta}\right) \frac{d\chi}{\sqrt{(1-\chi^2)(\chi^2-\alpha)}}$$

The evaluation of I_{12} can be found in [19] and is given by

$$I_{12,n} = \begin{cases} \ell n(-\beta) & n = 0 \\ \dfrac{(-1)^{n+1}}{n} & n > 0 \end{cases}$$

The remaining two integrals can both be evaluated by recognizing that [25]

$$T_n(u) - T_{n+2}(u) = 2(1-u^2)U_n(u)$$

where

$$\sqrt{1-u^2} = \frac{-2}{\beta} \sqrt{(1-\chi^2)(\chi^2-\alpha)}$$

and

$$u = \frac{2\chi^2 - 1 - \alpha}{\beta}$$

197

Thus, if we take $I_{11,n} - I_{11,n+2}$ we can convert the integral into one for which the square root is now in the numerator. This integral can then be integrated by parts to obtain the following recursion relation

$$I_{11,n+2} = \frac{2\left(\frac{1+\alpha}{1-\alpha}\right)(2n+2) I_{11,n+1} - (2n+1) I_{11,n} + J_{11,n}}{(2n+3)} \qquad (i = 1,2) \qquad (2.1)$$

where

$$J_{11,n} = \frac{16}{\pi\beta^2} \int_{\sqrt{\alpha}}^{1} U_n\left(\frac{2\chi^2-1-\alpha}{\beta}\right)\left(\frac{\chi^2-\alpha}{1-\chi^2}\right)^{\frac{1}{2}} \chi \, d\chi$$

and

$$J_{21,n} = 0 .$$

J_{21} is zero because the integrand of I_{21} does not contain a logarithmic function as does I_{11}. The evaluation of J_{11} is easily accomplished by substituting

$$\chi^2 = \cos^2\theta + \alpha\sin^2\theta$$

to give

$$J_{11,n} = \frac{4}{\beta} (-1)^{n+1} .$$

The starting values for the recurrence relations given in (2.1) are given as [26]

$$I_{11,0} = K(\sqrt{\alpha})$$

$$I_{11,1} = \frac{1}{\beta}\left\{2[1+K(\sqrt{\alpha})-E(\sqrt{\alpha})] - (1+\alpha) K(\sqrt{\alpha})\right\}$$

$$I_{21,0} = K(\sqrt{-\beta})$$

and

$$I_{21,1} = \frac{1}{\beta} \left[2E(\sqrt{-\beta}) - (1+\alpha) \, K \, (\sqrt{-\beta}) \right]$$

where K and E are complete elliptic integrals of the first and second kind, respectively.

APPENDIX 3. DERIVATION OF THE INFINITE MATRIX EQUATIONS

The procedure for deriving the infinite matrix equations for the four cases, even and odd TE and TM, is basically the same. Therefore, we will derive only the odd TE case and quote the results for the remaining cases. We begin with the definition at H_{11} defined in (23), i.e.,

$$H_{11}(v) = \int_0^g U(t') \partial_t \hat{G}^{TE}(t,t') \, dt' \, /2\sin\left(\frac{\pi t}{2a}\right) \tag{3.1}$$

From the definition of $\hat{G}^{TE}$ given in (15) we can derive the following result

$$\frac{\partial_t \hat{G}^{TE}}{2\sin\left(\frac{\pi t}{2a}\right)} = \frac{\pi}{4a} \sum_{n=0}^{\infty} (2n+1)A_{2n+1} \cos\left(\frac{\pi t'}{2a}\right) \left\{ \frac{\sin[(2n+1)\frac{\pi t}{2a}]}{\sin\left(\frac{\pi t}{2a}\right)} \frac{\cos\,[(2n+1)\frac{\pi t'}{2a}]}{\cos\left(\frac{\pi t'}{2a}\right)} \right\}. \tag{3.2}$$

If we use the following expansion in (3.2),

$$\frac{\sin\,[(2n+1)\frac{\pi t}{2a}]}{\sin\left(\frac{\pi t}{2a}\right)} = \sum_{m=0}^{n} r_{mn} U_m(v)$$

insert (3.2) into (3.1), and use the expression for H_{11} given in (25) we obtain the following

$$\sum_{n=0}^{\infty} P_{11,n} U_n(v) = \frac{\pi}{4a} \sum_{n=0}^{\infty} \sum_{m=0}^{n} (2n+1)A_{2n+1} r_{mn} \int_0^g U(t')\cos\left(\frac{\pi t'}{2a}\right) \left\{ \frac{\cos[(2n+1)\frac{\pi t'}{2a}]}{\cos\frac{\pi t'}{2a}} \right\} dt' U_m(v) .$$

$$\tag{3.3}$$

We can now equate coefficients of $U_n(v)$ to obtain

$$P_{11,m} = \frac{\pi}{4a} \sum_{n=m}^{\infty} (2n+1)A_{2n+1} r_{mn} \int_0^g V(t') \cos\left(\frac{\pi t'}{2a}\right) \left\{ \frac{\cos[(2n+1)\frac{\pi t'}{2a}]}{\cos\left(\frac{\pi t'}{2a}\right)} \right\} dt' \tag{3.4}$$

If we now transform the integration in (3.4) from t' to u via (21) and use the expansion given in (1.10), we obtain the following

$$P_{11,m} = \frac{\beta}{4} \sum_{n=m}^{\infty} \sum_{k=0}^{n} (2n+1) A_{2n+1}\; r_{mn}\; P_{kn} \int_{-1}^{1} F_{11}(u)\; T_k(u)\; du \ . \qquad (3.5)$$

Next, we insert the expression for $F_{11}(u)$ given in (27) and note that the integration in (3.5) can be performed using the orthogonality relation given in (1.3). Equation (3.5) then reduces to the following

$$P_{11,m} = \frac{\pi\beta}{8} \sum_{n=m}^{\infty} \sum_{k=0}^{n} \frac{(2n+1)\; A_{2n+1}\; r_{mn}\; P_{kn}\; P_{11,k-1}}{\Delta_k}$$

where we have defined $P_{11,-1} \equiv C_{11}$.

The final step involves substituting for C_{11} from (29) with the result that

$$P_{11,m} = \frac{\pi\beta}{8} \sum_{n=m}^{\infty} (2n+1)\; A_{2n+1}\; r_{mn} \left[(1-\delta_{no}) \sum_{k=0}^{n-1} P_{k+1,n}\; P_{11,k} - \frac{2p_{on}}{R_{11,0}} \sum_{k=0}^{\infty} R_{11,k+1}\; P_{11,k} \right] \ .$$

$$(3.6)$$

Equation (3.6) is thus the infinite matrix equation desired. The following equations for the other three cases can be derived in an analogous manner.

$$P_{12,m} = \frac{\pi\beta}{2} \sum_{n=m}^{\infty} (n+1)\; A_{2n+2}\; s_{mn} \left[\sum_{k=0}^{n} q_{k+1,n+1}\; P_{12,k} - \frac{2q_{o,n+1}}{R_{12,0}} \sum_{k=0}^{\infty} R_{12,k+1}\; P_{12,k} \right]$$

$$P_{21,m} = \frac{a\beta}{4} \sum_{n=m}^{\infty} B_{2n+1}\; r_{mn} \left[(1-\delta_{no}) \sum_{k=0}^{n-1} P_{k+1,n}\; P_{21,k} - \frac{2p_{on}}{R_{21,0}} \sum_{k=0}^{\infty} R_{21,k+1}\; P_{21,k} \right]$$

and

$$P_{22,m} = \frac{a\beta}{2} \sum_{n=m}^{\infty} \sum_{k=0}^{n} B_{2n+2} \, s_{mn} \, q_{k+1,n+1} \, P_{22,k}$$

where we have made use of the following expansion

$$\frac{\sin\left((n+1)\frac{\pi t}{a}\right)}{\sin\left(\frac{\pi t}{a}\right)} = \sum_{m=0}^{n} s_{mn} \, U_m(v)$$
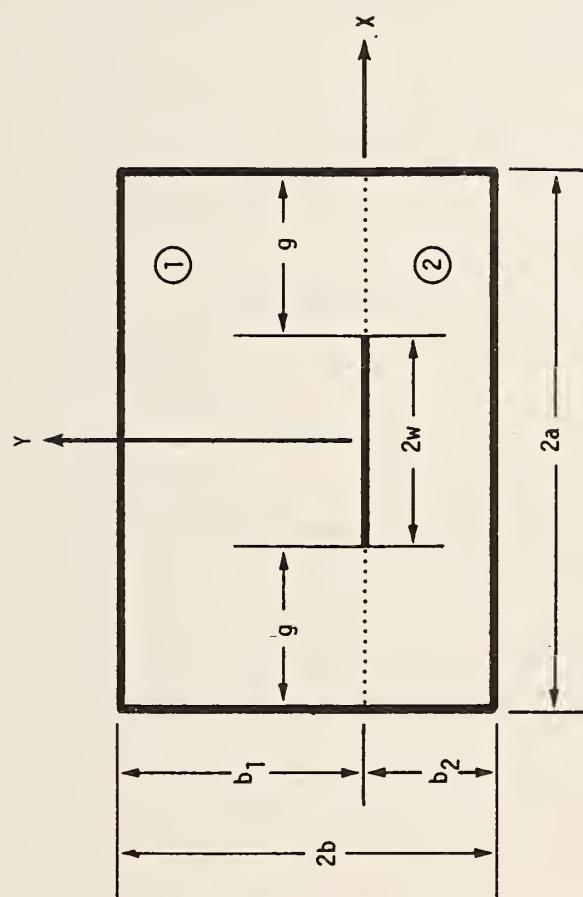
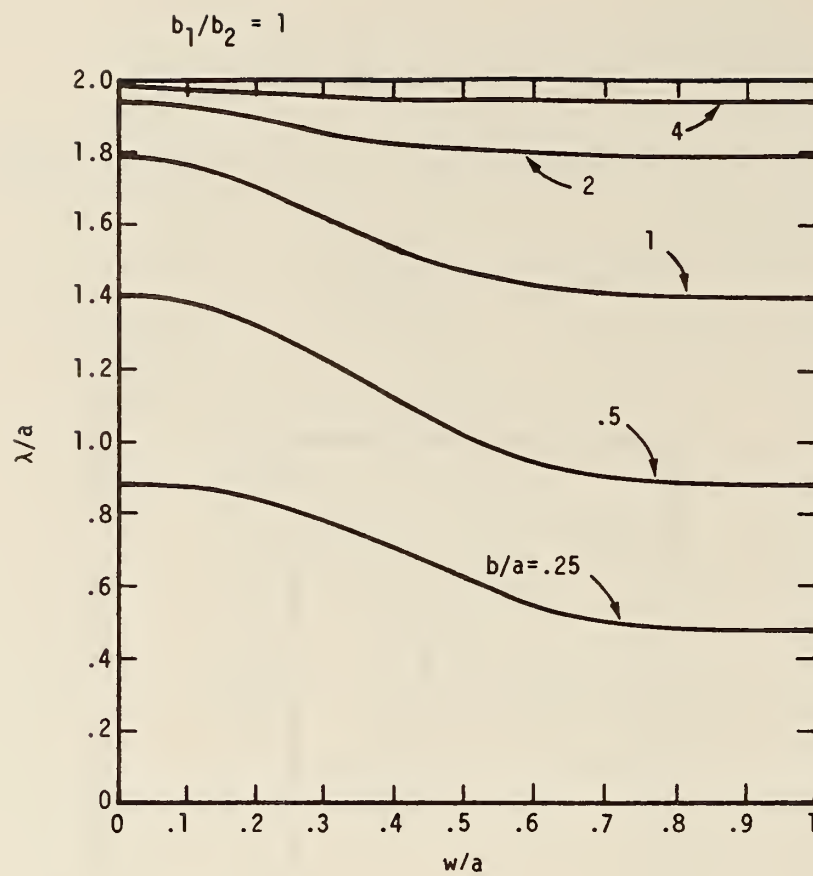Fig. 1. Cross Section of a rectangular coaxial line.

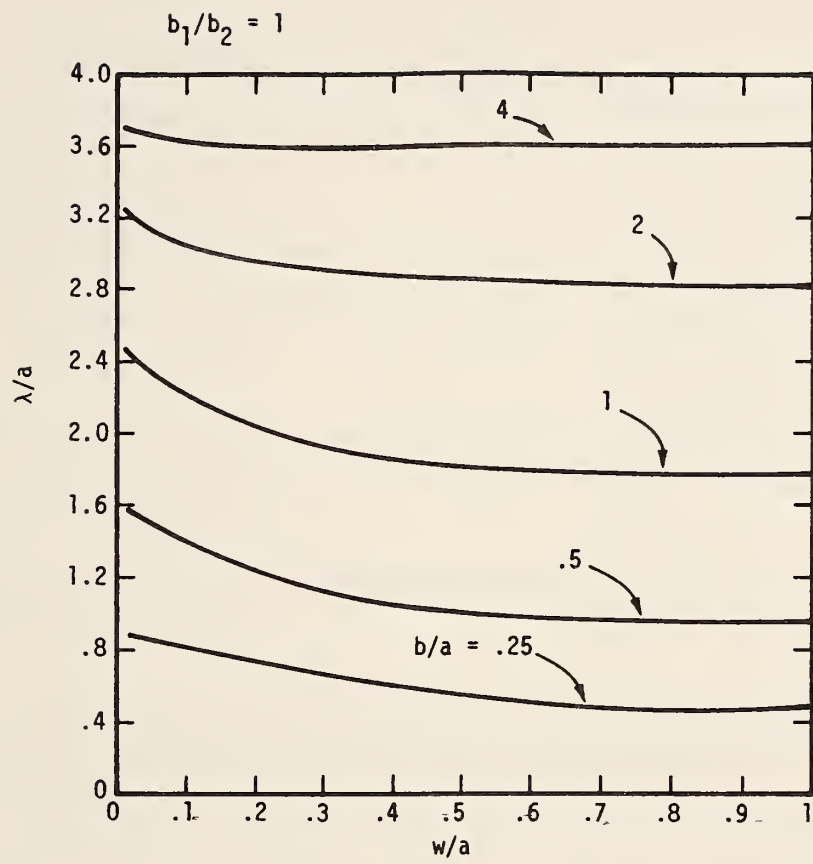Fig. 2. Cutoff wavelength vs. strip width of the TM$_{21}$ mode.

Fig. 3. Cutoff wavelength vs. strip width of the TM_{11} mode.
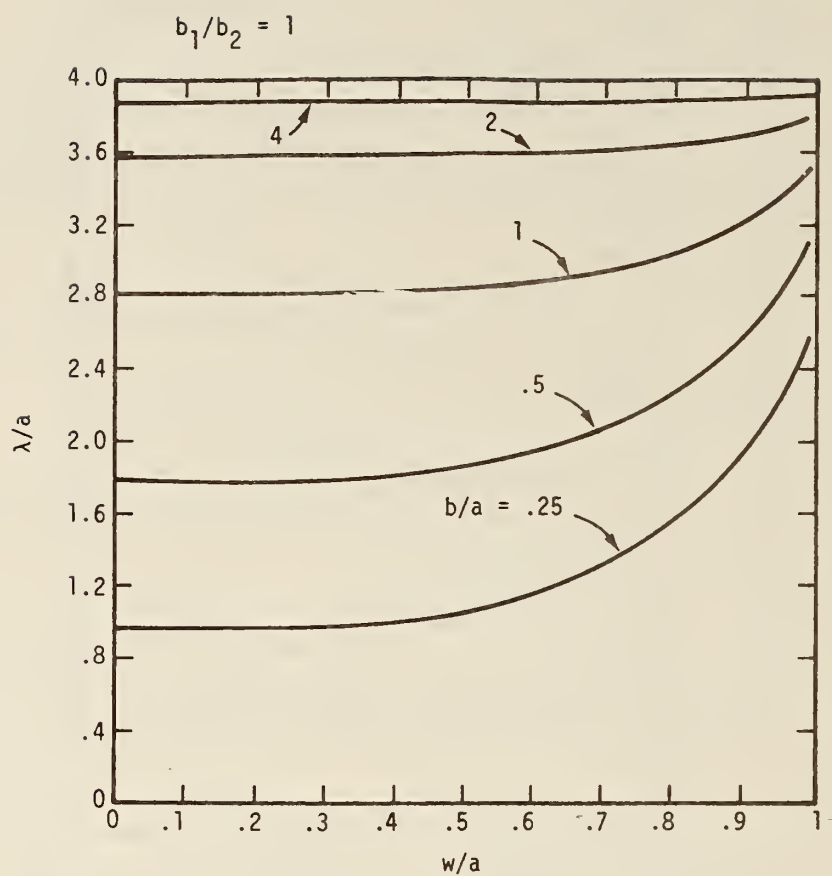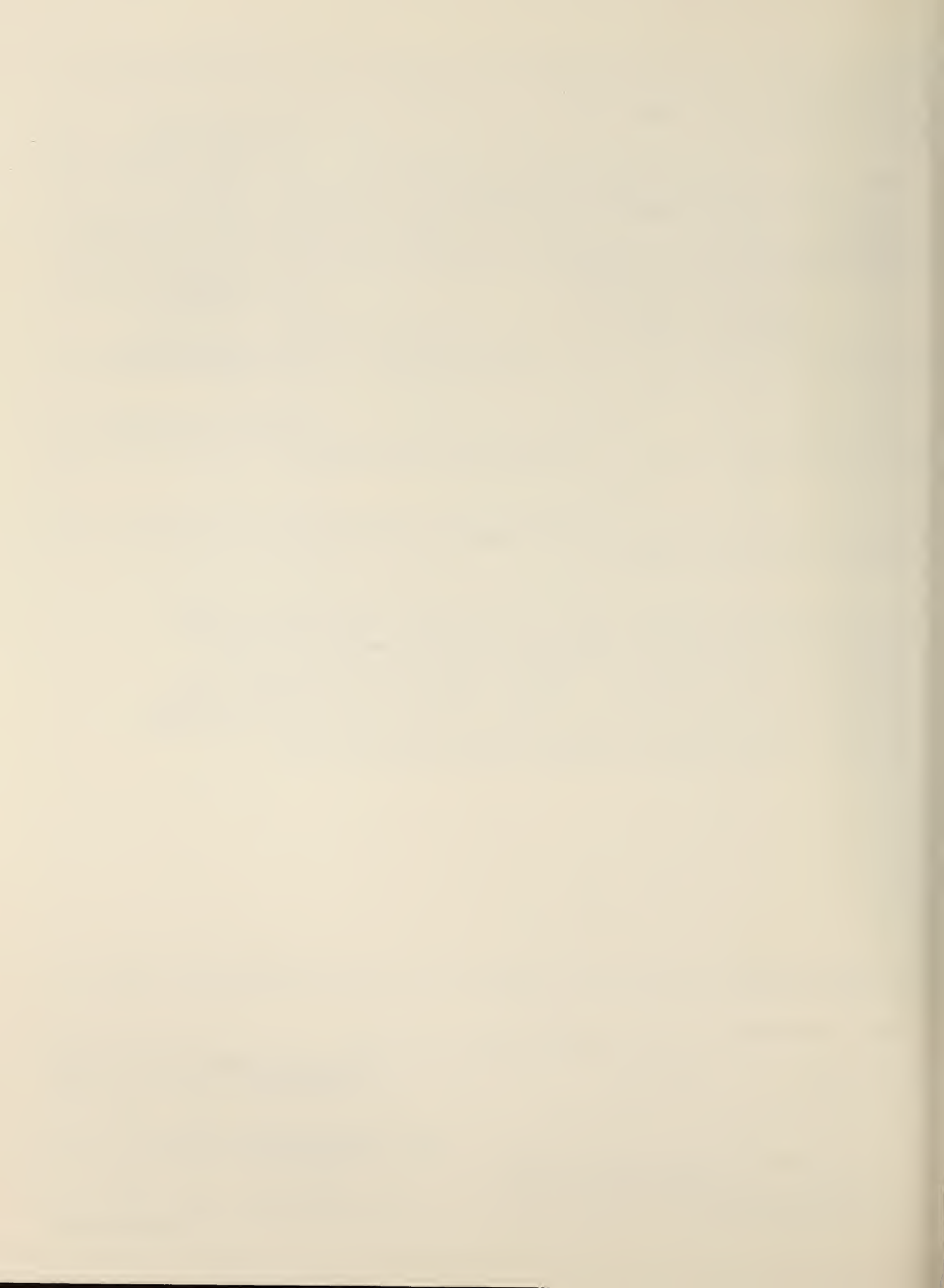
Fig. 4. Cutoff wavelength vs. strip width of the TE_{11} mode.

U.S. DEPT. OF COMM. BIBLIOGRAPHIC DATA SHEET	1. PUBLICATION OR REPORT NO. NBSIR 78-873	2. Gov't Accession No.	3. Recipient's Accession No.

4. TITLE AND SUBTITLE	5. Publication Date
Higher Order Modes in Rectangular Coaxial Line with Infinitely Thin Inner Conductor	March 1978
	6. Performing Organization Code 276.00

7. AUTHOR(S) John C. Tippet and David C. Chang	8. Performing Organ. Report No.

9. PERFORMING ORGANIZATION NAME AND ADDRESS	10. Project/Task/Work Unit No. 2763280
NATIONAL BUREAU OF STANDARDS DEPARTMENT OF COMMERCE WASHINGTON, D.C. 20234	11. Contract/Grant No. NOAACST-8393

12. Sponsoring Organization Name and Complete Address (Street, City, State, ZIP)	13. Type of Report & Period Covered
Same as #9.	14. Sponsoring Agency Code

15. SUPPLEMENTARY NOTES

16. ABSTRACT (A 200-word or less factual summary of most significant information. If document includes a significant bibliography or literature survey, mention it here.)

The singular integral equation approach is used to derive the secular equations for both TE and TM waves in a rectangular coaxial line with zero thickness inner conductor. Approximations for the secular equations are found that reduce to simple expressions in terms of well-known special functions (elliptic integrals). When the strip width is exceedingly small or nearly equal to the width of the outer conductor, closed form expressions for the cut-off frequencies can be found by replacing the elliptic integrals by their asymptotic forms for modulus either near zero or one.

17. KEY WORDS (six to twelve entries; alphabetical order; capitalize only the first letter of the first key word unless a proper name; separated by semicolons)

Higher order modes; rectangular coaxial line; striplines.

18. AVAILABILITY [X] Unlimited	19. SECURITY CLASS (THIS REPORT)	21. NO. OF PAGES
[ ] For Official Distribution. Do Not Release to NTIS	UNCLASSIFIED	42
[ ] Order From Sup. of Doc., U.S. Government Printing Office Washington, D.C. 20402, SD Cat. No. C13	20. SECURITY CLASS (THIS PAGE)	22. Price
[X] Order From National Technical Information Service (NTIS) Springfield, Virginia 22151	UNCLASSIFIED	$4.50

USCOMM-DC 29042-P74

Appendix J

Weil, C.; Gruner, L.   "High-order mode cutoff in rectangular striplines."

Short Papers

High-Order Mode Cutoff In Rectangular Striplines

CLAUDE M. WEIL, MEMBER, IEEE, AND LUCIAN GRUNER, MEMBER, IEEE

Abstract —The higher order mode cutoff characteristics of rectangular stripline structures, with thin center conductors, are discussed. Data are given, using an alternative method of presentation, on the normalized cutoff of the first eleven higher order modes. Discussions are included on the physical reasons why cutoff is altered for some modes, relative to that in rectangular waveguides, but not for others.

I. INTRODUCTION

Large-scale rectangular strip-transmission lines containing a propagating transverse electromagnetic (TEM) field are now widely used for such purposes as electromagnetic susceptibility and emissions testing, calibration of field probes and survey meters, and studies on the biological effects of radiofrequency (RF) radiation exposure. These structures are characterized by an air dielectric and a thin center conductor (septum) surrounded by a rectangularly shaped shield. This provides for an optimally sized test space within the line in which equipment, field probes, or experimental animals,·etc., are exposed to a well-defined and reasonably uniform field. Crawford [1] has discussed the properties of such lines and has described a family of TEM "cells" constructed at the National Bureau of Standards. These devices are commercially available and have been termed "Crawford Cells" or "TEM Transmission Cells" by their manufacturers.

The usable frequency range of these devices is of obvious importance to those involved in their use. Whereas it had been thought that these structures could not be used above the cutoff frequency where the first higher order mode is predicted to occur [2], it has recently been shown by Hill [3] that such is not necessarily the case. In his important study, Hill has shown that significant perturbation of the internal fields within the structure exists primarily at certain discrete frequencies where resonances of the higher order mode fields occur. Such resonances will occur when the equivalent electrical length of the strip-transmission line

$l_{(mn)}$ is equivalent to multiples of a half-guide-wavelength $\lambda_{g(mn)}/2$, for the particular higher order mode being considered, i.e.

$$l_{(mn)} = p\lambda_{g(mn)}/2; \quad p = 1,2,3,\cdots. \qquad (1)$$

The subscripts m, n denote the higher order mode. Substituting (1) into the well-known relationship for wavelength in waveguides

$$\frac{1}{\lambda^2} = \frac{1}{\lambda_{g^2}} + \frac{1}{\lambda_{c^2(mn)}} \qquad (2)$$

where $\lambda_{c(mn)}$ represents the cutoff wavelength value, gives an expression by which the various resonant frequencies $f_{R(mnp)}$ can be predicted

$$f_{R(mnp)}^2 = f_{c(mn)}^2 + \left(\frac{pc}{2l_{(mn)}}\right)^2 \qquad (3)$$

where $f_{c(mn)} = \dfrac{c}{\lambda_{c(mn)}}$; '$c$' is the velocity of light.

Note that the equivalent electrical length $l_{(mn)}$ given in (3) generally exceeds the actual physical length of the transmission line due to the presence of fringing fields at the line terminations. The magnitude of this difference varies with the mode being excited as well as the cross-sectional dimensions of the line and depends on whether the termination is abrupt (i.e., the line has a box-like shape with square ends) or gradual (tapered ends). Hill [3] was able to derive empirical values of l_{mn} for two different tapered cells, based on measured values of the resonant frequency $f_{R(mnp)}$. Attempts at predicting the fringing field correction are presently being undertaken in order to confirm the accuracy of Hill's empirical estimates.

To what extent these structures are usable when higher order mode resonances are present and whether or not they are usable at frequencies between such resonances depends very much on the particular application for which the transmission line is being used and the manner in which it is loaded (i.e., the composition and size of the object placed in the line). Some modes have been shown to interact strongly with any sizable load within the line while others interact little, owing to the differing field patterns of these modes. For some applications such as, for example, field-probe calibrations, it is possible to correct for the presence of the higher order mode fields by alternately positioning the probe on both sides of the center plate and averaging the two response curves versus frequency.

Accurate prediction of the various resonant frequencies in rectangular stripline structures using (3) requires a knowledge of the cutoff frequency $f_{c(mn)}$ for a number of the first higher order modes that can propagate in such structures. The purpose of this short paper is to review some of the existing data on this subject, as well as to present some additional data, as yet unpublished, in a form that is readily usable by those working with TEM-mode cells.

II. CUTOFF DATA

The higher order mode problem in rectangular coaxial structures (i.e., those with a center conductor of appreciable thickness) has been independently studied by Brackelmann et al. [4] and Gruner [5]. Baier [6] published additional data on cutoff in rectangular coaxial lines of varying dimensional parameters. More recently, Gruner [7] published data on the TE_{01} mode cutoff in rectangular lines with thin center conductors ($t/b \leqslant 0.1$ where 't' is the conductor thickness and 'b' is the vertical side-wall dimension; see Fig. 1). Details of the numerical techniques employed are provided in both of Gruner's papers and will not be further
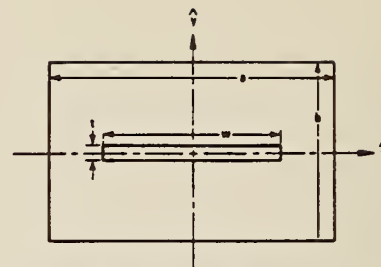
Fig. 1. Cross section of rectangular stripline structure.
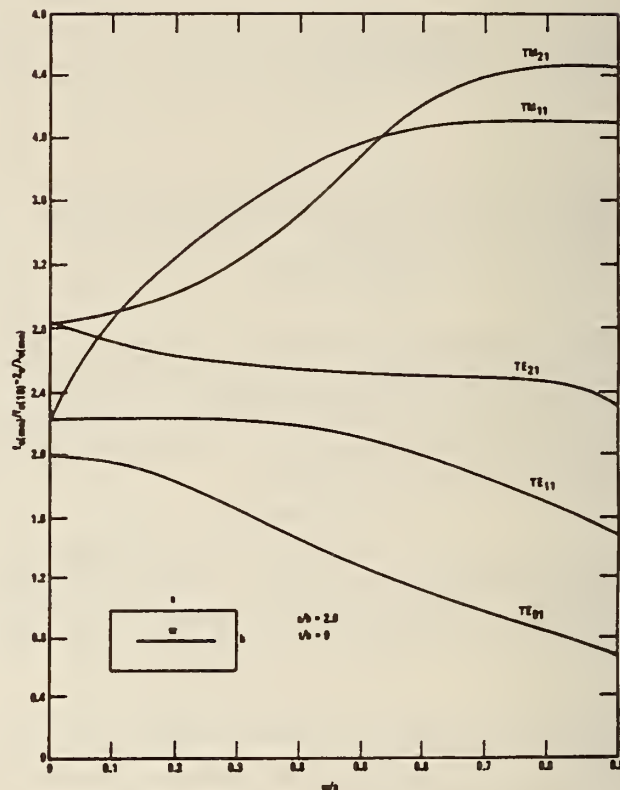
Fig. 2. Normalized cutoff frequency versus the parameter w/a for five of the altered modes (case $a/b = 2.0$, $t/b = 0$).

elaborated on here. Similar data for the TE_{11}, TM_{11}, and TM_{21} modes were published by Tippet and Chang [9] in a NBS report that has not been widely disseminated.

It has been shown [7], [9] that, for rectangular structures having a zero-thickness center conductor, the cutoff frequency for all modes with n-odd subscripts will be altered relative to that of its rectangular waveguide counterpart where no center conductor is present; i.e.

$$TE_{m,2n+1} \qquad (m,n = 0,1,2\cdots)$$
$$TM_{m,2n-1} \qquad (m,n = 1,2,3\cdots).$$

Cutoff for all of the remaining modes having n-even subscripts

$$TE_{m,2n} \qquad (m,n = 0,1,2\cdots, m \neq n \neq 0)$$
$$TM_{m,2n} \qquad (m,n = 1,2,3\cdots)$$

remain unchanged relative to that of their waveguide counterpart. The physical reasons for this effect are discussed in the next section. For the unaltered modes, the normalized cutoff frequency, relative to that of the dominant TE_{10} mode, can be conveniently
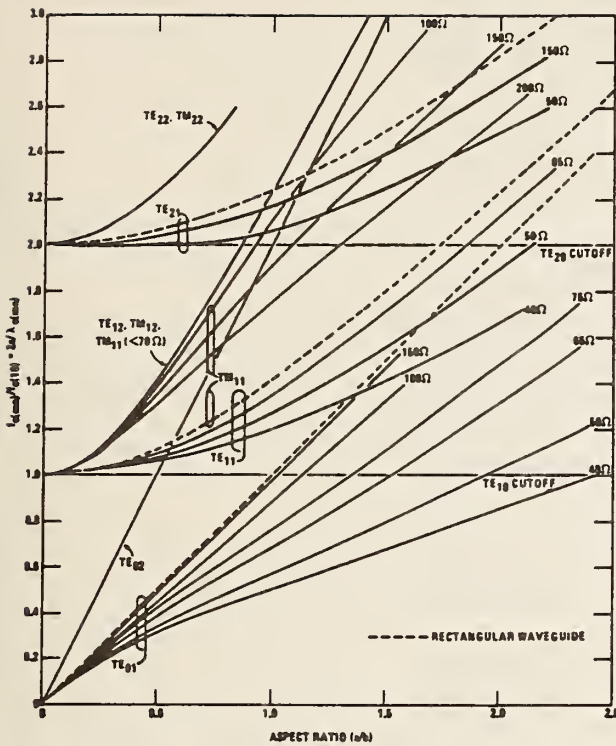
Fig. 3.   Normalized cutoff frequency versus a/b for the lowest higher order modes.

expressed as follows:

$$\frac{f_{c(mn)}}{f_{c(10)}} = \frac{2a}{\lambda_{c(mn)}} = \sqrt{m^2 + n^2 (a/b)^2} \qquad (4)$$

where 'a' is the horizontal width dimension; see Fig. 1. Of the modes where cutoff values are altered, the first four are of particular significance, namely the TE_{01}, TE_{11}, TE_{21}, and TM_{11} modes. Fig. 2 shows the normalized frequency cutoff ($f_{c(mn)}/f_{c(10)}$) versus the dimensional ratio w/a, where 'w' is the horizontal width of the center plate for five of the altered modes. These curves are shown for an aspect ratio value of $a/ib = 2.0$; changing the aspect ratio significantly alters the normalized cutoff values.

The curves of Fig. 2 represent the traditional manner in which cutoff data have been presented. This method of presentation is not optimal because, in practice, most rectangular striplines possess a fixed characteristic impedance, Z_0 (usually 50 Ω) but use differing aspect ratio values that cover the range $0.5 < a/b < 2$. It is felt that the data can be better interpreted if the normalized cutoff data are presented as a function of the aspect ratio over the range $0 \leqslant a/b \leqslant 2$ for various chosen values of Z_0. This has been done in Fig. 3 which shows normalized cutoff data for the four altered modes; seven of the unaltered modes are also included for comparison purposes. The dotted lines represent the limiting case for a rectangular waveguide with no center strip present. Additional higher order modes such as, for example, the TE_{03}, $TE_{04}, \cdots, TE_{13}, TE_{14}, \cdots, TE_{23}, TE_{24}, \cdots$, etc., are only significant for structures with $a/b < 0.5$ and have been omitted from Fig. 3 in order to avoid excessive detail. The curves of Fig. 3 were generated using the characteristic impedance data shown in Fig. 4, i.e., the required value of w/a could be determined for given values of Z_0 and a/b. The data of Fig. 4 were obtained
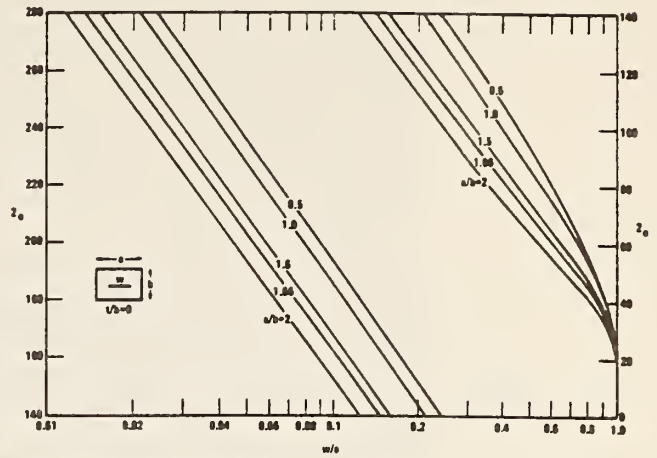
Fig. 4.   Characteristic impedance. Z_0 versus w/a for various a/b values (case $t/b = 0$).

using the technique described by Weil and includes a correction for the edge-interaction effect [10]. Note that the data given in Figs. 3 and 4 of Tippet and Chang [9] for the TE_{11} and TM_{11} cutoff agree well with the data shown in Fig. 3.

III. Discussion

The data presented in Fig. 3 show well how the presence of the center conductor in the rectangular structure alters the cutoff of certain modes relative to that in rectangular waveguide. It can be clearly seen that, for the three altered TE-modes (TE_{01}, TE_{11}, and TE_{21}), the cutoff frequencies are reduced, with the reduction increasing markedly as the characteristic impedance value is lowered. It is evident that, for a 50-Ω line, the first higher order mode is always the TE_{01} for $a/b \leqslant 1.94$.

Such effects are physically explainable as follows: for all of the TE-modes having even numbered values of the y-axis subscript 'n', there exists an electrical wall along the x-axis, parallel to the center conductor (see Fig. 1). This means that for the n-even case, the E-field level is zero along the x-axis and no capacitive coupling can exist between the center-strip edges and the vertical side walls. Consequently, the presence of the center strip does not alter cutoff for the n-even modes. For the TE-modes having n-odd subscripts, however, the reverse situation exists. A magnetic wall, where maximum E-field exists, is present along the x-axis. Capacitive coupling now exists between the center-strip edges and the vertical side walls that causes the structure to appear electrically larger in the vertical b-dimension than its actual physical dimension. Consequently, cutoff frequencies are lowered for these modes relative to their rectangular waveguide counterparts, as seen in Fig. 3.

The electrical enlargement of rectangular structures in the b-dimension is a useful concept for explaining the changes in the cutoff characteristics of the altered TE-modes. If b' represents the enlarged dimension (i.e., the vertical height of the equivalent rectangular waveguide without center strip), then, for the TE_{01} mode, the normalized cutoff frequency is given by

$$\frac{2a}{\lambda_{c(01)}} = \frac{a}{b'}. \qquad (5)$$

By inverting the TE_{01} cutoff data in Fig. 3, a plot of the normalized cutoff wavelength against b/a is obtainable, i.e., $\lambda_{c(01)}/2a = b'/a$ against b/a.

For lines with very low characteristic impedance ($Z_0 \to 0$), the center plate occupies an increasingly larger proportion of the rectangular width, a of the structure. For this case, the center strip coupling becomes large so that $b' \gg b$ and $a/b' \to 0$. Hence, from (4), it is evident that, for this case, $2a/\lambda_{c(01)} \to 0$ for all a/b. Similarly, for the cases of the TE_{11} and TE_{21} modes, it can be seen that $2a/\lambda_{c(11)} \to 1$ and $2a/\lambda_{c(21)} \to 2$ for all a/b. Both Gruner's and Baier's results for the rectangular coaxial line [5], [6] confirm the above.

Referring back to Fig. 3 again, it is apparent that, for the only altered TM-mode shown (TM_{11}), the cutoff frequency is increased. Whereas when no center conductor is present (waveguide case), the TM_{11} mode will always propagate before the TE_{21} mode, this situation generally becomes reversed when the center strip is present. For the case of a 50-Ω line, it is apparent that the TE_{21} cutoff is below that of the TM_{11} mode for all $a/b \geqslant 0.9$. Note that the presence of a relatively narrow center strip ($w/a < 0.2$) causes a marked increase in the TM_{11} cutoff, but that this increase does not exceed that corresponding to the TM_{12} cutoff. In fact, for lines with $Z_0 < \sim 70$ Ω, the TM_{11} cutoff is essentially the same as that for the TM_{12} mode. In this case, when the center conductor occupies an appreciable fraction of the width ($0.6a$ or more), it apparently acts as an electrical wall, causing the TM_{11} mode field structure to break up into a TM_{12} structure that contains an H-field null along the x-axis. These results are confirmed by Gruner's data [5] which show the curves for the TM_{11} and TM_{12} cutoff, as well as those for the TM_{21} and TM_{22} modes merging for values of $w/a > 0.6$.

ACKNOWLEDGMENT

REFERENCES

[1] M. L. Crawford, "Generation of standard EM fields using TEM transmission cells," *IEEE Trans. Electromagn. Compat.*, vol. EMC-16, no. 4, pp. 189–195, Nov. 1974.

[2] C. M. Weil, W. T. Joines, and J. B. Kinn, "Frequency range of large-scale TEM mode rectangular strip lines," *Microwave J.*, vol. 24, pp. 93–100, Nov. 1981.

[3] D. A. Hill, "Bandwidth limitations of TEM cells due to resonances," *J. Microwave Power*, vol. 18, no. 2, pp. 181–195, June 1983.

[4] W. Brackelmann, D. Landmann, and W. Schlosser, "Die Grenzfrequenzen von Hohren Eigenwellen in streifenleitungen," *Arkiv der Elektrischen Übertragung*, vol. 21, pp. 112–120, Mar. 1967.

[5] L. Gruner, "Higher-order modes in rectangular coaxial waveguides," *IEEE Trans. Microwave Theory Tech.*, vol. MTT-15, pp. 483–485, Aug. 1967.

[6] W. Baier, "Wellentypen in Leitungen aus Leitern rechteckigen Querschnitts (Modes in waveguides consisting of conductors of rectangular cross section)," *Arkiv der Elektrischen Übertragung*, vol. 22, no. 4, pp. 179–185, 1968. Portions of the above are also reproduced in: *Microwave Engineers Handbook*, T. S. Saad, Ed. Dedham, Mass: Artech House, 1971, vol. 1, pp. 145–146.

[7] L. Gruner, "Estimating rectangular coax cutoff," *Microwave J.*, vol. 22, pp. 88–92, Apr. 1979.

[8] J. C. Tippet, D. C. Chang, and M. L. Crawford, "An analytical and experimental determination of the cut-off frequencies of higher-order TE modes in a TEM cell," National Bureau of Standards Report NBSIR 76-841, June 1976. Available from NTIS, PB 256319.

[9] J. C. Tippet and D. C. Chang, "Higher order modes in rectangular coaxial line with infinitely thin inner conductor," National Bureau of Standards Report NBSIR 78-873, Mar. 1978.

[10] C. M. Weil, "The characteristic impedance of rectangular transmission lines with thin center conductor and air dielectric," *IEEE Trans. Microwave Theory and Tech.*, vol. MTT-26, pp. 238–242, Apr. 1978.

Appendix K

Hill, D. A. "Bandwidth limitations of TEM cells due to resonances."

Reprinted with permission from J. Microwave Power. 18(2):181-195; 1983.

Copyright (c) 1983 by the International Microwave Power Institute.

Bandwidth Limitations of TEM Cells due to Resonances

Douglas A. Hill[1]

ABSTRACT

The first eight to ten TE_{mnp} resonances have been identified in one large $(6.1 \times 7.3 \times 13.0$ m) and one small $(1.0 \times 0.6 \times 2.0$ m) TEM cell. The resonant frequencies fit a new equivalent coaxial box model with the effective length of the box depending on the mode. Weakly propagating TE_{mn} modes were also detected at frequencies above their respective first-resonance frequencies. A biological body or metal box at the center of the test zone interacts strongly with the TE_{10p} and TE_{11p} resonances, but not with the TE_{01p} resonances. These interactions cause bandwidth limitations in the use of TEM cells for bioeffects dosimetry studies, EMC testing, and probe calibration work.

I. INTRODUCTION

A TEM cell is a rectangular-coaxial transmission line sharply tapered at each end to form a closed cell. These cells are currently used for radiofrequency radiation dosimetry [1−5] and bioeffects [2, 6, 7] studies, for the calibration of field-strength meters [8−10], and for EMC testing of electronic equipment [11−13].

The center section of a TEM cell is a uniform-cross-section transmission line that will propagate a single TEM mode at all frequencies and a set of TE_{mn} and TM_{mn} higher-order modes at frequencies above their respective cut-off frequencies. Field patterns for the higher-order modes have been reported by Baier [14, 15] and the cut-off frequencies calculated by Baier [14, 15], Gruner [16−18], Crawford [8], and Tippet et al. [19, 20] using different methods. Weil et al. [6, 21] have reported possible evidence of a strongly propagating TE_{01} mode in two different TEM cells and have noted that this is consistent with Gruner's finding [17] that the TE_{01} mode is usually the first to propagate in a TEM cell.

The TEM mode propagates through the tapered ends of the cell without significant alteration. Each higher-order mode, however, is always reflected at some point within the taper where it becomes too small to propagate the mode. The propagating energy in the higher-order mode undergoes multiple reflections, end to end, within the cell until it is dissipated. At certain frequencies a resonance condition is satisfied, in which the cell's effective length for the mode is `p` half guide wavelengths long $(p = 1, 2, 3, \ldots)$. At these resonant frequencies, $f_{R(mnp)}$, a TE_{mnp} resonant field pattern exists. Thus the TE_{mn} mode in a given TEM cell has one cut-off frequency, $f_{c(mn)}$, associated with it and an infinite set of resonant frequencies, $f_{R(mnp)}$, with $p = 1, 2, 3, \ldots$. The same is true for the TM_{mn} higher-order modes, although these only occur at higher frequencies. While many of these resonances have been observed several times [11−13, 19, 22] and one has been calculated, neither of the first two resonances, TE_{011} and TE_{101}, have been properly identified or calculated to date.

This paper will identify, by resonant frequencies and field patterns, the first eight to ten TE_{mnp} resonances in two different TEM cells. Propagating higher-order modes will then be discussed. We will also report the interactions between the cell resonances and two test objects: a human body in a large $(6.1 \times 7.3 \times 13.0$ m) TEM cell used for dosimetry studies [5]; and a rectangular metal box in a small $(1.0 \times 0.6 \times 2.0$ m) TEM cell used for EMC studies (Narda Microwave model 8802).

The goal of this study is to determine the extent to which TEM cells may be used above the cut-off frequency of the first higher-order mode, $f_{c(01)}$. More specifically, $f_{c(01)}$ for the large cell is 15.2 MHz and it is desired to extend the usable frequency range as high as possible, to the ISM frequency of 27.12 MHz and perhaps even to 50 MHz in an attempt to measure the predicted peak absorption in a grounded person at about 47 MHz [23, 24].

Figure 1   Detection of the TE_{011} resonance at 20.70 MHz by swept-frequency measurements. (a) Electric field (E_b) at position B1. (Field components and positions are defined in Fig. 3 and the text). (b) Incident (I), transmitted (T), and reflected (R) power. Ordinate scales are linear in (a) electric field, or (b) power, but otherwise arbitrary.

II. RESONANCE ANALYSIS OF A LARGE TEM CELL

A. *Detection of Resonances*

The cell resonances were detected by swept-frequency measurements of electric field strength within the cell, and of reflected and transmitted power at the cell ends. As Crawford reported [8], filtering of second to fourth harmonics to levels at least 40 to 50 dB below the fundamental was found to be essential. Field-strength measurements were made using a dipole and loop, each 10 cm in size, of Greene's type [25] which use high-resistance leads to avoid RF pick-up problems. Electric-field measurements were found to be a reliable way of detecting all cell resonances, whereas reflected power (or input-port VSWR) and transmitted power (or insertion loss) were not. This is clearly illustrated in Figs. 1 and 2 where the detection of the first two cell resonances is shown. The strong resonance at 30.0 MHz, later shown to be the TE_{101} resonance, is not detected in the reflected and transmitted power measurements. If the strength of a resonance is defined by the peak-to-peak change in power or in the largest resonant E-field component, it was found that the first eight TE_{mnp} resonances could be better detected using E-field measurements than using power measurements; the signal-to-noise ratio is 20 to 30 dB larger. (The resonance at 20.7 MHz is 10 dB stronger for a different E-field component than shown in Fig. 1(a).) The four weakest of the first eight resonances were undetectable using power measurements.

B. *Identification of Resonances*

The first seven cell resonances were positively identified using two kinds of evidence, taken together: the measured resonances (and antiresonances) of the main component of the TEM-mode E field at selected sites in the transverse plane; and the comparison of measured and calculated resonant frequencies.

In order to understand the expected E-field pattern of the resonances the mode patterns for the higher-order modes are first compared to the TEM-mode field pattern in Fig. 3. That figure shows the more general case of a finite-thickness septum, while the septum is actually infinitesimally thick in
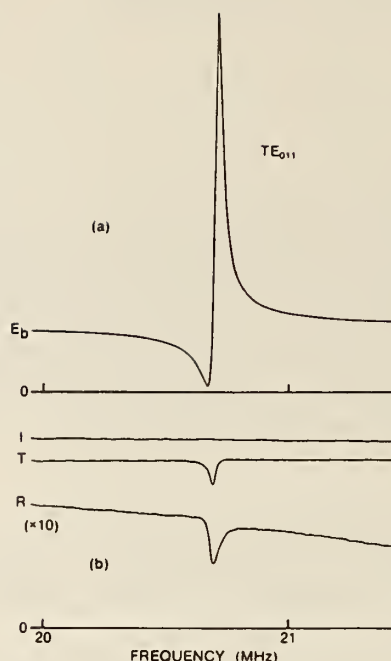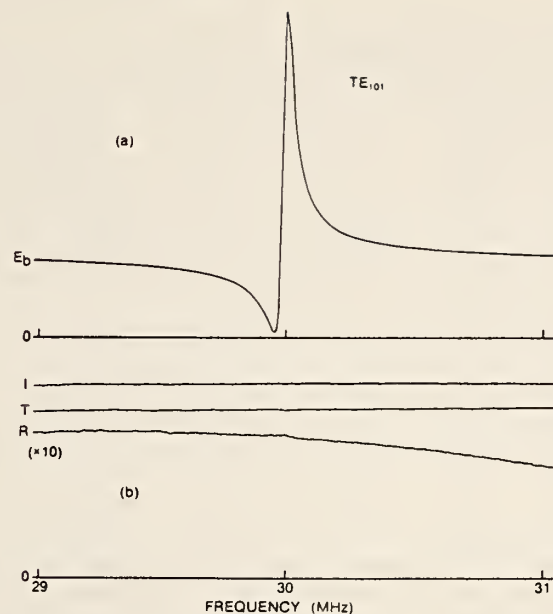
Figure 2 Detection of the TE_{101} resonance at 30.01 MHz by swept-frequency measurements. (a) Electric field (E_b) at position B1. (b) Incident (I), transmitted (T), and reflected (R) power.
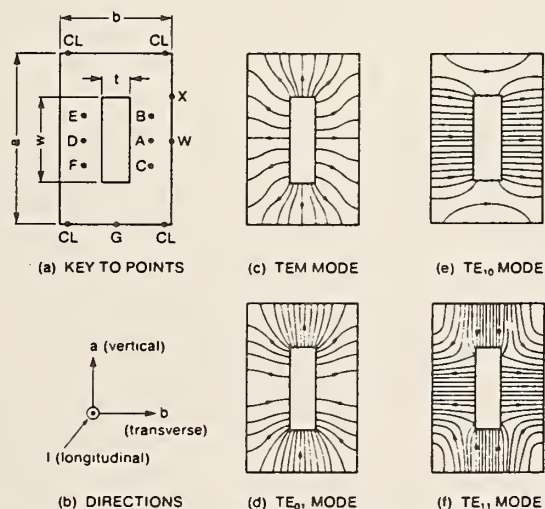
Figure 3 Cross-section of a rectangular-coaxial transmission line with a septum of finite thickness. Points and dimensions are defined in (a), and directions in (b). E-field patterns are sketched for the fundamental mode in (c), and accurately drawn (from [14]) for the first three higher-order modes in (d)−(f).

the two cells investigated. A number of reference points in the transverse plane are defined in Fig. 3(a): points A to F are all located midway between septum and wall; points A and D are also midway between the other two walls. Figure 3(b) also defines the directions a, b, and ℓ in the transmission line. The size of a cell will be denoted by its dimensions in the a, b, and ℓ directions, in that order. The ℓ dimension is the cell length, tip to tip. The use of the directions a, b, and ℓ, rather than directions in space, will facilitate intercomparison of results between TEM cells oriented differently in space (compare, for example, [5], [7], and [8]).

219

Table 1   Identification of resonances in the large (6.1 × 7.3 × 13.0 m) TEM cell from E-field and circumferential-current characteristics. Positions A0 to X1 are defined in the text

TE$_{mnp}$ resonance				Form of E_b resonance					Circumferential currents on floor and wall						Detected in VSWR or trans. power?	Largest E-field component	
				O	$\sqrt{\ }$R	$\bigwedge$λ			0 = zero; N = non-zero								
f_R (MHz)	m,	n,	p	A0	A1	B1	C1	E1	W0	W1	G0	G1	X0	X1		E_i	$\left(\dfrac{\Delta E_i}{E_b}\right)$
20.70	0	1	1	O	O	R	A	R	N	N	O	O	N	N	yes	E_a	16
31.51	0	1	2	O	O	R	A	R	O	N	O	O	O	N	no	E_a	3.1
42.06	0	1	3	O	O	A	R	A	N	N	O	O	N	N	no	E_a	1.3
30.01	1	0	1	R	R	R	R	A	O	O	N	N	N	N	no	E_b	4.0
40.98	1	0	2	O	A	A	A	R	O	O	O	N	O	N	yes	E_b	4.6
36.08	1	1	1	R	R	R	R	R	O	O	O	O	N	N	yes	E_b	11
47.2	1	1	2	O	R	R	R	R	O	O	O	O	O	N	yes	E_b	27
44.77	0	2	1*	O	O	R	A	A	N	N	N	N	N	N	no	E_a	1.8

*This identification not certain (see text).

The total E-field pattern due to the presence of some RF energy in a propagating higher-order mode can be qualitatively understood by adding (or subtracting) the pattern of the higher-order mode to (or from) the TEM-mode pattern. Thus, for example, when the TE$_{01}$ pattern is added to the TEM pattern, the relationships for E_b at the six points A to F become: $E_b(B) = E_b(E) > E_b(A) = E_b(D) > E_b(C) = E_b(F)$. Similarly, the addition of the TE$_{10}$ pattern to the TEM pattern results in the relationships $E_b(A) > E_b(B) = E_b(C) > E_b(D) > E_b(E) = E_b(F)$.

Returning now to the resonances in a transmission line of finite length, the fields at the points A to F will depend not only on the mode but also on the longitudinal position in the cell. For example, when two half guide wavelengths of a TE$_{mn}$ mode equals the cell length, the TE$_{mn2}$ standing wave pattern is created, which has an E-field null at the mid-point of the cell, and is not detectable there. In assessing E-field patterns, it was found useful to employ positions located either 0 meters (A0, B0...X0) or 1 m (A1, B1,...X1), approximately 0.1 λ, towards the load from the cell center.

It was also found very useful to measure the wall currents associated with the resonances. They were determined by measuring the H fields parallel to the metal walls and using the well known boundary condition that the tangential H field is equal to the surface current density in the perpendicular direction. (Surface charges and current patterns for the case of higher-order modes propagating in circular coaxial transmission lines have been well illustrated by King et al. [26].) For example, for the TE$_{011}$ resonance, the maximum charge on the wall (maximum concentration of E-field lines) is at position G0 and there is no surface charge at W0. The current maximum, however, occurs at W0 a quarter of a cycle later, and a current null occurs at G0. Similarly, the TE$_{101}$ resonance has a current null at W0 and a maximum at G0, while the TE$_{111}$ resonance has a current null at both W0 and G0. For the $p = 2$ resonances, similar results to the above occur at the positions W1 and G1, and the currents at W0 and G0 are all zero regardless of the mode.

The measured E fields and wall currents at the resonant frequencies are characterized in Table 1. The frequency evidence for this identification of the resonances is given in Table 2. All the observations in Table 1 for the TE$_{01p}$, TE$_{10p}$, and TE$_{11p}$ resonances can be shown to agree with the theoretical expectations from the kind of arguments illustrated above. The results for the TE$_{021}$ resonance likely fit the theoretical expectations as well, but this is not certain because a drawing of the TE$_{02}$ mode pattern has not been published.

The only theoretical ambiguity in identifying resonances is that the pattern of E-field resonances (R) and antiresonances (A) may be inverted when the phase of the higher-order mode with respect to the TEM mode is inverted. For example, the pattern of R,A,R for the positions B1, C1, and E1 for the TE$_{011}$ and TE$_{012}$ resonances is inverted into A,R,A for the TE$_{013}$ resonance.

Apart from the above theoretical ambiguity, the E-field and current characteristics listed in Table 1 are universal characteristics for all TEM cells of any size or shape. The currents at X1 are all non-zero, as expected theoretically. The same is true for the four positions marked CL in Fig. 3(a). In a future paper, we will report on an attempt to suppress the resonances by cutting the cell longitudinally at the four cutting lines, CL, in order to eliminate the circumferential currents that

Table 2 Identification of resonances in the large (6.1 × 7.3 × 13.0 m) TEM cell from the resonant frequencies, $f_{R(mnp)} \leq 53$ MHz

Higher-order mode					Resonance					
Type TE$_{mn}$ or TM$_{mn}$:	$f_{c(mn)}$ (MHz)		X_{mn}	$\left(\dfrac{c}{2L_{mn}}\right)$	Type TE$_{mnp}$ or TM$_{mnp}$		$f_{R(mnp)}$ (MHz)			
	Waveguide formula [7]	Series expansion [16, 27]					Calculated using			
m n			(±0.02)	(MHz)	m n p		L_0†	L_{mn}	Measured
TE					TE				
0 1	20.5*	15.2	0.74	13.7	0 1 1		22.1	20.5	20.70
					0 1 2		35.4	31.3	31.51
					0 1 3		50.3	43.8	42.06
1 0	24.6	24.6	0.45	16.6	1 0 1		29.3	29.7	30.01
					1 0 2		40.4	41.3	40.98
1 1	32.0*	31.3	0.35	17.9	1 1 1		35.2	35.9	36.08
					1 1 2		44.8	47.4	47.2
0 2	41.0	41.0	0.34	18.0	0 2 1		44.0	44.8	44.77
2 1	53.3*	45.4	—∮	—	2 1 1		48.1	—	—
1 2	47.8	47.8	—	—	1 2 1		50.4	—	—
2 0	49.2	49.2	—	—	2 0 1		51.7	—	—
TM					TM‡				
1 1	32.0*	47.5	1.00	11.6	1 1 1		50.1	48.9	48.9
1 2	47.8	47.8	—	—	1 2 1		50.4	—	—

*Figures known wrong but shown for comparison purposes.

†$L_0 = L_c + 0.5 L_E$. $\left(\dfrac{c}{2L_0}\right) = 16.0$ MHz.

∮Resonance not detected.

‡See note added in proof.

support the resonances. The effect of the cuts on the resonant currents will be monitored at position X1. The last column of Table 1 gives the relative strength of each resonance. It is defined as the ratio of the largest peak-to-peak change in any of the three components of E to the magnitude of E_b near the resonance; all measurements are taken at position B1 since all resonances are detectable there.

In Table 2, the resonant frequencies have been theoretically predicted with the data arranged by modes in increasing order of $f_{c(mn)}$. The latter is calculated from the cell dimensions in the transverse plane. While Crawford [8] has suggested the use of the waveguide formula to calculate $f_{c(mn)}$ for all TE$_{mn}$ and TM$_{mn}$ modes, Gruner's analysis [16, 17] shows that the waveguide formula is only valid for n even. Gruner calculated $f_{c(mn)}$ for n odd using a series expansion method. His results [27] for the large TEM cell are compared to the waveguide-formula results in Table 2. Some of the correct values of $f_{c(mn)}$ may be obtained from other publications. For example, the value of 15.2 MHz for $f_{c(01)}$ is also obtained by interpolating in Fig. 2 of Weil et al. [21, 28] for the large cell (70 Ω [5], and $a/b = 0.833$). Furthermore, the one-term approximate solution of Tippet and Chang [20] gives values of $f_{c(mn)}$ for the TE$_{11}$ and TM$_{11}$ modes which are in agreement, within 5%, with Gruner's results. Finally, it is noteworthy that $f_{c(21)} < f_{c(20)}$ for the TE modes since this ordering of the modes is reversed from the predictions of the waveguide formula.

The resonant frequencies, $f_{R(mnp)}$, are ideally calculated from the values of $f_{c(mn)}$ and the cell's length and taper dimensions using a resonance mode chart. While such a chart has not been published for TEM cells, a good approximate calculation can be done by modeling the cell as a transmission line with flat transverse ends instead of tapered ends — the 'equivalent coaxial box' model. The condition for the resonances of the TE$_{mn}$ mode is that the effective length of the box for that particular mode, L_{mn}, equals an integral number of half guide wavelengths for the mode:

$$L_{mn} = p(\lambda_{g(mn)}/2); \qquad p = 1,2,3, \ldots \tag{1}$$

L_{mn} will be taken to be an adjustable parameter which is the same for all resonances of a given mode. This is based on the reasonable assumption that the septum and wall current patterns in the tapered ends of the cell, which determine the effective cell length, are similar for all resonances of the same

Table 3   Analysis of resonances in the small (1.0 × 0.6 × 2.0 m) TEM cell.* $f_{R(mnp)}$ ≤ 360 MHz

Higher-order mode				Resonance						
Type TE_{mn}	$f_{c(mn)}$	X_{mn}	$\left(\frac{c}{2L_{mn}}\right)$	Type TE_{mnp}			$f_{R(mnp)}$	(MHz)	Detected in VSWR or trans. power?	Strength $\left(\frac{\Delta E_b}{E_b}\right)$
m n	(MHz)		(MHz)	m	n	p	calc.	meas.		
0 1	129	0.81	83	0	1	1	155±3	156.3	no	0.4
	±3	±0.04	±1	0	1	2	210±4	212.9	no	2.0
				0	1	3	280±6	282.1	no	0.4
				0	1	4	356±8	351.3	no	0.3
1 0	150	0.49	101	1	0	1	181±4	184.3	yes	4.3
	±1	±0.04	±2	1	0	2	252±5	255.7	no	1.9
				1	0	3	338±7	329.6	no	1.2
1 1	260	0.52	98	1	1	1	278±9	272.7	yes	4.8
	±8	±0.11	±2	1	1	2	326±10	331.8	yes	9.2
0 2	—†	—	—	0	2	1	—†	318.0	no	0.5

*Narda Microwave Model 8802: a = 100.3, b = 60.0, w = 72.1, L_c = 100.3, L_E = 101.2 (cm); Z_0 = 50 Ω.
†$f_{c(02)}$ and $f_{R(021)}$ not known; resonance identified from field characteristics.

mode. Thus, one parameter, L_{mn}, is adjusted to get good agreement between measured and calculated frequencies for between two and four resonances, depending on the mode. L_{mn} is related to the cell dimensions by the equation

$$L_{mn} = L_c + X_{mn} L_E \qquad (2)$$

where L_c is the length of the uniform-cross-section center part of the cell (6.10 m), L_E is the length (along the center line) of the two tapered ends of the cell (6.86 m), and X_{mn} is the fraction of the two ends included in the value of L_{mn}.

By using the standard waveguide formula for $\lambda_{g(mn)}$ [29], $(\lambda^{-2} = \lambda_{g(mn)}^{-2} + \lambda_{c(mn)}^{-2})$ and the usual conversions from wavelength to frequency $(f_{R(mnp)} = c/\lambda, f_{c(mn)} = c/\lambda_{c(mn)})$ the resonance condition (eq. 1) becomes

$$f_{R(mnp)}^2 = f_{c(mn)}^2 + \left(\frac{pc}{2L_{mn}}\right)^2; \qquad (p > 0; m, n \geq 0) \qquad (3)$$

C. M. Weil has pointed out (private communication) that λ_g in the tapered regions of the cell is actually larger than given by the waveguide formula applied to the center section of the cell. Hence, λ_g as used in the resonance condition (eq. (1)) and the waveguide formula is an average of the values applying to the center and tapered sections of the cell.

Using eq. (3) with $(c/2L_{mn})$ as an adjustable parameter, good agreement between measured and calculated frequencies for the first eight TE_{mn} resonances was obtained. $f_{R(mnp)}$ was also calculated for all resonances, for comparison purposes, using the average cell length of $L_0 = L_c + 0.5 L_E = 9.38$ m. The agreement between measured frequencies and those calculated using the average cell length can be seen to be significantly worse than for the calculation using an adjustable cell length. The values of X_{mn} corresponding to the best-fit values of L_{mn} are also given in Table 2.

The first TM resonance was uniquely identified by the presence of a resonant longitudinal E field, as well as by the measured frequency.

III. RESONANCE ANALYSIS OF A SMALL TEM CELL

A. Resonance Analysis

The resonances in a smaller (1.0 × 0.6 × 2.0 m) TEM cell were also investigated using the same methods as for the larger cell. The results are presented in Table 3. The cut-off frequencies were calculated from the waveguide formula for $f_{c(10)}$ and from Figs. 1 and 2 of Weil et al. [21, 28] for $f_{c(11)}$, and $f_{c(01)}$, respectively. The uncertainties shown for $f_{c(mn)}$ result primarily from interpolation in the figures of Weil et al. The uncertainty shown for X_{mn} takes into account both the uncertainty in $f_{c(mn)}$

Table 4   Comparison of X_{mn} determined for the first three TE_{mn} modes in two TEM cells

Cell outer dimensions $a \times b \times \ell$ (m)	Cell parameters			X_{mn}		
	$\dfrac{a}{b}$	$\dfrac{w}{a}$	$Z_0(\Omega)$	TE_{01}	TE_{10}	TE_{11}
6.1×7.3×13.0	0.83	0.67	70	0.74 ±0.02	0.45 ±0.02	0.35 ±0.02
1.0×0.6×2.0	1.67	0.72	50	0.81 ±0.04	0.49 ±0.04	0.52 ±0.11
Average ±½ (difference)	1.25 ±0.42	0.70 ±0.03	60 ±10	0.77 ±0.04	0.47 ±0.02	0.43 ±0.08

and the estimated uncertainty from adjusting $(c/2L_{mn})$ for the best fit to the measured frequencies. The agreement between measured and calculated frequencies is excellent, the largest difference being 3% for the TE_{103} resonance. As with the large cell, all resonances except for the TE_{021} were positively identified in terms of the universal E field characteristics of Table 1. In the small cell the largest resonant E-field component for the TE resonances was always found to be E_b, so that the strength of the resonance is simply defined as $\Delta E_b/E_b$ for the purposes of Table 3.

B. *Comparison With Large Cell*

The results for the resonance field strengths in the two cells were compared. In both cases it was found that resonances with a relative E-field strength $(\Delta E_i/E_b)$ of less than 4 were consistently not observable by power measurements, while stronger resonances were. Two of the strongest resonances in both cells were found to be the TE_{112} and TE_{111} resonances, in that order. This is likely explained by the similarity of the TE_{11} mode to the TEM mode since a transfer of power between two similar modes is more likely than between two dissimilar modes. The group at NBS [12, 13, 19] also found the first large resonance to be the TE_{111} resonance (which they called the first TE_{10} resonance using a different notation — see section VI. B).

Generally, the resonances in the large cell are more strongly excited. This is particularly true of the TE_{011} resonance. The stronger excitation of the resonances could be due to a number of factors but the most likely one is the presence of the two wooden platforms in the large cell (see Fig. 1 of [5]), which would scatter radiation into the higher-order modes.

The effective lengths of the two cells, expressed in terms of the fraction of the tapered ends included for each mode, are compared in Table 4. Considering the large differences in cell parameters, the agreement in the values of X_{mn} is considered good.

IV. PROPAGATING HIGHER-ORDER MODES

A search was made for the presence of propagating higher-order modes in the empty cell at all non-resonant frequencies. The modes were detected by comparing (within ±2%) the E_b fields at appropriate sites in the transverse plane. In searching for the presence of the TE_{01} mode, E_b at position B was compared to E_b at position C. A difference of 8% in the two fields would be recorded as a 4% contribution of the TE_{01} mode to the total E field since that mode adds to the TEM field at position B and subtracts from it at position C (or vice versa). Similarly, the presence of the TE_{10} mode was detected by comparing E_b at positions E and C. The presence of the TE_{11} mode can only be detected by comparing E_b at a given point above and below each resonant frequency; it does not produce asymmetries in the region of points A to F.

Using these methods, it was established that none of the first three higher-order modes (TE_{01}, TE_{10}, and TE_{11}) is present between its own cut-off frequency and its own first-resonance frequency in either of the two cells tested. For example, the TE_{01} mode is undetectable in the large cell between $f_{c(01)}$ (15.2 MHz) and $f_{R(011)}$ (20.7 MHz) but makes a 4% contribution to the E-field pattern above $f_{R(011)}$. Similarly, the TE_{10} mode is undetectable between $f_{c(10)}$ and $f_{R(101)}$, but makes a 5% contribution to the field pattern above $f_{R(101)}$. The field contributions of each of the first three higher-order modes in each TEM cell are given in Table 5. A range is shown when the results depend on frequency. The $p = 2$ or 3 resonances were found to cause negligible changes in the contribution of each propagating higher-order mode.

Table 5   E-field contributions of the propagating higher-order modes above their respective first-resonance frequencies. Upper left figures apply to the large (6.1 × 7.3 × 13.0 m) TEM cell and lower right figures to the small (1.0 × 0.6 × 2.0 m) TEM cell

Higher-order mode (TE$_{mn}$)	TE$_{01}$		TE$_{10}$		TE$_{11}$	
$f_{R(mnl)}$ (MHz)	20.7	156	30.0	184	36.1	273
Contribution to E_b from propagating TE$_{mn}$ mode (%)	4	≤3	5	10–15	8–10	10–15

It may be that each TE$_{mn}$ mode does not propagate at frequencies between $f_{c(mn)}$ and $f_{R(mnl)}$ because the cell length is less than half a guide wavelength in that range and a length of at least half a guide wavelength is required for the wave to develop. For example, in the large cell, $f_{c(10)}$ = 24.6 MHz and $f_{R(101)}$ = 30.0 MHz; at an intermediate frequency of 27.12 MHz. $\lambda_{g(10)}/2$ is 13.1 m which is much larger than the effective cell length for that mode, 9.0 m.

Weil et al. [22] investigated E-field patterns in a 50-Ω TEM cell of cross-sectional dimensions 33.5 × 30.5 cm. At 425 MHz they found large E fields near the edge of the septum, which they interpreted as evidence for the propagation of the TE$_{01}$ mode. Using the parameters: $L_c = L_E$ = 1.52 m (private communication); X_{01} = 0.77 (from Table 4); and $f_{c(01)}$ = 275 MHz; the first six TE$_{01p}$ resonant frequencies were calculated. Their measurement frequency was found to lie between $f_{R(015)}$ (392 MHz) and $f_{R(016)}$ (434 MHz). Thus, the field pattern they observed could have been either the propagating TE$_{01}$ mode or one of the higher (p = 5 or 6) resonances of that mode, or a combination of both.

Despite the presence of resonances and propagating higher-order modes, 50-Ω TEM cells can still be used to reliably calibrate field probes at most frequencies between $f_{c(01)}$ and $f_{R(111)}$. This is done by averaging calibration data taken at points A0 and D0. Neither the TE$_{01}$ mode nor its resonances are detectable at these points and the effect of the propagating TE$_{10}$ mode is eliminated by averaging the two results. The TE$_{10p}$ resonances, however, must be avoided. Thus. for example, the small cell is usable for probe calibration work up to 273 MHz ($f_{R(111)}$) except for frequencies within ±5 MHz of the TE$_{10p}$ resonances at 184 and 256 MHz. This is consistent with the manufacturer's stated frequency limit of 250 MHz except for frequencies of 184 ± 5 MHz, near the TE$_{101}$ resonance.

V. BANDWIDTH LIMITATIONS FOR BIOEFFECTS DOSIMETRY STUDIES

A. *Resonance Interactions in the Large TEM Cell*

The interactions between resonances and RF-absorbing biological bodies can be qualitatively studied by measuring E_b as a function of frequency near each resonance for the empty and loaded cell. The results for the TE$_{101}$ resonance are shown in Fig. 4. It can be seen that the presence of the human body in the cell inverts, shifts, and broadens the resonance. The effect is more pronounced for the grounded case since the interaction is stronger and the subject absorbs more RF power. The results for the TE$_{111}$ resonance at 36 MHz are very similar to those for the TE$_{101}$ resonance at 30 MHz.

The interaction of the body with the TE$_{011}$ resonance at 20.7 MHz, however. is quite different. The traces of Fig. 5 show clearly that the body does not interact significantly with the resonance, but does cause a slight frequency-independent reduction in E_b. This is thought to be nothing more than a slight shadowing effect of the body on the probe. There is negligible interaction because the E_b fields of the TE$_{01}$ mode and its resonances are zero at position A. Consequently. the body does not interact with, or absorb energy from the resonant fields. The use of multiple bodies at positions including B, C, E, and F could result in interactions with the TE$_{01p}$ resonances.

The same pattern of interaction between the body and the resonances also holds for the higher resonances of the same modes: a body in an E orientation at position A0 or A1 interacts with all TE$_{10p}$ and TE$_{11p}$ resonances but with none of the TE$_{01p}$ resonances.

Plots such as those of Fig. 4 give semiquantitative evidence that for frequencies near the resonances the effective exposure fields are altered significantly from those measured in the empty cell. That this is so may be seen in the dosimetry measurements of Table 6. Compared to the expected approximately frequency-squared dependence [30]. the absorption rates for the saline-filled cylinder
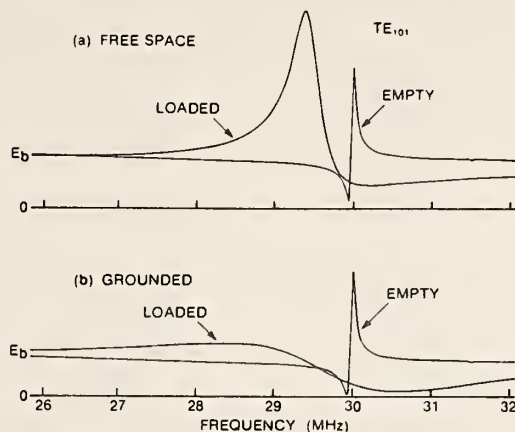
Figure 4 The interaction of a human subject with the TE_{101} E-field resonance. E_b is recorded for the empty cell and again when loaded with a subject in an E orientation under (a) free-space, or (b) grounded, conditions. For (a) the subject is centered on position A0 (defined in the text) and the probe at A1. For (b), the subject's bare feet are touching the wall and the probe is in the same position, relative to the subject, as for (a).
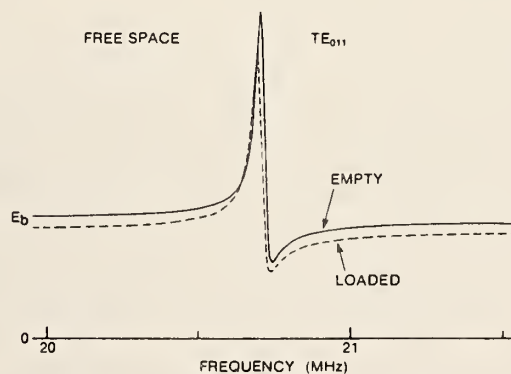

Figure 5 The lack of interaction between a human subject and the TE_{011} E-field resonance. The probe records E_b at position C1. The 'loaded' trace is with a subject in an E orientation at position C0.

and human subject F are anomalously high at the two frequencies (27.12 and 34.30 MHz) just below the two main interacting resonances (30.0 (TE_{101}) and 36.0 (TE_{111}) MHz), and anomalously low at the two frequencies (30.5 and 38.5 MHz) just above the resonances. This result is exactly as suggested by the traces of Fig. 4. Unfortunately, we do not have a way of quantitatively evaluating the altered effective exposure fields. Because of this, the large TEM cell cannot be used, in its present form, for bioeffects dosimetry work above about 25 MHz, or 83% of $f_{R(101)}$, the first interacting resonance.

Tests were also done for a second kind of possible dosimetry error resulting from the propagation of higher-order modes. Radiation scattered by the body from the TEM mode into one of the higher-order modes would never leave the cell and would eventually be absorbed by the cell. This would make a false addition to the detected absorption of the human subject. This possibility was tested by measuring the apparent absorption of a test object found to interact with the resonances like a human subject, but presumed to be nonabsorbing: a full-sized commercial manikin covered with a layer of thick aluminum foil. It can be seen in Table 6 that the measured "absorption" of the metal manikin is detectable at some frequencies above 25 MHz, but that it is within acceptable limits (<10% of the absorption of the human subject or saline model).

Table 6   Normalized specific absorption rates, NSAR, for three test objects exposed to RF fields. The objects are in an E orientation at position A0 in the large (6.1 × 7.3 × 13.0 m) TEM cell

Frequency (MHz)	NSAR (mW/kg per mW/cm²) Mean ± SE(N)		
	Subject F	Saline cylinder†	Metal manikin
18.50	22.3±3.1(8)	28.3±2.4(8)	3.3±3.0(10)
			1.0±3.1(10)
23.25	38.6±1.3(6)	47.9±4.6(6)	−1.9±1.5(9)
27.12	63.1±3.8(6)	106.4±4.7(6)	6.5±1.9(10)**
			8.6±4.9(9)
30.50	32.3±2.1(6)	13.8±4.4(11)	0.4±1.9(9)
34.30	106.4±1.5(6)	129.4±10.0(6)	4.9±2.4(9)*
38.50	75.2±2.9(6)	88.9±3.0(6)	3.5±1.1(9)*
Height (cm)	175.3	183.0	183.0
Mass (kg)	84.0	62.0	(70.0)

†Saline at 23°C. $\epsilon' = 80$, $\sigma = 0.43$ S/m.
Significance levels using a   *$p < 0.05$
one-tailed Student's t test   **$p < 0.01$

In conclusion, two different bioeffects dosimetry limitations due to resonances and higher-order modes have been investigated and only one has been found to be important — the interaction between some of the resonances and the human subject.

B. Discussion of Other Bioeffects Dosimetry Work in TEM Cells

While several authors are using TEM cells for RF bioeffects studies, only Allen et al. [1], Joines et al. [2] and Marshall et al. [3] have used their measurement systems to determine the ratio of absorption rate to exposure power density for the animals or preparation used. The possible application of resonance interaction concepts to their work will be briefly considered.

Allen et al. [1] measured RF absorption in rhesus monkeys and monkey phantoms from 10 to 50 MHz in a 50-Ω, 2.82 × 1.45 × 9.15 m TEM cell. Using their cell dimensions [1, 31] and assuming $L_c = L_E$, the first two cut-off and resonant frequencies were calculated to be $f_{c(01)} = f_{c(10)} = 53$ MHz, $f_{R(011)} = 56$ MHz, and $f_{R(101)} = 58$ MHz. Their highest operating frequency, 50 MHz, appears to have been sufficiently below $f_{R(101)}$ to minimize the interaction effect. This is confirmed by the lack of anomalous absorption results at 50 MHz in their measured curves.

Joines et al. [2] operated at 147 MHz, which is so far below the calculated value of $f_{c(01)}$ for their cell, 930 MHz, that resonance interactions would not have been a problem in their experiments.

Marshall et al. [3] measured the absorption of mice and prolate-spheroidal models of mice from 200 to 500 MHz, in a 50-Ω, 0.50 × 0.30 × 1.00 m TEM cell. Since their TEM cell is a half-sized scale model of the cell analysed in Table 3, their resonant frequencies are all double those given in Table 3. In particular, $f_{R(011)} = 313$ MHz, $f_{R(101)} = 369$ MHz, $f_{R(012)} = 426$ MHz and $f_{R(102)} = 511$ MHz. Their E-polarization absorption results for the models (Fig. 6 of [3]) show an anomalously high absorption rate at 500 MHz, consistent with the field anomalies they detected, and likely due to the TE_{102} resonance. Other anomalies are also apparent in the 300- to 400-MHz range and are likely due to interactions of the six mice models with the TE_{011}, TE_{101}, and TE_{012} resonances. In their experiments, an interaction with the TE_{01p} resonances is possible since four of the six mice in their cell are offset from position A0 in both the a and ℓ directions.

VI. BANDWIDTH LIMITATIONS FOR EMC STUDIES

A. Resonance Interactions in the Small TEM Cell

The small TEM cell is rated by the manufacturer for use in EMC studies up to 250 MHz provided the equipment under test (EUT) is no larger than 10 × 20 × 30 cm. The interaction of a metal box of that size with the TE resonances was studied using the methods described above for the large cell. Several of the interactions are shown in Figs. 6 and 7. In Fig. 6 the interaction with the TE_{101} resonance is seen to be strong, while the TE_{011} resonance is barely detected, with or without the metal box
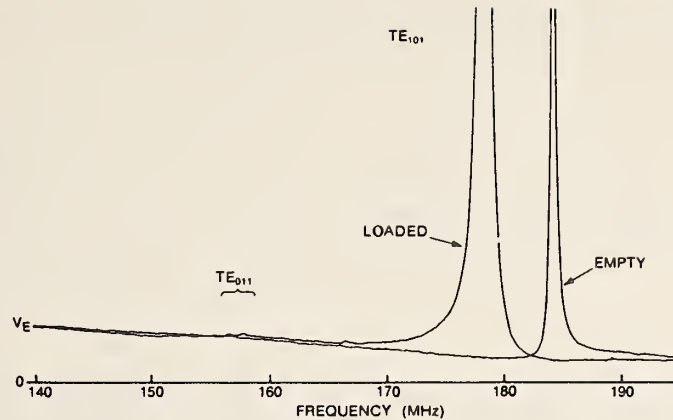
Figure 6   The interaction of a small rectangular metal box with the TE_{101} resonance in the small (1.0 × 0.6 × 2.0 m) TEM cell. The box is centered on position A0 and oriented with its dimensions of 30 × 20 × 10 cm in the ℓ, a, and b directions, respectively. The probe is at position A2 (0.2 λ towards the load from position A0). V_E is the E-probe voltage (in arbitrary units) and is approximately proportional to $\dot{E}_b^2$ at the low power levels used.
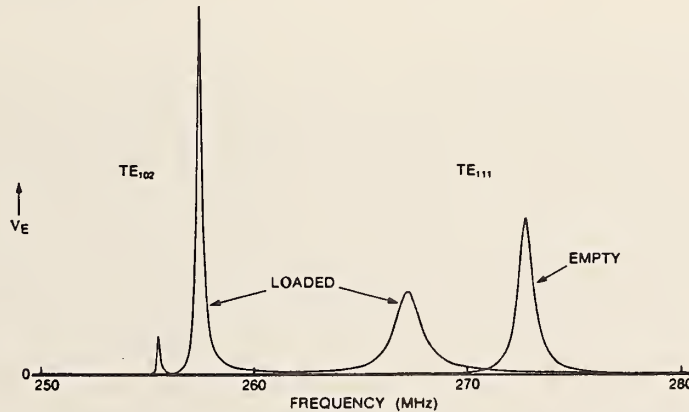

Figure 7   The interactions of a small rectangular metal box with two of the higher resonances in the small (1.0 × 0.6 × 2.0 m) TEM cell. Details regarding box, probe, and ordinate scale are the same as for Figure 6.

present, because both box and probe are centered on position A in the transverse plane. In Fig. 7 the metal box is shown to interact strongly with both the TE_{102} and TE_{111} resonances. On the scale used to show the resonances in Fig. 7, E_b for the TEM mode is barely measurable. It can be seen in both Figs. 6 and 7 that the presence of the EUT sometimes strengthens a resonance. It is also noteworthy that some resonances are shifted up in frequency when interacting with an EUT at position A0. This was found for the TE_{102} resonance (Fig. 7) and the TE_{112} resonance (not shown).

In general the interactions of the metal box or human subject with the resonances are similar. Both test objects are conductors, with the metal box being a good conductor (tan δ ≫ 1) and the human subject being a poor conductor (tan δ $\doteq$ 4 at 20 MHz [30]). The values of tan δ account for the small relative changes in Q of the resonances interacting with the metal box and the larger changes in Q of the resonances interacting with the human subject.

The small TEM cell is usable for EMC studies up to 250 MHz with the exception of a range near 180 MHz. The range would appear, from Fig. 6, to be 20 MHz, but Crawford's experience with actual EMC testing would correspond to 40 MHz for this resonance (private communication). It would also be usable, with reduced accuracy, at inter-resonance frequencies above 250 MHz.

227

Table 7   Analysis of resonances in the NBS 3.0 × 3.0 × 6.0 m TEM cell.* $f_{R(mnp)} < 100$ MHz

Higher-order Mode					Resonance					
									$f_{R(mnp)}$ (MHz)	
										Detected by:
TE_{mn} or TM_{mn}	$\left(\dfrac{2a}{\lambda_c}\right)$	$f_{c(mn)}$ (MHz)	X_{mn}	$\left(\dfrac{c}{2L_{mn}}\right)$ (MHz)	Type m	n	p	calc. from (3)	E_b†	VSWR or insertion loss
TE_{01}	0.58	29.0	0.77	28.2	0	1	1	40	—∮	—
					0	1	2	63	—	—
					0	1	3	89	—	—
TE_{10}	1.00	50.0	0.47	34.0	1	0	1	60	60	—
					1	0	2	84	—	—
TE_{11}	1.27	63.5	0.43	35.0	1	1	1	73	74	—
					1	1	2	95	—	—
TM_{11}	—	—	—	—	1	1	1‡	—	97	97

*[10]. $a = b = L_c = L_E = 3.00$ m; $Z_0 = 50\ \Omega$; $(2a/\lambda_c)$ from [26]; X_{mn} from Table 4.

†Measured at position A0.

∮Resonance not detected in original study [10]. In recent measurements of E_b at positions A0 and A1, Crawford has detected resonances in this cell (without absorber) at the following frequencies: 38, 50, 61, 65, 74, and 85 MHz. The frequency was stepped digitally in 2-MHz increments (private communication).

‡See note added in proof.

B. Discussion of the NBS TEM Cells

The group at NBS, in a series of papers [8, 11−13, 19−21], has been developing the use of TEM cells in EMC work. The application of our findings to their work will be discussed below.

Unfortunately, they use a different nomenclature regarding the identification and labeling of the first cell resonance. They take the first cell resonance to be either the first resonance [11], or the first large resonance [19], detected in input VSWR. In either case the one they are referring to is called the first resonance of the "TE_{10} mode" [12, 13] or of the "perturbation to the TE_{10} mode in a rectangular waveguide" [19]. The mode in question is described in [19] as being the antisymmetric type of perturbed TE_{10} mode, in which the electric field is oppositely directed on each side of the septum. In our notation of Fig. 3(a), this is the TE_{11} mode. That they are referring to the TE_{11} mode is further confirmed by using their formula [12] to calculate f_c for the large TEM cell; the calculated value of 30.4 MHz is much closer to $f_{c(11)} = 31.3$ MHz than to $f_{c(10)} = 24.6$ MHz. Thus, what they refer to as the first resonance is actually the TE_{111} resonance. Our results are consistent with Crawford's in the sense that we both found the TE_{111} resonance to be the first resonance which is consistently strongly excited. I should also add that the lower resonances were often observed in their data (e.g., Figs. 17−20 of [13]) but never identified or discussed.

The NBS 3 × 3 × 6 m, 50-Ω, TEM cell has been re-analysed in Table 7. The cell dimensions, from [11], are given in the table and w is calculated to be 2.48 m since $w = 0.825\,b$ for any 50-Ω cell of square cross section [8, Table 1].

Assuming that the resonance at 97 MHz is the first TM resonance, as postulated, and that the TE_{mnp} resonances are weakly excited, all of the observations in Table 7 are consistent with our resonance analysis. With only weak excitation, the TE_{mnp} resonances would not have been observable in the VSWR and insertion loss measurements (Figs. 6 and 7, respectively, of [11]). Furthermore, with a field probe at the center of the test zone (position A0), only the TE_{101} and TE_{111} resonances at 60 and 74 MHz were observable while all the TE_{01p} and $p = 2$ resonances were not, as expected from the 'A0' column of Table 1. Thus the fact that five of the first seven (TE) resonances were not detected by Crawford et al.'s [11] measurements of E_b(A0) does not mean they were not present — on the contrary, a field probe at position B1 would likely have revealed them all.

Based on our observations on the small TEM cell, the four TE_{10p} and TE_{11p} resonances at 60, 75, 84, and 95 MHz would all interact with an EUT in the NBS cell. Furthermore, the interacting resonances could be stronger in the EUT-loaded cell than in the empty cell, as was found for the TE_{10p} resonances in the small cell. Additionally, any cables between the EUT and points outside the cell

Table 8 Dependence of the unusable bandwidth near the first interacting resonance (TE_{101}) on the TEM-cell application*

Type of application	Discussed in section	$f_{R(101)}$ (MHz)	Unusable bandwidth	
			(MHz)	% of $f_{R(101)}$
Bioeffects dosimetry	V.A	30	10	33
EMC/EMI	VI.A	184	20–40	11–22
Probe calibration	IV	184	10	6

*The probe or test object is in free space at position A0, the center of the test zone.

might interact with the resonances, possibly even with the TE_{01p} resonances, depending on the cable positions. For the above reasons, further studies of possible EUT-resonance interactions in the NBS cells are warranted. Crawford and Workman [13] noted the same thing when they said that measured fields "obviously will be influenced by inserting the EUT, especially at frequencies above the cell's resonances and multimode, and will require further evaluation".

The absorber loading of the NBS cells does reduce the strength of the E_b resonances and this may prove, after further investigation, to be an effective damper on the interactions of the EUT with the lower-frequency resonances.

SUMMARY

The first eight to ten TE_{mnp} resonances have been identified in one large (6.1 × 7.3 × 13.0 m) and one small (1.0 × 0.6 × 2.0 m) TEM cell. Many of the weaker resonances were undetectable by means of cell VSWR or insertion-loss measurements. Furthermore, many of them (e.g., the TE_{01p} and TE_{mn2} resonances) were not detected with a probe measuring E_b at the center of the test zone (position A0). They were all detectable, however, by means of swept-frequency measurements of E_b and circumferential wall currents at selected sites within the cell. They were identified by the field characteristics of the resonances and by matching measured and calculated resonant frequencies. The resonant frequencies fit the equivalent coaxial box model where the effective length of the box, L_{mn}, depends on the mode (m, n), but not on the number (p) of half guide wavelengths in the resonance. The effective cell length for the TE_{mnp} resonances was found to include between 0.3 and 0.8 of the length of the cell's two tapered ends.

Each of the first three higher-order modes (TE_{01}, TE_{10}, TE_{11}) was found to propagate at frequencies above its first resonance, but not between its cut-off frequency and first resonance. The propagating higher-order modes alter the TEM-mode E field in the test volume of the cell by up to ±15%.

A biological or metallic test object at the center of the test zone interacts with all TE_{10p} and TE_{11p} resonances but not with the TE_{01p} resonances. As a result of the interaction the resonances shift in frequency and broaden, with the effect being stronger for a grounded test object. The frequency shift is downwards for most resonances but upwards for the TE_{102} and TE_{112} resonances.

The test object may interact strongly with a resonance too small to be detected in VSWR measurements, such as the TE_{101} resonance in both cells. There can also be a large interaction with a resonance not detected by a probe at the center of the test zone, such as the TE_{102} resonances in both cells. For these reasons, it is important to find all resonances within the frequency range used. This is done with swept-frequency measurements of E_b at position B1.

At frequencies near interacting resonances, the power absorbed by a biological object can be measured but the effective exposure field cannot be determined. For this reason the large cell is usable for bioeffects dosimetry work only to about 25 MHz, which is 65% larger than f_{c01} (15.2 MHz) and 21% larger than $f_{R(011)}$ (20.7 MHz) but 17% below $f_{R(101)}$ (30.0 MHz), the first interacting resonance.

A TEM cell is usable for field-probe calibration work up to $f_{R(111)}$, except near $f_{R(101)}$. The effects of the TE_{01p} resonances and the propagating TE_{01} and TE_{10} modes are all eliminated by averaging the two calibration curves taken at positions A0 and D0 on opposite sides of the septum. In particular, the small cell is usable up to 250 MHz, except for frequencies within ±5 MHz of the TE_{101} resonance at 184 MHz.

229

The relative size of the unusable bandwidth near an interacting resonance depends on the particular application of the TEM cell. This effect is illustrated for the first interacting resonance, the TE_{101} resonance, in Table 8. As expected, the relative unusable bandwidth is seen to be smallest for the small metal object (probe undergoing calibration), intermediate for the larger metal object (EUT undergoing EMC testing) and biggest for the larger lossy object (human subject).

To design a TEM cell for maximum usable bandwidth, the frequency of the first interacting resonance, TE_{101}, should be as high as possible. This is accomplished primarily by making cell dimension a as small as possible which causes $f_{c(10)}$ to be as large as possible. To a lesser extent, keeping L_c and L_E (and hence L_{10}) as small as possible also helps.

A method of partially suppressing the TE resonances will be published soon [32].

ACKNOWLEDGMENTS

Note added in proof: E. D. Mantiply has suggested that $p = 0$ is possible for the TM resonances. Based on the discussion of resonances in cylinders and coaxial lines in Moreno [29], I agree. Thus, the first TM resonance is TM_{110} and not TM_{111} as given in Tables 2 and 7.

REFERENCES

1   S. J. Allen, W. D. Hurt, J. H. Krupp, J. A. Ratliff, C. H. Durney, and C. C. Johnson. Measurement of radiofrequency power absorption in monkeys, monkey phantoms and human phantoms exposed to 10−50 MHz fields. Biological Effects of Electromagnetic Waves (Selected Papers of the USNC/URSI Annual Meeting, Boulder, CO), Vol. II, Oct. 20−23, 1975, pp. 83−95. (HEW Publication (FDA) 77-8011, U.S. Govt. Printing Office, Washington, DC 20402).

2   W. T. Joines, C. F. Blackman, and M. A. Hollis. Broadening of the RF power-density window for calcium-ion efflux from brain tissue. IEEE Trans. Biomed. Eng. BME-28, 568−573, Aug. 1981.

3   S. V. Marshall, R. F. Brown, C. W. Hughes, and P. V. Marshall. An environmentally controlled exposure system for irradiation of mice at frequencies below 500 MHz. Proc. 1981 IEEE Int. Symp. on Electromag. Compat., 1981, pp. 99−104.

4   D. A. Hill. Human radiowave absorption from 7 to 40 MHz. Proceedings of a Workshop on the Protection of Personnel Against Radiofrequency Electromagnetic Radiation, J. C. Mitchell, Ed., USAF School of Aerospace Medicine, Aeromedical Review, 3-81, Sept. 1981, pp. 170−175.

5   D. A. Hill. Human whole-body radiofrequency absorption studies using a TEM-cell exposure system. IEEE Trans. Microwave Theory Tech., MTT-30, 1847−1854, November 1982.

6   C. F. Blackman, J. A. Elder, C. M. Weil, S. G. Benane, D. C. Eichinger, and D. E. House. Induction of calcium-ion efflux from brain tissue by radiofrequency radiation: effects of modulation frequency and field strength. Radio Science, 14(6S), 93−98, Nov.−Dec. 1979.

7   R. J. Smialowicz, J. S. Ali, E. Berman, S. J. Bursian, J. B. Kinn, C. G. Liddle, L. W. Reiter, and C. M. Weil. Chronic exposure of rats to 100-MHz (CW) radiofrequency radiation: assessment of biological effects. Radiation Research, 86, 488−505, June 1981.

8   M. L. Crawford. Generation of standard EM fields using TEM transmission cells. IEEE Trans. Electromagn. Compat. EMC-16, 189−195, Nov. 1974.

9   P. S. Ruggera. E- and H-field instrumentation and calibration below 500 MHz. Biological Effects of Electromagnetic Waves (Selected Papers of the USNC/URSI Annual Meeting, Boulder, CO) Vol. II, Oct. 20−23, 1975, pp. 281−296. (HEW Publication (FDA) 77−8011, U.S. Govt. Printing Office, Washington, DC 20402.)

10   E. B. Larsen. Techniques for producing standard EM fields from 10 kHz to 10 GHz for evaluating radiation monitors. Proceedings of the 1978 Symposium on Electromagnetic Fields in Biological Systems, Ottawa, Canada, June 28−30, 1978. IMPI (1979), pp. 96−112.

11   M. L. Crawford, J. L. Workman, and C. L. Thomas. Generation of EM susceptibility test fields using a large absorber-loaded TEM cell. IEEE Trans. Instrum. Meas. IM-26, 225−230, Sept. 1977.

12   M. L. Crawford, J. L. Workman, and C. L. Thomas. Expanding the bandwidth of TEM cells for EMC measurements. IEEE Trans. Electromag. Compat. EMC-20, 368−375, Aug. 1978.

13   M. L. Crawford and J. L. Workman. Using a TEM cell for EMC measurements of electronic equipment. National Bureau of Standards. Technical Note #1013, April 1979.

14   W. Baier. Wellentypen in Leitungen aus leitern rechteckigen Querschnitts. (Modes in waveguides consisting of conductors of rectangular cross section), Arkiv der Elektrischen Übertragung, 22, 179−185, 1968.

15 T. S. Saad (Ed.), R. C. Hansen and G. J. Wheeler (Co-editors). Microwave Engineers' Handbook. Dedham, Mass.: Artech House Inc., 1971, Vol. 1, pp. 145–147.

16 L. Gruner. Higher order modes in rectangular coaxial waveguides. IEEE Trans. Microwave Theory Techn. MTT-15, 483–485, Aug. 1967.

17 L. Gruner. Estimating rectangular coax cutoff. Microwave Journal, 22, 88–92, April 1979.

18 L. Gruner. Characteristics of crossed rectangular coaxial structures. IEEE Trans. Microwave Theory Techn. MTT-28, 622–627, June 1980.

19 J. C. Tippet, D. C. Chang, and M. L. Crawford. An analytical and experimental determination of the cutoff frequencies of higher-order TE modes in a TEM cell. National Bureau of Standards Report #NBSIR 76-841, June 1976.

20 J. C. Tippet and D. C. Chang. Higher order modes in rectangular coaxial line with infinitely thin inner conductor. National Bureau of Standards report #NBSIR 78-873, March 1978.

21 C. M. Weil, W. T. Joines, and J. B. Kinn. Frequency range of large-scale TEM mode rectangular strip lines. Microwave Journal, 24, 93–100, Nov. 1981.

22 M. L. Crawford, and J. L. Workman. Asymmetric versus symmetric TEM cells for EMC measurements. IEEE 1978 International Symposium on EMC, Atlanta, GA, June 20–22, 1978. (78-CH-1304-5 EMC)

23 M. F. Iskander, C. H. Durney, H. Massoudi, and C. C. Johnson. Approximate calculation of SAR for planewave irradiation of man model near a ground plane. Proceedings of the 1978 Symposium on Electromagnetic Fields in Biological Systems, Ottawa, Canada, June 28–30, 1978. IMPI (1979), pp. 304–323.

24 M. J. Hagmann and O. P. Gandhi. Numerical calculation of electromagnetic energy deposition in models of man with grounding and reflector effects. Radio Science, 14(6(S)), 23–29, Nov.–Dec. 1979.

25 F. M. Greene. Development of electric and magnetic near-field probes. National Bureau of Standards (Boulder, Colo.) Technical Note No. 658, Jan. 1975.

26 R. W. P. King, H. R. Mimno, and A. H. Wing. Transmission Lines, Antennas and Waveguides, New York: Dover, 1st. edn., 1965. Ch. III, pp. 254–257.

27 L. Gruner. Private communication, calculations of $f_{c(mn)}$ for the large TEM cell using the computer program of [16,17]. Cell dimensions are (meters): $a = 6.10$, $b = 7.32$, $w = 4.06$, $t = 0$.

28 C. M. Weil. Private communication, full-sized copies of Figs. 1–3 of [21] were made available for accurate calculations.

29 T. Moreno. Microwave Transmission Design Data, New York: McGraw-Hill, 1st. edn., 1948, Ch. 7, p. 123, equation 7-44.

30 C. C. Johnson, C. H. Durney, P. W. Barber, S. J. Allen, and J. C. Mitchell. Radiofrequency Radiation Dosimetry Handbook. Rep. SAM-TR-76-35, USAF School of Aerospace Medicine/RZP, Brooks Air Force Base, TX 78235, Sept. 1976.

31 J. C. Mitchell. A Radiofrequency Radiation Exposure Apparatus. USAF School of Aerospace Medicine, Report SAM-TR-70-43, July 1970.

32 D. A. Hill and J. A. Walsh. Resonance suppression in a TEM cell. J. Microwave Power, in press.

Appendix L

Wilson, P. F.; Ma, M. T.   "Simple approximate expressions for higher order mode cutoff and resonant frequencies in TEM cells."

Simple Approximate Expressions for Higher Order Mode Cutoff and Resonant Frequencies in TEM Cells

PERRY F. WILSON, MEMBER, IEEE, AND MARK T. MA, FELLOW, IEEE

Abstract—Simple approximate expressions for determining the cutoff frequencies of the first few higher order modes and the associated resonant frequencies in transverse electromagnetic (TEM) cells are presented. Both symmetric (seven TE and two TM modes) and asymmetric (three TE modes) cells are discussed.

Key Words—Higher order modes, resonant frequencies, TEM cells.

Index Code—A3 d/e.

I. INTRODUCTION

THE transverse electromagnetic (TEM) cell, as shown in Fig. 1 (configured for a susceptibility measurement), is essentially a large section of rectangular coaxial transmission line (RCTL) used to establish an isolated known test environment. High field levels can be achieved with minimal power requirements and without interfering with nearby equipment.

A basic TEM-cell limitation is the appearance of resonances which tend to destroy the desired TEM-mode field distribution. Recent papers by Weil and Gruner [1] and Hill [2] have addressed this resonance problem. Weil and Gruner present numerical solutions for the normalized cutoff frequency of the initial higher order modes as a function of the inner conducting width. These results may be used to predict the appearance of higher order TEM-cell resonances if the effective length of the cell is known. However, determining the resonant length of a cell is nontrivial since the tapered sections affect each higher order mode differently. Therefore the effective length needs to be determined mode-by-mode and cannot be readily specified universally, or theoretically. Hill discusses TEM-cell resonances in some detail based on experimental data from various cells. He specifies both how to detect and how to identify the various resonances, and compares measured results to predicted values based on Weil and Gruner's numerical calculations. Each paper stresses that, because the TEM cell is a high-Q cavity, the higher order resonances appear at sharply defined frequencies. Thus there may well exist windows between resonances where TEM-cell usage is still quite valid. Knowing where to expect these resonances and the associated windows should be of aid in many TEM-cell applications.

This paper outlines some approximate analytical expressions for determining the cutoff frequencies of the first few higher order modes. The expressions are readily evaluated on

a hand calculator. As such, they should supplement the more accurate results of Weil and Gruner if a numerical solution is not available, or if interpolation from existing figures is undesirable. Many of the results presented in this paper are derived from various National Bureau of Standards Technical Notes based on the work of Tippet et al. [3], and Tippet and Chang [4], as well as of the present authors [5], [6]. Because many TEM-cell users may be unfamiliar with these scattered results (Weil and Gruner make a comment to this effect), this paper serves to collect them in a convenient reference. Some additional formulas have also been generated as needed.

Throughout, we will assume that the gaps between the inner conductor and the outer side walls are small, both with respect to the relevant TEM-cell dimensions and with respect to the operating wavelength. In practice, this small-gap requirement is usually met. A wide inner conductor is desirable to increase the usable test section as well as to achieve a 50-Ω impedance, thus matching the cell to standard cables and equipment. The basic analytical approach leading to the cutoff-frequency expressions given in this paper is to formulate an integral equation for the unknown gap fields. The small-gap assumption can then be used to simplify the integral equation kernel [3], [5], [6], which leads to approximate modal equations, or, if the integral equation is solved exactly [4], to simplify the resulting infinite matrix equations. The details of these derivations may be found in the references, and highlights of the TE-mode analysis are given in the Appendix. The modal equations listed here will be used to analyze various cells that have appeared in the literature. Good agreement is found. Both symmetric and asymmetric TEM cells will be discussed.

II. CUTOFF FREQUENCIES OF HIGHER ORDER MODES—SYMMETRIC CELL

The cross section of a general asymmetric TEM cell is shown in Fig. 2. The relevant dimensions (a, b_1, b_2, b, w, g) conform to [3]–[6], and therefore differ slightly from those used in [1] and [2]. For a symmetric cell, $b_1 = b_2 = b$. The modal equations for determining the cutoff frequencies of the first nine higher order modes in a symmetric TEM cell are listed in Table I. The small-gap approximation used to generate the gap-dependent formulas involves neglecting terms like $(\pi g/2a)^2$ and $(k_c g)^2$ when compared to unity, where k_c is the wavenumber at cutoff for the mode of interest. As is well known [1], the TE$_{m,2n}$ and TM$_{m,2n}$ modes are unaffected
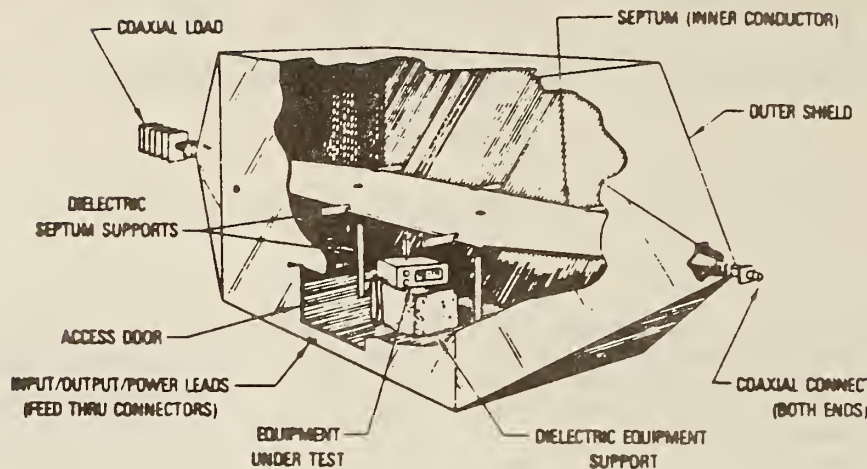
Fig. 1.   An NBS TEM cell.

TABLE I
SYMMETRIC TEM-CELL SMALL-GAP MODAL EQUATIONS

Mode [ref]	Modal Equation ($f_c = \frac{150}{\pi} \frac{x}{b}$ (MHz))
TE$_{01}$ [3]	$x \tan x = \frac{\pi}{2} (\frac{b}{a}) [\ln (\frac{2a}{\pi g}) + R_{TE_{01}}]^{-1}$ $R_{TE_{01}} = \sum\limits_{p=1}^{\infty} \frac{1}{p} (\coth \frac{p \pi b}{a} - 1) \cos^2(\frac{p \pi g}{a})$
TE$_{10}$	$x = \frac{\pi}{2} (\frac{b}{a})$
TE$_{11}$ [3,5]	$x = [y^2 + (\frac{\pi b}{2a})^2]^{1/2}$ $y \tan y = \frac{\pi}{\cos^2 (\frac{\pi g}{2a})} (\frac{b}{a}) [\ln(\frac{8a}{\pi g}) - 2 \cos^2 (\frac{\pi g}{2a}) + R_{TE_{11}}]^{-1}$ $R_{TE_{11}} = 2 \sum\limits_{p=1}^{\infty} \frac{1}{2p+1} (\coth \frac{(2p+1) \pi b}{2a} - 1) \cos^2 (\frac{2p+1}{2a} \pi g)$
TE$_{02}$	$x = \pi$
TE$_{12}$, TM$_{12}$	$x = \pi [1 + (\frac{b}{2a})^2]^{1/2}$
TE$_{20}$	$x = \pi \frac{b}{a}$
TE$_{21}$ [3]	$\frac{\cot x}{x} + \frac{2\cos^2(\frac{\pi g}{a}) \cot y}{y} = \frac{2}{\pi} (\frac{a}{b}) [\ln(\frac{2a}{\pi g}) - \cos^2(\frac{\pi g}{a}) + R_{TE_{21}}]$ $y = [x^2 - (\pi \frac{b}{a})^2]^{1/2}$ $R_{TE_{21}} = \sum\limits_{p=2}^{\infty} \frac{1}{p} (\coth \frac{p \pi b}{a} - 1) \cos^2 (\frac{p \pi g}{a})$
TM$_{11}$ [5]	$x = [y^2 + (\frac{\pi b}{2a})^2]^{1/2}$; $\frac{\tan y}{y} = \frac{2}{\pi} (\frac{a}{b}) [(\frac{2a}{\pi g})^2 + 1 - R_{TM_{11}}]^{-1}$ $R_{TM_{11}} = \frac{4a}{\pi g} \sum\limits_{p=1}^{\infty} [\coth \frac{(2p+1)\pi b}{2a} - 1] J_1[\frac{(2p+1)\pi g}{2a}]$
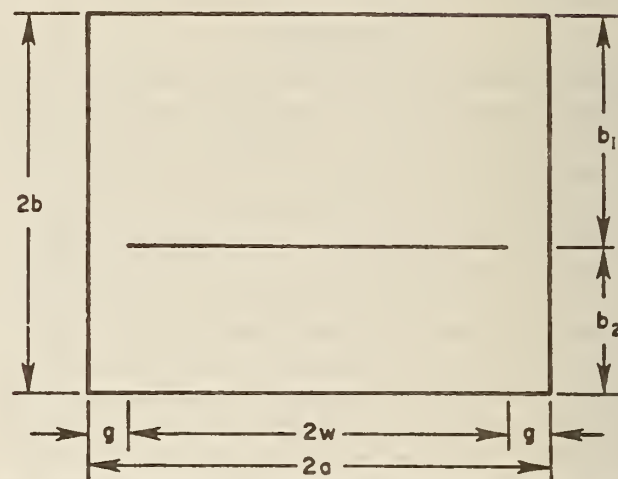
Fig. 2.   The cross section of an asymmetric TEM cell. For a symmetric cell, $b_1 = b_2 = b$.

meaningful. For each mode, the cutoff frequency $f_{c(m,n)}$ is related to the dimensionless modal equation variable x via

$$f_{c(m,n)} = \frac{x}{2\pi} \left(\frac{c}{b} \right) \text{ (Hz)}$$

$$= \frac{150}{\pi} \frac{x}{b} \text{ (MHz)} \qquad (1)$$

where $c \approx 3 \times 10^8$ m/s and MKS units are used throughout. Alternately, the normalized cutoff wavelength is

$$\frac{\lambda_{c(m,n)}}{a} = \frac{2\pi}{x} \left(\frac{b}{a} \right) . \qquad (2)$$

Once the cutoff frequency of a particular mode has been determined, the associated resonance frequencies $f_{R(m,n,p)}$ follow via [2]

$$f^2_{R(m,n,p)} = f^2_{c(m,n)} + \left(\frac{pc}{2L_{mn}} \right)^2 \qquad (3)$$

where L_{mn} is the effective length of the cell for that particular mode. Hill expresses L_{mn} as the length of the cell central

by the presence of the inner conductor for a symmetric cell and, therefore, straightforward rectangular waveguide ($2a \times 2b$) cutoff-frequency results apply. Expressions for these simple modes (TE$_{10}$, TE$_{02}$, TE$_{12}$, TE$_{20}$, TM$_{12}$) are included in Table I for completeness and to make the modal ordering more

section L_c plus a taper-dependent term, that is,

$$L_{mn} = L_c + X_{mn} L_E \qquad (4)$$

where L_E is the length of the two taper sections, and X_{mn} is an empirically determined fraction, different for each cell as well as for each mode.

The modal equations in Table I may be applied to a symmetric TEM cell of dimensions $a = 3.05$ m, $b = 3.66$ m, and $g = 1.02$ m and compared to results given in Hill's paper [2] based on numerical calculations by Gruner, as well as the exact waveguide formulas. The results are given in Table II. The perturbed-mode cutoff frequencies agree quite well except for the TE_{21} (45.4 versus 52.9 MHz) and the TM_{11} (47.5 versus 52.2 MHz) modes. However, the TE_{21}-mode cutoff frequency should be greater than that of the TE_{20} mode (49.2 MHz), thus Hill's entry is likely in error. Based on Weil and Gruner's results [1], the TE_{21}-mode cutoff frequency should be approximately 50.4 MHz.

The TM_{11}-modal equation result does not agree as well. The integral equation for the TM case is somewhat different from that for the TE case. The basic small-gap approximation is weaker and agreement is not expected to be quite as good [5].

A second example is a symmetric NBS cell ($a = b = 1.5$ m; $g = 0.26$ m; $L_c = L_E = 3.0$ m) also analyzed in Hill's paper. Weak resonances were detected at 38, 50, and 65 MHz, while relatively strong resonances appeared at 61, 74, 85, and 97 MHz. From these data, Hill generates the results listed in Table III. We have added a column showing $f_{c(m,n)}$ values based on Table I, which agree well with Hill's figures. Hill essentially leaves the TM_{11} entries empty so we have an added $f_{c(1,1)}$ value of 115 MHz interpolated from a figure found in [4] and completed the line based on this value. The $f_{R(m,n,p)}$ column shows both Hill's numbers and those found via (3) with Table I $f_{c(m,n)}$ values inserted. The X_{mn} values used in Table III are averages generated by Hill (see Table IV, [2]) based on an analysis of two different cells. Table III may now be used to identify the measured resonances. The weak resonances at 38 and 65 MHz are the TE_{011} and TE_{012} resonances, respectively. Resonances at 61, 74, 85, and 97 MHz can be recognized as TE_{101}, TE_{111}, TE_{102}, and TE_{112} resonances, respectively. The expected TE_{013} resonance at 89 MHz may have been masked by the large TE_{112} resonance or the probe placement may have been such that this resonance was not detected. The apparent weak resonance at 50 MHz was probably a voltage standing-wave ratio (VSWR) problem due to mismatches.

The weak/strong resonance effect illustrates an important point. The TE_{01} mode in a small-gap TEM cell has strong gap-fringing fields while not exhibiting significant fields in the central test area. Therefore, although the TE_{011} is the first possible resonance, it is usually not excited unless a large test object or some other perturbation is present. The TE_{01}-mode gap confinement also accounts for its large taper factor (X_{01}) relative to those associated with the other TE modes, such as X_{10} for the TE_{10} or X_{11} for the TE_{11}. The TE_{01}-mode gap fields penetrate beyond the cutoff point more effectively than modes with more uniformly distributed fields.

For the above TEM cell, depending on the usage, we may be able to extend its usable frequency range beyond the

TABLE II
CUTOFF FREQUENCIES IN A LARGE ($a = 3.05$, $b = 3.66$, AND $g = 1.02$ m) SYMMETRIC TEM CELL
Exact agreement for the TE_{10}, TE_{02}, TE_{12}, TE_{20}, and TM_{12} modes follows from the use of rectangular waveguide formulas.

Mode	$f_{c(m,n)}$ (MHz)	
	Hill [2]	Table 1
TE_{01}	15.2	15.5
TE_{10}	24.6	24.6
TE_{11}	31.3	31.9
TE_{02}	41.0	41.0
TE_{12}	47.8	47.8
TE_{20}	49.2	49.2
TE_{21}	45.4	52.9
TM_{11}	47.5	52.2
TM_{12}	47.8	47.8

nominal limit of the TE_{011} resonance (40.6 MHz). For example, Hill [2] suggests that the unusable bandwidth about the TE_{101} resonance ranges from 33 percent of $f_{R(101)}$ (60.5 MHz) for bioeffects dosimetry to 6 percent for probe calibrations. The earlier TE_{011} resonance (40.6 MHz) interacts negligibly with centrally placed test objects. Thus this cell could be used up to 50 MHz for bioeffects dosimetry and up to 53 MHz for probe calibrations. Additional windows above the TE_{101} resonance may exist, especially for small test objects.

III. CUTOFF FREQUENCIES OF HIGHER ORDER MODES—ASYMMETRIC CELL

Most TEM cells are symmetric. However, some thought has been given to the use of asymmetric cells for EMI/EMC measurements [7]. A vertical offset of the inner conductor, as shown in Fig. 2, would create two chambers of unequal size. These might allow the testing of both large equipment and small probes without increasing the overall size of the cell and, consequently, reducing its bandwidth. However, one sacrifices field uniformity and strength in the larger chamber, and the asymmetric cell will have a more complicated modal structure.

The modal equations listed in Table I are actually special cases of the asymmetric formulas derived in [3]–[6]. We will list in Table IV only the first three asymmetric TEM-cell modal equations, all TE modes. Crawford and Workman [7] have published some data on resonances in an asymmetric cell based on VSWR measurements.

However, a number of problems present themselves when

TABLE III
ANALYSIS OF A LARGE ($a = b = 1.5$, $g = 0.26$, $L_c = L_E = 3.0$ m) NBS
TEM CELL

Mode	$f_{c(m,n)}$ (MHz)		X_{mn}	$\frac{c}{2L_{mn}}$ (MHz)	Resonance Type $m\ n\ p$	$f_{R(m,n,p)}$ (MHz)	
	Hill [2]	Table 1				Hill [2]	Table 1
TE$_{01}$	29.0	29.2	0.77	28.2	0 1 1	40.0	40.6
					0 1 2	63.0	63.5
					0 1 3	89.0	89.5
TE$_{10}$	50.0	50.0	0.47	34.0	1 0 1	60.0	60.5
					1 0 2	84.0	84.4
TE$_{11}$	63.5	64.3	0.43	35.0	1 1 1	73.0	73.2
					1 1 2	95.0	95.0
TM$_{11}$	115.0[4]	115.9	1.00	11.6	1 1 0	115.0[4]	115.9

TABLE IV
ASYMMETRIC TEM-CELL SMALL-GAP MODAL EQUATIONS

Mode [ref]	Modal Equation: $f_{c(m,n)} = \frac{150}{\pi}\frac{x}{b}$ MHz
TE$_{01}$ [3]	$\frac{1}{x}[\cot\frac{b_1}{b}x + \cot\frac{b_2}{b}x] = \frac{4}{\pi}(\frac{a}{b})[\ln(\frac{2a}{\pi g}) + R_{TE_{01}}]$ $R_{TE_{01}} = \frac{1}{2}\sum_{p=1}^{\infty}\frac{1}{p}(\coth\frac{p\pi b_1}{a} + \coth\frac{p\pi b_2}{a} - 2)\cos^2(\frac{p\pi g}{a})$
TE$_{10}$	$x = \frac{\pi}{2}(\frac{b}{a})$
TE$_{11}$ [3,5]	$x = [y^2 + (\frac{\pi b}{2a})^2]^{1/2}$ $\cos^2(\frac{\pi g}{2a})\frac{1}{y}[\cot\frac{b_1}{b}y + \cot\frac{b_2}{b}y]$ $= \frac{2}{\pi}(\frac{a}{b})[\ln(\frac{8a}{\pi g}) - 2\cos^2(\frac{\pi g}{2a}) + R_{TE_{11}}]$ $R_{TE_{11}} = \sum_{p=1}^{\infty}\frac{1}{2p+1}[\coth\frac{(2p+1)\pi b_1}{2a} + \coth\frac{(2p+1)\pi b_2}{2a} - 2]\cos^2(\frac{(2p+1)\pi g}{2a})$

trying to identify resonances. Hill [2] points out that VSWR measurements do not necessarily detect all resonances. Another difficulty is setting the proper taper fraction X_{mn}. In order to analyze properly their cell [7], a more careful resonance-detection measurement procedure, as in [2], would be desirable.

IV. CONCLUSION

This paper has reviewed a number of modal equations governing higher order modes and resonances in TEM cells. Both symmetric and asymmetric cells are discussed. These equations are simple to use and should aid TEM-cell users in predicting and detecting cell resonances, thereby extending usable bandwidth of a cell.

APPENDIX

The derivation of the gap-perturbed modal equations listed in Tables I and IV follows essentially the same steps in each case. First, the unknown fields in the entire RCTL cross section are expanded in terms of a set of orthogonal basis functions [3]. These basis functions correspond to the rectangular-waveguide modes in either the upper ($2a \times b_1$) or lower ($2a \times b_2$) RCTL chambers (see Fig. 2). Field continuity across the gap yields integral equations of the form [3]

$$\int_0^g f(t')G(t,\ t')\ dt' = 0 \qquad (5)$$

where t and t' are gap variables, $(t,\ t') \epsilon\ [0,\ g]$, $f(t')$ is an unknown field component in the gap, and $G(t,\ t')$ is a known symmetric kernel. In each case, the kernel becomes singular as $|t - t'| \to 0$. This dominant singular behavior $G^{(1)}(t,\ t')$ may be extracted leaving a finite secondary term $G^{(2)}(t,\ t')$, i.e.,

$$G(t,\ t') = G^{(1)}(t,\ t') + G^{(2)}(t,\ t'). \qquad (6)$$

Assuming a small gap allows one to approximate both kernel contributions. The resulting simplified integral equation may then be solved directly.

As examples, consider the gap-perturbed TE modes. As derived by Tippet et al. [3], the TE-kernel components $G^{(1)}(t,\ t')$ and $G^{(2)}(t,\ t')$ are given by

$$G^{(1)}(t,\ t') = \frac{2}{\pi}\ln\left[\tan\frac{\pi}{4a}|t+t'|\ \tan\frac{\pi}{4a}|t-t'|\right]$$

$$G^{(2)}(t,\ t') = \frac{1}{\pi}\sum_{j=1}^{2}\frac{b_j}{a}\sum_{p=0}^{\infty}g_{2p+1}^{(j)}(t,\ t') \qquad (7)$$

for the $\text{TE}_{2m+1,\,2n+1}$ (odd, gap-perturbed) modes; and

$$G^{(1)}(t,\ t') = \frac{1}{\pi} \ln \left[4 \sin \frac{\pi}{2a} |t+t'| \sin \frac{\pi}{2a} |t-t'| \right]$$

$$G^{(2)}(t,\ t') = \frac{1}{\pi} \sum_{j=1}^{2} \frac{b_j}{a} \left\{ \frac{\pi \cot b_j K}{2 b_j K} + \sum_{p=1}^{\infty} g_{2p}^{(j)}(t,\ t') \right\} \quad (8)$$

for the $\text{TE}_{2m,2n}$ (even, gap-perturbed) modes. All dimensions (a, b_1, b_2, g) are defined in Fig. 2, and

$$g_p^{(j)}(t,\ t') = \left[\frac{\cot \pi \alpha_p^{(j)}}{\alpha_p^{(j)}} + \frac{2a}{p b_j} \right] \cos \frac{p \pi t}{2a} \cos \frac{p \pi t'}{2a}$$

$$\alpha_p^{(j)} = \frac{b_j}{\pi} \left[K^2 - \left(\frac{p \pi}{2a} \right)^2 \right]^{1/2} \quad (9)$$

$$K^2 = k^2 - \gamma^2$$

where $k = 2\pi/\lambda$, and γ is the propagation constant in the RCTL.

Now, assume that the gap is small. In the singular terms this allows us to replace the tangent and sine functions by their small argument approximations, i.e.,

$$G^{(1)}(t,\ t') \approx \frac{2}{\pi} \ln \left[\left(\frac{\pi}{4a} \right)^2 |t^2 - t'^2| \right] \quad (\text{TE}_{2m+1,2n+1})$$

$$G^{(1)}(t,\ t') \approx \frac{1}{\pi} \ln \left[\left(\frac{\pi}{a} \right)^2 |t^2 - t'^2| \right] \quad (\text{TE}_{2m,2n+1}) \quad (10)$$

for the odd and even cases, respectively. Since $|t \pm t'|$ is bounded by $2g$, terms like $(\pi g/2a)^2/3$ and $(\pi g/2a)^2/6$ are neglected when compared to unity in approximating the tangent and sine terms.

Next, consider the finite kernel terms $G^{(2)}(t,\ t')$, noting that for large p, i.e., $(p\pi/a)^2 \gg K^2$,

$$\cot \frac{\pi \alpha_p^{(j)}}{\alpha_p^{(j)}} \sim \frac{2a}{p b_j} \quad (11)$$

implies that the summand $g_p^{(j)}(t, t')$ decays rapidly.

Thus only a few terms should contribute significantly. If, in addition, $(p \pi g/2a) \ll 1$ for these initial terms, then the cosines may be replaced with unity and $G^{(2)}(t,\ t') \approx G^{(2)}$, a constant, in each case

$$G^{(2)} = \frac{1}{\pi} \sum_{j=1}^{2} \frac{b_j}{a} \sum_{p=0}^{\infty} g_{2p+1}^{(j)}(0,\ 0) \quad (\text{TE}_{2m+1,2m+1})$$

$$G^{(2)} = \frac{1}{\pi} \sum_{j=1}^{2} \frac{b_j}{a} \left\{ \frac{\pi \cot b_j K}{2 b_j K} + \sum_{p=1}^{\infty} g_{2p}^{(j)}(0,\ 0) \right\} \quad (\text{TE}_{2m,2n+1}).$$

$$(12)$$

These are the proper limits for $G^{(2)}_{(t,t')}$ as $g \to 0$ and, in fact, those used in [3]. These approximations tend to yield good results for the TE_{01} and TE_{11} modes. However, as additional modes are considered, K increases and larger p indices need to

be retained. Thus the cosine terms (9) may no longer be near unity over the range $(t, t') \in [0, g]$. An alternate approximation is to replace the cosines by their value at gap edge. The justification is that, for TE modes, $f(t')$ in (5) is proportional to the horizontal component of the electric field which diverges at the gap edge. Thus we will weight the approximate kernel toward this point. This again reduces $G^{(2)}(t,\ t')$ to a constant, which aids in solving the integral equation (5), but also retains more information about the gap size. Thus we replace $g_p^{(j)}(0, 0)$ in (12) with $g_p^{(j)}(g, g)$, resulting in

$$G^{(2)} = \frac{1}{\pi} \sum_{j=1}^{2} \frac{b_j}{a} \sum_{p=0}^{\infty} g_{2p+1}^{(j)}(g,\ g) \quad (\text{TE}_{2m+1,2n+1})$$

$$G^{(2)} = \frac{1}{\pi} \sum_{j=1}^{2} \frac{b_j}{a} \left\{ \frac{\pi \cot b_j K}{2 b_j K} + \sum_{p=1}^{\infty} g_{2p}^{(j)}(g,\ g) \right\} \quad (\text{TE}_{2m,2n+1}).$$

$$(13)$$

Clearly, these reduce to (7) as $(g/a) \to 0$.

The approximate integral equation now becomes

$$\int_0^g f(t') \{ G^{(1)}(t,\ t') + G^{(2)} \} \ dt' = 0 \quad (14)$$

where $G^{(1)}(t, t')$ is a simple logarithmic kernel and $G^{(2)}$ is a constant. This type of equation may be readily solved [3] with the result that

$$G^{(2)} = \frac{2}{\pi} \ln \left[\frac{8a}{\pi g} \right] \quad (\text{TE}_{2m+1,2n+1})$$

$$G^{(2)} = \frac{2}{\pi} \ln \left[\frac{2a}{\pi g} \right] \quad (\text{TE}_{2m,2n+1}). \quad (15)$$

Together, (13) and (15) generate the TE modal equations.

For example, begin with the $\text{TE}_{2m,2n+1}$ modal equation which is

$$\frac{1}{\pi} \sum_{j=1}^{2} \frac{b_j}{a} \left\{ \frac{\pi \cot b_j K}{2 b_j K} + \sum_{p=1}^{\infty} \left[\frac{\cot \pi \alpha_{2p}^{(j)}}{\alpha_{2p}^{(j)}} + \frac{a}{p b_j} \right] \right.$$
$$\left. \cdot \cos^2 \frac{p \pi g}{a} \right\} = \frac{2}{\pi} \ln \left[\frac{2a}{\pi g} \right]. \quad (16)$$

If the gap is very small, then the right-hand side of (16) will be large. One possible solution is to let $b_j K$ be small; thus the first term in parentheses dominates. Note that K small implies that $\gamma^2 \approx k^2$, the TEM-mode propagation constant. Thus this mode will not be cut off in the limit as $(g/a) \to 0$, and may be identified as the TE_{01} mode. Noting that $K^2 \ll (p\pi/a)^2$ for $p \geq 1$ in $\alpha_{2p}^{(j)}$, we arrive at TE_{01} asymmetric-cell modal equation

$$\frac{\cot b_1 K + \cot b_2 K}{2aK} = \frac{2}{\pi} \left\{ \ln \left(\frac{2a}{\pi g} \right) + \frac{1}{2} \sum_{p=1}^{\infty} \frac{1}{p} \right.$$
$$\left. \cdot \left[\coth \frac{p \pi b_1}{a} + \coth \frac{p \pi b_2}{a} - 2 \right] \cos^2 \frac{p \pi g}{a} \right\}. \quad (17)$$

239

This reduces to the TE_{01} form given in Table IV if we let $x = bK$, and to the symmetric-cell equation given in Table I if we let $b_1 = b_2 = b$.

The next solution is to let the cot $\alpha_{2p}^{(j)}/\alpha_{2p}^{(j)}$ term dominate for $p = 1$. This means $K^2 \approx (\pi/a)^2$; thus $\gamma^2 \approx k^2 - (\pi/a)^2$, which is the TE_{20} propagation constant. Thus this solution will yield the TE_{21} modal equation. Letting $K^2 \lll (p\pi/a)^2$ for $p \geq 2$ in $\alpha_{2p}^{(j)}$, we arrive at

$$\frac{\cot b_1 K + \cot b_2 K}{2aK} + \left[\frac{b_1 \cot \pi\alpha_2^{(1)}}{a\pi\alpha_2^{(1)}} + \frac{b_2 \cot \pi\alpha_2^{(2)}}{a\pi\alpha_2^{(2)}} \right]$$

$$\cdot \cos^2 \frac{\pi g}{a} = \frac{2}{\pi} \ln \left(\frac{2a}{\pi g} \right) - \cos^2 \frac{\pi g}{a}$$

$$+ \frac{1}{2} \sum_{p=2}^{\infty} \frac{1}{p} \left(\coth \frac{p\pi b_1}{a} + \coth \frac{p\pi b_2}{a} - 2 \right) . \quad (18)$$

Letting $x = bK$ and $y = [x^2 - (\pi b/a)^2]^{1/2}$ reduces this to the result listed in Table IV, and so forth. The TE_{11} modal equation follows from the $TE_{2m+1,2n+1}$ set of equations if we

set $p = 1$ as the dominant term and let $y = [x^2 - (\pi b/2a)^2]^{1/2}$. The TM modal equations are based on a similar analysis as outlined in [5] and [6].

REFERENCES

[1] C. M. Weil and L. Gruner, "Higher order mode cutoff in rectangular striplines," *IEEE Trans. Microwave Theory Tech.*, vol. MTT-32, pp. 638–641, June 1984.

[2] D. A. Hill, "Bandwidth limitations of TEM cells due to resonances," *J. Microwave Power*, vol. 18, pp. 181–195, June 1983.

[3] J. C. Tippet, D. C. Chang, and M. L. Crawford, "An analytical and experimental determination of the cutoff frequencies of higher-order TE modes in a TEM cell," Nat. Bur. Stand., Boulder, CO, Rep. NBSIR 76-841, June 1976.

[4] J. C. Tippet and D. C. Chang, "Higher order modes in rectangular coaxial line with infinitely thin inner conductor," Nat. Bur. Stand., Boulder, CO, Rep. NBSIR 78-873, Mar. 1978.

[5] P. F. Wilson, D. C. Chang, and M. T. Ma, "Excitation of a TEM cell by a vertical electrical hertzian dipole," Nat. Bur. Stand., Boulder, CO, Tech. Note 1073, Mar. 1981.

[6] P. F. Wilson, "On slot-coupled waveguide and transmission line structures," Ph.D. dissertation, Dept. Elec. Eng., Univ. Colorado, Boulder, CO, 1983.

[7] M. L. Crawford and J. L. Workman, "Asymmetric versus symmetric TEM cells for EMI measurements," in *IEEE 1978 Int. Symp. EMC-Symp. Rec.* (Atlanta, GA), June 1978, pp. 204–208.

U.S. DEPT. OF COMM. **BIBLIOGRAPHIC DATA** **SHEET** (See instructions)	1. PUBLICATION OR REPORT NO. NBS/TN-1319	2. Performing Organ. Report No.	3. Publication Date August 1988

4. TITLE AND SUBTITLE

Generation of Standard Electromagnetic Fields in a TEM Cell

5. AUTHOR(S)

Motohisa Kanda and R. David Orr

6. PERFORMING ORGANIZATION (If joint or other than NBS, see instructions) **NATIONAL BUREAU OF STANDARDS** **DEPARTMENT OF COMMERCE** **WASHINGTON, D.C. 20234**	**7. Contract/Grant No.** **8. Type** of Report & Period Covered

9. SPONSORING ORGANIZATION NAME AND COMPLETE ADDRESS (Street, City, State, ZIP)

10. SUPPLEMENTARY NOTES

☐ Document describes a computer program; SF-185, FIPS Software Summary, is attached.

11. ABSTRACT (A 200-word or less factual summary of most significant information. If document includes a significant bibliography or literature survey, mention it here)

This paper documents the facilities and procedures used by the National Bureau of Standards to calibrate radio frequency electric field probes using a transverse electromagnetic (TEM) cell. The advantages, limitations, and physical characteristics of TEM cells are presented. Impedance, field uniformity, and mode structure, critical aspects of a cell as a standard field enclosure, are discussed. The paper concludes with sections on setup and measurement procedures for users, uncertainty in the standard field, and statistical control of the calibration system. Copies of key references are included to provide ready access to the details of topics summarized in the text.

12. KEY WORDS (Six to twelve entries; alphabetical order; capitalize only proper names; and separate key words by semicolons)

antenna; antenna calibration; calibration; electromagnetic field; radio frequency; standard field; TEM cell; transverse electromagnetic cell.

13. AVAILABILITY

☒ Unlimited

☐ For Official Distribution. Do Not Release to NTIS

☒ Order From Superintendent of Documents, U.S. Government Printing Office, Washington, D.C. 20402.

☐ Order From National Technical Information Service (NTIS), Springfield, VA. 22161.

14. NO. OF PRINTED PAGES

246

15. Price

NBS Technical Publications

Periodical

Journal of Research—The Journal of Research of the National Bureau of Standards reports NBS research and development in those disciplines of the physical and engineering sciences in which the Bureau is active. These include physics, chemistry, engineering, mathematics, and computer sciences. Papers cover a broad range of subjects, with major emphasis on measurement methodology and the basic technology underlying standardization. Also included from time to time are survey articles on topics closely related to the Bureau's technical and scientific programs. Issued six times a year.

Nonperiodicals

Monographs—Major contributions to the technical literature on various subjects related to the Bureau's scientific and technical activities.

Handbooks—Recommended codes of engineering and industrial practice (including safety codes) developed in cooperation with interested industries, professional organizations, and regulatory bodies.

Special Publications—Include proceedings of conferences sponsored by NBS, NBS annual reports, and other special publications appropriate to this grouping such as wall charts, pocket cards, and bibliographies.

Applied Mathematics Series—Mathematical tables, manuals, and studies of special interest to physicists, engineers, chemists, biologists, mathematicians, computer programmers, and others engaged in scientific and technical work.

National Standard Reference Data Series—Provides quantitative data on the physical and chemical properties of materials, compiled from the world's literature and critically evaluated. Developed under a worldwide program coordinated by NBS under the authority of the National Standard Data Act (Public Law 90-396).
NOTE: The Journal of Physical and Chemical Reference Data (JPCRD) is published quarterly for NBS by the American Chemical Society (ACS) and the American Institute of Physics (AIP). Subscriptions, reprints, and supplements are available from ACS, 1155 Sixteenth St., NW, Washington, DC 20056.

Building Science Series—Disseminates technical information developed at the Bureau on building materials, components, systems, and whole structures. The series presents research results, test methods, and performance criteria related to the structural and environmental functions and the durability and safety characteristics of building elements and systems.

Technical Notes—Studies or reports which are complete in themselves but restrictive in their treatment of a subject. Analogous to monographs but not so comprehensive in scope or definitive in treatment of the subject area. Often serve as a vehicle for final reports of work performed at NBS under the sponsorship of other government agencies.

Voluntary Product Standards—Developed under procedures published by the Department of Commerce in Part 10, Title 15, of the Code of Federal Regulations. The standards establish nationally recognized requirements for products, and provide all concerned interests with a basis for common understanding of the characteristics of the products. NBS administers this program as a supplement to the activities of the private sector standardizing organizations.

Consumer Information Series—Practical information, based on NBS research and experience, covering areas of interest to the consumer. Easily understandable language and illustrations provide useful background knowledge for shopping in today's technological marketplace.
Order the above NBS publications from: Superintendent of Documents, Government Printing Office, Washington, DC 20402.
Order the following NBS publications—FIPS and NBSIR's—from the National Technical Information Service, Springfield, VA 22161.

Federal Information Processing Standards Publications (FIPS PUB)—Publications in this series collectively constitute the Federal Information Processing Standards Register. The Register serves as the official source of information in the Federal Government regarding standards issued by NBS pursuant to the Federal Property and Administrative Services Act of 1949 as amended, Public Law 89-306 (79 Stat. 1127), and as implemented by Executive Order 11717 (38 FR 12315, dated May 11, 1973) and Part 6 of Title 15 CFR (Code of Federal Regulations).

NBS Interagency Reports (NBSIR)—A special series of interim or final reports on work performed by NBS for outside sponsors (both government and non-government). In general, initial distribution is handled by the sponsor; public distribution is by the National Technical Information Service, Springfield, VA 22161, in paper copy or microfiche form.